MARTA AGNIESZKA BRZEZIŃSKA

BEYOND THE TEN-FOLD WAY: NOVEL TOPOLOGICAL PHASES IN LOW-DIMENSIONAL SYSTEMS

BEYOND THE TEN-FOLD WAY: NOVEL TOPOLOGICAL PHASES IN LOW-DIMENSIONAL SYSTEMS

A dissertation submitted to attain the degree of

DOCTOR OF SCIENCES of WROCŁAW UNIVERSITY OF SCIENCE AND TECHNOLOGY

presented by

MARTA AGNIESZKA BRZEZIŃSKA

Master of Science in Physics,

Wrocław University of Science
and Technology, Poland

born on 22 August 1991

Supervisors:

Prof. Arkadiusz Wójs,

Prof. Titus Neupert,

Auxiliary supervisor:

Dr. Paweł Potasz

2020

ABSTRACT

Topological states of matter have arisen as one of the rapidly growing fields in condensed matter physics, holding promise for future technologies, including spintronics and quantum computing. The notion of topology underlies exotic phenomena such as emergent collective excitations or protected edge modes exhibited in the low-energy spectrum. In particular, in non-interacting fermionic systems the connection between bulk and boundary degrees of freedom is established by the celebrated *bulk-boundary correspondence*. In the presence (or absence) of fundamental symmetries: time-reversal, particle-hole and chiral, it is possible to classify free-fermionic, gapped systems in different spatial dimensions by the means of the ten-fold way. This classification scheme of topological insulators and superconductors tabulates all possible combinations of aforementioned symmetries and assigns a relevant topological invariant to each symmetry class. Despite its immense success, the ten-fold way turned out to be incomplete in the light of recent theoretical developments and experimental efforts.

This thesis discusses topological aspects of selected free-fermionic systems in low dimensions ($d \leq 2$) that go *beyond* the ten-fold way. We address three distinct research directions in which the existing classification can be extended. In the first part, we investigate the Hofstadter model on two fractal geometries, namely the Sierpiński carpet and gasket. While being embedded in two-dimensional space, these fractals are characterized by a non-integer Hausdorff dimension. In addition, their connectivity properties are in a stark contrast to regular lattices as there is no clear distinction between edges and bulk. We numerically study the spectral and eigenstates localization properties, and observe a hierarchy of edge-like states located at different fractal depths. We employ topological invariants defined in real space: the Bott index and the Chern number, and identify regions in the energy spectrum with non-trivial topology. We further compute the phase diagram in the presence of disorder and conclude that characteristic features of the integer quantum Hall effects are also observed in *almost* two-dimensional systems.

The second part of this dissertation is devoted to the significance of spatial symmetries. We start with concrete examples of group-V monolayers: atomically thin layers of bismuth and antimony, described within a tight-binding approximation. We show that a free-standing layer of bismuth hosts a quantum spin Hall phase, whereas a single layer of antimony has a trivial $\mathbb{Z}_2$ invariant. Applying a moderate strain to free-standing buckled layers, however, results in completely flat structures called bismuthene and antimonene, which are realizing a topological crystalline insulating phase protected by the mirror symmetry along the z axis. Apart from the direct computations of relevant topological invariants, we use entanglement measures as complementary tools to define the bulk topology. We present how the full spectrum of the reduced density matrix corresponding to a spatially separated subsystem allows to differentiate between distinct topological states. Additionally, we study the scaling of the entanglement entropy across different topological phase transitions driven by doping, external electric field and strain. An even more profound consequence of the crystal symmetries is the existence of *obstructed atomic limits*, i. e. systems for which the strong topological indices are trivial, but are not adiabatically connected to a trivial atomic limit. We propose a classification scheme for obstructed atomic limits in two dimensions, where Wilson loops and symmetry indicators play the role of topological invariants. We find that a buckled monolayer of antimony, among other

suggested material candidates, is actually an obstructed limit and exhibits symmetry-protected corner charges.

In the third part, we discuss the interplay between topology and non-Hermiticity in Hamiltonians providing an effective description of open systems. Introducing non-Hermiticity leads to unique features such as exceptional points or the anomalous localization of all eigenstates at the boundary (the so-called skin effect). Using the π-flux model on a square lattice with a non-Hermitian extension, we demonstrate a novel phenomenon dubbed the *reciprocal* skin effect, which does not require any direction-dependent hoppings. Theoretical predictions are supported by experimental results obtained by measuring a topolectrical circuit, which realizes the desirable physics of the non-Hermitian π-flux model.

Keywords: topological phases, tight-binding models, fractals, the Hofstadter model, entanglement, topological (crystalline) insulators, non-Hermitian Hamiltonians

STRESZCZENIE

Topologiczne fazy materii stały się jedną z niezwykle szybko rozwijających się dziedzin fizyki materii skondensowanej ze względu na obiecujące przyszłościowe zastosowania na polu spintroniki oraz informatyki kwantowej. Pojęcie topologii leży u podstaw egzotycznych zjawisk takich jak kolektywne wzbudzenia lub chronione stany brzegowe występujące w niskoenergetycznej części widma. W szczególności, dla układów nieoddziałujących fermionów istnieje *zasada korespondencji* między stopniami swobody materiału objętościowego a jego brzegu. W obecności (lub przy braku) wewnętrznych symetrii: odwrócenia w czasie, typu cząstka-dziura i chiralnej, możliwa jest klasyfikacja układów swobodnych fermionów posiadających przerwę w widmie energetycznym materiału objętościowego zdefiniowanych w różnych wymiarach przestrzennych. Zestawienie wszystkich możliwych kombinacji wyżej wymienionych symetrii prowadzi do wyróżnienia dziesięciu klas symetrii i przypisania im odpowiednich niezmienników topologicznych. Pomimo ogromnego sukcesu tej klasyfikacji izolatorów i nadprzewodników topologicznych, okazała się ona niewystarczająca w świetle ostatnich dokonań teoretycznych i eksperymentalnych.

Przedłożona rozprawa doktorska dotyczy efektów topologicznych w wybranych nieoddziałujących układach elektronowych, które *nie* należą do jednej z dziesięciu wspomnianych klas symetrii. Przedstawione zostaną trzy odrębne kierunki badań, na bazie których można rozszerzyć istniejącą klasyfikację. W pierwszej części analizowany jest model Hofstadtera zdefiniowany na dwóch geometriach fraktalnych: dywanie i trójkącie Sierpińskiego. Fraktale te, osadzone w przestrzeni dwuwymiarowej, charakteryzują się niecałkowitym wymiarem Hausdorffa. Istotną różnicą w porównaniu do sieci regularnych jest brak możliwości określenia które węzły sieci stanowią materiał objętościowy, a które należą do brzegu. Numerycznie przestudiowane zostały własności spektralne i lokalizacja stanów własnych, gdzie zaobserowano hierarchię stanów krawędziowych usytuowanych na różnych poziomach głębokości fraktalnej. Przy pomocy liczby Cherna w przestrzeni rzeczywistej oraz indeksu Botta, zidentyfikowano regiony w widmie energetycznym, w których stany mają nietrywialną topologię. Następnie przeanalizowano diagram fazowy w funkcji nieporządku i wywioskowano, że charakterystyczne cechy całkowitego kwantowego efektu Halla są również obserwowane w układach *prawie* dwuwymiarowych.

Druga część rozprawy poświęcona jest znaczeniu symetrii wynikających ze struktury przestrzennej sieci krystalicznych. Konkretnymi przykładami są tutaj monowarstwy grupy V: atomowo cienkie warstwy bizmutu i antymonu, opisane w ramach modeli ciasnego wiązania. Wykazano, że wolnostojąca warstwa bizmutu wykazuje kwantowy spinowy efekt Halla, podczas gdy pojedyncza warstwa antymonu jest opisana trywialnym niezmiennikiem $\mathbb{Z}_2$. Naprężanie tych układów prowadzi do otrzymania całkowicie płaskich warstw zwanych bizmutenem i antymonenem, które realizują fazę topologicznego izolatora krystalicznego chronionego przez symetrię lustrzaną wzdłuż osi z. Oprócz bezpośrednich obliczeń odpowiednich niezmienników topologicznych, zostały zastosowane miary splątania jako uzupełniające narzędzia do zdefiniowania topologii. Zaprezentowano w jaki sposób pełne widmo zredukowanej macierzy gęstości, odpowiadające przestrzennie oddzielonemu podsystemowi, pozwala na rozróżnienie między różnymi stanami topologicznymi. Dodatkowo zbadano skalowanie entropii

splątania podczas topologicznych przejść fazowych spowodowanych przez domieszkowanie, zewnętrzne pole elektryczne oraz naprężenie. Jeszcze bardziej fundamentalną konsekwencją symetrii krystalicznych jest istnienie *ograniczonych izolatorów atomowych* (ang. *obstructed atomic limits*), tj. układów dla których silne indeksy topologiczne (jak liczba Cherna) są trywialne, ale nie są topologicznie równoważne izolatorom trywialnym w których stany elektronowe lokalizują się na węzłach sieci krystalicznej. Została zaproponowana klasyfikacja dwuwymiarowych ograniczonych izolatorów atomowych na bazie pętli Wilsona i wskaźników symetrii. Okazuje się, że monowarstwa antymonu, pośród innych przedstawionych potencjalnych materiałów, jest w rzeczywistości takim ograniczonym izolatorem i wykazuje chronione symetrią ładunki zlokalizowane na rogach sieci.

W trzeciej części omawiane jest wzajemne oddziaływanie topologii i niehermitowskości w hamiltonianach opisujących efektywnie układy otwarte. Wprowadzenie członu niehermitowskiego prowadzi do wyjątkowych zjawisk takich jak punkty wyjątkowe (ang. exceptional points) oraz anomalna lokalizacja wszystkich stanów własnych na brzegu zwana efektem naskórkowości (ang. skin effect). Posługując się modelem π-flux na sieci kwadratowej z dodatkowym członem niehermitowskim, został zademonstrowany nowy efekt nazwany *odwrotnym* efektem naskórkowości, który nie wymaga żadnych całek przeskoku zależnych od kierunku. Przewidywania teoretyczne zostały poparte wynikami eksperymentalnymi uzyskanymi poprzez pomiary specjalnie zaprojektowanego obwodu elektrycznego, który realizuje fizykę niehermitowskiego modelu π-flux.

Słowa kluczowe: fazy topologiczne, modele ciasnego wiązania, fraktale, model Hofstadtera, splątanie kwantowe, (krystaliczne) izolatory topologiczne, hamiltoniany niehermitowskie

ACKNOWLEDGEMENTS

This thesis would not have been possible to complete without the support and guidance that I received from many wonderful individuals to whom I want to say *thank you*.

I am deeply grateful to my supervisor from the Wrocław University of Science and Technology, Arkadiusz Wójs, for encouraging me to work in the field of condensed matter physics and accepting me as a PhD student. His good advices and assistance, especially at the beginning of my scientific career, have been invaluable.

I am fully indebted to Titus Mangham-Neupert from the University of Zurich for giving me the life-changing opportunity to pursue the research in his group. His enthusiasm, creativity and wisdom are inspirational. I do appreciate his endless patience and continued support of my work.

I would like to acknowledge Paweł Potasz for helping me during my master studies and first years of doctorate. His experience in numerical methods and willingness to share the knowledge were crucial at early stages of my serious coding.

My appreciation extends to my colleagues from UZH. I have benefited a lot from our joint projects and not work-related discussions. In particular, I would like to thank Frank for having fruitful collaborations and great time during many conferences.

Living in Switzerland would have been more complicated without the assistance of the administrative staff at UZH. I am especially grateful to Gaby Aeppli-Koller and Brigitte Freund for helping me with all problems related to the Swiss bureaucracy. I also cannot forget about the people outside the workplace that helped me in settling down in Zurich: Samuel, Antonio and Martin.

Many thanks to my fellow doctoral students from Wrocław, with a special mention of Maciek and Adam; the laughs we shared will be remembered. I would like to express my heartfelt gratitude to Karolina for our friendship and being someone I can count on.

Thank you, Beata, for being a close friend, despite the kilometres that separate us. I hope we will see each other more often soon!

I cannot thank Kasia enough for our long-lasting friendship. Thanks for being supportive and helping me in surviving the ups and downs all these years.

I owe a great debt of gratitude to Loïc, who carefully proofread my thesis and gave a lot of helpful suggestions. I thank you so much for the incredible moral support over the last months.

Above all, I would like to thank my family for their endless love and not letting me give up.

To my Mom

LIST OF PUBLICATIONS

ARTICLES INCLUDED IN THE THESIS

1. T. Hofmann, T. Helbig, F. Schindler, N. Salgo, **M. Brzezińska**, M. Greiter, T. Kiessling, D. Wolf, A. Vollhardt, A. Kabaši, C. H. Lee, A. Bilušič, R. Thomale, T. Neupert, "Reciprocal skin effect and its realization in a topolectrical circuit", *Phys. Rev. Research* **2**, 023265 (2 2020), Editors' Suggestion
   Author contributions: T. H., T. H., F. S., M. B., M. G, T. K., D. W., C. H. L., R. T., and T. N. conceived the project. T. H. and T. H. performed numerical simulations. A. V., A. K., and A. B. were responsible for circuit implementation. T. H., T. H., and N. S. perfomed the measurements. T. H., T. H., F. S., M. B., C. H. L., R. T., and T. N. worked out the theoretical results.
2. F. Schindler, **M. Brzezińska**, W. A. Benalcazar, M. Iraola, A. Bouhon, S. S. Tsirkin, M. G. Vergniory, T. Neupert, "Fractional corner charges in spin-orbit coupled crystals", *Phys. Rev. Research* **1**, 033074 (3 2019),
   Author contributions: F. S., M. B., W. A. B., A. B., and T. N. conceived the project and worked out the theoretical results, M. I., S. S. T, and M. G. V. performed first-principled calculations.
3. **M. Brzezińska**, A. M. Cook, T. Neupert, "Topology in the Sierpiński-Hofstadter problem", *Phys. Rev. B* **98**, 205116 (20 2018),
   Author contributions: M. B., A. M. C., and T. N. convinced the project and worked out the theoretical results.
4. N. Nouri, M. Bieniek, **M. Brzezińska**, M. Modarresi, S. Z. Borujeni, G. Rashedi, A. Wójs, P. Potasz, "Topological phases in Bi/Sb planar and buckled honeycomb monolayers", *Physics Letters A* **382**, 2952–2958 (2018),
   Author contributions: N. N., M. B., M. B., S. Z. B., G. R., A. W., and P.P convinced the project. N. N., M. B., M. B., and P. P. carried out the theoretical analysis and model calculations. M. M. performed first-principle calculations.
5. **M. Brzezińska**, M. Bieniek, T. Woźniak, P. Potasz, A. Wójs, "Entanglement entropy and entanglement spectrum of Bi_{1-x} Sb_x (111) bilayers", *Journal of Physics: Condensed Matter* **30**, 125501 (2018),
   Author contributions: M. B., M. B., P. P., and A. W. convinced the project. M. B., M. B., and P. P. carried out the model calculations. T. W. performed first-principle calculations.

OTHER ARTICLES

1. **M. Brzezińska**, S. S. Tsirkin, M. H. Fischer, T. Neupert, "Hybrid density functional theory with neural networks", in preparation, working title.
2. Z. Guguchia, D. J. Gawryluk, **M. Brzezińska**, S. S. Tsirkin, R. Khasanov, E. Pomjakushina, F. O. von Rohr, J. A. T. Verezhak, M. Z. Hasan, T. Neupert, H. Luetkens, A. Amato, "Nodeless superconductivity and its evolution with pressure in the layered Dirac semimetal 2M-WS_2", *npj Quantum Materials* **4**, 50 (2019).

3. W. Radosz, A. Mielnik-Pyszczorski, **M. Brzezińska**, K. Sznajd-Weron, "Q-voter model with nonconformity in freely forming groups: Does the size distribution matter?", *Phys. Rev. E* **95**, 062302 (6 2017).
4. P. Potasz, B. Jaworowski, M. Kupczyński, **M. Brzezińska**, P. Kaczmarkiewicz, A. Wójs, "Topological phase transitions in Chern insulators within three-band models", arXiv:1710.06631 (2017).

CONTENTS

LIST OF FIGURES

LIST OF TABLES

ABBREVIATIONS

1D, 2D, ...	one-dimensional, two-dimensional, ...
AZ	Atland-Zirnbauer
BZ	Brillouin zone
CB	conduction band
CS	chiral symmetry
DFT	density functional theory
DOS	density of states
EBR	elementary band representation
EE	entanglement entropy
ES	entanglement spectrum
HOTI	higher-order topological insulator
HSP	high-symmetry point
IR	irreducible representation
NN	nearest-neighbour
NNN	next-to-nearest neighbour
OAL	obstructed atomic limit
PHS	particle-hole symmetry
(I/F)QHE	(integer/fractional) quantum Hall effect
QSHE	quantum spin Hall effect
SG	space group
SLS	sublattice symmetry
SOC	spin-orbit coupling
SPT phase	symmetry-protected topological phase
SSH	Su-Schrieffer-Heeger
TCI	topological crystalline insulator
TI	topological insulator
TRIM	time-reversal invariant momentum
TRS	time-reversal symmetry
VB	valence band

INTRODUCTION

The classification of the different states of matter and the transition between them is a theme that lies at the heart of condensed matter physics. For a long time it was believed that Ginzburg-Landau theory [1], based on the spontaneous symmetry breaking paradigm, provides a complete description of phase transitions. It states that continuous transitions between phases can be described by a local physical observable – the order parameter – which vanishes in the high-symmetry (disordered) phase and becomes non-zero in the low-symmetry (ordered) phase. In magnetic systems, for instance, a magnetization serves as the order parameter at the ferromagnetic-paramagnetic transition. Crystals, on the other hand, break the continuous translational symmetry, leading to a characterization in terms of space groups. Superconductivity is another example, where the $\mathrm{U}(1)$-gauge symmetry is broken in the superconducting state.

However, Berezinskii [2, 3], in parallel with Kosterlitz and Thouless [4, 5], pointed out that the Ginzburg-Landau description is not exhaustive. They investigated a two-dimensional classical magnet with $\mathrm{U}(1)$ symmetry, the XY model, in which the phase transition is not accompanied by the breaking of any symmetry. The model describes interacting planar spins. At zero-temperature, the system is ferromagnetic as the spins are perfectly arranged. At finite but small temperatures, the system still has long-range correlations, but local spin structures called vortices may be created. Vortices are said to be topological excitations as the only way to destroy them is to annihilate a vortex with another vortex that rotates in an opposite direction, an antivortex. With increasing temperature, more vortex-antivortex pairs are created. Above a critical temperature, the pairs are no longer bounded together, and as a consequence, long-range correlations are destroyed. This constitutes the Kosterlitz-Thouless (KT) phase transition, where the system undergoes a transition to a phase with short-range correlations without spontaneous symmetry breaking[1]. In particular, the KT transition exemplified the importance of the abstract language of topology in the context of phase transitions.

The notion of topology became even more salient with the discovery of the quantum Hall effect in its integer (IQHE) [6] and, subsequently, fractional (FQHE) version [7]. When an electron gas confined in two dimensions and at low temperature is exposed to a strong magnetic field, the transverse Hall conductivity exhibits perfectly flat plateaus, while the longitudinal conductivity vanishes. In the bulk, the electronic states form Landau levels with a finite gap between them. At each plateau, the Hall conductivity σ_{xy} is a multiple integer of the quantum conductance e^2/h, $\sigma_{xy} = \nu\,(e^2/h)$, where ν is the electronic filling fraction. ν is either an exact integer (IQHE) or a well-defined fraction (FQHE), and has been experimentally measured to an astonishing precision of 10^{-9} [8]. This quantization is universal, i. e., it is observed regardless of the microscopic details of the sample such as disorder. In an open geometry, the bulk material remains insulating (if a chemical potential lies within a gap), but the current flows in one fixed direction along the physical edge. In fact, the quantized σ_{xy} and the existence of robust chiral edge modes are distinct manifestations of the topological nature of the system. Thouless, Kohmoto, Nightingale, and den Nijs [9] linked the Hall

1 The KT phase transition does *not* violate the Mermin-Wagner theorem because the transition from a phase with power-law correlations to a phase with exponentially decaying correlations occurs via the unbinding vortex-antivortex pairs.

conductivity in IQH systems to a topological invariant called the (first) Chern number. The Chern number was found to be also related to the number of gapless states at the boundaries of the system [10], justifying the celebrated bulk-boundary correspondence. The FQHE, on the other hand, cannot be explained through a simple single-particle, non-interacting picture. The FQHE is a paradigmatic example of topological order where exotic properties emerge from the collective behavior of electrons. The presence of electron-electron interactions may give rise to, for example, low-energy fractionalized excitations (carrying fractions of the elemental charge) with anyonic exchange statistic (neither bosonic nor fermionic) or long-range entanglement pattern characterized by a non-vanishing topological entanglement entropy [11]. In addition, topologically ordered phases exhibit a robust ground state degeneracy depending on the manifold on which they are defined. These properties are very promising ingredients for devising a fault-tolerant quantum computer [12].

In 1988, Haldane [13] showed that it is possible to realize quantum Hall states without a net magnetic field, now known as Chern insulators. But a breakthrough in the field of topological matter occurred almost 20 years later with a proposal by Kane and Mele [14, 15]. The authors studied the effect of a strong spin-orbit coupling on electronic structure of graphene and discovered that the constraints imposed by time-reversal symmetry could lead to a novel gapped state of matter with metallic edge states. The quantum spin Hall (QSH) insulating phase, in contrast to the quantum Hall effect, is solely protected by time-reversal symmetry and described by a different topological invariant called the $\mathbb{Z}_2$ index. Soon after, a realization of QSH in HgTe/CdTe quantum wells was suggested theoretically [16] and confirmed experimentally [17], where the key mechanism to obtain non-trivial bulk topology is a band inversion. The concept of $\mathbb{Z}_2$ topological states carries on to three dimensions [18–20] with conducting surfaces as characteristic features, which were firstly observed in bismuth-based materials [21–23].

One of the milestones in the field was the construction of the topological classification of gapped, free-fermionic systems by Ryu, Schnyder, Furusaki and Ludwig [24, 25] and independently by Kitaev [26]. Any generic quadratic Hamiltonian can be assigned to one of ten symmetry classes (as noticed by Altland and Zirnbauer [27]) based on its spatial dimensionality and the presence (or absence) of time-reversal, particle-hole and chiral symmetries and labeled by a relevant topological invariant. The so-called symmetry-protected topological (SPT)[2] phases cannot be adiabatically connected to a trivial insulating limit (i. e. product state) without closing the bulk gap or breaking the relevant symmetries. This includes topological insulators (TIs) and topological superconductors (TSCs) with internal symmetries [28]. Although the ten-fold way is regarded as a well-established classification scheme, it is clearly not exhaustive.

Given the recent developments in the context of topological phases of matter, the topological classification based on ten symmetry classes can be extended in several ways. For instance, the topological classification can carry on to bosonic systems [29] or even to classical systems [30]. The notion of SPT phases has also been extended to gapless phases, such as topological semimetals [31] revealing the linear dispersion around the nodes and unconventional superconductors with point (or line) nodes [32]. Topological metals and semimetals can be categorized by the dimensionality of the topologically protected band degeneracies [33–35].

2 Note that this abbreviation also stands for the symmetry-protected topological order (or symmetry-enriched topological, SET) described by a Hamiltonian with a spectral many-body gap and equipped with certain symmetries. These phases are beyond the scope of the thesis.

Periodic, time-dependent Hamiltonians are also the subject of generalization of the ten-fold way [36].

The interplay between topology and symmetries is still an exceptionally active research area. Spatial symmetries, which are ubiquitous in crystals, enrich the list of possible gapped and gapless topological phases [37, 33, 34, 38] with topological crystalline insulators (TCIs) [39] and higher-order topological insulators (HOTIs) [40]. Open dissipative systems described by non-Hermitian Hamiltonians can be systematized in a same manner as Hermitian systems [41–43]. The topological properties of all the aforementioned systems can be explained in terms of non-interacting or mean-field Hamiltonians. Nevertheless, a general unifying framework has not been yet constructed.

OUTLINE

In this thesis, we study selected free-fermionic topological systems whose properties cannot be deduced from the ten-fold classification. The topics we will explore can be thought as three research directions in which the existing classification remains incomplete. Firstly, in Chapter 2, we present the systems which are defined in *non-integer spatial dimensions*. Then, in Chapters 3 and 4, we discuss the importance of *spatial symmetries* on the realization of symmetry-protected topological phases and also cast light on the effect of topology in the presence of crystalline symmetries. Finally, in Chapter 5, we explain how *non-Hermiticity*, originating from the effective description of open systems, may profoundly affect topological properties and enrich the classification. The thesis is organized as follows:

Chapter 1 serves as an introduction to topological band theory. We start with key definitions related to band topology, the role of internal symmetries and the classification with respect to them, together with relevant topological invariants. We discuss in more details the properties of the ten-fold way and give an overview of the bulk-boundary correspondence. For illustration purposes, we provide several examples of models in different symmetry classes.

In Chapter 2, we investigate whether general graphs – in particular fractals – can host topological states by the means of case studies. Here, we consider the Hofstadter model defined on two fractal lattices: the Sierpiński carpet and gasket, and combine several numerical techniques to characterize their topological properties. Starting from the analysis of numerically obtained energy spectra and eigenstates, we then move to direct calculations of topological invariants. Due to the lack of translational invariance, we compute the Bott index and the Chern number represented in real space. In addition, we examine the effect of on-site disorder through the level spacings statistics and the Chern number. We also compare the results with regular lattices. The content of this Chapter is based on the article *Topology in the Sierpiński-Hofstadter problem*.

Chapter 3 includes studies on topological properties of atomically thin bismuth and antimony layers described within a tight-binding formalism. Their completely flat counterparts – bismuthene and antimonene – exhibit a topological crystalline insulating phase protected by mirror symmetry, which we confirm by computing the mirror Chern number. We show that the entanglement entropy and entanglement spectrum, conveniently expressed in terms of the eigenvalues of the two-point correlation matrix, can be used as complementary tools for defining bulk topology. Additionally, we investigate topological phase transitions induced by doping, external electric field and strain. The effect of experimentally relevant silicon carbide

(SiC) substrate on the monolayers is also discussed. The content of this Chapter is based on the articles *Entanglement entropy and entanglement spectrum of Bi_{1-x} Sb_x (111) bilayers* and *Topological phases in Bi/Sb planar and buckled honeycomb monolayers*.

Chapter 4 is devoted to obstructed atomic limits, a novel class of insulating states stemming from the crystalline symmetries. We extend the classification of these phases in two dimensions to the spinful case with time-reversal symmetry by employing (nested) Wilson loop invariants and symmetry indicators. To predict the presence of quantized, symmetry-protected corner charges – the boundary manifestations of non-trivial bulk topology – we provide useful formulas based on Bloch wavefunctions. Our theoretical findings are supported by density functional theory results for arsenic and antimony monolayers in an open flake geometry. The content of this Chapter is based on the article *Fractional corner charges in spin-orbit coupled crystals*.

The interplay between topology and non-Hermiticity is investigated in Chapter 5. We discuss the phenomena intimately related to the non-Hermiticity: the presence of degeneracies in the complex spectrum called exceptional points and the breakdown of bulk-boundary correspondence associated with the anomalous localization of the eigenstates named the skin effect. To demonstrate these effect, we examine the π-flux model on a square lattice with additional non-Hermitian hopping terms. Based on results obtained for a quantum lattice model, we design, describe, and measure a non-Hermitian topolectrical circuit realizing a new, reciprocal type of the skin effect. The content of this Chapter is based on the article *Reciprocal skin effect and its realization in a topolectrical circuit*.

Finally, Chapter 6 summarizes the results and indicates potential research directions. Additional definitions and derivations are given in Appendices at the end of the main text.

1

TOPOLOGICAL STATES OF MATTER

In this Chapter, we introduce some notions from the mathematical field of topology in the context of topological states of matter. We focus on non-interacting fermionic systems and treat them in the general framework of band theory in the tight-binding formalism. In the following, we assume the locality of the Hamiltonians (i. e. no infinite-range hoppings) and focus on the properties of ground states at zero temperature. As a starting point, we provide a description of fundamental symmetries in quantum mechanics, which are the basis for further considerations. We elaborate on the classification of topological states with respect to ten distinct symmetry classes and substantiate its connection to the edge physics. Finally, we illustrate these concepts in more details using paradigmatic examples of topological phases. In particular, we provide an accessible explanation of topological invariants.

1.1 TOPOLOGICAL BAND THEORY

Topology is a branch of mathematics that deals with properties of smooth, continuous transformations such as stretching or bending. The geometrical details of objects are then ignored and only global features, characterized by topological invariants, are of interest. For instance, a sphere can be continuously deformed into a cube, hence both objects are said to be topologically equivalent (or homeomorphic). A deformation from a sphere to a torus is, on the other hand, not a smooth procedure as it requires making a hole.

To differentiate between topologically distinct objects, we can assign to each of them the number of holes called the genus g. As depicted in Fig. 1, a sphere is characterized by $g = 0$, whereas a torus has $g = 1$. As long as all deformations are smooth, the genus remains unchanged. The criterion for possible smooth deformations is given by the Gauss-Bonnet

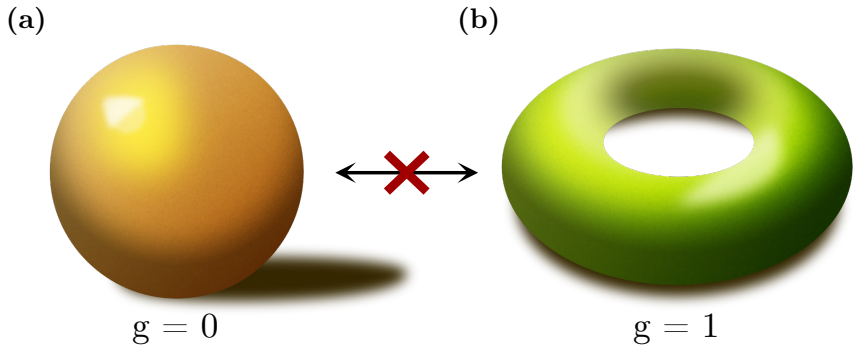

Figure 1: Topological inequivalence. From a perspective of topology, **(a)** a sphere and **(b)** a torus are distinct as one cannot be smoothly deformed into the other. A sphere has a genus g equal to zero, while a torus has one punctured hole and therefore $g = 1$.

theorem. In two dimensions, for a given Riemannian manifold M without boundary (e. g. a torus), the surface integral of the local Gaussian curvature $K(\mathbf{x})$ is related to the genus g as

$$2 - 2g = \int_M K(\mathbf{x})\, d^2\mathbf{x}. \tag{1}$$

The Gaussian curvature is proportional to the angle mismatch before and after the parallel transport (called holonomy) of a tangent vector enclosing a loop on M.

In the realm of band theory, topological equivalence can be understood by answering the following: Given two band insulators described by Bloch Hamiltonians $\mathcal{H}(\mathbf{k})$ and $\mathcal{H}'(\mathbf{k})$, can we adiabatically deform one to the other without closing the gap? Let us introduce relevant definitions. Quantum lattice free-fermionic models can be described by a Hamiltonian H within a tight-binding approximation, whose most general form reads

$$H = \sum_{ij\alpha\beta} c^\dagger_{i\alpha} H^{\alpha\beta}_{ij} c_{j\beta}. \tag{2}$$

Here, i, j correspond to lattice sites, while α, β denote internal degrees of freedom such as orbitals or spin. $c^\dagger_{i\alpha}(c_{i\alpha})$ stands for the second-quantized creation (annihilation) operators on sites i and species α, which obey the anticommutation relations

$$\{c^\dagger_{i\alpha}, c_{j\beta}\} = \delta_{ij}\delta_{\alpha\beta}, \qquad \{c_{i\alpha}, c_{i\alpha}\} = \{c^\dagger_{i\alpha}, c^\dagger_{i\alpha}\} = 0. \tag{3}$$

In the case of a perfectly regular arrangement of sites and with periodic boundary conditions (PBC), the Hamiltonian in Eq. (2) can be conveniently represented in reciprocal space. This can be achieved by performing the Fourier transform of the operators

$$c_{i\alpha} = \frac{1}{\sqrt{V}} \sum_{\mathbf{k}\in \mathrm{BZ}} c_{\mathbf{k}\alpha}\, e^{i\mathbf{k}\cdot\mathbf{r}}, \qquad c_{\mathbf{k}\alpha} = \frac{1}{\sqrt{V}} \sum_{\mathbf{r}} c_{i\alpha}\, e^{-i\mathbf{k}\cdot\mathbf{r}}, \tag{4}$$

where $\mathbf{r}$ describes the position of the i-th site and V is a volume of the d-dimensional system, $V = L^d$. Thus, the momentum-space Hamiltonian is

$$\mathcal{H} = \sum_{\mathbf{k}\alpha\beta} c^\dagger_{\mathbf{k}\alpha} \mathcal{H}^{\alpha\beta}(\mathbf{k}) c_{\mathbf{k}\beta} \tag{5}$$

with a size given by the total number of degrees of freedom in the unit cell N. $\mathbf{k}$ is the momentum defined in the Brillouin zone (BZ). In the thermodynamic limit (with $L \to \infty$), the BZ is topologically equivalent to a torus $\mathbf{k} \in T^d$. $\mathcal{H}(\mathbf{k})$ can therefore be seen as a map from T^d to the set of $N \times N$ Hermitian matrices, which we denote by $\mathrm{Hn}(N)$

$$\begin{aligned} \mathcal{H} : T^d &\to \mathrm{Hn}(N), \\ \mathbf{k} &\mapsto \mathcal{H}(\mathbf{k}). \end{aligned} \tag{6}$$

The band structure refers to the eigenspectrum $\{\epsilon_a\}$ of $\mathcal{H}(\mathbf{k})$ at every $\mathbf{k}$, i. e., the energy bands. In fermionic systems, a ground state generally forms a Fermi sea due to the Pauli exclusion principle. If there is a spectral gap between n lowest eigenvalues (the occupied energy bands) and the remaining m (empty bands) with $N = n + m$ for $\forall \mathbf{k} \in \mathrm{BZ}$, then the system is said to

be *gapped* at filling n/N. In contrast, the system is *gapless* if this spectral gap vanishes, namely there exists a shared eigenvalue between the bands n and $n+1$ in the Brillouin zone.

1.1.1 *Flat band Hamiltonian*

Topological classification is based on the global properties of band structures. As long as the Bloch Hamiltonian $\mathcal{H}(\mathbf{k})$ has a finite gap separating occupied and unoccupied states, it can be continuously deformed to the spectrally flattened Hamiltonian $\mathcal{Q}(\mathbf{k})$. This deformation removes the system-dependent information about the energies, but leaves topological properties intact. We focus on an illustrative example of an insulating system without any symmetries.

The Hamiltonian $\mathcal{H}(\mathbf{k})$ can be diagonalized at every $\mathbf{k} \in \mathrm{BZ}$ using a unitary transformation $U(\mathbf{k})$, $U^\dagger(\mathbf{k})\mathcal{H}(\mathbf{k})U(\mathbf{k}) = \mathrm{diag}\,(\epsilon_N, \epsilon_{N-1}, \ldots, \epsilon_1)$, where the eigenenergies ϵ_a are sorted in a descending order. We assume that n out of N bands are occupied, which is equivalent to setting the chemical potential between the bands n and $n+1$. The *flat band Hamiltonian* $\mathcal{Q}(\mathbf{k})$ reads

$$\mathcal{Q}(\mathbf{k}) = U(\mathbf{k}) \begin{pmatrix} \mathbb{1}_m & 0 \\ 0 & -\mathbb{1}_n \end{pmatrix} U^\dagger(\mathbf{k}); \qquad \mathcal{Q}^2(\mathbf{k}) = 1 \tag{7}$$

and its energies are either -1 for all occupied bands or $+1$ for states above the gap. In general, $\mathcal{Q}(\mathbf{k})$ is a $\mathrm{U}(m+n)$ matrix with an extra $\mathrm{U}(n) \times \mathrm{U}(m)$ gauge symmetry due to independent basis rotations in the occupied and unoccupied eigenspaces, respectively. If these conditions are taken into account, the flattened and original Hamiltonians belong to the coset space known as the complex Grassmannian $G_{m,n}(\mathbb{C})$. The set of topologically distinct Hamiltonians $\mathcal{H}$ is given by the homotopy classes of the mappings

$$\begin{aligned} \mathcal{Q} : \mathrm{BZ} \to G_{n+m,\,m}(\mathbb{C}) &= \frac{\mathrm{U}(n+m)}{\mathrm{U}(n) \times \mathrm{U}(m)}, \\ \mathbf{k} &\mapsto \mathcal{Q}(\mathbf{k}). \end{aligned} \tag{8}$$

In the continuum case, the BZ corresponds to the d-sphere S^d, while for lattice models – to the d-dimensional torus T^d. The fact that two maps $k \mapsto \mathcal{Q}(\mathbf{k})$ and $k \mapsto \mathcal{Q}'(\mathbf{k})$ can be adiabatically deformed into each other (e. g. by changing the model parameters) implies that the corresponding Hamiltonians $\mathcal{H}(\mathbf{k})$ and $\mathcal{H}'(\mathbf{k})$ are *topologically equivalent* and can be smoothly transformed into each other *without* closing the gap. In other words, any continuous transformation that preserves the gap does not change the topology of $\mathcal{H}$. The number of topologically distinct Hamiltonians $\mathcal{H}$ is given by the homotopy group[1] $\pi_d(G_{m,n}(\mathbb{C}))$ [44]

$$\begin{aligned} &\pi_d(G_{m,n}(\mathbb{C})) = \mathbb{Z}, \ d \text{ even}; \\ &\pi_d(G_{m,n}(\mathbb{C})) = \{1\}, \ d \text{ odd}. \end{aligned} \tag{9}$$

This result states that in two (and any other even) dimensions, there is an infinite number of topologically distinct states labeled by an integer *topological invariant*. It is exactly the case of the

1 Although the homotopy group uses a sphere as the base space for the mappings, the topological classification discussed in this Chapter is most often not affected if the BZ is a torus. In the special cases where this distinction is relevant, the corresponding system is actually a *weak* topological insulator requiring additional spatial symmetries to protect edge modes.

integer quantum Hall effect, which we discuss in Section 1.5.1. Conversely, all non-interacting fermionic Hamiltonians in odd dimensions without imposed symmetries are topologically equivalent. In general, the system is said to be *trivial* if it is adiabatically connected to an ordinary insulator of isolated atoms. A deformation leading from a Hamiltonian to another one in a distinct topological class has to pass through a gap closing. The system is then said to undergo a *topological phase transition*.

1.1.2 *Internal symmetries*

The set of possible deformations that keep the systems adiabatically connected can be further constrained by the presence of symmetries. This gives rise to the notion of *symmetry-protected topological states*, which cannot be deformed into a trivial state unless the gap closes or a relevant symmetry is broken. According to Wigner's theorem [45], any symmetry in quantum mechanics can be represented by an operator that preserves the inner product and therefore the transition probabilities. Hence, an operator S representing a symmetry has to be either linear and unitary

$$\langle S\psi, S(\lambda_1\phi_1 + \lambda_2\phi_2)\rangle = \lambda_1 \langle \psi, \phi_1\rangle + \lambda_2 \langle \psi, \phi_2\rangle \tag{10}$$

or antilinear and antiunitary

$$\langle S\psi, S(\lambda_1\phi_1 + \lambda_2\phi_2)\rangle = \lambda_1^* \langle \phi_1, \psi\rangle + \lambda_2^* \langle \phi_2, \psi\rangle . \tag{11}$$

An operator S is a symmetry of the system if it commutes with the Hamiltonian H

$$[H, S] = 0. \tag{12}$$

Moreover, any antiunitary transformation S can be written as the product of a unitary transformation U and the complex conjugation operator $\mathcal{K}$

$$S = U\mathcal{K}. \tag{13}$$

A unitary symmetry allows to represent the Hamiltonian in a block-diagonal form and reduce the problem to the independent study of each separate block. Antiunitary symmetries, however, are more interesting as they impose certain spectral constraints on the irreducible blocks of the Hamiltonian. Here, we focus on *internal* symmetries acting locally in real space.

A fundamental antiunitary operator is the time-reversal symmetry $\mathcal{T}$ (TRS), which takes the time $t \to -t$ and reverses the time-evolution $\mathcal{T}e^{-itH}\mathcal{T}^{-1} = e^{itH}$

$$\mathcal{T}H\mathcal{T}^{-1} = +H. \tag{14}$$

The $\mathcal{T}$ operator belongs to a class of involutional operators, which leave an arbitrary state $|\psi\rangle$ unchanged up to a phase factor when applied twice, $\mathcal{T}^2 = e^{i\phi}\mathbb{1}$. By defining $\mathcal{T} = T\mathcal{K}$ with T being unitary, $T^{-1} = T^\dagger = (T^{\mathrm{T}})^*$, one can show that $\mathcal{T}^2 = T\mathcal{K}T\mathcal{K} = TT^*$ and $\mathcal{T}^2 = \eta\,\mathbb{1} = T(T^{\mathrm{T}})^{-1}$ as $T^* = (T^{\mathrm{T}})^{-1}$. Hence, $T = \eta T^{\mathrm{T}} = \eta^2 T$, which implies that $\eta = \pm 1$ and

$\mathcal{T}^2$ may give either $+1$ or -1. To show that more explicitly, let us take a spin$-1/2$ system as an example. We can write the TRS operator in the σ_z basis as

$$\mathcal{T} = \exp(-\mathrm{i}\pi S_y/\hbar)\mathcal{K} = \exp(-\mathrm{i}\pi\sigma_y/2)\mathcal{K} = \mathrm{i}\sigma_y\mathcal{K} \tag{15}$$

with $\mathrm{i}\sigma_y$ being unitary. The $\mathcal{T}$-operator defined in Eq. (15) squares to -1. Using Eq. (14), we can write

$$H(\mathcal{T}\,|\psi\rangle) = \mathcal{T}H(\mathcal{T}^{-1}\mathcal{T})\,|\psi\rangle = \mathcal{T}H\,|\psi\rangle = E(\mathcal{T}\,|\psi\rangle). \tag{16}$$

For an eigenstate $|\psi\rangle$, $\mathcal{T}\,|\psi\rangle$ is also an eigenstate with the same energy and the states are orthogonal $\langle\psi|\mathcal{T}\psi\rangle = 0$. We conclude that all eigenstates are at least two-fold degenerated, which is known as the Kramers degeneracy. On the other hand, the Bloch Hamiltonian $\mathcal{H}(\mathbf{k})$ is transformed upon the action of the time-reversal operator Θ in momentum space as

$$\Theta\mathcal{H}(\mathbf{k})\Theta^{-1} = +\mathcal{H}(-\mathbf{k}). \tag{17}$$

As a consequence of the time-reversal symmetry, eigenvalues come in pairs $\epsilon_{\mathbf{k}} = \epsilon_{-\mathbf{k}}$, i. e. the two partners of the Kramers pairs come at opposite momenta.

Another antiunitary symmetry, naturally arising in the mean-field description of superconductivity, is the particle-hole (often called the charge conjugation) symmetry $\mathcal{P}$ (PHS)

$$\mathcal{P}H\mathcal{P}^{-1} = -H, \tag{18}$$

which *anticommutes* with the single-particle Hamiltonian[2]. Similar to TRS, it also has two projective representations $\mathcal{P}^2 = \pm 1$. For a Bloch Hamiltonian, it translates to

$$\Xi\mathcal{H}(\mathbf{k})\Xi^{-1} = -\mathcal{H}(-\mathbf{k}). \tag{19}$$

The presence of the particle-hole symmetry constraints the structure of energy spectrum such that each energy $\epsilon_{\mathbf{k}}$ has a $-\epsilon_{-\mathbf{k}}$ partner.

In addition, we can define the chiral symmetry (CS) $\mathcal{C}$ as the combination of the time-reversal and particle-hole symmetries, $\mathcal{C} = \mathcal{T}\mathcal{P}$,

$$\mathcal{C}H\mathcal{C}^{-1} = -H. \tag{20}$$

$\mathcal{C}$ is represented by a unitary operator, which further implies that it only squares to 1, if present. Expressing $\mathcal{T} = T\mathcal{K}$ and $\mathcal{P} = P\mathcal{K}$, where T and P are the respective unitaries, $\mathcal{C} = T\mathcal{K}P\mathcal{K} = TP^* = C$. Even in the absence of PHS and TRS, a system can possess a chiral symmetry. In the case of Bloch Hamiltonian $\mathcal{H}(\mathbf{k})$, it follows

$$\Pi\mathcal{H}(\mathbf{k})\Pi^{-1} = -\mathcal{H}(\mathbf{k}), \tag{21}$$

so that the eigenvalues come in pairs $\{\epsilon_{\mathbf{k}}, -\epsilon_{\mathbf{k}}\}$.

Similar considerations to those presented in Section 1.1.1 can be applied to systems equipped with additional symmetries. In particular, the procedure is straightforward for systems with

2 All three symmetries $\mathcal{T}$, $\mathcal{P}$, and $\mathcal{C}$ are commuting with the fully second-quantized Hamiltonian defined in the Fock space. It is only the case for the single-particle Hamiltonian, where the particle-hole $\mathcal{P}$ and the chiral $\mathcal{C}$ operators become anticommuting. Nevertheless, we treat them on the same footing.

a chiral symmetry only. For antiunitary symmetries acting non-locally in reciprocal space, finding all possible mappings is rather convoluted.

1.2 CLASSIFICATION OF TOPOLOGICAL INSULATORS AND SUPERCONDUCTORS

The periodic table of topological insulators and superconductors, also known as the ten-fold way or Cartan-Altland-Zirnbauer classification scheme [24–26] is a topological classification of gapped, single-particle fermionic Hamiltonians in d spatial dimensions based on the symmetries introduced above. Taking into account all the combinations of the $\mathcal{T}$ and $\mathcal{P}$ symmetries, we arrive at $3 \times 3 = 9$ possibilities. If both $\mathcal{T}$ and $\mathcal{P}$ are absent, $\mathcal{C}$ can be either 0 or 1, hence there are two additional possibilities. However, if a system only has either $\mathcal{T}$ or $\mathcal{P}$, it cannot have a chiral symmetry, which gives the total number of $(3 \times 3 - 1) + 2 = 10$ distinct symmetry classes.

The classification discussed here dates back to the idea of Élie Cartan's classification of symmetric spaces in differential geometry. For a generic $N \times N$ Hamiltonian H, the corresponding time-evolution operator $U_H = e^{-itH}$ belongs to the group of unitary matrices $\mathrm{U}(N)$, which Cartan labeled as the class A. With an additional TRS squaring to $+1$, the Hamiltonian can be always chosen to be real and symmetric and then $U_H \in \mathrm{U}(N)/\mathrm{O}(N)$, where $\mathrm{O}(N)$ is an orthogonal group, is called the AI class. In the case of $\mathcal{T}^2 = -1$, U_H belongs to the different group $U_H \in \mathrm{U}(2N)/\mathrm{Sp}(2N)$ (Sp stands for a symplectic group) named AII class. These considerations were used as a basis for the classification done by Wigner and Dyson [46] within random matrix theory, which was subsequently extended by Altland and Zirnbauer [27] to ten classes. All possible symmetry classes in $d = 1, \ldots, 8$ spatial dimensions are tabulated in Table 1.

Several approaches exist in order to deduce the entries of the ten-fold way. One of them is based on the algebraic structure of Clifford algebras and the K-theory [26]. A more physically justified strategy proposed in Ref. [25] relies on the Anderson localization theory [47], where the authors investigated the presence of boundary modes and their stability against a strong disorder. The answer is obtained by the long wavelength description of non-linear sigma models in the given symmetry class and dimension.

Let us now focus on the structure of the Table 1 in more details. The ten classes, conveniently labeled according to the Cartan's nomenclature, are divided into three broad categories: standard, chiral and Bogoliubov-de Gennes (BdG). The first group corresponds to the three symmetry classes originally treated by Wigner and Dyson, where only TRS was considered. Imposing additional chiral symmetry to these classes leads to the group of the so-called chiral classes. Finally, the remaining four classes arise from description of superconductors within the mean-field approximation. The entries $\mathbb{Z}$ and $\mathbb{Z}_2$ denote the set of possible topological invariants, while '–' indicates that no meaningful topological invariant can be defined in a given symmetry class and spatial dimensions[3].

To emphasize the importance of the classification, we now provide a few well-known examples. The class A describes systems without any symmetry and in two dimensions accounts for a $\mathbb{Z}$ classification. It corresponds to the generic case discussed in Section 1.1.1,

3 Taking into account the interactions may alter the classification. For example, in Ref. [48] it was shown that the topological invariant for the free fermion classification lies in $\mathbb{Z}$, but with the introduction of interactions the $\mathbb{Z}$ is broken down to $\mathbb{Z}_8$.

leading to the integer quantum Hall effect and Chern insulators, which will be discussed in Sections 1.5.1 and 1.5.2. Topological insulators protected by the time-reversal symmetry admit a $\mathbb{Z}_2$ classification and belong to the class AII; we will explore them in Section 1.5.3. In the case of the BdG classes, some notable mentions are two-dimensional spinless chiral $p + ip$-wave superconductors in class D [49] or three-dimensional superfluid ^{3}He categorized in DIII class [50]. In one dimension, the Su-Schrieffer-Heeger model (see Section 1.5.4) and the Kitaev p-wave superconductor [51] are relevant examples of the BDI class.

system	Cartan label	$\mathcal{T}$	$\mathcal{P}$	$\mathcal{C}$	1	2	3	4	5	6	7	8
standard	A (unitary)	0	0	0	-	$\mathbb{Z}$	-	$\mathbb{Z}$	-	$\mathbb{Z}$	-	$\mathbb{Z}$
	AI (orthogonal)	1	0	0	-	-	-	$\mathbb{Z}$	-	$\mathbb{Z}_2$	$\mathbb{Z}_2$	$\mathbb{Z}$
	AII (symplectic)	-1	0	0	-	$\mathbb{Z}_2$	$\mathbb{Z}_2$	$\mathbb{Z}$	-	-	-	$\mathbb{Z}$
chiral	AIII (chiral unitary)	0	0	1	$\mathbb{Z}$	-	$\mathbb{Z}$	-	$\mathbb{Z}$	-	$\mathbb{Z}$	-
	BDI (chiral orthogonal)	1	1	1	$\mathbb{Z}$	-	-	-	$\mathbb{Z}$	-	$\mathbb{Z}_2$	$\mathbb{Z}_2$
	CII (chiral symplectic)	-1	-1	1	$\mathbb{Z}$	-	$\mathbb{Z}_2$	$\mathbb{Z}_2$	$\mathbb{Z}$	-	-	-
BdG	D	0	1	0	$\mathbb{Z}_2$	$\mathbb{Z}$	-	-	-	$\mathbb{Z}$	-	$\mathbb{Z}_2$
	C	0	-1	0	-	$\mathbb{Z}$	-	$\mathbb{Z}_2$	$\mathbb{Z}_2$	$\mathbb{Z}$	-	-
	DIII	-1	1	1	$\mathbb{Z}_2$	$\mathbb{Z}_2$	$\mathbb{Z}$	-	-	-	$\mathbb{Z}$	-
	CI	1	-1	1	-	-	$\mathbb{Z}$	-	$\mathbb{Z}_2$	$\mathbb{Z}_2$	$\mathbb{Z}$	-

Table 1: Classification of non-interacting fermionic Hamiltonians with respect to time-reversal $\mathcal{T}$, particle-hole $\mathcal{P}$ and chiral $\mathcal{C}$ symmetries and dimensionality d [26, 25]. The first two columns label the symmetry classes in the Cartan nomenclature, while the realization of the three symmetries are listed in the next three columns. $\mathcal{T}$ and $\mathcal{P}$ symmetry operators can square to 1 or -1; for the $\mathcal{C}$ symmetry, 1 specifies its presence. An entry 0 states that the operation is not a symmetry. Topological classification is either given by a set of integers ($\mathbb{Z}$ classification) or two-valued invariant $\mathbb{Z}_2$. '–' states that all Hamiltonians are topologically equivalent, thus they do not have any topological invariant.

At first glance, the cases with $d > 3$ may not look to be physically accessible. However, higher-dimensional topological phases can be realized in synthetic dimensions [52], where coupling suitable degrees of freedoms allows to simulate the motion of a particle along an extra spatial dimension. The full table shows also an interesting structure; for instance, there are exactly five classes of topological insulators and superconductors in each spatial dimension d, where three of them are characterized by an integer $\mathbb{Z}$ and the remaining two by a $\mathbb{Z}_2$ index. Two classes, A and AIII, do not have any antiunitary symmetry which imposes reality constraints and therefore are said to be complex. In contrast, the other eight classes are called real classes as they have at least one antiunitary symmetry. It was pointed out by Kitaev [26] that topological invariants in all classes follow a periodic pattern with respect to dimensionality known as the Bott periodicity. Complex classes exhibit a periodicity of two, while real classes a periodicity of eight. Moreover, there is a staggered pattern between distinct symmetry classes, in particular clearly seen for the complex classes. Starting from the AIII class in $d = 1$ described by $\mathbb{Z}$ invariant, breaking the chiral symmetry and moving to a higher dimension $d \to d + 1$

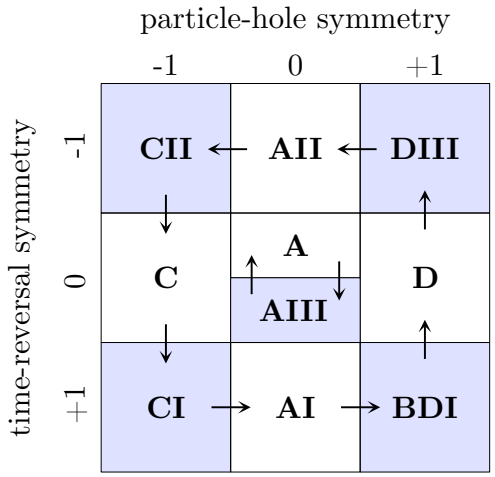

Figure 2: The Bott clock [26]. Light blue color labels the chiral classes and the arrows show the direction in which dimensional extension $d \to d+1$ conserves the topological classification. The complex classes are located in the center of the table and have a periodicity of two, while the real classes (with periodicity of eight) are represented around the clock.

results in obtaining the A class. By inspecting the Table 1, we observe that the class AIII in d-dimensions follows the same topological classification as the class A in $(d+1)$-dimensions. A general procedure of breaking (or imposing) the symmetries and adding an extra dimension is called the *dimensional extension*, which can be illustrated in the form of the Bott clock (see Fig. 2).

It is important to note that while all these properties are formally derived relying on the clean, periodic Hamiltonians, the topological classification is robust against any small perturbations preserving the gap, including the effect of disorder.

1.3 BULK-BOUNDARY CORRESPONDENCE

Up to now, we have observed that systems can be classified into distinct symmetry classes based on their bulk properties. In reality, boundary effects are inevitable due to finite sizes of samples. A striking feature of non-interacting fermionic systems[4] is that the bulk topology is intimately connected to the edge physics. More precisely, opening the boundaries of an initially periodic system with assigned non-zero topological invariant results in the presence of robust boundary modes[5]. These modes survive any small local perturbations of the Hamiltonian as long as the topological properties of the bulk are not affected. This observation is the essence of the *bulk-boundary correspondence*.

The first instance of the correspondence between bulk and boundary appeared in the context of anomalies in quantum field theory, with the prominent example of the Adler–Bell–Jackiw anomaly for chiral fermions [53]. It was observed that the effective field theories for bulk and boundary degrees of freedom, when defined separately, lead to quantum anomalies. To overcome the issue, both bulk and boundary have to be treated simultaneously and therefore

4 Indeed, this is a rather generic property of free fermions. The toric code, for instance, is a topologically ordered phase, but has no gapless excitations on the boundary.

5 Given that the symmetries required to protect a topological phase are still preserved on the boundary.

the anomalies cancel out. Despite a lack of general proof[6], the bulk-boundary correspondence has been rigorously studied in several symmetry classes [54–57].

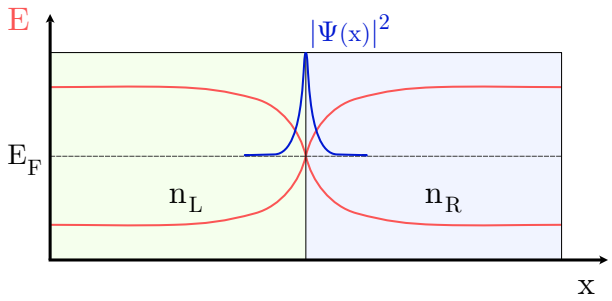

Figure 3: Schematic representation of the bulk-boundary correspondence. If two systems L and R, characterized by the invariants n_L and n_R ($n_L \neq n_R$), are joined at interface, there have to be gapless states localized at a domain wall associated with a band gap closing. The number of boundary states is determined by the difference $|n_L - n_R|$.

An heuristic explanation behind the correspondence is the following. Suppose we have two semi-infinite systems L and R, illustrated in Fig. 3. The systems belong to the same symmetry class (thus are characterized by the index n), but the values of their invariants are different, $n_L \neq n_R$. As a topological invariant can only change if the bulk gap closes and no relevant symmetries are broken, a topological phase transition between two distinct gapped systems must be accompanied by the local gap closing. As a consequence, gapless states localize at the interface of the two materials and their number depends on the difference between indices $|n_L - n_R|$. In particular, this relation holds for a single sample with a non-zero topological invariant, where the edge modes appear at the border with trivial (by definition) vacuum.

Most often, the bulk-boundary correspondence refers to the relation between d-dimensional bulk and boundary modes in $(d-1)$-dimensions [58]. However, topological line and point defects can be also predicted from the periodic table [59]. A new type of the correspondence was established for the so-called higher-order topological insulators, in which the boundary states are manifested in codimensions $(d - D)$, with $D > 1$ [60].

1.4 GEOMETRIC PHASES

For a long time, the importance of the phase factor associated with an adiabatic evolution of a quantum state was rather overlooked. However, if a cyclic evolution is considered, an accumulated phase can have a purely geometric character with potentially observable consequences. This phase factor is known as the Berry phase [61].

1.4.1 *Introduction to the Berry phase*

To explain the concept of the Berry phase, consider a system that has an implicit dependence on some external parameter $\boldsymbol{\xi}$. The parameter $\boldsymbol{\xi}$ may, in general, vary in time and the Hamiltonian is then $H(\boldsymbol{\xi}(t))$. According to the adiabatic theorem, a physical system initially in an eigenstate

6 Probably the most general proof was presented in Ref. [10] for IQH systems.

$|\psi_n(0)\rangle = |n(\boldsymbol{\xi}(0))\rangle$ will remain in its instantaneous eigenstate if a given perturbation is acting on it slowly enough

$$H(\boldsymbol{\xi}(t))\,|n(\boldsymbol{\xi}(t))\rangle = E_n(\boldsymbol{\xi}(t))\,|n(\boldsymbol{\xi}(t))\rangle\,. \tag{22}$$

During the adiabatic evolution, the state does not only acquire a standard time-dependent phase, but also an extra phase factor γ_n

$$|\psi_n(t)\rangle = \exp\left(\mathrm{i}\gamma_n(t)\right)\exp\left(-\frac{\mathrm{i}}{\hbar}\int_0^t \epsilon_n(\boldsymbol{\xi}(t'))\,dt'\right)|n(\boldsymbol{\xi}(t))\rangle\,. \tag{23}$$

The phase factor γ_n can be written as

$$\gamma_n = \int_C \mathcal{A}_n(\boldsymbol{\xi})\,d\boldsymbol{\xi}; \qquad \mathcal{A}_n(\boldsymbol{\xi}) = \mathrm{i}\,\langle n(\boldsymbol{\xi})|\frac{\partial}{\partial\boldsymbol{\xi}}|n(\boldsymbol{\xi})\rangle\,, \tag{24}$$

where $\mathcal{A}_n$ is the gauge-dependent connection and C denotes the contour along which the parameter $\boldsymbol{\xi}$ evolved. After performing a U(1) gauge transformation, the connection and the state transform according to

$$\begin{aligned} |n(\boldsymbol{\xi}(t))\rangle \to |n'(\boldsymbol{\xi}(t))\rangle &= e^{\mathrm{i}\varphi(\boldsymbol{\xi})}\,|n(\boldsymbol{\xi}(t))\rangle\,, \\ \mathcal{A}_n \to \mathcal{A}'_n &= \mathcal{A}_n - \frac{\partial}{\partial\boldsymbol{\xi}}\varphi(\boldsymbol{\xi}). \end{aligned} \tag{25}$$

These equations exactly correspond to the gauge freedom of the vector potential in an electromagnetic field. It should not come as a surprise as the Berry phase and its connection exactly matches the phase picked up by an electron moving in a magnetic field, the so-called Aharonov-Bohm effect.

Let $\boldsymbol{\xi}(0)$ and $\boldsymbol{\xi}(t_F)$ be the endpoints of the contour C. If $\boldsymbol{\xi}(0) \neq \boldsymbol{\xi}(t_F)$, that is the evolution does not follow a closed contour, φ can be chosen in a way that γ_n vanishes. On the other hand, if a cyclic evolution is considered (so $\boldsymbol{\xi}(0) = \boldsymbol{\xi}(t_F)$), there is a constraint for the values of φ arising from the gauge transformation of the wave function in Eq. (25)

$$\varphi(\boldsymbol{\xi}(0)) - \varphi(\boldsymbol{\xi}(t_F)) = 2\pi m, \qquad m \in \mathbb{Z}. \tag{26}$$

Therefore, the phase γ_n called *the Berry phase*

$$\gamma_n = \oint_C \mathcal{A}_n(\boldsymbol{\xi})\,d\boldsymbol{\xi} \tag{27}$$

becomes finite and well-defined.

1.4.2 *Berry phases in band theory*

The Berry phase effects can be naturally studied in the context of band theory as they are directly connected to the electronic properties of a system [62]. The parameter space is therefore the reciprocal space, with a set of Bloch states $|\psi_{n\mathbf{k}}\rangle$ at each $\mathbf{k}$ momentum. For a single, isolated band n, we can rewrite a connection $\mathcal{A}_n$ in Eq. (24) in $\mathbf{k}$-space

$$\mathcal{A}_n(\mathbf{k}) = \mathrm{i}\,\langle u_{n\mathbf{k}}|\nabla_{\mathbf{k}}|u_{n\mathbf{k}}\rangle\,, \tag{28}$$

which is known as the Berry connection. Note that we use the lattice-periodic part of a Bloch eigenstate, $|u_{n\mathbf{k}}\rangle = e^{-i\mathbf{k}\cdot\mathbf{r}}|\psi_{n\mathbf{k}}\rangle$, as its derivative $\partial_k |u_{n\mathbf{k}}\rangle$ behaves well and spans the same Hilbert space as $|u_{n\mathbf{k}}\rangle$. The form of $\mathcal{A}$ resembles the electromagnetic vector potential and it is also gauge-dependent. In analogy to the magnetic field, we can define the Berry curvature

$$\mathcal{F}(\mathbf{k}) = \nabla_{\mathbf{k}} \times \mathcal{A}(\mathbf{k}), \tag{29}$$

which is gauge invariant. Extending the considerations to the case of N bands separated from the rest of the spectrum results in the non-Abelian generalization of Eqs. (28) and (29)

$$\begin{aligned} \mathcal{A}(\mathbf{k})_{mn,\mu} &= i\,\langle u_{m\mathbf{k}}|\partial_{k_\mu}|u_{n\mathbf{k}}\rangle\,, \\ \mathcal{F}_{mn,\mu\nu}(\mathbf{k}) &= i\left(\langle\partial_{k_\mu}u_{n\mathbf{k}}|\partial_{k_\nu}u_{m\mathbf{k}}\rangle - \langle\partial_{k_\nu}u_{n\mathbf{k}}|\partial_{k_\mu}u_{m\mathbf{k}}\rangle - [\mathcal{A}_\mu,\mathcal{A}_\mu]_{mn}\right). \end{aligned} \tag{30}$$

Remarkably, the Berry phase of the electronic wavefunctions and associated quantities – curvatures and connections – allow to compute the macroscopic polarization, which underlies the formulation of the modern theory of polarization [63]. As in the case of the Gaussian curvature in the Eq. (1), an integral of the Berry curvature $\mathcal{F}(\mathbf{k})$ over the BZ should give an integer. In two dimensions, the corresponding topological invariant is the (first) Chern number C

$$C = \frac{1}{2\pi}\int_{\mathrm{BZ}} d\mathbf{k}\,\mathcal{F}(\mathbf{k}). \tag{31}$$

If $\mathcal{F}(\mathbf{k})$ is a continuous function, then the Chern number vanishes. This indicates that the Chern number is associated with a non-trivial structure of the Berry curvature of a band.

The eigenstates obtained from a numerical diagonalization of the Hamiltonian $\mathcal{H}(\mathbf{k})$ yield random phases at different $\mathbf{k}$-points on the finite mesh. A particularly useful, gauge-invariant expression for the Chern number of the nth band is based on the Kubo formula

$$C_n = \frac{i}{2\pi}\int_{\mathrm{BZ}} d\mathbf{k}\sum_{n\neq m}\frac{\langle u_{n\mathbf{k}}|\partial_{k_x}\mathcal{H}(\mathbf{k})|u_{m\mathbf{k}}\rangle\,\langle u_{m\mathbf{k}}|\partial_{k_y}\mathcal{H}(\mathbf{k})|u_{n\mathbf{k}}\rangle - (n\leftrightarrow m)}{(E_{n\mathbf{k}}-E_{m\mathbf{k}})^2}, \tag{32}$$

where $E_{n\mathbf{k}}$ and $|u_{n\mathbf{k}}\rangle$ are, respectively, the energies and eigenstates of $\mathcal{H}(\mathbf{k})$. The total Chern number of a multiband system is a sum over all occupied states n

$$C = \sum_{n\in\mathrm{occ}} C_n. \tag{33}$$

As we will see in Section 1.5.1, the Chern number is directly connected to the experimentally observed quantization of the Hall conductivity.

1.5 TOPICAL EXAMPLES

In order to give a more concrete footing to the notions introduced in this Chapter, we present a short overview of several models belonging to different symmetry classes. The goal is to explain how topology is connected to physically demonstrated phenomena. We start with the integer quantum Hall effect and Chern insulators (especially the Haldane model) as representatives of the symmetry class A. We then discuss topological insulators with time-reversal symmetry characterized by $\mathbb{Z}_2$ invariants, in particular the Kane-Mele model as a prototypical example. In

the end, we discuss the role of the chiral symmetry in the one-dimensional Su-Schrieffer-Heeger model in the BDI class.

1.5.1 *Integer quantum Hall effect*

To begin with, consider a two-dimensional system in the xy-plane, exposed to a fixed magnetic field in the z-direction, $\mathbf{B} = B_z \mathbf{e}_z$. We can then study the 2D current densities $\mathbf{j}$ and electric fields $\mathbf{E}$, which are related by Ohm's law

$$\mathbf{j} = \begin{pmatrix} \sigma_{xx} & \sigma_{xy} \\ \sigma_{yx} & \sigma_{yy} \end{pmatrix} \begin{pmatrix} E_x \\ E_y \end{pmatrix} = \sigma \mathbf{E}, \qquad \mathbf{E} = \begin{pmatrix} \rho_{xx} & \rho_{xy} \\ \rho_{yx} & \rho_{yy} \end{pmatrix} \begin{pmatrix} J_x \\ J_y \end{pmatrix} = \rho \mathbf{j}. \tag{34}$$

The resistivity[7] matrix ρ is the inverse of the conductivity σ, $\rho \cdot \sigma = 1$. For an isotropic sample, we can assume that $\sigma_{xx} = \sigma_{yy}$ and $\sigma_{yx} = -\sigma_{xy}$ (and similarly for the conductance). In the classical Hall effect setup, the charge carriers (holes or electrons) with current density $\mathbf{j} = j_x \mathbf{e}_x$ are affected by the Lorentz force $\mathbf{F}_l = q(\mathbf{v} \times \mathbf{B})$, leading to an electric field $\mathbf{E} = E_y \mathbf{e}_y$ in the transverse direction to the current. Using the Drude model [64], one can show that the Hall resistivity is related linearly to the applied magnetic field

$$\rho_{xy} = B_z \mathcal{R}_H = -\frac{B_z}{ne}, \tag{35}$$

where we assumed the carriers to be electrons. The Hall coefficient $\mathcal{R}_H = -1/ne$ is a material dependent parameter, where n is the electron density and e is the elementary charge. The classically derived formula breaks down in the low-temperature, high-magnetic field regime, where quantum effects play a substantial role. The discovery of the quantum Hall effect by von Klitzing and co-workers [6] paving the way to the studies of topological phenomena was that ρ_{xy} is not proportional to B_z anymore, but has plateaus at quantized values

$$\rho_{xy} = \frac{1}{\nu} \frac{h}{e^2}, \tag{36}$$

while both the longitudinal resistance σ_{xx} and conductivity ρ_{xx} vanish. This is possible because of the matrix formulation of σ and ρ. Therefore, the Hall conductivity and resistivity are related by $\sigma_{xy} \cdot \rho_{xy} = -1$, leading to $\sigma_{xy} = \nu e^2/h$. The vanishing conductivity $\sigma_{xx} = 0$ means that a quantum Hall system is an insulator parallel to the electric field, while the vanishing resistivity $\rho_{xx} = 0$ means that there is no voltage drop parallel to the current. For the integer quantum Hall effect, ν is an integer.

1.5.1.1 *Quantum picture*

The quantum treatment of the IQHE starts with a simple Hamiltonian for a two-dimensional electron gas (2DEG) in a magnetic field $\mathbf{B} = B\mathbf{e}_z$. We neglect the interactions between electrons and focus on the single-particle description. In the Landau gauge, the electromagnetic vector potential is $\mathbf{A} = Bx\mathbf{e}_y$ satisfying $\nabla \times \mathbf{A} = \mathbf{B}$. A minimal coupling to the electromagnetic field

7 Resistivity is defined as the ratio of the product of the resistance and area to the length of the conductor. In two dimensions, both resistivity and resistance have the same dimension. This also applies to the conductivity/conductance.

is taken into account by the substitution of the momentum operator $\mathbf{p} \to \mathbf{p} + e\mathbf{A}$. Hence, the Hamiltonian for a non-interacting, non-relativistic 2DEG becomes

$$H = \frac{\hbar}{2m^*}(\mathbf{p} + e\mathbf{A})^2 = \frac{\hbar}{2m^*}p_x^2 + \frac{\hbar}{2m^*}(p_y + eBx)^2. \tag{37}$$

Here, m^* denotes the renormalized effective mass. The Hamiltonian in Eq. (37) is translationally invariant in the y-direction and therefore commutes with the momentum operator p_y. As a consequence, the eigenstates of H can be chosen to be the eigenstates of p_y and p_y can be replaced by its eigenvalues $\hbar k_y$ and H can be rewritten as

$$H = \frac{1}{2m^*}p_x^2 + \frac{1}{2}m^*\omega_c^2(x + k_y l_B^2)^2, \tag{38}$$

where $\omega_c = eB/m$ is the cyclotron frequency and $l_B = \sqrt{\hbar/eB}$ is the magnetic length. $\sqrt{2}l_B$ can be seen as the radius of the electron orbits in the semiclassical picture. The Hamiltonian resembles a quantum harmonic oscillator with a potential shifted by $-k_y l_B^2$, which has its energy eigenvalues of the form

$$E_n = \hbar\omega_c\left(n + \frac{1}{2}\right), \quad n \in \mathbb{N} \tag{39}$$

called the Landau levels. These energy levels are highly degenerate and the number of states per level N_L can be approximated as

$$N_L \approx \frac{A}{2\pi l_B^2} = \frac{\Phi}{\Phi_0} \tag{40}$$

with $\Phi_0 = h/e$ the quantum of flux and $\Phi = AB$ the total flux through the sample of area A. The Landau levels are similar to the energy bands in a band insulators. They are separated by a finite gap and the chemical potential can be tuned to lie in the gap. In the presence of a confining potential, the bulk of these Landau levels stay unchanged (corresponding in the classical picture to electrons orbiting in the bulk of the system), while at the edges, they are strongly deformed, with an energy following the form of the confining potential (consult Fig. 4). By fixing the chemical potential μ to be in between two of the flat bulk Landau levels, it will now also cross exactly once (at each edge) each of the occupied Landau levels. Each crossed Landau level acts as a band in a typical metal or band insulator, and will therefore contribute exactly one unit e^2/h of conductance. The total σ_{xy} therefore measures the number of occupied bands. This correspond to the observed plateau of the Hall resistance as the conductance is left unchanged as long as the chemical potential does not cross another Landau level.

1.5.1.2 *Quantized Hall conductance and the Chern number*

We see that the Landau levels picture provides an intuitive explanation of the experimentally observed plateaus. However, it does not tell why the exact quantization is robust and occurs in the QH systems regardless of the microscopic details such as disorder or the geometry of a sample. The link to a topological origin of the quantization was first made by Laughlin based on a gauge argument [65]. Subsequently, Thouless, Kohmoto, Nightingale, and den Nijs (TKNN) [66], in parallel to Avron, Seiler, and Simon [67], related the Hall conductivity to the

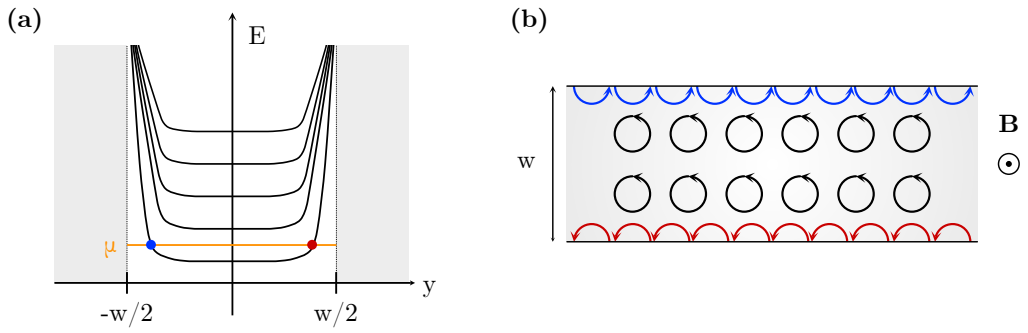

Figure 4: (a) The Landau levels in a confining potential and **(b)** the semiclassical cyclotron orbits. If the chemical potential μ is fixed between two Landau levels, the system remains insulating in the bulk, which corresponds to the closed cyclotron orbits. At the boundaries, however, gapless edge states appear due to the Landau levels bending. The edge states can be schematically represented as cyclotron orbits bouncing on the interfaces, each carrying the current in a single direction.

sum of the Chern numbers of all occupied bands times the quantum of conductance e^2/h. Starting from the Kubo formula of conductivity based on linear response theory (compare to Eq. (32)), TKNN showed that the Hall conductivity can be expressed as

$$\sigma_{xy} = \frac{e^2}{h} \sum_{n \in \text{occ}} C_n \tag{41}$$

with C defined as in Eq. (31). This formulation does not depend in any way on the energies of a system, but only on the Bloch wavefunctions.

The boundary modes arising from the confining potential or the boundary of the systems are actually topologically protected and related to a non-zero Chern number. This comes as another instance of the bulk-boundary correspondence. We pictorially present the band structure and a chiral edge state in a system with $C = 1$ in Figs. 6 (a) and (c). In a quantum Hall system, the left and right propagating modes are protected against the backscattering as they are macroscopically spatially separated on opposite edges of the sample.

1.5.2 *Chern insulators*

Even with zero net magnetic field, the system can realize a non-zero Chern number. This gives rise to the notion of the Chern insulators (CIs), also known as the quantum anomalous Hall effect. Experimentally, the CIs have been realized in a magnetic topological insulator [68], but also in fermionic ultracold atoms [69] or classical wave systems [70]. The simplest Chern insulator is modeled by a two band Hamiltonian $\mathcal{H}(\mathbf{k})$, whose general form is given by[8]

$$\mathcal{H}(\mathbf{k}) = d_0(\mathbf{k})\sigma_0 + \mathbf{d}(\mathbf{k})\sigma, \tag{42}$$

where $\boldsymbol{\sigma} = (\sigma_x, \sigma_y, \sigma_z)$ are the Pauli matrices and $\sigma_0 = \mathbb{1}_{2\times 2}$. The three-dimensional $\mathbf{d}(\mathbf{k})$ describes the internal structure of Bloch states, while the energies are given by $d_0(\mathbf{k}) \pm |d(\mathbf{k})|$.

8 In fact, any two-state Hermitian Bloch Hamiltonian admit such a representation.

If the system is insulating, we can define a unit vector $\mathbf{n}(\mathbf{k})$, which maps a point on a torus to a two-dimensional sphere S^2 known as the Bloch sphere.

$$\mathbf{n}(\mathbf{k}) = \frac{\mathbf{d}(\mathbf{k})}{|\mathbf{d}(\mathbf{k})|}, \qquad \mathbf{n} : T^2 \to S^2. \tag{43}$$

The Chern number can be written as

$$C = \frac{1}{4\pi} \int_{T^2} \mathbf{n} \cdot \left(\frac{\partial \mathbf{n}}{\partial k_x} \times \frac{\partial \mathbf{n}}{\partial k_y} \right) d\mathbf{k}, \tag{44}$$

which has a simple interpretation: it measures how many times the $\mathbf{n}$ vector wraps around the sphere as we integrate over the BZ.

1.5.2.1 *Haldane model*

In the seminal paper [13], Haldane proposed a model to describe spinless electrons in a single honeycomb lattice with a staggered magnetic flux pattern that leads to zero net magnetic flux. In addition to NN hopping terms appearing in the tight-binding description of graphene, there are also NNN hoppings with complex phases (illustrated in Fig. 5 (a)). These Aharonov-Bohm phases arise due to the time-reversal breaking staggered flux pattern, which are incorporated in the Hamiltonian through a Peierls substition, $t_1 \to t_1$, $t_2 \to t_2 e^{\mathrm{i}\phi}$. The model can be written as

$$H_{\text{Haldane}} = t_1 \sum_{\langle ij \rangle} c_i^\dagger c_j + t_2 \sum_{\langle\langle ij \rangle\rangle} e^{\pm \mathrm{i}\phi} c_i^\dagger c_j + M \sum_i \xi_i c_i^\dagger c_j + \text{h.c.}. \tag{45}$$

The last term with $\xi = \pm 1$ assigns the on-site energies $+M$ for sites of sublattice A and $-M$ for sublattice B. Hence, a non-zero M breaks inversion symmetry.

To represent the Hamiltonian in Eq. (45) in momentum space, we use the property defined in Eq. (42) with the following components of the $\mathbf{d}(\mathbf{k})$ vector

$$\begin{aligned} d_0(\mathbf{k}) &= 2t_2 \cos\phi \left[\sum_i \cos(\mathbf{k} \cdot \mathbf{a}_i) \right], \\ d_x(\mathbf{k}) &= t_1 \left[1 + \cos(\mathbf{k} \cdot \mathbf{a}_1) + \cos(\mathbf{k} \cdot \mathbf{a}_2) \right], \\ d_y(\mathbf{k}) &= t_1 \left[\sin(\mathbf{k} \cdot \mathbf{a}_1) - \sin(\mathbf{k} \cdot \mathbf{a}_2) \right], \\ d_z(\mathbf{k}) &= M - 2t_2 \sin\phi \left[\sum_i \sin(\mathbf{k} \cdot \mathbf{a}_i) \right]. \end{aligned} \tag{46}$$

$\mathbf{a}_i$ are the lattice vectors connecting the next-nearest neighbors (see Fig. 5 (a)), which we choose to be

$$\mathbf{a}_1 = a\,(1, 0), \quad \mathbf{a}_2 = a \left(\frac{1}{2}, \frac{\sqrt{3}}{2} \right), \quad \text{and} \quad \mathbf{a}_3 = \mathbf{a}_1 - \mathbf{a}_2 = a \left(\frac{1}{2}, -\frac{\sqrt{3}}{2} \right). \tag{47}$$

As far as the topology is concern, we can ignore the energy shift $d_0(\mathbf{k})$. Firstly, we point out that the terms $d_x(\mathbf{k})$ and $d_y(\mathbf{k})$ are time-reversal symmetric for any value of ϕ. $d_z(\mathbf{k})$, on the other hand, satisfies $d_z(\mathbf{k}) = d_z(-\mathbf{k})$ only for $\phi = 0$, π. The gap closes if and only if $d_x = d_y = d_z = 0$. For $M = 0$ and $\phi = 0$, π, d_z vanishes and the Hamiltonian is nothing but the

celebrated low-energy graphene model. The gap then closes at the Dirac points K and K' (see Fig. 5 (b)) with a linear dispersion, forming two Dirac cones of opposite chirality.

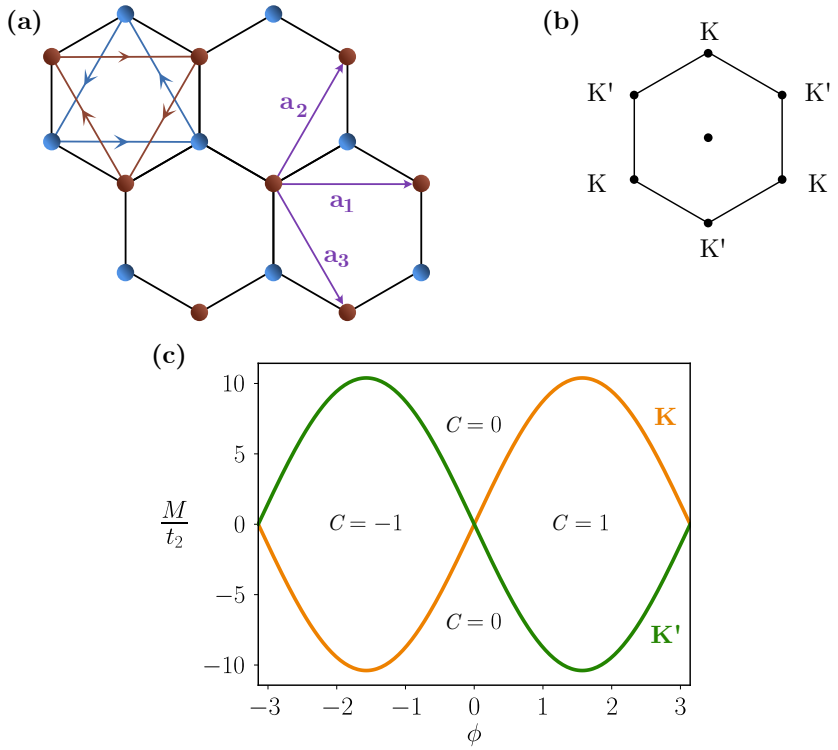

Figure 5: (a) Schematic representation of the Haldane model on the honeycomb lattice. The two sublattices, A and B, are denoted by the blue and red colors, respectively. Next-nearest neighbor hoppings carry a phase ϕ with a sign $+$ $(-)$ along blue (brown) links, resulting in the total zero flux. **(b)** The band gap closing occurs at the Dirac points $K = \left(\frac{2\pi}{3a}, \frac{2\pi}{3a\sqrt{3}}\right)$ and $K' = \left(\frac{2\pi}{3a}, -\frac{2\pi}{3a\sqrt{3}}\right)$ in the Brillouin zone. **(c)** The phase diagram on the plane $(\phi, M/t_2)$ with the Chern number of the lowest band. The gap closes at the critical lines $|M| = 3\sqrt{3}t_2 \sin\phi$. Orange line corresponds to the band gap closing at the K point, while green line to a band gap closing at the K' point.

For non-zero M and ϕ, the gap can still only close at the K and K' points. Therefore, it is convenient to work with a low-energy effective model. We can write the low energy expansion of the full Hamiltonian around the K point as

$$\mathcal{H}_L(\mathbf{q}) = \hbar v_F \mathbf{q} \cdot \boldsymbol{\sigma}_{2D} + m\sigma_z \tag{48}$$

where $\mathbf{q} = \mathbf{k} - K = (q_x, q_y)$, $\boldsymbol{\sigma}_{2D} = (\sigma_x, \sigma_y)$, and $m = d_z(K)$. The linearization leads to a massive Dirac Hamiltonian with mass m. A similar form emerges at the K' point with a mass m'. For the Haldane model, the masses m and m' at K and K' points, respectively, are (with $\hbar v_F = 1$)

$$m = d_z(K) = M - 3\sqrt{3}t_2 \sin\phi \quad \text{and} \quad m' = d_z(K') = M + 3\sqrt{3}t_2 \sin\phi. \tag{49}$$

We can now construct the phase diagram with respect to the model parameters (M, ϕ). In a generic case, the system is an insulator, except when $|M| = 3\sqrt{3}t_2|\sin\phi|$. For $|M| > 3\sqrt{3}t_2|\sin\phi|$ both K and K' points have a mass of the same sign, hence the Hall conductivity

vanishes and the system is in a trivial phase. Conversely, if $|M| < 3\sqrt{3}t_2|\sin\phi|$, then the Chern number is ± 1, depending on the signs of M and ϕ. In the trivial phase, m and m' have the same sign, whereas in topological case $m = -m'$. Two insulating phases with different Chern numbers are separated by a semimetalic transition point with low-energy Dirac cones. Between a phase with a Chern number ± 1 and the trivial phase with $C = 0$, the gap closes at a single K point, and the system admits only a single Dirac cone. The two topological phases are separated by a graphene-like critical point with two Dirac cones. We illustrate the full phase diagram in Fig. 5 (c).

Here, a simple formula for the Chern number is

$$C = \frac{\mathrm{sgn}(m) - \mathrm{sgn}(m')}{2}, \tag{50}$$

which can be applied to any two bands model described by $\mathbf{d}(\mathbf{k})$ vector, where the low-energy Hamiltonian is given by Eq. (48) close to the gap closing momenta. Similar to the QHE, the edge states in the Haldane model are chiral, as depicted in Fig. 6 (c).

1.5.3 *Quantum spin Hall effect*

Time-reversal symmetry breaking is an essential ingredient for the non-vanishing Hall conductivity σ_{xy}; the current $\mathbf{j}$ is odd under time-reversal, but the electric field $\mathbf{E}$ is even. However, the family of quantum Hall states can be extended by a new class of insulating states whose metallic edge modes are protected by the time-reversal symmetry, which was firstly theoretically proposed in graphene [14, 15][9] and in strained zinc-blende semiconductors [73]. The quantum spin Hall (QSH) effect was subsequently predicted in HgTe/CdTe quantum wells [16] and confirmed experimentally one year later [17].

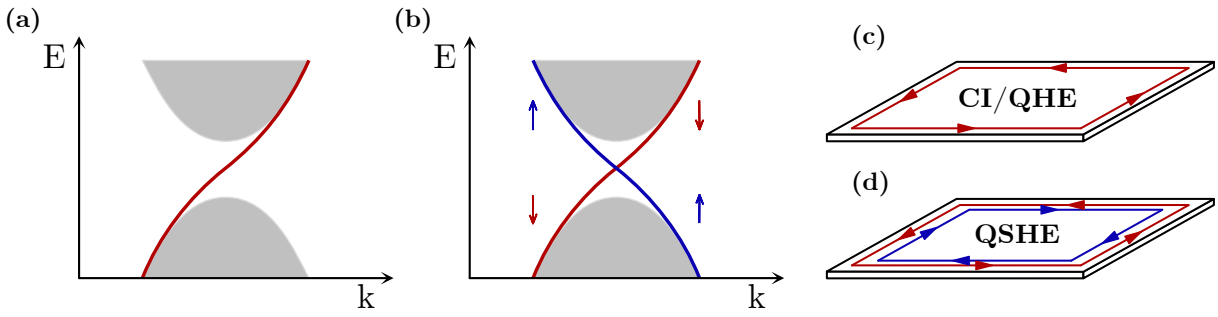

Figure 6: Schematic representation of the band structures of **(a)** a Chern insulator with $C = +1$ and **(b)** a quantum spin Hall system constructed as two copies of Chern insulators with opposite Chern numbers, together with conserved z-spin component. Edge states have **(c)** chiral character for a phase with broken time-reversal symmetry, while **(d)** TRS systems exhibit helical edge modes.

In QSH systems, a pair of spin-polarized edge states counter-propagate along the boundary is usually referred to as *helical* edge states (schematically depicted in Fig. 6 (d)). The helical boundary modes lead to a spin accumulation at the two edges transverse to the current direction rather than to a charge accumulation. The spin current $\mathbf{j}^S$ is even under TRS, which

9 However, due to the negligible spin-orbit coupling and therefore small SOC-induced band gap $\sim 10^{-3}$ meV, it is not realizable experimentally under realistic conditions [71, 72].

allows for the non-zero spin Hall conductivity σ^S_{xy}. In contrast to the charge current in QH systems, the spin current is not necessarily quantized [74, 75]. Two edge modes within a helical pair are time-reversal conjugates of one another, forming a Kramers pair. The TRS symmetry $\mathcal{T}^2 = -1$ forbids the backscattering between states in a Kramers pair, which explains the robust nature of the edge states. As long as there are an odd number of Kramers pairs [76] and no magnetic impurities (breaking time-reversal symmetry), the edge spectrum is stable against disorder. The fact that TRS does not preclude an even number of Kramers pairs to couple and gap out explains why the topological invariant is taken modulo 2 and results in the $\mathbb{Z}_2$ classification.

1.5.3.1 *Kane-Mele model*

A canonical example of the QSH system is the Kane-Mele model [14], describing spinful electrons in a honeycomb lattice. The Hamiltonian H_{KM} in real space is given by

$$\begin{aligned} H_{\mathrm{KM}} = &-t_1 \sum_{\langle ij\rangle\alpha} c^\dagger_{i\alpha} c_{j\alpha} + \mathrm{i}\lambda_{\mathrm{SO}} \sum_{\langle\langle ij\rangle\rangle\alpha\beta} \nu_{ij} c^\dagger_{i\alpha} \sigma^z_{\alpha\beta} c_{j\beta} \\ &+ \mathrm{i}\lambda_{\mathrm{R}} \sum_{\langle ij\rangle\alpha\beta} c^\dagger_{i\alpha} \left(\boldsymbol{\sigma}_{\alpha\beta} \times \hat{\mathbf{d}}_{ij}\right)_z c_{j\beta} + \lambda_{\mathrm{v}} \sum_{i\alpha} \xi_i c^\dagger_{i\alpha} c_{i,\alpha}. \end{aligned} \tag{51}$$

The first term corresponds to the hopping between nearest-neighbors with strength t_1. The second term λ_{SO} is the mirror-symmetric spin-orbit coupling with spin-dependent NNN hopping. The coefficients $\nu_{ij} = (2/\sqrt{3})(\hat{\mathbf{d}}_1 \times \hat{\mathbf{d}}_2)$ are equal to ± 1 with a sign that depends on whether a particle traverse from i to j clockwise ($\nu_{ij} = +1$) or counterclockwise ($\nu_{ij} = -1$), as in the Haldane model (consult Fig. 5 (a)). The third term λ_{R} describes the Rashba-type spin-orbit coupling. Here, $\boldsymbol{\sigma}$ stands for the vector of Pauli matrices $\sigma = (\sigma_x, \sigma_y, \sigma_z)$, acting on the spin degrees of freedom denoted by the α and β indices. Finally, the last term λ_{v} is a staggered sublattice potential with $\xi_i = 1$ for the A sublattice and -1 for the B sublattice. Non-zero λ_{SO} term breaks the SU(2) spin symmetry down to U(1) (conservation of the total spin polarization along the z axis). The Rashba term breaks it further into a discrete $\mathbb{Z}_2$ symmetry (parity of the total spin polarization along the z axis) and, in addition, breaks the mirror symmetry $z \to -z$. Introducing a finite λ_{v} leads to the breaking of the inversion symmetry $\mathcal{I}$ and the opening a trivial gap.

The system can be understood from the simple limit $\lambda_{\mathrm{R}} = 0$. Then, the Kane-Mele model is basically two copies of the Haldane model with opposite chiralities and conserved spin component S_z pointing out of the 2D plane (consult Fig. 6). Conveniently, the momentum-space Hamiltonian can be then written in a block-diagonal form

$$\mathcal{H}_{\mathrm{KM}}(\mathbf{k}) = \begin{pmatrix} \mathcal{H}_\uparrow(\mathbf{k}) & 0 \\ 0 & \mathcal{H}_\downarrow(\mathbf{k}) \end{pmatrix}. \tag{52}$$

In TRS systems, the total Chern number at half-filling always vanishes, however it is possible to assign a non-zero C to the spin sectors separately. Each band is doubly degenerate, i. e. spin-up and spin-down states have the same energy, which therefore leads to the constraint $C_\uparrow = -C_\downarrow$ as their sum must vanish.

We can then define the spin Chern number [77]

$$C_s = \frac{C_\uparrow - C_\downarrow}{2}. \tag{53}$$

In the presence of any spin-nonconserving processes, it is not possible to compute separately the Chern number of each spin flavour, thus the definition of C_s in Eq. (53) breaks down. However, time-reversal symmetry allows to define a more general $\mathbb{Z}_2$-valued invariant.

1.5.3.2 $\mathbb{Z}_2$ *invariant*

There exist several expressions for the $\mathbb{Z}_2$ invariant. Historically, the first formulation was given by Kane and Mele [15], where they interpreted the non-zero $\mathbb{Z}_2$ index as an obstruction to define a smooth gauge over the whole BZ. The idea is to consider the Pfaffian Pf of the antisymmetric matrix m connecting the Bloch states $|u_j(\mathbf{k})\rangle$ with their partners related by the time-reversal symmetry Θ

$$m_{ij}(\mathbf{k}) = \langle u_i(\mathbf{k})|\Theta|u_j(\mathbf{k})\rangle\,, \tag{54}$$

with i, j labeling the occupied states. The matrix m is not unitary, but antisymmetric $m^{\mathrm{T}}(\mathbf{k}) = -m(\mathbf{k})$. Moreover, the number of filled bands is always even due to time-reversal symmetry, hence the Pfaffian is well-defined. Recall that the Pffafian $\mathrm{Pf}(A)$ of a $2n \times 2n$ skew-symmetric matrix A is defined as

$$\mathrm{Pf}(A) = \frac{1}{2^n n!} \sum_{\mathcal{P}} \mathrm{sgn}(\mathcal{P}) \prod_{i=1}^{n} A_{\mathcal{P}(2i-1)\mathcal{P}(2i)}, \tag{55}$$

where the summation is over all permutations $\mathcal{P}$ of its indices and the permutation group has $2n$ elements. The Pfaffian of A verifies $(\mathrm{Pf}(A))^2 = \det A$.

The zeros of $\mathrm{Pf}(m)$ correspond to phase vortices that can only occur in isolated points in the BZ and always come in pairs as $|\mathrm{Pf}(m(\mathbf{k}))| = |\mathrm{Pf}(m(-\mathbf{k}))|$, except at the *time-reversal invariant momenta* (TRIMs). These momenta are special points Γ_i in the BZ satisfying $\Gamma_i + G = -\Gamma_i$ for a reciprocal lattice vector G, i. e. the TRS maps them onto themselves. We represent TRIMs in two- and three-dimensional BZ in Fig. 7.

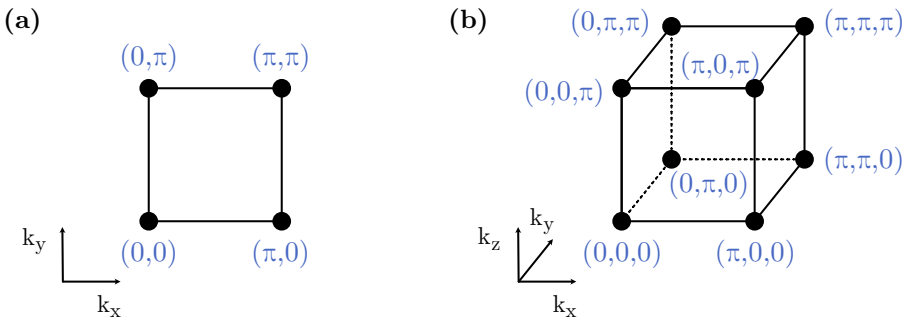

Figure 7: Time-reversal invariant momenta in **(a)** two- and **(b)** three-dimensional Brillouin zone for a square or cubic lattice.

At TRIMs, all bands exhibit Kramers' degeneracy. The subspace spanned by occupied Bloch states $|u_i(\mathbf{k})\rangle$ is the same as for their $\Theta\,|u_i(\mathbf{k})\rangle$ partners, hence the Pfaffian has unit modulus $|\mathrm{Pf}(m(\Gamma_i))| = 1$. Now, the zeros of the Pfaffian can only be gapped out if two vortices are

brought together. A single pair of vortices can only meet at a TRIM. However, as the Pfaffian is always of unit modulus there, the vortices cannot be supported and therefore cannot annihilate. On the other hand, two (or any even number of) pairs of vortices can always meet away from the TRIMs, and therefore be smoothly removed by a continuous deformation of the Hamiltonian. Consequently, the parity of the number of pairs of vortices of the Pfaffian $\mathrm{Pf}(m(\mathbf{k}))$ can serve as a $\mathbb{Z}_2$-valued topological invariant ν.

As the time-reversal symmetry maps $\mathbf{k}$ to $-\mathbf{k}$, there is a redundancy in a description based on the whole BZ. Instead, one may define an effective Brillouin zone (EBZ), which includes only one state out of each Kramers pair $(\mathbf{k}, -\mathbf{k})$, excluding the boundary. Hence, we can compute the invariant ν that corresponds to the parity of the number of vortices in the EBZ

$$\nu = \frac{1}{2\pi \mathrm{i}} \int_{\partial \mathrm{EBZ}} d\mathbf{k} \nabla_{\mathbf{k}} \log(\mathrm{Pf}(m(\mathbf{k}))). \tag{56}$$

A more practical expression of the ν invariant based on the sewing matrix w was proposed by Fu and Kane [78]

$$w_{ij}(\mathbf{k}) = \langle u_i(-\mathbf{k}) | \Theta | u_j(\mathbf{k}) \rangle \,. \tag{57}$$

The matrix w is unitary and, a priori, antisymmetric only at TRIMs, where it coincides with the m matrix defined in Eq. (54). There, we can express the ν invariant as

$$(-1)^{\nu} = \prod_i \delta_i \quad \text{with} \quad \delta_i = \frac{\mathrm{Pf}(w(\Gamma_i))}{\sqrt{\det w(\Gamma_i)}} = \pm 1. \tag{58}$$

If inversion symmetry is present, the expression further simplifies. Each Kramers pair n has a well-defined parity $\xi_{2n}(\Gamma_i) = \xi_{2n-1}(\Gamma_i) = \pm 1$, thus

$$(-1)^{\nu} = \prod_i \delta_i \quad \text{with} \quad \delta_i = \prod_{n=1}^{N} \xi_{2n}(\Gamma_i). \tag{59}$$

1.5.3.3 *Topological insulators in three dimensions*

Both QHE and QSHE are intrinsically two-dimensional phenomena. However, according to the ten-fold way, the concept of time-reversal symmetric band insulators can be extended to three dimensions [19, 18]. For a $3D$ Brillouin zone, it is possible to define four $\mathbb{Z}_2$ invariants $(\nu_0; \nu_1, \nu_2, \nu_3)$, where ν_1, ν_2, ν_3 are obtained by applying the formula in Eq. (58) in each of the three planes $k_x k_y$, $k_x k_z$ and $k_y k_z$, fixing the remaining momentum to π, giving 16 topologically distinct phases in total. If all four invariants are even, the system is topologically trivial. The phases with $\nu_0 = 1$ are said to be strong topological insulators, which have no analogy with 2D systems. It is in contrast to weak topological insulators with $\nu_0 = 0$, but $\nu_i \neq 0$ for at least one $i \in \{1, 2, 3\}$. These phase can be regarded as a stacking construction of 2D layers and therefore require additional protection by a translation symmetry in the stacking direction.

Apart from topological phase transition, 2D systems always have an even number of Dirac cones according to the *fermion doubling theorem*[10]. In strong TIs, the pairs appear at two spatially separated surfaces such that there are an odd number of surface Dirac cones around the time-reversal invariant points of each surface Brillouin zone. The spin of these surface Dirac cones is locked to their momentum, a phenomenon known as the spin-momentum locking [79].

10 Nielsen-Ninomiya theorem states that in two dimensions, the chiral Dirac cones can only appear in pairs.

1.5.4 *Su-Schriffer-Heeger chain*

The Su-Schriffer-Heeger (SSH) model, firstly introduced to characterize the properties of the polyacetylene [80], is a representative example of a topological system protected by the chiral symmetry[11]. The model describes a one-dimensional chain of spinless fermions, shown in Fig. 8 (a). A unit cell consists of two atomic species A and B, connected by alternating hoppings v and w. In real space, the Hamiltonian H_{SSH} is

$$H_{\mathrm{SSH}} = v \sum_i (c^\dagger_{i,A} c_{i,B} + \mathrm{h.c.}) + w \sum_i (c^\dagger_{i+1,A} c_{i,B} + \mathrm{h.c.}), \tag{60}$$

where v, $w > 0$ is assumed. There are two gapped phases with energy gap $\Delta E = 2\,|v - w|$, separated by a gapless line at $v = w$. By defining the spinor $\Psi_k = (c_{kA}, c_{kB})$ acting on the sublattice degrees on freedom, we can represent the Hamiltonian from Eq. (60) in reciprocal space

$$\mathcal{H}_{\mathrm{SSH}}(k) = \sum_k \Psi^\dagger_k \begin{pmatrix} 0 & v + we^{\mathrm{i}k} \\ v + we^{-\mathrm{i}k} & 0 \end{pmatrix} \Psi_k. \tag{61}$$

The bulk dispersion relation reads $E_\pm(k) = \pm\sqrt{v^2 + w^2 + 2vw\cos k}$ and the bulk gap closing occurs at $k = \pi$ for $w = v$. The SSH chain is a Hermitian two-band model, hence it can be expressed in terms of Pauli matrices as in Eq. (42). The $\mathbf{d}(k)$ vector for the $\mathcal{H}_{\mathrm{SSH}}$ is therefore

$$\mathbf{d}(k) = (v + w\cos k)\ \sigma_x + (v \sin k)\ \sigma_y = d_x(k)\,\sigma_x + d_y(k)\,\sigma_y. \tag{62}$$

The chiral symmetry $\mathcal{C} = \sigma_z$ constrains the values of $\mathbf{d}(k)$ vector to the xy-plane, so that $\mathbf{d}(k) = (d_x, d_y, 0)$ and $d_0(k) = 0$. In the $d_x - d_y$ space, the $\mathbf{d}(k)$ vector traces a trajectory as the momentum k varies from 0 to 2π. This trajectory is necessarily closed due to the periodicity of the Brillouin zone. For a gapped system with $v < w$, the $\mathbf{d}(k)$ vector encloses the origin (corresponding to a gap closing point), whereas for an insulating phase with $v > w$ it does not. In fact, one cannot smoothly deform $\mathbf{d}(k)$ to go from a trajectory enclosing the origin to the one which does not without the closing the gap.

The number of times $\mathbf{d}(k)$ winds around the origin, that is to say the *winding number* W, therefore naturally arises as a relevant topological invariant. In general, the winding number can take any integer value, but for the SSH model is either $W = 1$ (if $v < w$) or $W = 0$ ($v > w$) as illustrated in Figs. 8 (d) and (e). In the eigenbasis of the chiral symmetry $\mathcal{C}$, the Bloch Hamiltonian has a block off-diagonal structure

$$\mathcal{H}(k) = \begin{pmatrix} 0 & h(k) \\ h^*(k) & 0 \end{pmatrix}, \quad h(k) = d_x(k) - \mathrm{i}d_y(k), \tag{63}$$

which reduces the computation of the winding number ν to

$$W = \frac{1}{2\pi\mathrm{i}} \int_0^{2\pi} dk\, \frac{\partial}{\partial k} \log h(k). \tag{64}$$

11 The SSH chain belongs to the BDI class, hence TRS and PHS are also present. However, they are not responsible for topological protection.

A non-trivial bulk winding has also consequences on the spectrum in an open geometry. The phase with $W = 1$ is characterized by the presence of a pair of edge modes at exactly zero energy, in contrast to the fully gapped system with $W = 0$, where all eigenstates uniformly spread over all lattice sites (see Figs. 8 (b) and (c)). These edge states are therefore predicted by the topological invariant W. They will be gapped out only when the bulk gap closes, or when the chiral symmetry is broken. The breaking of chiral symmetry can be achieved, for instance by introducing long-range hoppings connecting the sites belonging to the same sublattice. Conversely, introducing longer range hoppings between sites of different sublattices allows for potentially higher winding numbers, and therefore more edge states if the TRS is also preserved.

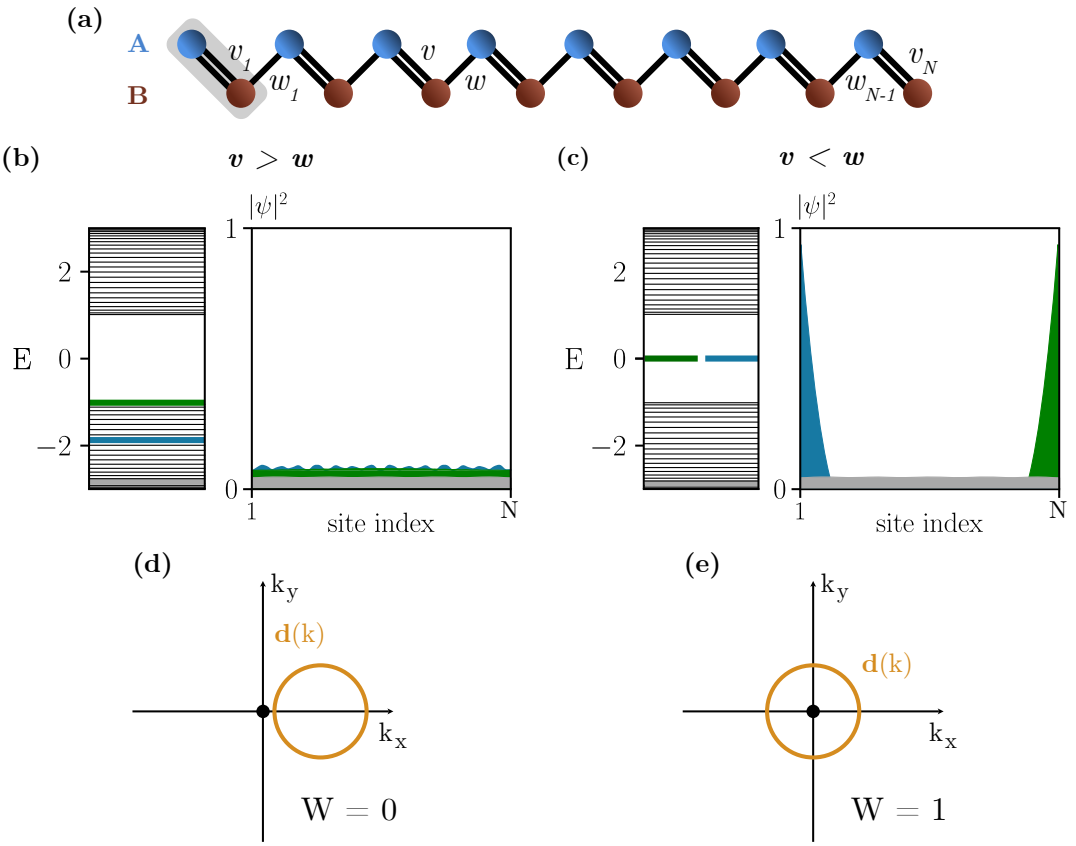

Figure 8: The Su-Schriffer-Heeger model. **(a)** schematic picture of a 1D chain. There are two inequivalent sublattices A and B (colored with blue and red, respectively) in a unit cell marked with a shaded area. Model has two type of hoppings: intracell with a strength v and intercell denoted by w. **(b)** Energy spectra and **(c)** localization of representative eigenstates in two parameter regimes for the system with open boundary conditions. Depending on the values of v and w, the model exhibits two topologically distinct phases: if $w < v$, the system is in a trivial phase (with $w = 0$ as a fully dimerized case) and all states have bulk-like density profile shown in **(b)**. Conversely, if $w > v$, the system is in a topological phase with zero-energy gapless edge models (see **(c)**). Hybridization of the edge states is exponentially small in the system size. **(d)** and **(e)** are corresponding windings of the $\mathbf{d}(k)$-vector around the origin, which defines the bulk winding number W.

Part I:

TOPOLOGICAL STATES IN NON-INTEGER-DIMENSIONAL SPACE

2

TOPOLOGICAL STATES IN FRACTAL LATTICES

In the previous Chapter, we have shown the importance of internal symmetries and dimensionality in construction of classification of free-fermionic Hamiltonians. Most of the topological phases in distinct symmetry classes are studied by considering clean systems limit, where it is possible to employ the concepts relying on the existence of the Brillouin zone and compute relevant topological invariants based on bundles of occupied Bloch states. However, disordered systems or lattice models without translational symmetries may also host topological states. For instance, quasicrystals, aperiodic systems that possess long-range order [81], exhibit topological properties which arise from higher-dimensional space in which these structures are truly translational invariant [82]. Several tilings were used to construct quasicrystalline structures hosting topological states protected by the symmetries which are forbidden for conventional crystals, including five- or twelve-fold rotations [83, 84]. Moreover, topological phases can be realized in completely random point sets [85]. Another interesting example is the so-called statistical topological insulator, where the gapless surface states are immune to Anderson localization as long as the disorder ensemble is invariant under a certain symmetry [86].

This Chapter is devoted to another family of irregular lattices, namely *fractal lattices*, which may also harbor topologically non-trivial states. Here, we specifically interested in the integer quantum Hall effect as a prototypical example of a topological phase and examine the topological properties of fractals exposed to the magnetic field. To familiarize the reader with the problem, we start by introducing the concept of fractals and their properties, in particular the notion of fractal dimension and the significance of lattice connectivity, in Section 2.1. Then, in Section 2.2, we present the crucial aspects of the Hofstadter model which explains the topological nature of IQH states defined on the lattice. After describing the model on a regular lattice, we move to formulating the problem on two chosen fractal geometries in Section 2.3 and discussing the results obtained by combining several numerical tools.

2.1 INTRODUCTION TO FRACTALS

Self-affine[1] lattices, in particular fractals [87], also fall into the category of aperiodic systems. Rather than a translational invariance, they possess a (discrete) scale invariance and are characterized by a Hausdorff dimension d_H, which is not necessary an integer. The concept of fractals has been extensively studied in the context of condensed matter physics, ranging from spin models defined on fractal lattices [88, 89] to the multifractal structure of wave functions at the Anderson metal-insulator transition point [90]. More recent studies covered quantum transport [91] and optoelectronic properties [92, 93] in fractal geometries, localization in deterministic and random fractal lattices [94–96], or defects in regular lattices arranged in a fractal manner [97]. Progress in the field in not only restricted to theoretical predictions – artificial fractal structures have been already experimentally realized using focused ion beam epitaxy [98], by depositing CO atoms on a Cu(111) surface [99] or assembling molecules [100].

1 Self-affinity is a generalization of self-similarity, which includes unequal scaling in different directions.

To introduce fractals in a realm of quantum lattice models, we begin with a brief discussion on fundamental concepts such as a notion of fractal dimension and connectivity properties of non-regular geometrical sets. The goal is to bring up several characteristics of fractal geometries, which determine the physical properties of systems.

2.1.1 *Scale invariance and fractal dimension*

Intuitively, scale invariance tells that the object looks exactly the same by zooming it in or out. Suppose we have an object of volume $V(L)$, a function of the linear extend L. Expanding the system size by a factor x, $L \to xL$, leads to rescaling the volume by a factor x^d

$$V(xL) = x^d V(L) \tag{65}$$

If some constrains are imposed on the allowed values of x (and therefore x^d), continuous scale invariance is replaced by a weaker, discrete version. For regular objects in $D-$dimensional Euclidean space, $d = D$. However, in case of self-similar objects embedded in D-dimensional space, an exponent d may be a non-integer smaller than D. Therefore, d was coined the fractal dimension (or Hausdorff dimension) and can be seen as a generalization of the topological dimension

$$d \equiv d_H = \lim_{L\to\infty} \frac{\log V(L)}{\log L}. \tag{66}$$

A practical definition of the fractal dimension is based on box-counting analysis. Let $N(s, r)$ be the smallest number of closed balls of radius r needed to cover a given set of sites. Then, one may define the box dimension (also called the Minkowski dimension)

$$d_B = \lim_{r\to 0} \frac{\log N(r)}{\log(1/r)} \tag{67}$$

In general, d_H is always less or equal to d_B, $d_H \leq d_B$, but for self-similar sets both dimensions are equivalent [101].

2.1.2 *Connectivity properties*

However, a fractal dimension does not uniquely determine the behavior of models defined on fractals and other geometrical characteristics play crucial roles. Connectivity properties of lattices were widely studied in the past in relation to classical spin models and phase transitions [102–104, 89]. One of them, the lacunarity $\mathcal{L}$, serves to measure how far an object is from being translationally invariant. High lacunarity means that a fractal has large gaps or holes, while $\mathcal{L} \to 0$ corresponds to the almost perfect lattice with translational symmetry. As one approaches the critical point in models defined on regular geometries with translational invariance, the correlation length is larger than the lattice spacings and the details of the lattice become redundant, thus all relevant information are encoded in the critical exponents and universality classes. Such universal description on criticality is lost in systems with large $\mathcal{L}$ [105].

Another property is the ramification number $\mathcal{R}$, which characterizes how many links between sites must be removed to disconnect an arbitrarily large part of a system. It was

pointed out that the value of $\mathcal{R}$ indicates whether the systems can exhibit a phase transition in classical models [106]; with a finite order of ramification, there is no phase transition at finite temperatures[2]. Moreover, a finite $\mathcal{R}$ is a necessary condition for the renormalization group in real space to be exact.

Quantum systems may be usually mapped to classical systems in one higher dimension, hence a significance of connectivity properties also holds for quantum phase transitions [107].

2.1.3 *Motivation*

From now, we focus on two fractal lattices, the Sierpiński carpet (SC) and gasket (or triangle, SG), which we illustrate accordingly in Figs. 9 and 10. The choice of these lattices are dictated by their distinct dimensionality and connectivity properties. For SC, the Hausdorff dimension is $d_H \approx 1.892$, while for SG $d_H \approx 1.585$. Also the ramification is opposite: SC has an infinite ramification, $\mathcal{R} = \infty$, while SG has finite $\mathcal{R}$ being equal to 4.

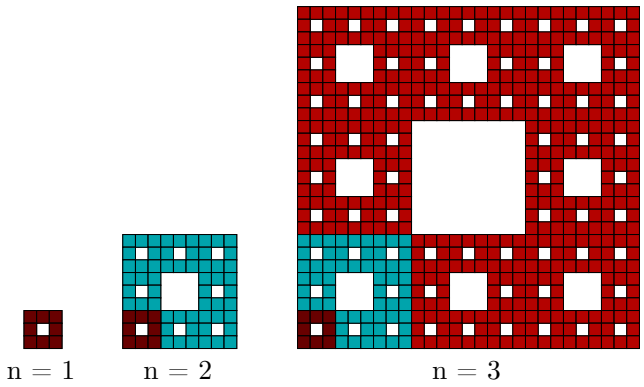

Figure 9: Iterative scheme for constructing Sierpiński carpet. Having a square lattice of the size $3^n \times 3^n$, we divide it in 9 smaller squares and remove the lattice sites within the central square. The process is then performed for remaining 8 squares and repeated as long as the smallest blocks are of a length 3 with a one hole in the middle (are equivalent to the first-order generation of the carpet, $n = 1$).

Even though spectral properties of the SC and the SG were investigated before [108–111], the topological aspects of the Hamiltonians defined on fractal lattices remain not fully explored. Only recently, results on BHZ model defined on fractal geometries were reported in Ref. [112] and the construction of spinless chiral $p-$ and $p + ip-$wave superconductors on the SC and the SG was discussed in Ref. [113]. In particular, understanding the bulk-boundary correspondence in such systems is problematic as well as there is no sharp distinction between the bulk and the edge [114, 115]. A final motivation to investigate Hamiltonians on fractals is related to the fractons. Fractonic topologically ordered models host fractionalized point-like excitations, fractons, which are immobile. In some of them (called type-II model), operators that create excitations have support on a fractal subset of the three-dimensional lattice.

2 This is in interesting parallel with the case of $1D$ quantum systems, which cannot exhibit a transition at finite temperature and also have a finite ramification number $\mathcal{R} = 2$.

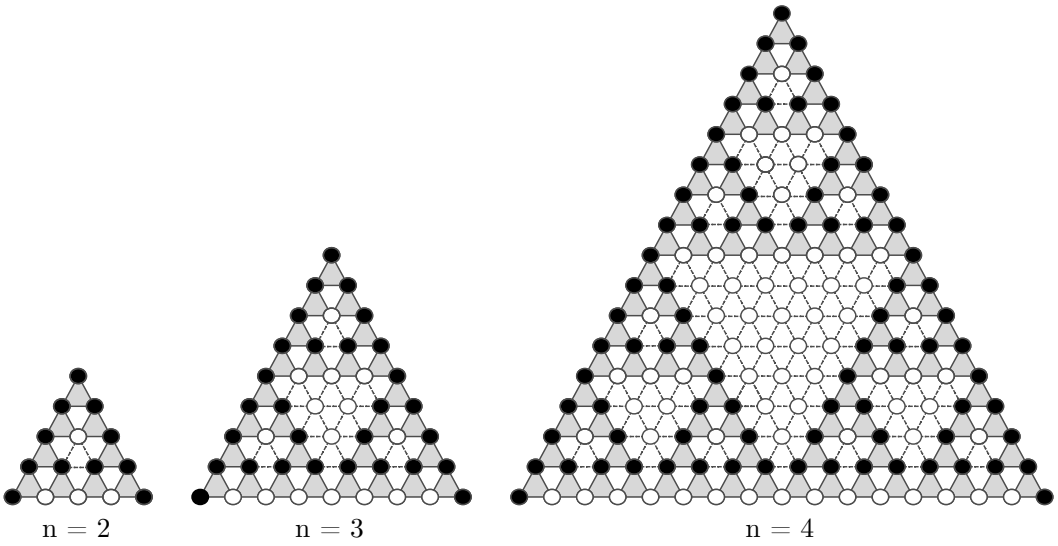

Figure 10: Iterative scheme for constructing Sierpiński gasket. To each site in a triangular lattice, we assign an integer and create a pattern which resembles the Pascal's triangle. If an associated value mod 2 is equal to one, then the site is filled with black color, otherwise is white; this procedure allows to determine which bonds have to be removed. For a white site located in c-th column and r-th row, three neighbouring hoppings are set to zero (denoted by a dashed black line): between white at (c, r) and black ones at $(c-1, r+1)$, $(c+1, r+1)$, respectively, as well between black sites at $(c-1, r+1)$ and $(c+1, r+1)$. Matrix elements in the Hamiltonian corresponding to the completely disconnected lattice sites are then removed.

For instance, the integer quantum Hall effect can be seen as one of the most robust topological phases as it does not require any symmetries (some authors consider IQH states as invertible topologically ordered states with long-range entanglement [116, 117]), but exists only in systems in even spatial dimensions[3]. All band insulators without any symmetry constraints are topologically equivalent in 1D, thus a strong topological phase cannot exist, and the 3D version of IQHE can be only constructed as a weak phase whose properties are inherited from the two-dimensional realization [25, 118]. Therefore, one may ask if quantum Hall states may be realized on almost two-dimensional lattices such as SC and SG. We firstly start with a short introduction to the lattice realization of the IQHE known as the Hofstadter model. After exemplifying the Hofstadter model on a square lattice, we then move to the investigations of this model on the lattice regularization of two aforementioned fractal geometries, i. e. the Sierpiński-Hofstadter problem.

2.2 THE HOFSTADTER MODEL

In the continuum limit, the quantum Hall effect is characterized by the macroscopically degenerated Landau levels and the quantized Hall conductivity which is directly linked to the number of occupied Landau levels. The essential properties of the IQHE can be captured by a simple tight-binding model of non-interacting electrons in a 2D periodic potential and in the presence of magnetic field. As one expects the electrons to be spin-polarized due to the magnetic field, we treat them effectively as spinless fermions.

3 In odd dimensions, IQH states are equivalent to trivial band insulators.

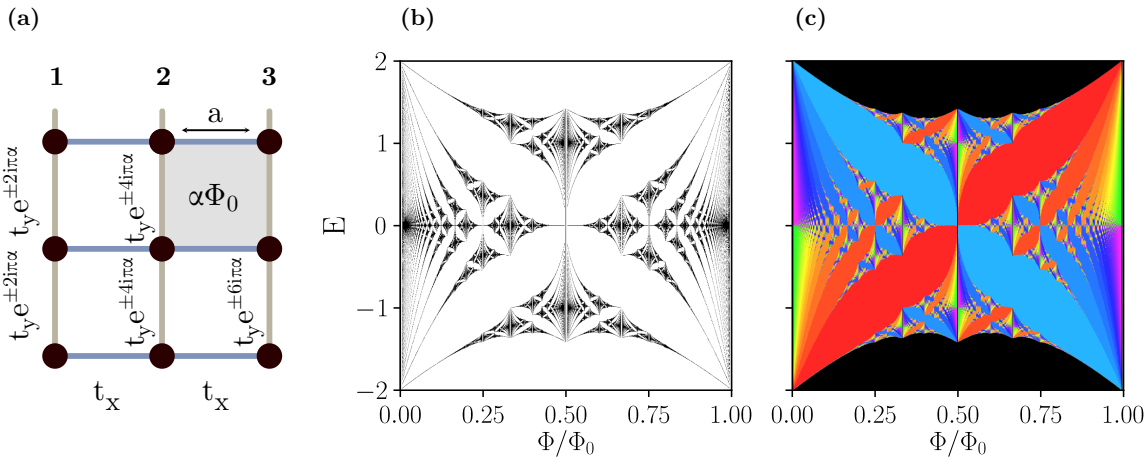

Figure 11: The Hofstadter model on a square lattice in the Landau gauge. **(a)** A schematic representation of hopping terms distribution on the lattice. Blue bonds correspond to the hoppings t_x along x direction and vertical grey bonds denote t_y hoppings with a x-dependent phase factor $2\pi i\alpha \cdot x$. Each lattice plaquette (represented by a gray square of a size $a \times a$) is pierced by a magnetic flux Φ being a fraction α of the flux quantum Φ_0. **(b)** Energy spectrum as a function of the magnetic flux α exhibits a self-similar pattern. The gapped regions can be colored by the corresponding Hall conductivity σ_{xy} in units of e^2/h as pictured in **(c)**.

Let us first consider the model without an external field, which includes only nearest-neighbors terms

$$H = -\sum_{\langle i,j \rangle} \left(t_x c^\dagger_{i+1,j} c_{i,j} + t_y c^\dagger_{i,j+1} c_{i,j} \right) + \text{h.c.} \tag{68}$$

$c^\dagger_{i,j}$ and $c_{i,j}$ are the electron creation and annihilation operators on the site labeled by i and j, while t_x and t_y are the hopping terms between neighboring sites in the x and y directions, respectively. If a magnetic field $\mathbf{B}$ is applied perpendicularly to the lattice, $\mathbf{B} = B\hat{\mathbf{z}}$, all lattice plaquettes are penetrated by a magnetic flux Φ. Using Stokes' theorem over a closed loop, we obtain a relation

$$\Phi = \int_A \mathbf{B} \cdot d\mathbf{S} = \int_A (\nabla \times \mathbf{A}) \cdot d\mathbf{S} = \int_{\partial A} \mathbf{A} \cdot d\mathbf{l} \tag{69}$$

with $\mathbf{A}$ being the electromagnetic vector potential around the loop enclosing the surface $A = a \times a$. Therefore, an electron travelling along a closed loop ∂A acquires an Aharonov-Bohm phase factor of $\exp(2\pi i \Phi/\Phi_0)$, where $\Phi_0 = h/e$ is the magnetic flux quantum. Within the tight-binding approximation, the Aharonov-Bohm phase can be incorporated by employing the Peierls substitution [119] in which all hopping terms t_{ij} are multiplied by an appropriate phase factor

$$t_{ij} \to t_{ij} e^{2\pi i A_{ij}/\Phi_0}, \qquad A_{ij} = \int_i^j \mathbf{A} \cdot d\mathbf{l}. \tag{70}$$

In the following, we choose the Landau gauge in which $\mathbf{A} = Bx\hat{\mathbf{y}}$ and the Hamiltonian reads

$$H = -\sum_{\langle i,j \rangle} \left(t_x c^\dagger_{i+1,j} c_{i,j} + t_y e^{-2\pi i \alpha \cdot i} c^\dagger_{i,j+1} c_{i,j} \right) + \text{h.c.} \tag{71}$$

This situation is depicted in Fig. 11 (a). If the values of the magnetic flux per plaquette $\alpha = \Phi/\Phi_0 = p/q$ are irrational, the energy spectrum consists of uncountably many points, which are all separated by finite gaps. The structure of the spectrum resembles the Cantor

set[4]. For rational values of α, where p and q are coprime integers, it is possible to define the magnetic unit cell being the smallest set of lattice plaquettes that encloses an integer number of flux quanta and transform the model into momentum space. The resulting Hamiltonian is not, however, translationally invariant with the translation operators of the underlying lattice. This is reflected by the fact that the Bloch Hamiltonian is not diagonal with respect to k and there is a mixing between different k-sectors, $(k_x, k_y) \to (k_x \pm 2\pi\Phi m, k_y)$ with m being an integer running over $m = 0, \ldots, q-1$ [120]. It is possible, though, to define translations with a periodicity of one lattice site in the y direction and q lattice sites in the x direction; as a consequence, the magnetic BZ is q times smaller. Then, the Hamiltonian is

$$H = \frac{a^2}{4\pi^2} \int_{-\frac{\pi}{qa}}^{\frac{\pi}{qa}} \int_{-\frac{\pi}{a}}^{\frac{\pi}{a}} H(k_x, k_y)\, dk_x dk_y \tag{72}$$

with

$$\begin{aligned} H(k_x, k_y) = &- t_x \left[\sum_{m=0}^{q-1} e^{ik_x a} a^\dagger_{k_x, \tilde{k_y}(m+1)} a_{k_x, \tilde{k_y} m} + e^{-ik_x a} a^\dagger_{k_x, \tilde{k_y}(m-1)} a_{k_x, \tilde{k_y} m} \right] \\ &- t_y \left[\sum_{m=0}^{q-1} \cos(k_y a + 2\pi\Phi m) a^\dagger_{k_x, \tilde{k_y} m} a_{k_x, \tilde{k_y} m} \right] + \text{h.c.} \end{aligned} \tag{73}$$

where $a^{(\dagger)}_{k_x, \tilde{k_y}}$ are new creation (annihilation) operators in reciprocal space with $\tilde{k_y} = k_y + 2\pi\Phi$. For weak fields, the model reproduces Landau levels, but at larger values of Φ the energies proceed to broaden and the spectrum has a remarkable self-similar structure known as the Hofstadter's butterfly [121] (shown in Fig. 11 (b)). Such spectrum arises from the interplay between two competing length scales: one associated with the periodicity of a lattice potential (lattice constant a) and the magnetic length l_B connected to the cyclotron radius of a uniform magnetic field. The key properties are:

1. The spectra for α and $\alpha + N$ (with $N \in \mathbb{Z}$) are identical; therefore, it is sufficient to study only the interval $\alpha \in [0, 1]$.
2. The Bloch bands break up into q distinct energy bands. If q is odd, all the bands are separated by a gap, whereas for even q, all energy bands except the central two (which touch at $E = 0$) are separated by finite energy gaps.
3. Each Hofstadter band is topologically non-trivial and carries a non-zero Chern number.

A relation between the fractal spectrum in the Hofstadter model and the Hall conductivity can be described by the Diophantine equation. Three positive integers r, p and q (where p and q are relatively prime) satisfy

$$pt_r + qs_r = r, \tag{74}$$

where t_r and s_r depend on the value of r. The equation has a solution for $t_r, s_r \in \mathbb{Z}$ if and only if r is a multiple of the greatest-common-divisor (GCD) of p and q. Because p and q are coprime, GCD is then 1 and Eq. (74) has a unique solution if

$$0 \le r \le q, \qquad |t_r| \le q/2. \tag{75}$$

4 The Cantor set is an uncountable set of real numbers in the unit interval of measure zero and can be constructed recursively by dividing the unit interval into three equal intervals of length 1/3 and then deleting the central one.

For a fixed magnetic flux p/q, an argument due to Středa [122] shows that such an equation must be satisfied by the Hofstadter model, with r corresponding to the number of occupied bands (that is, the Fermi energy lies inside the r-th gap) and t_r is the associated Hall conductivity in units of e^2/h

$$\sigma_{xy} = -\frac{e^2}{h} t_r. \tag{76}$$

We illustrate the Hall conductivities associated with the energy gaps in Fig. 11 (c).

2.3 THE SIERPIŃSKI-HOFSTADTER PROBLEM

To define the topology of quantum states, only a notion of locality and the possibility to take a thermodynamic limit are required. Since it is possible to specify quantum states on general graphs, it is important to ask what type of properties a graph must have to host topological states. Here, we would like to address this question by examining Sierpiński carpet and gasket in a homogeneous magnetic field and ask whether the features similar to those in conventional quantum Hall systems are observed.

Let us move to the Hofstadter model represented on the chosen fractal lattices with open boundary conditions (OBC). In general, it is possible to apply periodic boundary conditions (PBC) in both directions; for the carpet, the implementation is straightforward, but the gasket requires more attention[5]. Complex fractal pattern can be generated by an iterative procedure in which the system size increases with every step, but the distance between lattice sites remains the same. Such setting is most relevant to potential experiments on a nanoscopic scale as it introduces a natural cutoff. In order to construct the carpet, we start with a simple square lattice with $L(n) = 3^n$ sites along the outer edge, where n is an iteration step. Then, in every step n, $(1-(8/9)^n)\cdot 9^n$ lattice sites are removed (the procedure is illustrated in Fig. 9). From the Pascal's triangle modulo m (with m being a prime number) embedded in a triangular lattice having 2^n+1 rows, it is possible to obtain a series of gasket-like lattices with $d_H = 1+\log_m\left(\frac{m+1}{2}\right)$ and the case of $m=2$ corresponds to SG, which we demonstrate in Fig. 10.

Through the work, we consider the tight-binding Hamiltonian

$$H = -t\sum_{\langle i,j\rangle} e^{\mathrm{i}A_{ij}} c_i^\dagger c_j + \text{h.c.}, \tag{77}$$

with the vector potential satisfying relation $\mathbf{B} = \nabla \times \mathbf{A}$ and the phase factors distribution presented in Fig. 12. The hopping integral t between nearest-neighbors is the only energy scale in the model and it is set to $t = 1$. We assume that the magnetic field is homogeneous in the two-dimensional space in which the fractal lattice is embedded. The magnetic flux per smallest element of lattice-regulated versions of carpet and gasket (that is, the smallest square in the SC and the smallest triangle for the SG) is chosen to be Φ.

5 PBC can be realized, for instance, by representing the SG in a form of a rectangular triangle (which is topologically equivalent to the equilateral version), creating a mirror-symmetric copy with respect to its hypotenuse and treating two triangles together as a new, square-shaped system. The resulting structure has the same dimension d_H, but it may *not* share other properties with the original gasket. An alternative construction was proposed in Ref. [113], where four gaskets are arranged on alternating faces of an octahedron, hence all lattice site have the same coordination number equal to four.

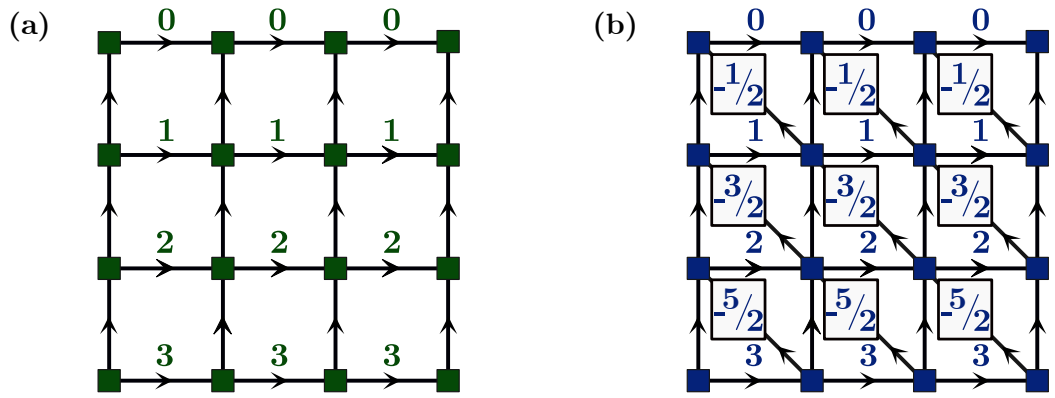

Figure 12: Phase distribution on 4×4 **(a)** square and **(b)** triangular lattices with open boundary conditions. A_{ij} phase between sites i and j is equal to the number shown above the bond in 2π units. A phase acquired with the respect to the direction pointed by arrows has a positive sign.

2.3.1 *Spectral properties*

Firstly, let us focus on the energy spectra obtained by diagonalizing the Hamiltonian given in Eq. (77) for different values of the magnetic flux. To describe the number of single-particle states within a given energy window $[\epsilon, \epsilon + \delta]$ that electrons are allowed to occupy, we compute the density of states (DOS)

$$D(\epsilon) = \sum_{\lambda=1}^{N} \delta\left(\epsilon - E_\lambda\right) \tag{78}$$

for sets of energy levels E_λ. Discrete DOS spectra can be smoothed using a Gaussian function, hence Eq. (78) can be rewritten as

$$D(\epsilon, \alpha) = \sum_{\lambda} \exp\left\{-\left[\epsilon - E_\lambda(\alpha)\right]^2 / \eta\right\} \tag{79}$$

with a broadening parameter η and $\alpha = p/q$. In Fig. 13 (a, d), we show DOS (with $\eta = 0.001$) for the SC at iteration $n = 4$ and the SG at iteration $n = 6$ with open boundary conditions. As in case of regular lattices, a presence of magnetic field gives rise to the Hofstadter's butterfly [121].

The spectrum of the SC (see Fig. 13 (a)) is reflection-symmetric with respect to the $E = 0$ and the $\alpha = 1/2$ lines due to a chiral symmetry of the Hamiltonian on this bipartite lattice. The spectrum is mostly gapless, but two finite gaps of maximal extend in energy ~ 0.1 are observed for small range of the flux around $\alpha = 1/4$, $3/4$ and $E = 0$. Regions of low DOS host states with distinct localization properties, which are discussed in more details in Section 2.3.2. If PBC are assumed, these regions are gapped with a few states in the middle of gaps (appearing as thin yellow branches in dark blue areas in Fig. 13 (a)).

Fig. 13 (d) shows the spectrum of the SG, which has only a point-inversion symmetry about $\alpha = 1/2$ and $E = 0$, while reflection symmetries are lost for this non-bipartite lattice. Various fully gapped regions are observed and large DOS appears around two points: $\alpha = 1/4$, $E \approx 1.4$, together with a symmetry-related point $\alpha = 3/4$, $E \approx -1.4$. It is known that at zero flux the spectrum is fractal and the energy levels are macroscopically degenerated [123]; introducing a

finite field leads to lifting this degeneracy. This degeneracy is mostly visible around $E = 2$ and $E = \pm 1$.

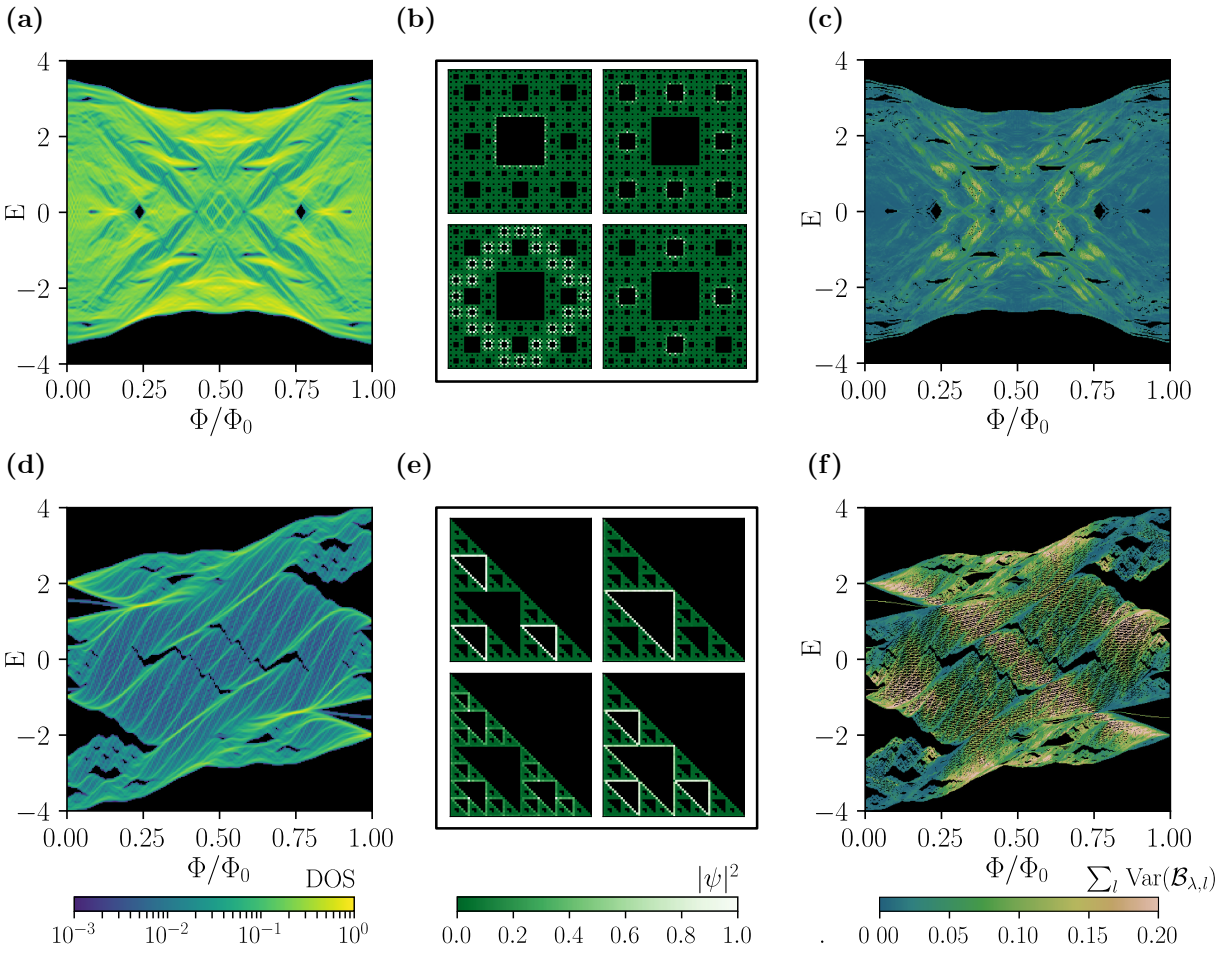

Figure 13: (a, d) Density of states in the energy-flux plane, **(b, e)** localization of the eigenstates, and **(c, f)** edge-locality marker. Low DOS regions are represented by dark blue color. Two energy gaps at $E = 0$ are seen for SC, while the energy spectrum of SG exhibits numerous gaps. Representative electronic densities at time-reversal symmetric point ($\alpha = 1/2$) around $E = 0$ are presented in **(b, e)** and the color scale corresponds to the square modulus $|\psi_i|^2$ of the wave function normalized by its maximum value. $\mathcal{B}_{\lambda,l}$ marker shown in **(c, f)** quantifies the changes in localization properties between consecutive eigenstates at fixed flux. Parts of the spectra with smaller density are associated with largely varying values of edge-locality marker.

2.3.2 *Edge modes*

A striking feature of a standard integer quantum Hall setup is the existence of protected edge modes. As the distinction between bulk and boundaries in fractal lattices is not sharp, it is not enough to simply point out that the edge modes are present. Hence, we would like to investigate the localization properties of the eigenstates in more details. Previous studies of fractal lattices suggested [124, 125] that introducing a magnetic field leads (on average) to

the delocalization of eigenstates. This observation can be confirmed by computing inverse participation ratio (IPR)

$$I_\psi = \frac{\sum_i |\psi_i|^4}{\left(\sum_i |\psi_i|^2\right)^2}, \tag{80}$$

for any wavefunction expandable in the real space basis $|\psi\rangle = \sum_i \psi_i |i\rangle$. The IPR takes values between 1 and the inverse of the number of sites N, where 1 corresponds to a perfect localization at one site and $1/N$ to evenly distributed weights over all lattice sites. At zero flux $\alpha = 0$ (Figs. 14 (a) and 15 (a)), the distribution of IPRs is peaked close to the inverse of the number of sites belonging to the edges of the second-smallest squares or triangles. For a finite field, the distribution of IPRs shifts to smaller, i. e., more delocalized values. This effect is more apparent for the SC compared to the SG.

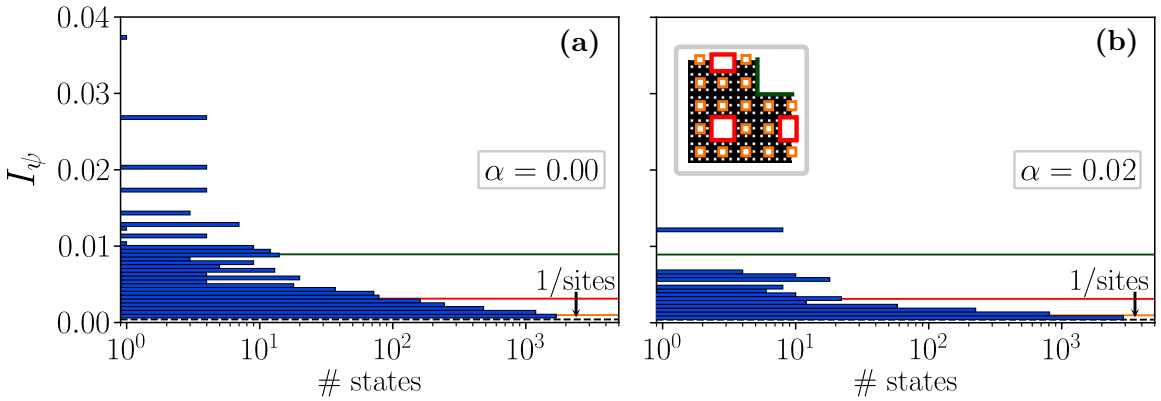

Figure 14: Distribution of IPR for the Sierpiński carpet: at **(a)** $\alpha = 0$ and **(b)** $\alpha = 0.02$. Inset presents a close-up of the carpet with the internal edges of different hierarchies marked with different colors. A finite magnetic field leads to the delocalization of the eigenstates.

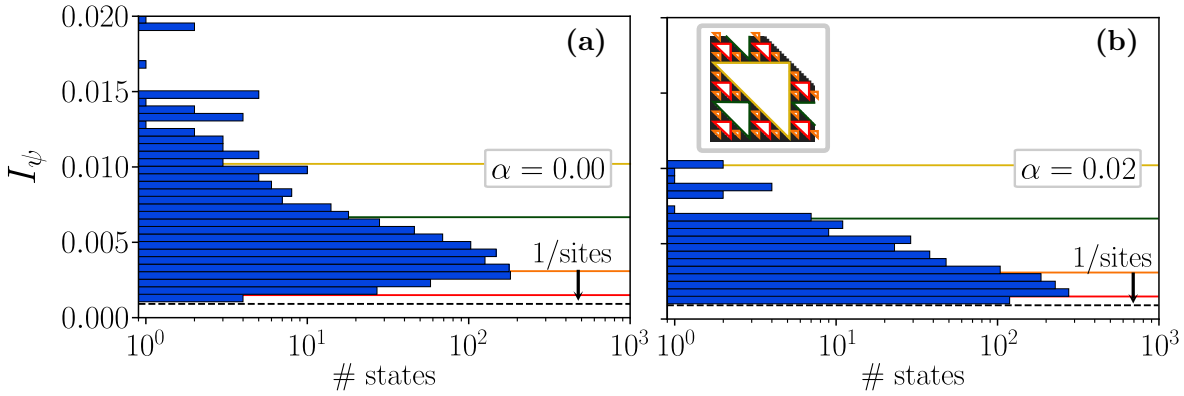

Figure 15: Distribution of IPR for the Sierpiński gasket at **(a)** $\alpha = 0$ and **(b)** $\alpha = 0.02$. Inset displays a close-up of the gasket with the highlighted edges of different hierarchies. Similar to the carpet, the distribution of IPRs is shifted towards more delocalized values for the non-zero magnetic field.

Remarkably, by contrasting the case of zero and non-zero magnetic field, we observe an intriguing change in the character of the most localized states. Fig. 13 (b, e) shows the electronic densities for the eigenstates at the time-reversal symmetric point ($\alpha = 1/2$) around zero energy. States are sharply localized at the internal edges of the fractal at different levels of the hierarchy

and they can be found in very close spectral proximity to one another in various places of the phase diagram at finite magnetic field. Conversely, at zero magnetic field, the most localized states exhibit complex interference pattern, but are usually not supported on internal edges. To quantify the degree of localization, we compute edge-locality marker defined as

$$\mathcal{B}_{\lambda,l} = \sum_{i \in \mathcal{E}_l} |\psi_{\lambda,i}|^2, \tag{81}$$

where $\langle i|\psi_\lambda\rangle = \psi_{\lambda,i}$ and the summation is taken over the edges $\mathcal{E}_l$ of all internal squares or triangle at level l of the hierarchy such that $l = 0$ corresponds to the lattice sites along all smallest squares/triangles and $l = n$ - to the outermost edge. Hence, $\mathcal{B}_{\lambda,l}$ measures how much an eigenstate $|\psi_\lambda\rangle$ with an energy E_λ has a support on the different edges of level l. With every state $|\psi_\lambda\rangle$, we associate a set of $\mathcal{B}_{\lambda,l}$ for $l = 0, \ldots, n$. In order to detect where in the phase diagram the localization properties are varying the most, we compute the variance for each entry of the set $\mathcal{B}_{\lambda,l}$ across three states with energies $E_{\lambda-1}$, E_λ and $E_{\lambda+1}$, and sum these variances over l: $\sum_l \mathrm{Var}\left(\{\mathcal{B}_{\lambda-1,l}, \mathcal{B}_{\lambda,l}, \mathcal{B}_{\lambda+1,l}\}\right)$. In regular lattices, peaks of the variance separate bulk states from edge states. Results shown in Fig. 13 (c, f) indicate that sharp changes in eigenstate localization appear mostly in the low DOS regions, thus we can interpret these regions as made of edge-like states at various levels of the fractal hierarchy.

2.3.3 *Real-space formulation of topological invariants*

Due to the lack of translational invariance, it is not possible to compute topological indices based on a bundle of occupied Bloch states. However, we may employ a real-space perspective on obstructions of filled states in a topological system. Non-zero topological index implies the existence of extended edge modes, therefore it is not possible to perturb the Hamiltonian such that it would lead to the exact localization of all the occupied states without breaking the symmetries or closing the gap (otherwise it would mean that the system is topologically trivial). This can be captured by using non-commutative geometry, which allows to define appropriate indices for each symmetry classes [126].

2.3.3.1 *Bott index*

The Bott index, introduced in the context of condensed matter physics by Loring and Hastings [127], tells whether a pair of unitary matrices can or cannot be approximated by a pair of commuting unitary matrices. In our case, we measure the commutativity of the projected position operators [56]. A degree of commutativity of these operators is directly related to the localization properties of the Wannier functions: a vanishing Bott index implies the existence of exponentially localized Wannier functions with a spread being small compared to the linear size of the system [128, 129]. A system that admits a representation in terms of exponentially localized Wannier functions has no strong topology, hence non-zero Bott index marks a non-trivial bulk topology.

Let us now define the Bott index and discuss its properties. Consider a representation of the position operators X and Y, defined as

$$X_{ij} = x_i \delta_{ij} \quad \text{and} \quad Y_{ij} = y_i \delta_{ij}. \tag{82}$$

Given the linear size of the system L and the coordinates rescaled to fit the interval $[0,1)$, $X \to X/L$ and $Y \to Y/L$, one constructs the matrices U and V

$$\begin{aligned} U &= Pe^{i2\pi X}P - (1-P), \\ V &= Pe^{i2\pi Y}P - (1-P) \end{aligned} \tag{83}$$

and computes their product using the formula

$$B = \frac{1}{2\pi}\mathrm{Im}\left(\mathrm{Tr}\left[\log(VUV^{\dagger}U^{\dagger})\right]\right), \tag{84}$$

where $P = \sum_{E<E_F} |\psi\rangle \langle\psi|$ is the orthogonal projector on the occupied bands below the Fermi energy E_F. If the Hamiltonian is short-ranged and E_F lies in a (mobility) gap, then the corresponding P operator is also local. Note that $(1-P)$ term appears if the system has boundaries or when the projector P onto the occupied subspace does not create an orthonormal basis [130]. U and V matrices are approximately unitary, $UU^{\dagger} \approx \mathbb{1}$ and $VV^{\dagger} \approx \mathbb{1}$, and almost commute, $[U,V] \approx 0$, if E_F is in a mobility gap; this indicates that $VUV^{\dagger}U^{\dagger}$ is then close to the identity.

We see that from the property $\det(VUV^{\dagger}U^{\dagger}) = \exp\left(\mathrm{Tr}\left[\log(VUV^{\dagger}U^{\dagger})\right]\right)$ and 2πi periodicity of the complex exponential, we can write

$$\mathrm{Tr}\left[\log(VUV^{\dagger}U^{\dagger})\right] = \log\left[\det\left(VUV^{\dagger}U^{\dagger}\right)\right] + 2\pi i m, \quad m \in \mathbb{Z}. \tag{85}$$

For unitary matrices, $|det(VUV^{\dagger}U^{\dagger})| = 1$, hence $\log\left[\det\left(VUV^{\dagger}U^{\dagger}\right)\right]$ vanishes and therefore the Bott index defined in Eq. (85) must be an integer. The Bott index is equal to zero if and only if U and V are (close to) a pair of commuting unitaries. If an eigenvalue of $VUV^{\dagger}U^{\dagger}$ is far from the branch cut of the logarithm (chosen to be the negative real axis), the value of B is not affected. However, if one of the eigenvalues crosses the branch cut, its phase changes by 2π and therefore the Bott index changes. It has been proven that for gapped, short-ranged Hamiltonians, the Bott index is equivalent to the Chern number in the thermodynamic limit [131, 132]. Also, its applicability has been extended to the spinful systems, where the spin Bott index is defined analogously to the spin Chern number computed for two spin sectors separately [133]. Therefore, we expect non-zero values of B in the parts of spectrum hosting topologically non-trivial states.

Stability of the computation of the Bott index can be ensured by performing a singular value decomposition (SVD) of the U and V matrices, $U = Z_U \Sigma_U W_U^{\dagger}$ and $V = Z_V \Sigma_V W_V^{\dagger}$ [134, 135]

$$\begin{aligned} U &\to \tilde{U} = Z_U W_U^{\dagger}, \\ V &\to \tilde{V} = Z_V W_V^{\dagger}. \end{aligned} \tag{86}$$

$\tilde{U}$ and $\tilde{V}$ matrices are unitary, because Z and W are unitary by definition, and the commutativity of the operators is preserved.

Motivated by the application of the Bott index to fractal lattices [112], we compute B as a function of magnetic flux at different Fermi levels. The resulting phase diagrams are presented in Fig. 16, where numerous regions of non-zero B are observed. We focus on the third generation of the carpet and $n = 5$ iteration for the gasket as numerical efficiency of the Bott index is rather restricted to small system sizes. Nevertheless, in case of SC low DOS regions are in agreement with $B \pm 1$. Larger values of B can be seen for fluxes around $\alpha = 0.4$ and $\alpha = 0.6$ at

$E = 0$. For SG, a region with consistently non-zero Bott index corresponds to the part of the spectrum with sharp changes in eigenstate localization properties. This is in agreement with the picture of the low DOS regions being the equivalent of bulk-gapped energy regions hosting edge states in conventional topological systems.

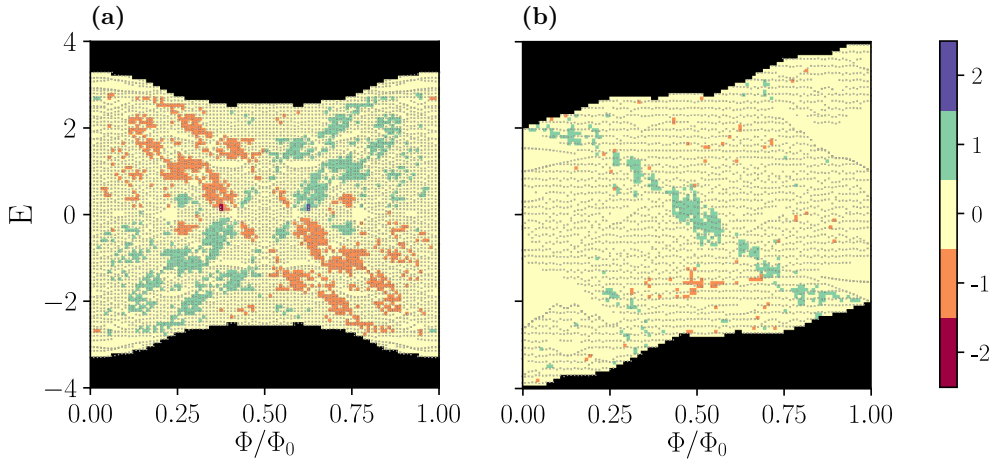

Figure 16: Bott index at different Fermi levels as a function of magnetic flux for **(a)** carpet with $n = 3$ and **(b)** gasket with $n = 5$. Overlaying small grey dots denote the energy spectrum. In case of the carpet, low DOS regions overlap with non-zero Bott index in the phase diagram; additionally, small regions with $B = \pm 2$ are observed around $E = 0$ and fluxes $\alpha \sim 0.4, 0.6$. For the gasket, an extended region with $B = 1$ coincide with a set of states having largely varying localization properties.

2.3.3.2 *Chern number*

A more efficient approach to compute real-space topological invariants is rather based on *local* markers, which allows to investigate larger systems. Instead of performing the calculations for a full lattice, it is enough to consider the local index computed over the finite patch. If this patch is chosen to be far from the edges, then the result is insensitive to boundary conditions. We hence employ the real-space formula for the Chern number based on an antisymmetric product of projection operators P [136], defined in the previous section

$$\mathcal{C} = 12\pi \mathrm{i} \sum_{j\in A} \sum_{k\in B} \sum_{l\in C} \left(P_{jk} P_{kl} P_{lj} - P_{jl} P_{lk} P_{kj} \right), \tag{87}$$

where j, k, l label the lattice sites in three distinct neighboring sectors A, B and C arranged in a counterclockwise manner (consult Fig. 17). As a remark, for a translational invariant case, Eq. (87) reduces to

$$\mathcal{C} = 2\pi \mathrm{i} \mathrm{Tr} \left(P \left[[X, P], [Y, P] \right] \right) \tag{88}$$

with X and Y being the operators of x and y coordinates, respectively, and the trace is taken over the unit cell. The sum in Eq. (87) should converge to an integer, when the summation region is large enough. If $\mathcal{C}$ is indeed quantized, it becomes then independent of the detailed choice of A, B, C in the limit where the number of sites in each part goes to infinity.

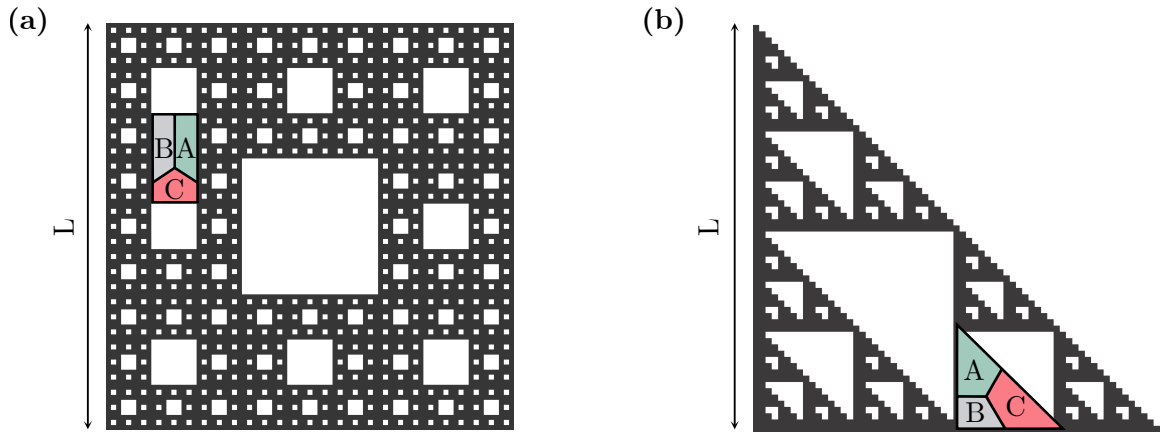

Figure 17: **(a)** The fourth iteration of the Sierpiński carpet with $L = 81$ and **(b)** the sixth iteration of the Sierpiński gasket with $L = 65$. Black squares depict the lattice sites which are kept from the underlying regular square (in case of the carpet) and triangular (gasket) lattices. Summation regions used in real-space Chern number calculations are labeled with A, B, C.

Using the SC as an example, in Fig. 18 we show how a real-space patch choice affects the quantization of $\mathcal{C}$. We compute $\mathcal{C}$ while varying the distance R between the center and the corners of the patch that makes up A, B, C sectors and keeping the aspect ratio of rectangle constant. When the summation region is too small or too large (close to the size of the entire system), $\mathcal{C}$ is far from a non-zero quantized value as expected. We focus on two Fermi levels, $E_F = -1.2$ and $E_F = -1.0$, which correspond to spectral regions with less and more quantized $\mathcal{C}$, respectively. For $E_F = -1.0$ which lies in low DOS region, $\mathcal{C}$ is very close to 1 over a large range of R. Conversely, for $E_F = -1.2$ (at large DOS), where $\mathcal{C}$ is not quantized, a strong R-dependence is found.

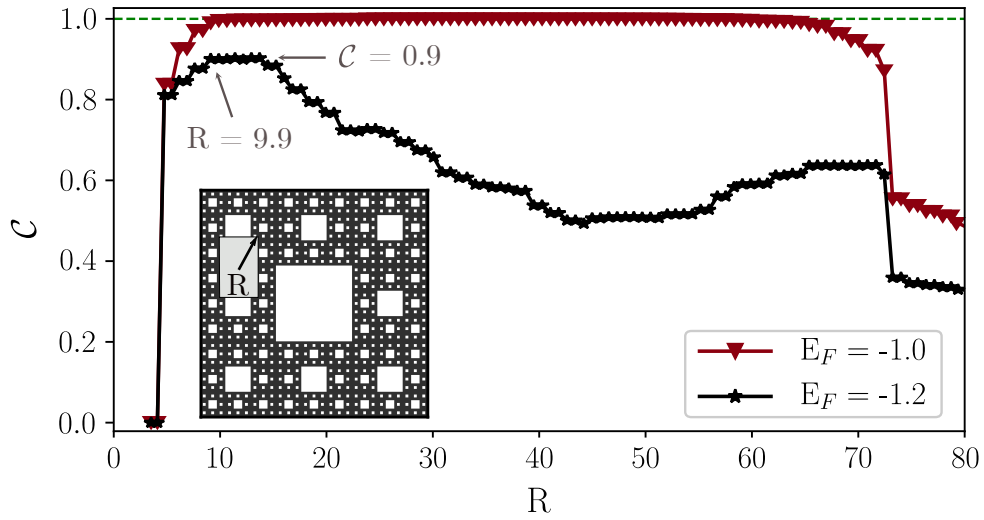

Figure 18: Real-space Chern number calculations for Sierpiński carpet as a function of the half of the diagonal of a rectangular patch R for two Fermi levels $E_F = -1.2$ and $E_F = -1.0$ at fixed flux $\alpha = 1/4$. For spectral regions exhibiting stable plateaus with quantized $\mathcal{C}$, this quantization is observed for a large range of patch sizes. In case of large DOS regions, in which we dominantly observe deviation from a quantized value of $\mathcal{C}$, the value of $\mathcal{C}$ is sensitive to the size and shape of the summation region. $R = 9.9$ corresponds to the size of the patch shown in Fig. 17 (a).

Figs. 19 (d) and 20 (d) present $\mathcal{C}$ as a function of the Fermi energy E at fixed value of flux $\alpha = 1/4$ for the $n = 4$ iteration of SC and the $n = 6$ iteration of the SG with a patch size corresponding to the most robust results. We arrive at following conclusions:

1. All fully gapped regions of the spectrum, for both lattices, carry $\mathcal{C} = 0$. Similar to the systems defined on regular lattices, an absence of in-gap states indicates that there are no topological edge modes[6].

2. Low DOS regions for the SC in Fig. 13 (a) are associated with stable plateaus $\mathcal{C} \sim \pm 1.0$ (for a wide range of energies $E = -1.5 \ldots -0.9$ and $E = 0.9 \ldots 1.5$), as well less quantized regions with $\mathcal{C} \sim \pm 0.96$ ($E = -2.6 \ldots -2.5$ and $E = 2.5 \ldots 2.6$). Deviations from quantized Chern numbers are observed when the DOS is enhanced, for example around $E = -1.2$ and $E = 1.2$. This suggests that edge modes are indeed chiral and contribute to the Chern number. In Refs. [112, 113], the authors studied a wave packet evolution in different models on the SG and found that the chirality of wave packets initialized on any of the inner edges is opposite to the case when the wave packet propagates along the outermost edge. Such situation is also expected in our case.

3. Identification of non-trivial regions for the SG is less clear, yet a plateau from $E = 1 \ldots 1.6$ converges to $\mathcal{C} \sim 1.0$.

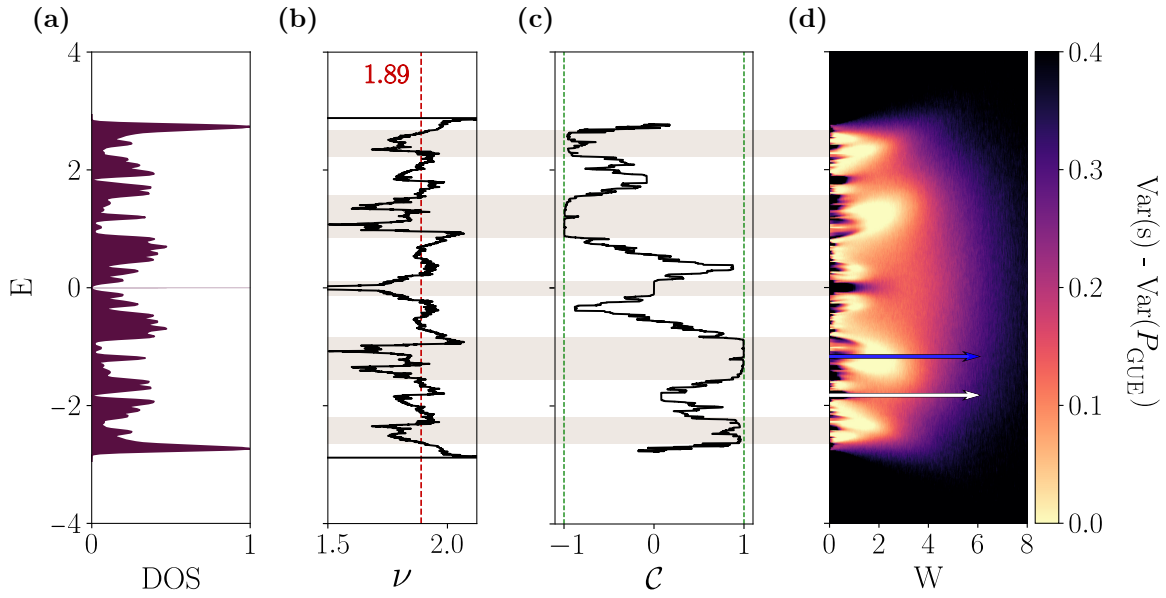

Figure 19: Topological properties of Sierpiński carpet at fixed flux $\alpha = 1/4$: **(a)** density of states, **(b)** scaling exponent ν of the DOS with system size, **(c)** Chern number as a function of E and **(d)** variance of level spacings in the energy-disorder strength plane. Grey rectangles are guide to the eye. We identify the full energy gaps to be trivial. Regions with quantized values of the Chern number close to 1 are separated by a delocalized state from the Anderson insulator limit (see blue arrow in **(d)**), which is a feature of quantum Hall states. This is in contrast to a direct transition to a fully localized phase for states carrying zero Chern number as a function of W (white arrow in **(d)**). Regions with $\mathcal{C} \neq 0$ are characterized by a DOS scaling exponent ν smaller than d_H in **(b)**.

6 Not all edge states appearing in the bulk band gap are topological; protected edge states arising from a non-trivial bulk topology exhibit *spectral flow* – they interpolate across the energy gap and spectrally connect the conduction band with the valence band.

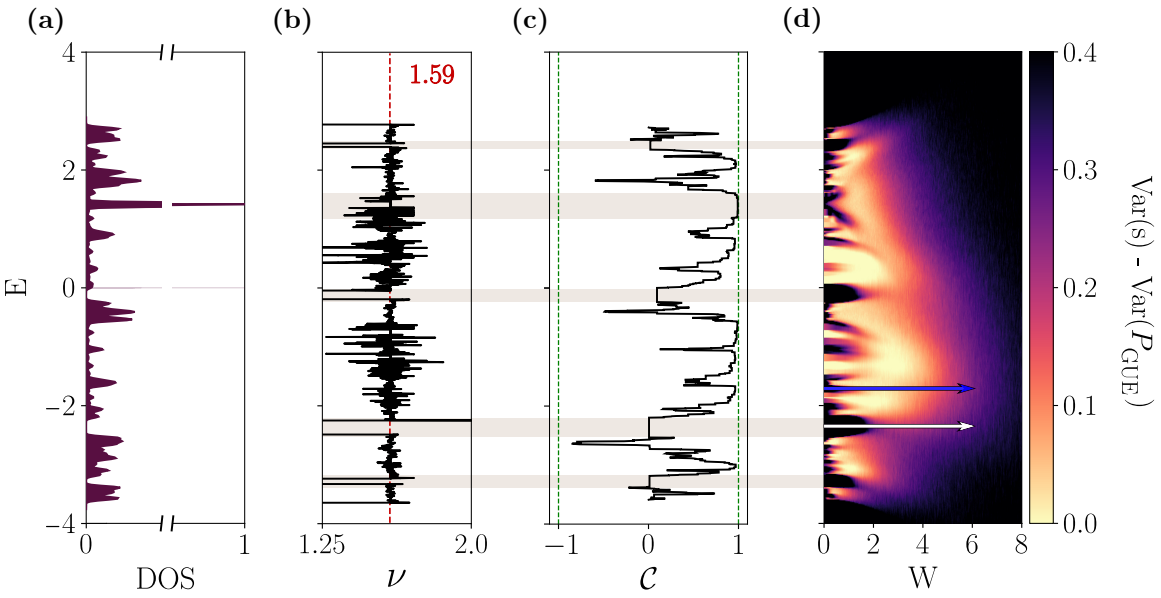

Figure 20: Topological properties of the Sierpiński gasket at fixed flux $\alpha = 1/4$: **(a)** density of states, **(b)** scaling exponent ν of the DOS with system size, **(c)** Chern number as a function of E and **(d)** variance of level spacings in the energy-disorder strength plane. Similar to the SC, spectral gaps are also topologically trivial. Quantization of the Chern number is less pronounced, but the levitation and pair annihilation mechanism is still observed (see **(d)**).

It is not obvious whether for fractals $\mathcal{C}$ tends to quantized values for almost all energies in the thermodynamic limit, that is the deviation from quantized $\mathcal{C}$ is solely due to finite-size effects. Because of the exponential increase in size for every iteration, performing systematic finite-size studies remains challenging. In the follow-up works on the SC [114, 115], the authors noted that the Hall conductivity σ_{xy} is not quantized and not necessarily proportional to $\mathcal{C}$, but vary with the depth of the fractal. On the other hand, the edge states corresponding to non-zero σ_{xy} are always present for a finite field strength and stable as one approaches the thermodynamic limit.

To discuss the connection between the DOS and the Chern number, we calculate the number of states at fixed flux α averaged over an energy interval $[\epsilon - \delta, \epsilon + \delta]$ (with $\delta = 0.1$ for the SC and $\delta = 0.05$ for the SG) for different system sizes, and compute the average scaling exponent ν of the number of states in that energy range with system size. On average, ν equals the Hausdorff dimension d_H. In Fig. 19 (b), we see that for the SC regions with a (nearly) quantized Chern number consistently show scaling with $\nu < d_H$. This indicates that the normalized DOS would scale to zero in the thermodynamic limit in regions with quantized Chern number. For the SG, the situation is less clear except in regions of trivial Chern number where no states are found (see Fig. 20 (b)).

An important comment has to be made on the discrepancies between the Bott index and the Chern number calculations, especially in case of the SG. Firstly, we would like to point out that larger lattices were investigated with local markers, hence the self-similar structure of energy spectrum is more complex and new subregions associated with a non-trivial topological index appear. In finite systems, it is not guaranteed that the Bott index is equivalent to the Chern number; yet, an agreement may be expected for larger, not necessarily numerically tractable, system sizes.

2.3.4 *Effect of disorder*

Topological matter is often defined in terms of its immunity to disorder. As suggested by Anderson [47], a constructive quantum interference between wavefunctions of particles may result in localization by a random potential. However, if carriers move along one edge of the sample, the physical separation between pairs of opposite edge channels precludes backscattering. This property underlies the robustness of topological systems. In QH setups, disorder splits the degeneracy of the bulk Landau levels, but the edge modes remain unaffected - because of their chirality, they cannot scatter in a single edge channel and scattering between edges is exponentially suppressed. Sufficiently strong disorder destroys this physical picture and the system enters into a global insulating phase [137].

For this reason, we would like to investigate the effect of disorder by adding extra term $\sum_i V_i c_i^\dagger c_i$ to the Hamiltonian defined in Eq. (77), where V_i is drawn from a uniform distribution $[-W/2, W/2]$ and W corresponds to the disorder strength. If the system is initially characterized by a non-vanishing Hall conductivity, introducing disorder does not lead to an instant transition to a trivial Anderson phase, where all states, including the protected boundary modes, are fully localized at lattice sites. Instead, a disorder-induced topological phase transition is accompanied by a so-called levitation and pair annihilation mechanism [138, 139]. As the disorder increases, the states characterized by non-zero Chern number move towards each other, they meet at intermediate disorder values and annihilate, ultimately leading to Anderson localization at large disorder strength exceeding the band width. Notably, the edge states are rather protected by the mobility gap – an interval in the spectrum of a Hamiltonian between mobility edges that are separating regions of localized and extended states, than by the band gap as in typical topological band insulators. Such protection is observed, for instance, in the topological Anderson insulators, where the disorder gives rise to the non-trivial topology [140, 141].

Potential disorder-induced transition can be captured by level spacing defined as the difference between neighbouring energy levels. For a given energy ϵ and disorder realization $\{V_i\}$, we find two closest eigenvalues satisfying $E_{\lambda,\{V_i\}} < \epsilon < E_{\lambda+1,\{V_i\}}$, then calculate level spacings

$$s_{\epsilon,m,\{V_i\}} = E_{\lambda+m+1,\{V_i\}} - E_{\lambda+m,\{V_i\}}, \tag{89}$$

where $m \in \{-k, k\}$, and normalize them. We set $k = 2$ as proposed in Refs. [142, 126] and point out that incorporating differences between further neighbouring levels does not affect the results. Hence, we can study the distribution of the level spacings and the variance $\mathrm{Var}(s_\epsilon) = \langle s_\epsilon^2 \rangle - \langle s_\epsilon \rangle^2$ to determine whether states are localized or extended. The average is taken over m and 10^3 disorder realizations for fixed ϵ. According to random matrix theory, Hamiltonians with broken time-reversal symmetry are modelled by the Gaussian unitary ensemble (GUE). If the states are delocalized, then the level spacings should follow the Wigner-Dyson distribution $P_{\mathrm{GUE}}(s) = \frac{32s^2}{\pi^2} e^{-\frac{4}{\pi}s^2}$ with variance $\mathrm{Var}(P_{\mathrm{GUE}}) = 0.178$. Localized states, on the other hand, are expected to obey the Poisson distribution $P(s) = \exp(-s)$ with a large variance $\sim \mathcal{O}(1)$. Consequently, we study the numerically obtained distributions of the level spacings for several disorder amplitudes W and compute the variance in order to demarcate between localized and delocalized states. Exemplary distributions are illustrated in Figs. 21 and 22.

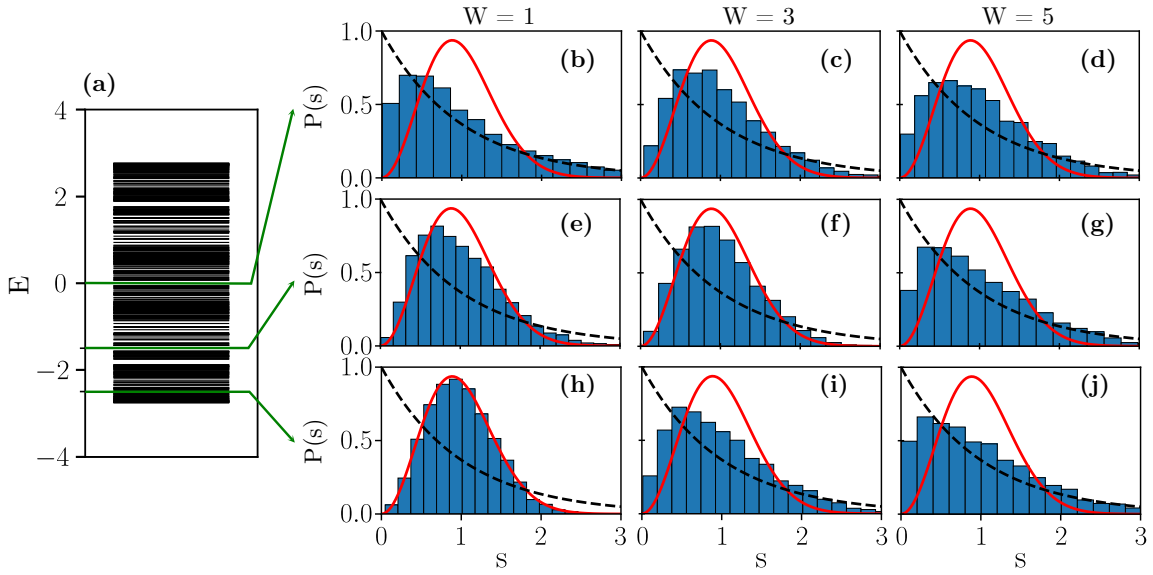

Figure 21: **(a)** Energy spectrum for the clean carpet at flux $\alpha = 1/4$, **(b) - (j)** distributions of the level spacings compared to GUE (red solid line) and Poisson (black dashed line). Set of histograms correspond to the energy around: $\epsilon = 0$ **(b, c, d)**, $\epsilon = -1.5$ **(e, f, g)**, $\epsilon = -2.5$ **(h, i, j)**.

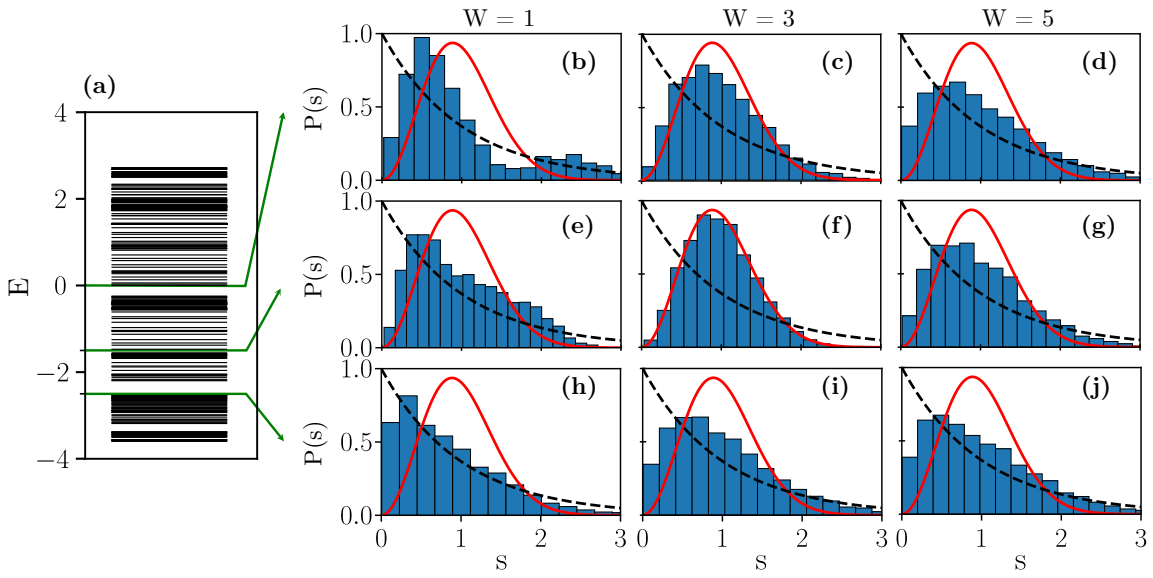

Figure 22: **(a)** Energy spectrum for the clean gasket at flux $\alpha = 1/4$, **(b) - (j)** distributions of the level spacings compared to GUE and Poisson statistics denoted by red solid and black dashed lines, respectively. Set of histograms correspond to the energy around: $\epsilon = 0$ **(b, c, d)**, $\epsilon = -1.5$ **(e, f, g)**, $\epsilon = -2.5$ **(h, i, j)**.

Since disorder calculations require exact diagonalization of the Hamiltonian repeatedly, we consider here smaller systems (iteration $n = 3$ in case of SC and $n = 5$ for SG). This is justified by the fact that fractals exhibit the same statistical properties at different scales. In Figs. 19 (d) and 20 (d), we present the difference between $\mathrm{Var}(s)$ and $\mathrm{Var}(P_{\mathrm{GUE}})$ at fixed flux $\alpha = 1/4$. Regions in energy for which the Chern number is quantized are characterized by a large $\mathrm{Var}(s)$ at small values of W. There are two possible transition scenarios, which can be observed by

following a line of increasing W at constant energy, represented by white and blue arrows. The former case corresponds to a direct transition to a fully localized system, without $\mathrm{Var}(s)$ ever becoming close to $\mathrm{Var}(P_{\mathrm{GUE}}) = 0.178$. In the latter case, a localized region at small W is separated from the Anderson insulating limit by a delocalized region with $\mathrm{Var}(P_{\mathrm{GUE}}) = 0.178$.

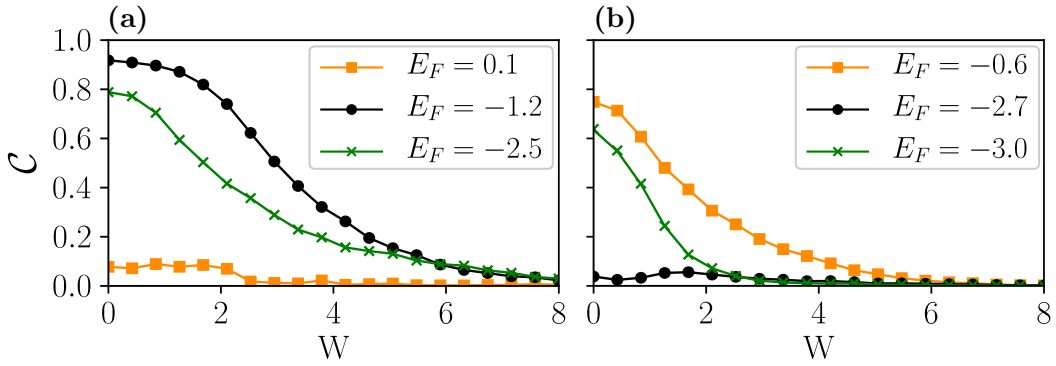

Figure 23: Chern number as a function of disorder strength for **(a)** the carpet and **(b)** the gasket at fixed flux $\alpha = 1/4$ and three different Fermi levels corresponding to the parts of energy spectra with different degree of quantization of $\mathcal{C}$. For states characterized by the Chern number close to quantized non-zero value in the clean limit, $\mathcal{C}$ is larger than zero in a presence of moderate disorder and slowly reaches zero in the strong disorder regime.

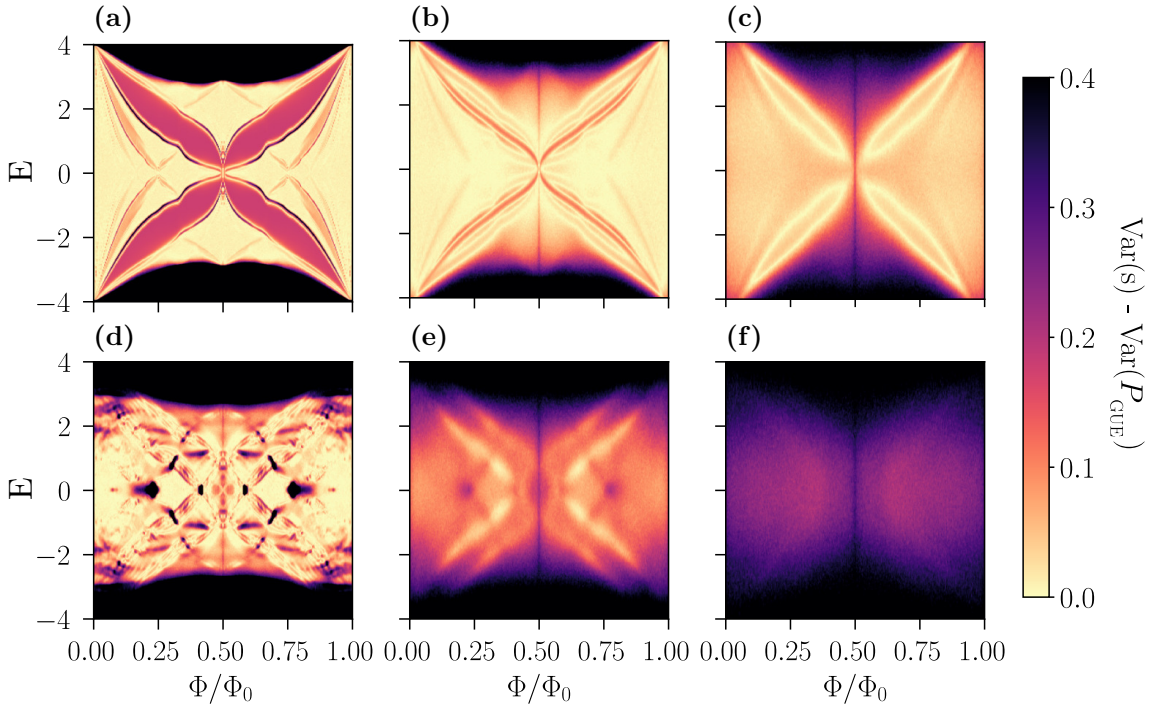

Figure 24: Variance of the level spacings for **(a, b, c)** a square lattice and **(d, e, f)** the Sierpiński carpet in the energy - flux plane at three disorder strengths: **(a, d)** $W = 1$, **(b, e)** $W = 3$, and **(c, f)** $W = 5$. At small disorder, $W = 1$, a model defined on a square lattice hosts delocalized states, which are separated by low DOS regions with a larger value of $\mathrm{Var}(s)$. For the SC, however, this separation is less clear. While increasing W, both systems undergo a transition through a point where all states become delocalized. A stronger disorder is needed to enter an Anderson insulating limit in case of a square lattice.

In Fig. 23, we show the Chern number averaged over 300 disorder realizations with respect to disorder strength W for three different Fermi levels. For states characterized by $\mathcal{C}$ close to one in the absence of disorder, the Chern number remains non-zero in a moderate disorder regime. At the same time, states with initially almost zero $\mathcal{C}$ stay near this value (up to small fluctuations). We conclude that in the energy regions where the Chern number is close to one, the topological features survive small disorder. As expected, in the Anderson insulating phase, $\mathcal{C}$ vanishes for all states.

As a cross-check of our calculations, we compare the variances of the level spacings computed over the whole flux range at three different disorder strengths $W = 1, 3, 5$ for regular and fractal lattices (results are illustrated in Figs. 24 and 25). In case of a square and the SC in a presence of moderate disorder, a large variance along a line $\alpha = 1/2$ is observed as systems become time-reversal invariant. In general, topological features in fractal lattices are less robust to disorder than in regular lattices.

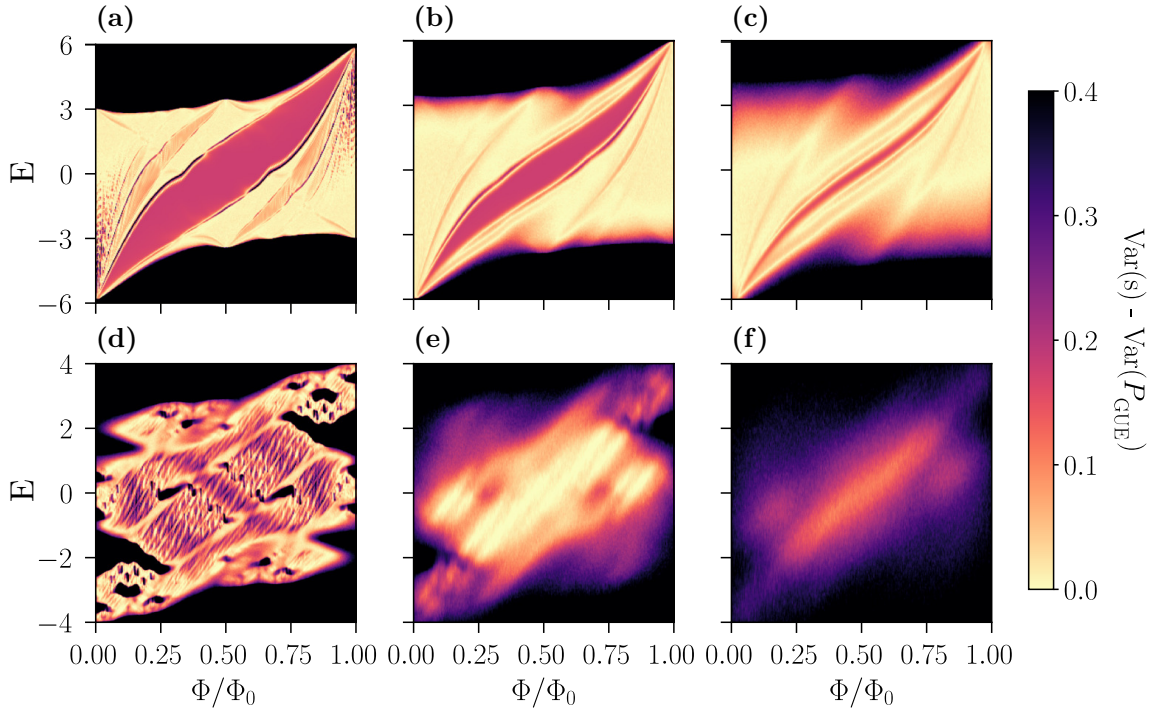

Figure 25: Variance of the level spacings for **(a, b, c)** a triangular lattice and **(d, e, f)** the Sierpiński gasket in the energy - flux plane at three disorder strengths: **(a, d)** $W = 1$, **(b, e)** $W = 3$, and **(c, f)** $W = 5$. In case of a triangular lattice, delocalized states are separated by the mobility gap, which decreases with respect to W. In contrast, the SG exhibits numerous small localized regions at $W = 1$, which ultimately become a one delocalized region at $W = 3$.

Part II:
CRYSTAL SYMMETRIES AND TOPOLOGY

3

GROUP-V MONOLAYERS AS VERSATILE PLATFORMS FOR TOPOLOGICAL PHASES

One of the most natural extensions of the ten-fold way is to include spatial symmetries represented by unitary operators, which are inherently present in crystalline solids. Those symmetries are point group symmetries, such as rotations and reflections, which leave at least one point in space invariant or space-group symmetries being the combinations of translational symmetry and symmetry operations like screw axes or glide planes. For 3D systems, a combination of 32 crystallographic point groups and 14 Bravais lattices leads to 230 space groups. Imposing crystal symmetries may have two possible outcomes on the ten-fold way:

1. topological classification remains the same, but topological invariants are easier to calculate [143],
2. spatial symmetries give rise to novel topological phases, hence the classification has to be refined.

For instance, the Fu-Kane formula relies on the presence of inversion symmetry and simplifies the computation of the $\mathbb{Z}_2$ invariant by taking into account only the parity eigenvalues at TRIMs [144]. On the other hand, the concept of topological crystalline insulators (TCIs) stems solely from the presence of spatial symmetries [145]. TCIs, which are a subset of symmetry-protected topological phases, cannot be adiabatically deformed to an atomic insulator without breaking the relevant symmetries. Given the complexity of the problem, the full classification of TCIs remains an open question. So far, the classification of TCIs in all 230 non-magnetic and 1651 magnetic space groups has been achieved for systems where symmetry indicators can be employed [146–149] (this approach is discussed in more details in Chapter 4). For more general symmetry configurations, a partial classification was provided in Ref. [150], but most of the works concerns the systems with point group symmetries [35, 37, 151, 152].

There are also further distinctions in the formulation of the bulk-boundary correspondence for TIs and TCIs. For TIs equipped with internal symmetries, gapless boundary modes are present at every boundary. In contrast, TCIs exhibit surface/edge states only at the boundaries which are unchanged upon the action of crystal symmetries. Therefore, the absence of protected modes in TCIs does not necessary indicates trivial bulk topology. It is the case for inversion-symmetric systems for which no boundaries respecting the inversion can exist[1]. In addition, a robustness against disorder can be seen from a slightly different perspective. Spatial disorder always breaks the crystal symmetries, but gapless boundary states may avoid the Anderson localization if the symmetries are retained on average [153, 33]. Such situation is similar to weak TIs [18], where the gapless surface states are protected by a discrete translation symmetry of a shift by one layer along the stacking direction. In both cases, protected conducting states are present if the disorder breaks the symmetries locally, but preserves them at the macroscopical

1 Suppose we have a material with inversion symmetry $\mathcal{I}$ in the bulk; if there is an atom at a point (x, y, z), then inversion implies the presence of another, identical one at $(-x, -y, -z)$, which is not true for *any* surface.

level. A notion of delocalization via average symmetry was formulated within the non-linear σ model [154] and, subsequently, confirmed numerically [155–157].

The first family of TCI materials in IV-VI semiconductors with rock-salt structure was predicted in 2012 [158]. In the paradigmatic tin telluride (SnTe), the mirror symmetry with respect to the (110) mirror planes protects the conducting surface states, which was verified by angle-resolved photoemission spectroscopy (ARPES) [159]. A TCI phase was also found in $Pb_{1-x}Sn_xSe$ [160], $Pb_{1-x}Sn_xTe$ [161, 162] and $Pb_{1-x}Sn_xSe$ [163] alloys. Another class of TCI protected by glide reflection and time-reversal symmetry was discovered in KHgSb [164], just after the theoretical proposition of hourglass fermions [165] relying on non-symmorphic symmetries. For 2D systems, however, experimental evidences for TCI phases enforced by the mirror symmetry along z direction, $\mathcal{M}_z$, are still lacking; this is mostly due to the fact that $\mathcal{M}_z$ is broken for layers grown on a substrate [166]. So far, a list of material candidates includes multilayer thin films of XY semiconductors (X = Ge, Sn, Pb and Y = S, Se, Te) below a critical thickness [167–169], electron-doped TlM (M = S and Se) (110) monolayer [170], PbPo monolayer [171], graphene multilayers [172] or even quantum wells consisting of trivial insulators (Sn/Pb)Te and Na(Cl/Br) [173].

In the following, we examine the properties of atomically thin layers of bismuth (Bi) and antimony (Sb), which are predicted to be excellent tunable platforms hosting distinct topological phases [174, 175]. To do so, we investigate these monolayers within the effective tight-binding model [176] and characterize TI and TCI phases, together with topological phase transitions induced by doping, external perturbations such as fields or strain and coupling to a substrate. In addition to computing relevant topological invariants, we employ methods based on quantum entanglement, namely entanglement entropy and entanglement spectrum, which in case of gapped, free-fermionic systems, can be deduced from a single-particle correlation matrix [177]. We illustrate that entanglement measures are useful not only in studying toy models, but can be also a viable complementary tool for realistic Hamiltonians. As an introduction, in Section 3.1 we discuss the role of mirror symmetry in the protection of surface states for a simple cubic lattice and define a suitable topological invariant, which can be also used for two-dimensional systems. Then, in Section 3.2, we shortly review how entanglement measures may be applicable in the realm of topological non-interacting systems. Section 3.3 is dedicated to the properties of buckled free-standing monolayers of Bi and Sb, while Section 3.4 addresses their completely flat counterparts. At the end, in Section 3.5 we consider the effect of the experimentally relevant silicon carbide (SiC) substrate on the properties of studied systems.

3.1 MIRROR SYMMETRIES AND THE MIRROR CHERN NUMBER

Similarly to Chern number or $\mathbb{Z}_2$ invariant, we can define new topological invariants for systems in which the gapless boundary modes are protected by a mirror symmetry. Suppose we have a 3D gapped system with time-reversal symmetry and reflection symmetry with respect to a mirror plane, see Fig. 26. The mirror operator $\mathcal{M}$ can be written as a product of the inversion symmetry $\mathcal{I}$ and C_2 describing a rotation by π around an axis perpendicular to the mirror plane, $\mathcal{M} = \mathcal{I}C_2$. Crystalline symmetry acts non-locally in real space, but also relates different parts of the BZ to each other. For instance, a reflection around z-axis sends the coordinates $(x, y, z) \to (x, y, -z)$ and transforms $(k_x, k_y, k_z) \to (k_x, k_y, -k_z)$. In the case of spinful systems, $\mathcal{M}$ also acts on spin degrees of freedom and satisfies $\mathcal{M}^2 = -1$. We then see

that the Bloch Hamiltonian commutes with the mirror operator $\mathcal{M}$ in the mirror-invariant planes, $k_z = 0$ and $k_z = \pi$.

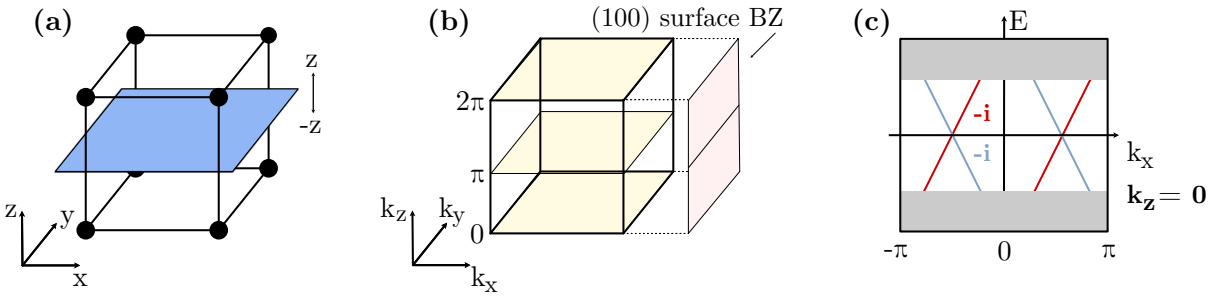

Figure 26: (a) 3D cubic lattice with a mirror symmetry along z-axis, **(b)** corresponding Brillouin zone with mirror-invariant planes (denoted by a light yellow color) and **(c)** schematic surface band structure for a time-reversal topological crystalline insulator with $\mathcal{C}_\mathcal{M} = 2$ along the projection of the $k_z = 0$ mirror-invariant plane. Two planes at $k_z = 0$ and at $k_z = \pi$ are left invariant upon the action of the mirror symmetry $\mathcal{M}$, hence they may be used to define the mirror Chern number $\mathcal{C}_\mathcal{M}$. A $\mathcal{C}_\mathcal{M} = 2$ implies the existence of two pairs of chiral modes along mirror-symmetric lines in the surface BZ constructed from the projection of the mirror-invariant planes.

The Bloch states $|u_{\mathbf{k}n}\rangle$ in these planes can be decomposed into two groups with mirror eigenvalues $\pm i$ [2]

$$\mathcal{M}\,|u^{\pm}_{\mathbf{k}n}\rangle = \pm i\,|u^{\pm}_{\mathbf{k}n}\rangle \tag{90}$$

where the momentum $\mathbf{k}$ is restricted to the mirror planes. The two mirror eigenspaces are decoupled; moreover, if the time-reversal symmetry is present, both subspaces have the same dimension. Each block separately breaks the time-reversal symmetry, hence we can assign a non-vanishing Chern number with each of them. Additionally, TR enforces the total Chern number to be zero, $\mathcal{C}_+ + \mathcal{C}_- = 0$; $\mathcal{T}$ implies the Berry curvature to be an odd function of the crystal momentum, $\mathcal{F}(\mathbf{k}) = -\mathcal{F}(-\mathbf{k})$, and as a consequence, the integral over the whole BZ vanishes. In analogy to the spin Chern number for QSH states, we can define the mirror Chern number as

$$\mathcal{C}_\mathcal{M} = \frac{\mathcal{C}_+ - \mathcal{C}_-}{2}. \tag{91}$$

Non-zero mirror Chern number implies the existence of gapless Dirac cones only on surfaces preserving reflection symmetry, with the total number of protected Dirac cones depending on the considered surface. To understand the nature of these surface states in more details, let us assume non-trivial $\mathcal{C}_\mathcal{M}$ at $k_z = 0$ plane, illustrated in Fig. 26 (c). $\mathcal{C}_\mathcal{M} = 2$ imposes the presence of two pairs of counterpropagating states along $k_z = 0$[3]. At $k_z = 0$, all states are eigenstates of the mirror symmetry $\mathcal{M}$ and the crossing occurs only between left- and right-movers, which belong to different mirror subspaces. This prevents a gap from opening and the crossing points are symmetry-protected. Away from $k_z = 0$, however, the states do not have a well-defined mirror eigenvalue and are generically gapped. If $\mathcal{C}_\mathcal{M}$ is odd (and TR symmetry is present), the system is a conventional topological insulator with an odd number of Dirac cones in the surface BZ, which are located at time-reversal invariant momenta. On the contrary, even $\mathcal{C}_\mathcal{M}$ implies an even number of Dirac cones existing only on mirror-symmetric surfaces, but at

2 For spinless fermions, the mirror eigenvalues are ± 1.
3 In general, the mirror Chern number $|\mathcal{C}_\mathcal{M}|$ gives rise to $\mathcal{C}_\mathcal{M}$ pairs of chiral states.

generic momenta [158]. Similar intuition applies to two-dimensional systems as well. Indeed, the 2D lattice defined in the xy plane has automatically the $\mathcal{M}_z$ symmetry and it consists of a single mirror plane located just at $z = 0$.

3.2 ENTANGLEMENT MEASURES

Subtle non-local correlations encoded in the topological ground state wavefunctions can be studied by employing the tools at intersection between quantum information theory and condensed matter physics. In particular, the entanglement entropy (EE) and the entanglement spectrum (ES) are amongst the most successful methods that allow to quantify entanglement in many-body systems (for more details on entanglement measures, we refer to the comprehensive review in Ref. [178]), which we briefly discuss in this Section.

3.2.1 *Von Neumann entanglement entropy*

Quantum correlations and superposition may prevent an observer from having a simple wavefunction description of a subpart of the system. The amount of entanglement, that is to say the shared information, between different parts of a quantum system can be measured by the von Neumann entanglement entropy (vNEE), which is an extension of the Shannon entropy of a statistical distribution to the quantum case. Consider a closed system $\mathcal{S}$ at zero temperature represented by a single state vector $|\Psi\rangle$, i. e., the system is in a pure state. Suppose the system $\mathcal{S}$ is composed of two spatial parts in real-space[4], namely A and B, as presented in Fig. 27. Correlations between two subsystems can be completely captured by the reduced density matrix ρ_A

$$\rho_A = \mathrm{Tr}_B \, |\Psi\rangle \langle\Psi| \,, \tag{92}$$

where the trace is taken over all degrees of freedom restricted to the subsystem B and the projector $|\Psi\rangle \langle\Psi|$ is constructed from the state $|\Psi\rangle$ in the Hilbert space corresponding to the full system $\mathcal{S}$, $\mathcal{H}_\mathcal{S} = \mathcal{H}_A \otimes \mathcal{H}_B$. We can then define the von Neumann entanglement entropy of ρ_A

$$S(\rho_A) = -\mathrm{Tr}(\rho_A \log \rho_A). \tag{93}$$

For a pure state, S does not change upon exchanging A and B, $S(\rho_A) = S(\rho_B)$. Other important properties of S include:

- If $|\Psi\rangle = |\psi_A\rangle \otimes |\psi_B\rangle$ (the state is separable), then $S(\rho_A) = 0$. For maximally entangled states, $S(\rho_A) = \log n$, with $n = \min(\dim\mathcal{H}_A, \dim\mathcal{H}_B)$.
- S is invariant under any local unitary transformation U, $S(\rho) = S(U\rho U^\dagger)$.
- Let $\rho_\mathcal{S}$ be the density matrix of the total system, then $|S(\rho_A) - S(\rho_B)| \leq S(\rho_\mathcal{S}) \leq S(\rho_A) + S(\rho_B)$. Subadditivity is an exclusively quantum property; in classical information theory, the entropy of a system can never be lower that that of its components.

4 Other bipartitions such as sublattice, particle or orbital are also possible and may reveal additional information on the topological nature of a system.

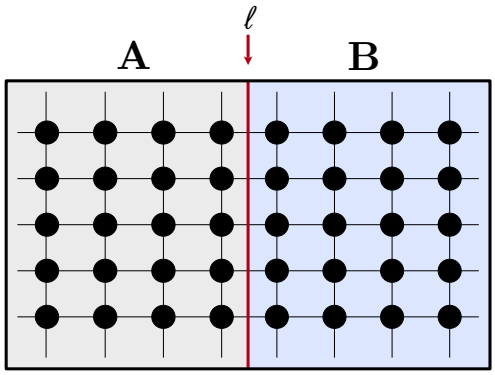

Figure 27: Spatial bipartition of a system $\mathcal{S}$ into two (not necessarily identical) parts, A and B. The length between two subsystems is denoted by ℓ.

For any vector $|\Psi\rangle$ representing a global state, there exists an orthonormal basis $\{|a_i\rangle\}$ (resp. $\{|b_j\rangle\}$) of $\mathcal{H}_A$ (resp. $\mathcal{H}_B$), such that $|\Psi\rangle$ may be rewritten using the Schmidt decomposition as

$$|\Psi\rangle = \sum_m^M \sqrt{\lambda_m}\,|a_m\rangle \otimes |b_m\rangle\,, \qquad \sum_m^M \lambda_m = 1, \tag{94}$$

where $\lambda_m \in [0,1]$ are Schmidt coefficients and M is the Schmidt rank (also called bond dimension), $M \leq \min(\dim \mathcal{H}_A, \dim \mathcal{H}_B)$, defined as the number of non-zero coefficients λ_m. Such decomposition provides a straightforward criterion for separability; $M = 1$ tells that the state is the product state and can be factorized into a tensor product of state vectors in $\mathcal{H}_A$ and $\mathcal{H}_B$, $|\Psi\rangle = |\psi_A\rangle \otimes |\psi_B\rangle$, otherwise (when $M > 1$) the state is entangled. The von Neumann entanglement entropy in Eq. (93) can be expressed in terms of the Schmidt coefficients λ_m

$$S(\rho_A) = -\sum_m \lambda_m \log \lambda_m. \tag{95}$$

3.2.1.1 *Area law*

For a d-dimensional system described by a gapped, local Hamiltonian with a finite correlation length, the entanglement entropy of the ground state typically follows [179]

$$S(A) \simeq \alpha \ell^{d-1} \tag{96}$$

with A a region of linear dimension ℓ with a smooth boundary and α a non-universal constant, which arises from a short-distance physics and strictly depends on the local properties of the system. This indicates that the EE is proportional to the area of the boundary between two subsystems, which is in contrast to generic excited states obeying volume-like scaling. The original motivation for studying area-like entropy scaling originally appeared in the context of black hole physics, where the Bekenstein-Hawking entropy turned out to be proportional to the surface area of the event horizon [180]. More importantly, the area law underlies the success of renormalization methods for many-body systems, because it determines which states are relevant in the low-energy sector - states scaling according to the area law belong to a tiny corner of the overall huge Hilbert space and focusing only on the sub-manifold of states significantly reduces the complexity of the problem. The validity of the area law was

rigorously proven in several cases, including 1D gapped chains [181] or discrete versions of real free Klein-Gordon fields [182].

The situation becomes quite different in systems at criticality. For instance, one-dimensional chains at critical points exhibit conformal invariance and therefore may be described by conformal field theories (CFTs)[5]. They then violate the area-like scaling with additional logarithmic corrections. In particular, if PBC are assumed and a subsystem A has a length x_A, the vNEE in the thermodynamic limit scales like

$$S(A) \sim \frac{c}{3} \log x_A, \tag{97}$$

with c being the central charge of the corresponding CFT and, in an intuitive picture, counts the number of degrees of freedom[6]. The central charge defines the general class of phase transitions and depends only on the low-energy physics of a model, hence it may be used to detect a (topological) phase transition. Away from a critical point, where the correlation length l is large but finite, the scaling of vNEE takes the form

$$S(A) \sim \frac{c}{3} \log l. \tag{98}$$

For $x_A \to \infty$, it therefore saturates to a finite value. Similar logarithmic violation of the area law occurs also for free fermions in d-dimensions with a Fermi surface [183–185].

3.2.1.2 *Topological entanglement entropy*

As a comment, we would like to point an important observation that was made for systems with intrinsic topological order. In 2D, the vNEE has an additional subleading term γ in the area law [179]

$$S(A) = \alpha \ell - \gamma + \mathcal{O}\left(\frac{1}{\ell}\right) \tag{99}$$

where $\mathcal{O}(1/\ell)$ represents terms vanishing in the limit $\ell \to \infty$. Global features of the entanglement are encoded in a universal term $-\gamma$, known as topological entanglement entropy (TEE) [186, 187]. TEE is directly related to the total quantum dimension $\mathcal{D}$, $\gamma = \log \mathcal{D}$, which characterizes anyonic quasiparticle excitations

$$\mathcal{D} = \sqrt{\sum_{\mu} d_{\mu}^2}, \tag{100}$$

where the sum is over all types of quasiparticles μ with quantum dimension d_μ. Abelian anyons have $d_\mu = 1$, while non-Abelian anyons $d_\mu > 1$; however, obtaining an exact number is more complicated and requires to the knowledge of fusion rules between individual anyons [188]. Extracting γ term heavily depends on the scaling analysis, which is not practical in numerical calculations [189–191], and the knowledge of γ is not sufficient to fully characterize a topologically ordered phase.

5 Conformal field theories are invariant under the action of the conformal group, which is the subgroup of coordinate transformations preserving angles and the background metric up to a scale factor.

6 c may not be an integer. For example, c of a free-bosonic system is 1, while the critical Ising model has $c = 1/2$.

3.2.2 *Entanglement spectrum*

Entanglement entropy quantifies the correlations between two subsystems, but even more information can be extracted from the full spectrum of the density matrix ρ_A. In Ref. [192], Li and Haldane introduced the concept of entanglement spectrum to describe FQH systems, which has become a standard tool for studying topological systems, including topological insulators and superconductors [193] or quantum spin chains [194]. A core idea is to represent the Hermitian ($\rho_A = \rho_A^\dagger$) and positive semidefinite ($\langle\phi|\rho_A|\phi\rangle \geq 0, |\phi\rangle \in \mathcal{H}_A$) matrix ρ_A in the form of a thermal density matrix

$$\rho_A = \frac{1}{Z} e^{-\beta^* H_A} \tag{101}$$

with the partition function $Z = \mathrm{Tr}\exp(-\beta^* H_A)$ by convention taken to be one as it only shifts the energy, and the effective inverse temperature $\beta^* = 1/T$ set to 1. H_A is the so-called entanglement Hamiltonian and the ES refers to the eigenvalues ε_m of H_A. Then, the entanglement spectrum is the logarithm of the eigenvalues of ρ_A

$$\varepsilon_m = -\ln \lambda_m. \tag{102}$$

Summing over the ES results in the vNEE for a given subsystem. Remarkably, the low-energy edge spectrum of the physical Hamiltonian corresponds to the low-lying spectrum of the entanglement Hamiltonian H_A [192, 195] as dividing the system into two parts creates artificial boundaries[7]. This indicates that the ES is related to the bulk topology in analogy to the bulk-boundary correspondence.

3.2.3 *Free-fermionic systems*

In non-interacting fermionic systems, i. e., systems that are described by Hamiltonians billinear in fermionic creation and annihilation operators, the entanglement spectrum can be directly computed from the one-body correlation matrix restricted to the subsystem [177]. Indeed, all higher-order correlation functions can be expressed in terms of two-point correlation functions due to Wick's theorem, and therefore the correlation matrix fully characterizes the system. For example, a four-point correlation function can be written as

$$\langle c_m^\dagger c_n^\dagger c_k c_l\rangle = \langle c_m^\dagger c_l\rangle \langle c_n^\dagger c_k\rangle - \langle c_m^\dagger c_k\rangle \langle c_n^\dagger c_l\rangle \tag{103}$$

or, in general, a n-point correlation function reads

$$\langle c_{i_1}^\dagger \dots c_{i_n}^\dagger c_{j_1} \dots c_{j_n}\rangle = (-1)^{n-1} \sum_{\sigma\in \mathbb{S}_n} (-1)^{P(\sigma)} \langle c_{i_1}^\dagger c_{j_{\sigma(1)}}\rangle \dots \langle c_{i_n}^\dagger c_{j_{\sigma(n)}}\rangle \tag{104}$$

with the sum carries over the space $\mathbb{S}_n$ of the permutations σ of $\{1, \dots, n\}$ and $P(\sigma)$ is the sign of the permutation σ. Let H be the bilinear Hamiltonian in the most general form, $H = \sum_{ij} t_{ij} c_i^\dagger c_j$, and C be the two-point correlation matrix

$$C_{ij} = \langle c_i^\dagger c_j\rangle = \langle\psi|c_i^\dagger c_j|\psi\rangle\,, \tag{105}$$

7 In special cases, this may not be true and the entanglement Hamiltonian falsely indicates a quantum phase transition, even if the physical system remains unchanged, see Ref. [196].

where i, j indices label lattice sites and $|\psi\rangle$ is an eigenstate of H (Slater determinant). From now, consider only the subsystem A, so that i, j indices are restricted to the A part. We can rewrite C_{ij} from Eq. (105) using the Gaussian density matrix $\rho_A \sim \exp(-H_A)$, $C_{ij} = \langle c_i^\dagger c_j \rangle = \mathrm{Tr}\left(\rho_A c_i^\dagger c_j\right)$, where H_A is the entanglement Hamiltonian. Assuming H_A to be also quadratic (as a consequence of Wick's theorem), the trace can be easily computed by transforming H_A to the diagonal basis[8], $H_A = \sum_l \varepsilon_l a_l^\dagger a_l$, where ε_l are the corresponding single-particle eigenvalues and $\rho_A \sim \exp\left(-\sum_l \varepsilon_l a_l^\dagger a_l\right)$. From there, we arrive at the relation

$$C = \frac{1}{1+e^{H_A}} \quad \text{or} \quad H_A = \ln\left[\frac{1-C}{C}\right]. \tag{106}$$

If we denote $\{\zeta_l\}$ the eigenvalues of the correlation matrix C, we see a one-to-one correspondence between the eigenvalues of C and H_A

$$\zeta_l = \frac{1}{1+e^{\varepsilon_l}}. \tag{107}$$

For periodic systems, where the momenta $\mathbf{k}$ remain good quantum numbers, the Hamiltonian H can be written in reciprocal space with the many-body ground state being a Fermi sea

$$|GS\rangle = \prod_{\mathbf{k}n} a_{\mathbf{k}n}^\dagger |0\rangle \tag{108}$$

with operators $a_{\mathbf{k}n}^\dagger$ corresponding to creation a particle with the momentum $\mathbf{k}$ and n running over the occupied single-particle Bloch states. Suppose we have a 2D system, where the spatial bipartition in position space is performed along a one chosen direction. Then, the translational symmetry is broken in a direction orthogonal to the cut, but the momentum k parallel to the cut can be still used to label the eigenstates of the system. Therefore, it is possible to evaluate the correlation matrix for each k-point separately. Such k-dependent C matrix is Hermitian and can be regarded as a spectrally flattened physical Hamiltonian with the eigenvalues $\zeta_k \in [0,1]$. Most of the eigenvalues in the spectrum of $C_{ij}(k)$ lie exponentially close to either 1 or 0, depending whether the bulk states are fully localized in the subsystem A or B, respectively, and do not contribute to the entanglement entropy. However, the states crossing the partition boundary give rise to the non-zero EE. If the system is in a topological phase, $C_{ij}(k)$ will reveal the spectral flow associated with a continuous set of intermediate eigenvalues [197, 198]. From now, we refer to the eigenvalues of the correlation matrix as the single-particle entanglement spectrum, which is a conventional practice in the literature [199, 198, 197]. Having the correlation matrix C_{ij} restricted to subsystem A, the entanglement entropy can be calculated by summing all eigenvalues of C

$$S(A) \equiv S_A = -\sum_a \left[\zeta_a \log \zeta_a + (1-\zeta_a)\log(1-\zeta_a)\right]. \tag{109}$$

We see that the contribution to S_A arises from the intermediate values of ζ_a; if $\zeta_a = 0$ or $\zeta_a = 1$, then S_A vanishes. In a case of the k-resolved correlation matrix, S_A is obtained by summing over the $S_A(k)$ at each k-momenta with a normalization factor being the total number of unit cells in the system [200].

8 Given a symmetric, positive matrix A, the trace of the matrix function $f(A)$ can be computed using the property $\mathrm{Tr}\left[f(A)\right] = \sum_{i=1}^n f(\lambda_i)$, where $\lambda_i, i = 1, \ldots, n$ are the eigenvalues of A.

3.3 BISMUTH AND ANTIMONY MONOLAYERS

Several topological aspects of bismuth and antimony-based systems have been investigated in the past. Elemental 3D Bi and Sb share the same rhomohedral R$\bar{3}$m crystal structure, which can be viewed as a set of stacked hexagonal atomic layers along the (111) crystallographic direction with the interlayer interaction much weaker than the interactions within each layer. The bulk systems are semimetals with a direct energy gap over the BZ, but a negative indirect gap due to band overlap. Remarkably, $Bi_{1-x}Sb_x$ alloy was the first experimentally confirmed topological insulator, where doping bulk Bi with Sb atoms leads to a band inversion around $x \sim 0.04$ and then to a topological phase observed in a range of $0.07 < x < 0.22$. Protected surface states were confirmed experimentally with ARPES [21], spin-resolved ARPES [201] and scanning tunneling microscope (STM) [202] and are in an agreement with theoretical calculations [203, 204]. With a decreasing thickness, these systems undergo a semimetal-semiconductor transition as quantum confinement plays substantial role [205]. A single layer of bismuth was predicted to host quantum spin Hall states [206], which was later on confirmed by the observation of one-dimensional protected edge modes using STM [207–209]. With a refined topological classification, bulk bismuth was also established as a higher-order topological insulator with conducting 1D hinge channels [40]. Moreover, protected one-dimensional edge states were detected in Bi_2Se_3 thin films [210, 211] and at an interface between heterostructures $Bi(111)/Bi_2Te_3$ [212]. Antimony films with less than four layers are expected to be topologically trivial [213]. To induce a transition between trivial and QSH insulating phases, appropriate structure modifications were proposed, including strain [214, 215] or a perpendicular electric field applied to an already strained layer [216].

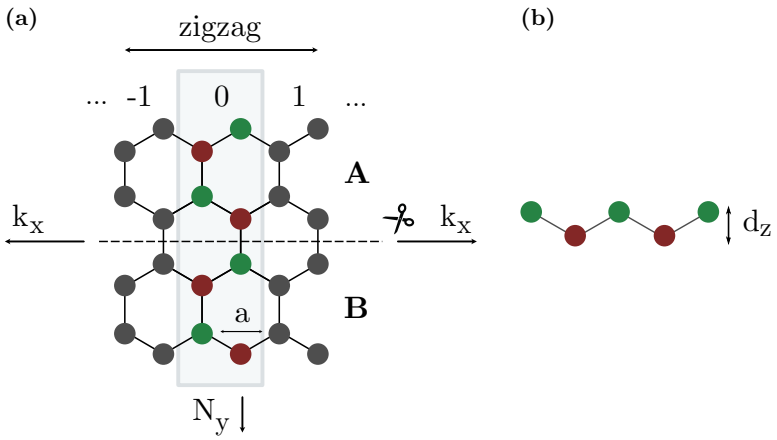

Figure 28: A schematic representation of bismuth and antimony monolayers. **(a)** top and **(b)** side views of a honeycomb lattice in a ribbon geometry with a zigzag edge termination and a layer thickness d_z. We investigate a finite strip with N_y unit cells consisting of four atoms and periodicity in x-direction, hence k_x is a good quantum number. Sites belonging to different sublattices forming a honeycomb lattice are distinguished by red and green colors. We divide system into two parts, A and B, with a cut performed in the middle of a ribbon denoted by a dashed line to compute the entanglement measures.

Free-standing monolayers of bismuth and antimony(111)[9] have a honeycomb lattice structure (such arrangement is often called a β-allotrope) as depicted in Fig. 28. A primitive unit cell contains two atoms, however a conventional hexagonal unit cell explicitly shows three-fold rotation C_3 and inversion $\mathcal{I}$ symmetries present in the systems. To describe the electronic properties, we use sp^3 tight-binding model developed in Ref. [176] for bulk bismuth and antimony, neglecting hoppings between monolayers as proposed in Ref. [206]. Interatomic hoppings up to the next-nearest neighbors and atomic spin-orbit coupling term $\lambda \mathbf{L} \cdot \mathbf{S}$ are parametrized within the Slater-Koster approach [217]. The Hamiltonian of the model is a 16×16 matrix (4 orbitals $\times$ 2 atoms per unit cell $\times$ spin) and reads

$$\begin{aligned} H = &\sum_{\alpha,\sigma,R} |\alpha,\sigma,R\rangle\, E_\alpha\, \langle\alpha,\sigma,R| + \sum_{\alpha,\beta,\sigma,R,R'} |\alpha,\sigma,R\rangle\, V'_{\alpha\beta}\, \langle\beta,\sigma,R'| + \\ &\sum_{\alpha,\beta,\sigma,R,R''} |\alpha,\sigma,R\rangle\, V''_{\alpha\beta}\, \langle\beta,\sigma,R''| + \frac{\lambda}{3} \sum_{\alpha,\sigma,\sigma',R} |\alpha,\sigma,R\rangle\, \mathbf{L}\cdot\mathbf{S}\, \langle\alpha,\sigma',R| + \text{h.c}, \end{aligned} \tag{110}$$

$\alpha, \beta = \{s, p_x, p_y, p_z\}$ label the orbitals and σ, $\sigma' = \{\uparrow, \downarrow\}$ denote the spin degrees of freedom. E_α are the on-site energies, $V_{\alpha\beta}$ correspond to Slater-Koster two-center integrals between α and β orbitals, and R are the atomic positions (with R' being NN atom and R'' – NNN atom). The last term describes the spin-orbit coupling (SOC) with strength λ. According to Ref. [218], 1/3 factor is introduced to the renormalized atomic SOC in order to obtain correct SOC splitting of the valence band. All model parameters are listed in Table 2. Most of them differ by less than 15% between bismuth and antimony crystals, but a stark difference appears in the SOC constant λ being 2.5 times larger in bismuth.

Parameter (eV)	Bi	Sb	Parameter (eV)	Bi	Sb
E_s	-10.906	-10.068	$V'_{sp\sigma}$	0.433	0.478
E_p	-0.486	-0.926	$V'_{pp\sigma}$	1.396	1.418
$V_{ss\pi}$	-0.608	-0.694	$V'_{pp\pi}$	-0.344	-0.393
$V_{sp\sigma}$	1.320	1.554	$V''_{ss\sigma}$	0	0
$V_{pp\sigma}$	1.854	2.342	$V''_{sp\sigma}$	0	0
$V_{pp\pi}$	-0.600	-0.582	$V''_{pp\sigma}$	0.156	0.352
$V'_{ss\sigma}$	-0.384	-0.366	$V''_{pp\pi}$	0	0
λ	1.5	0.6			
a (Å)	4.53	4.30	d_z (Å)	1.58*	1.64**
d_1 (Å)	3.062	2.902			

Table 2: Tight-binding parameters for bismuth and antimony taken from Refs. [176], [205]*, [215]**. d_1 denotes nearest-neighbor distance between sites in a honeycomb lattice.

In band insulators, the SOC plays a fundamental role in topological phase transitions and is associated with a band inversion – states of different symmetries are inverted at the conduction band minimum (CBM) and valence band maximum (VBM). The band inversion can occur between orbitals with different parities, for example between even s-orbitals and odd p-orbitals (which was observed, for instance, in HgTe/CdTe quantum wells [17]) or between different p

9 The term *bilayer* is sometimes used to indicate that a monolayer consists of atoms forming two spatially separated sublattices.

orbitals (as in 3D TIs with a single Dirac cone on the surface: Bi_2Se_3, Bi_2Te_3 and Sb_2Te_3 [22]). SOC effect is in particular noticeable in the materials containing heavy elements as SOC strength scales like Z^4 with Z being the atomic number. A further enhancement of the energy gap opening by SOC is possible by including additional effects such as electron-electron correlations, which leads to the band inversion between d and f orbitals; on that note, an idea of topological Kondo insulators with SmB_6 as a material example was introduced [219]. One way to quantify the SOC-driven band inversion is based on the so-called spin-orbit spillage, which measures the degree of mismatch between the occupied band projection operators with and without SOC [220].

In Fig. 29, we present the orbital-projected band structures for buckled bismuth and antimony single layers along the high-symmetry path K-Γ-M-K in the first BZ. Lowest energy bands are composed mostly of s-orbitals and are separated by a large gap from p-type bands close to the Fermi level. Bi monolayer has an indirect energy gap around Γ with $E_{gap} \sim 0.4$ eV, while Sb layer is a direct gap semiconductor with $E_{gap} \sim 1.3$.

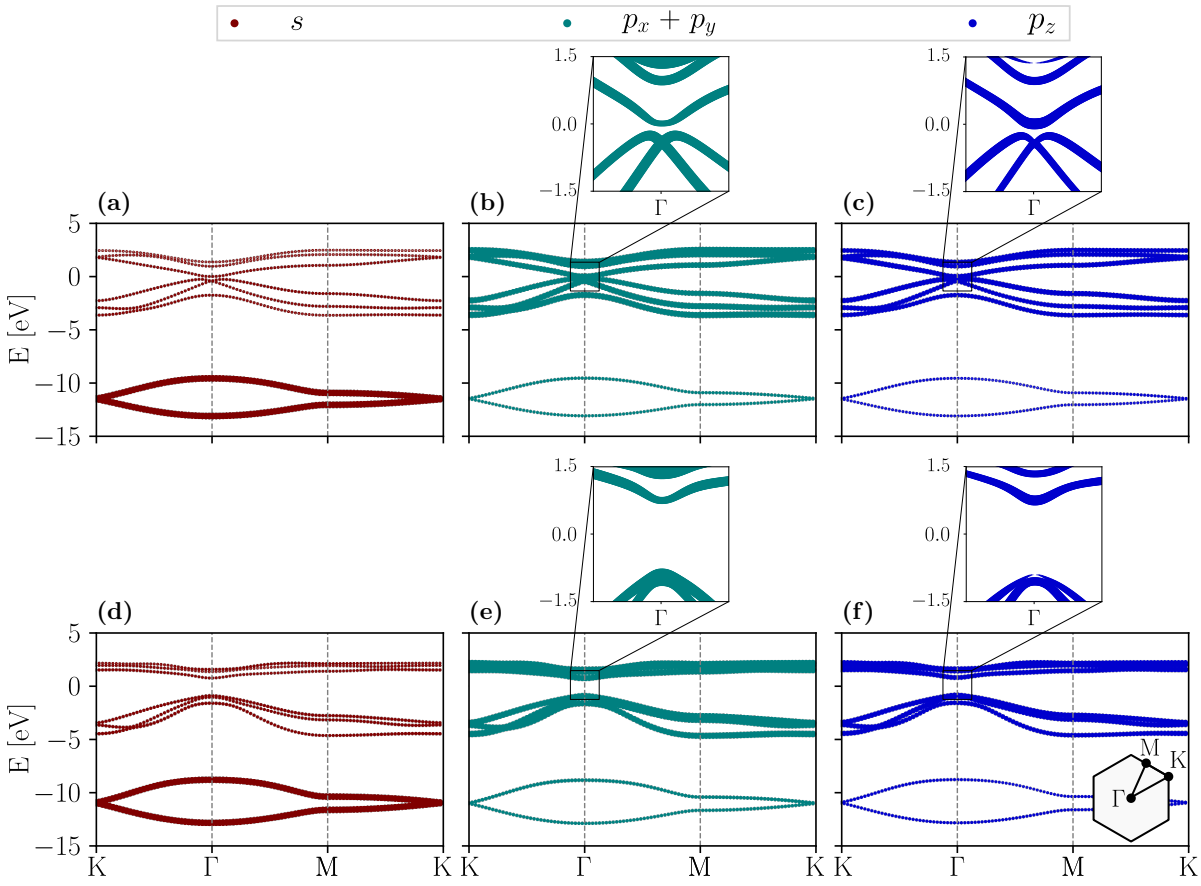

Figure 29: Band structures of infinite **(a, b, c)** bismuth and **(d, e, f)** antimony along the high-symmetry path K-Γ-M-K. Red, teal and blue colors correspond to the orbital contribution of s, in-plane $p_x + p_y$ and out-of-plane p_z orbitals, respectively, with the circle radius denoting the weight of the contribution. Low-energy bands have s-type character, while the bands close to the Fermi level are p-type. Both materials have a well-defined band gap around Γ-point. For a Bi layer, the conduction band minimum has p_z character, while the valence band maximum is $p_x + p_y$ mixture. In a case of Sb single layer, all p orbitals contribute to the conduction band, but the valence band retains $p_x + p_y$-like.

3.3.1 *Edge states in a ribbon geometry*

Equipped with useful formulations of entanglement measures for non-interacting systems, we now move to study topological properties of nanoribbons with periodicity in x direction and a zigzag edge termination[10], depicted in Fig. 28. We set the width of the strip $N_y = 6$, which corresponds to $N_{\text{at}} = 48$ atoms in the systems. This system size ensures that two opposite edges are sufficiently far, so no hybridization between edge states is expected and the spatial cut into two parts performed exactly in the middle of ribbons guarantees that the edge modes are perfectly confined within the subsystems. In Fig. 30, we compare the results for buckled bismuth and antimony. Edge states spectrally connecting the conduction and valence bands are observed for the Bi monolayer, which translates into the presence of spectral flow in the ES, see Fig. 30 (a) and (b). It is in contrast with the pure Sb structure, where almost flat dangling bonds are exhibited in the energy gap, but they are not associated with non-trivial bulk topology (consult Fig. 30 (d) and (e)). We note that mid-gap states with $\zeta = 0.5$ in the ES are related to the inversion symmetry present in the system.

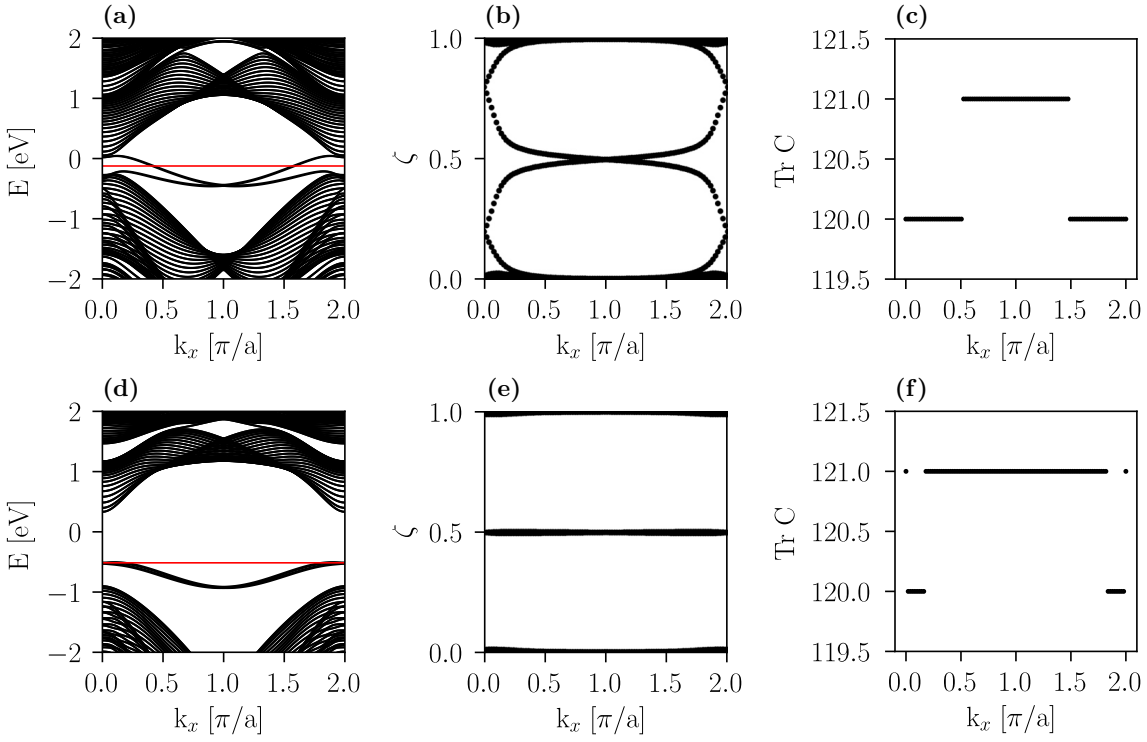

Figure 30: Energy and entanglement spectra, together with a trace index for **(a, b, c)** bismuth and **(d, e, f)** antimony monolayers. Non-trivial topological nature of Bi layer is manifested by a pair of edge modes connecting the conduction and valence bands, as well in the presence of a spectral flow in the entanglement spectrum and a single discontinuity in trace index in the half of BZ at $k_x = \pi/2$. In contrast, flat bands located in the gap in the energy spectrum of Sb layer are trivial, which is reflected by an even number of discontinuities in the trace index.

10 Armchair ribbons posses an extra pair of edge states in a gap, which leads to spurious modes in the ES. As we investigate topological properties inherited from a bulk, not an edge termination, the conclusions would hold for both types of edges.

In a semi-infinite geometry, the trace of the correlation matrix describing a subsystem, $\mathrm{Tr}(C)$, called trace index allows to easily distinguish whether the system is in a topological or a trivial phase by counting the number of discontinuities in the trace index. Physical edge states in the bulk gap that cross the Fermi level lead to discontinuities in $\mathrm{Tr}(C)$. For the systems in AII symmetry class, zero (non-zero) $\mathbb{Z}_2$ index corresponds to even (odd) number of discontinuities mod 2 in the half of BZ [197].

3.3.2 *Topological phase transitions*

Furthermore, we demonstrate the behavior of S_A defined in Eq. (109) across different topological phase transitions (TPTs). To avoid boundary effects, we apply periodic boundary conditions to the ribbon also in the y direction. As the system is now effectively a torus, dividing it into two spatial parts introduces two boundaries and results in a spectral symmetry with all the ES eigenvalues coming in pairs [196]. We perform calculations for $N_y = 7$, 10 and 13 unit cells, which corresponds to $N_{\mathrm{at}} = 28$, 48, 52 atoms in a stripe, respectively.

3.3.2.1 *Composition-induced phase transition in $Bi_{1-x}Sb_x$*

We begin with the transition to a trivial phase driven by the antimony content in $\mathrm{Bi}_{1-x}\mathrm{Sb}_x$ alloy and treat it within a virtual crystal approximation. Instead of considering a supercell consisting of different number of bismuth and antimony atoms (which would be required to maintain translational invariance), we replace atoms in a unit cell by a pseudoatom that has properties being weighted averages over the properties of Bi and Sb. Thus, the values of hopping integrals between all lattice sites are effectively scaled with respect to x

$$t_x = (1 - x) \cdot t_{\mathrm{Bi}} + x \cdot t_{\mathrm{Sb}}, \tag{111}$$

where $t_{\mathrm{Bi/Sb}}$ are parameters from taken Table 2. A transition from QSH insulating phase to trivial insulator with increasing x in $\mathrm{Bi}_{1-x}\mathrm{Sb}_x$ is related, in general, to a decreasing value of the spin-orbit coupling constant.

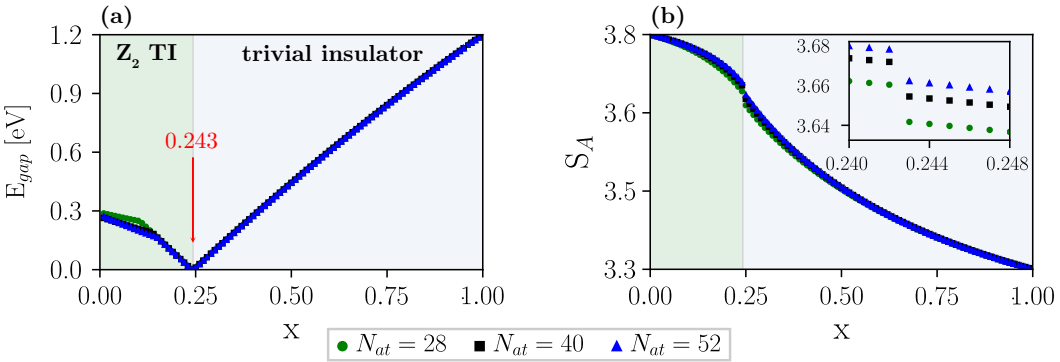

Figure 31: (a) Energy gap and **(b)** entanglement entropy as a function of composition x in a free-standing $\mathrm{Bi}_{1-x}\mathrm{Sb}_x$ layer. The transition from a $\mathbb{Z}_2$ topological insulator to a trivial insulator goes through a bulk gap closing point (indicated by a red arrow) at $x = 24.3\%$ antimony composition and is accompanied by a discontinuity in the scaling of entanglement entropy, regardless of system size (see inset).

In Fig. 31 (a), we show the band gap scaling with respect to x. Finite-size effects are manifested as a kink in the energy gap evolution around $x \sim 0.12$ for a system with $N_{\text{at}} = 28$ atoms. The energy gap of clean bismuth, $x = 0$, is $E_{\text{gap}} = 0.3$ eV and decreases as a function of x up to the point $x = 0.243$, where the band gap closing occurs (this value is in an agreement with calculations done for infinite 2D crystal). A further change of antimony concentration leads to the topological phase transition into a trivial phase, with E_{gap} increasing linearly to the value of 1.2 eV for elemental antimony. The dependence of S_A on the composition x is illustrated in Fig. 31 (b). Clean Bi layer is characterized by the largest value of the entanglement entropy which decreases monotonically with x to its minimal value for pure Sb. A finite discontinuity of S_A at $x = 0.243$ is observed for all investigated system sizes and coincides with the closing of the bulk gap.

3.3.2.2 *Electric field-driven transition in a bismuth layer*

External fields are convenient parameters that may be used for controlling band topology. Here, we show that a TI phase in a bismuth layer can be toggled off by applying a perpendicular electric field E_{Field}. The effect of E_{Field} can be modelled by including an electrostatic energy difference V_{Field} between the two sublattices. Due to the spatial separation d_z, atoms in the lattice are affected differently by the external field. Because the absolute values of the potentials on each sublattice does not matter, but only their difference, we can therefore capture the effect of E_{Field} by adding potentials on two sublattices with opposite signs, $V^R_{Field} = -V^G_{Field}$, similar to a staggered potential. R and G refer to, respectively, the red and green sites in Fig. 30 belonging to different sublattices.

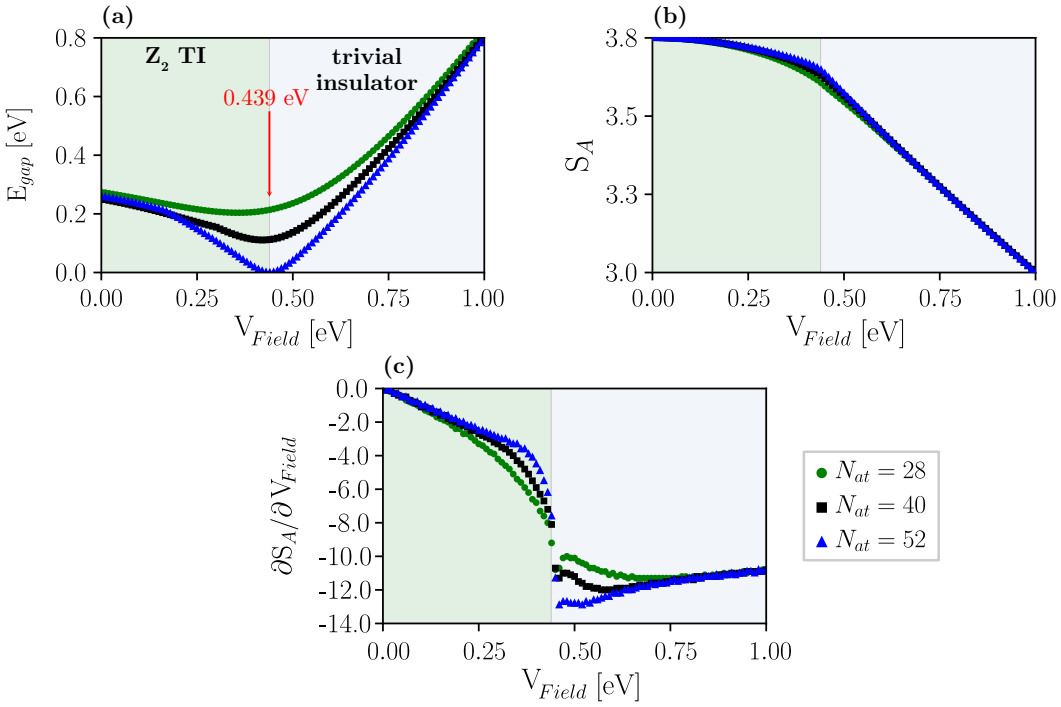

Figure 32: **(a)** Energy gap, **(b)** entanglement entropy and **(c)** its second derivative as a function of external potential V_{Field} due to electric field. For a sufficiently wide system, the band gap closes at $V_{Field} = 0.439$ eV, which is indicated by a red arrow. Entanglement entropy remains a continuous function, while the derivative becomes discontinuous at band gap closing point.

The energy band gap as a function of the external potential V_{Field} is plotted in Fig. 32 (a). Firstly, we point out that the band gap does not close completely even for a wide system with 52 atoms, but in the limit of $N \to \infty$ we checked that it closes at $V_{Field} = 0.439$ eV. Interestingly, S_A is sensitive to the bulk gap closing in finite systems, which is indicated by an inflection point in the scaling of entanglement entropy (consult Fig. 32 (b)) and a corresponding discontinuity in the numerically obtained first derivative of S_A with respect to V_{Field}, $\partial S_A / \partial V_{Field}$, in Fig. 32 (c). This point is more visible for larger system sizes as the sharpness of the discontinuity in the derivative is strongly size-dependent. In the large V_{Field} limit, the energy scale given by the hopping integrals and the SOC is relatively negligible and the states are fully localized on the lattice sites. As a consequence, two sublattices become energetically disconnected and the entanglement entropy saturates to almost zero value and the ES spectrum consisting only of 0's and 1's. Moreover, the inversion symmetry is broken by a strong external perturbation, which is reflected in the single-particle entanglement spectrum. In Fig. 33, we show two spectra: before (at $V_{Field} = 0.24$ eV) and after ($V_{Field} = 0.54$ eV) the topological phase transition. The separated branches of states seen in Fig. 33 (b) are moving towards 0's and 1's eigenvalues by increasing V_{Field}.

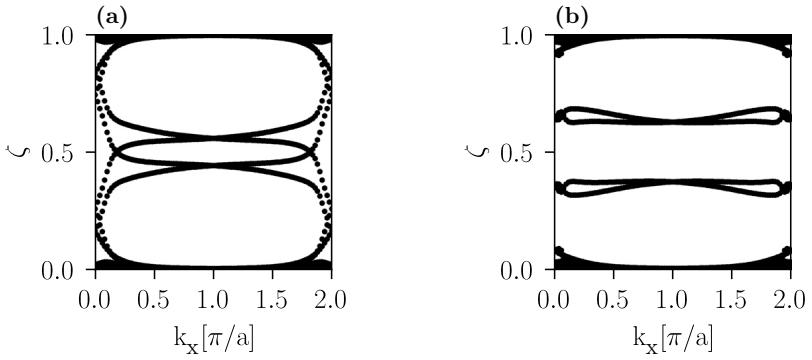

Figure 33: Entanglement spectrum **(a)** before and **(b)** after topological phase transition induced by an electric field. For large V_{Field} values, the inversion symmetry is lost as states pinned to $\zeta = 0.5$ are not observed anymore.

3.3.2.3 *Effect of strain on an antimony layer*

A free-standing monolayer of antimony is characterized by a vanishing $\mathbb{Z}_2$ invariant, but a TI phase can be induced by applying a tensile strain [215]. We model this transition by scaling the hopping integrals due to the change of bond lengths and angles. Following Harrison [221], all hopping parameters in the model are then modified by a constant factor

$$V_{\alpha\beta} = V^0_{\alpha\beta} \cdot \left(\frac{d}{d_0}\right)^{-n}, \tag{112}$$

where $V^0_{\alpha\beta}$ are values taken from Table 2 corresponding to the unstrained case, while d and d_0 are, respectively, new and unmodified bond lengths. Within this approach, no structural phase transitions are expected as all hopping terms are scaled by the same factor and the symmetries of the system are preserved. The band gap decreases monotonically with a strain up to a critical value of 13.8%, when it closes, which we illustrate in Fig. 34 (a). As in case of the composition-induced TPT, a small discontinuity in the entanglement entropy is also observed.

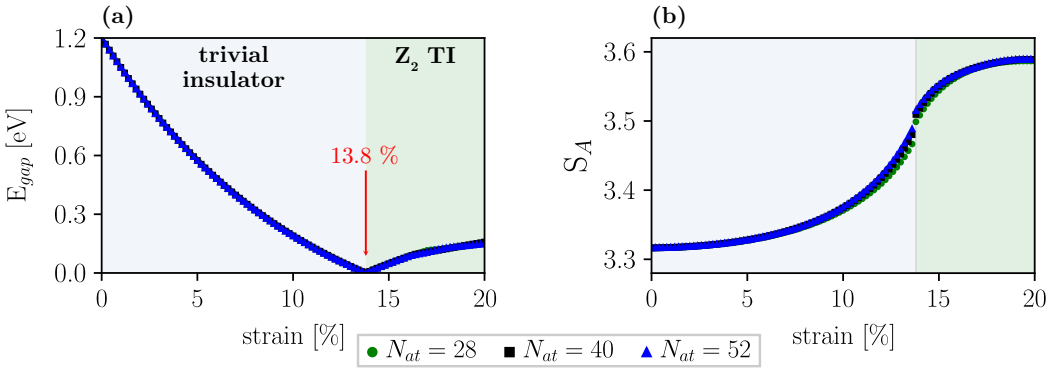

Figure 34: (a) Energy gap evolution and **(b)** entanglement entropy scaling with respect to strain. The band gap closes at 13.8% value of strain and occurs with a discontinuity of finite extend in entanglement entropy.

3.4 BISMUTHENE AND ANTIMONENE

We now move to completely planar structures of bismuth and antimony called, in analogy to graphene, bismuthene and antimonene. Recent experimental works have reported a growth of bismuthene on silicon carbide SiC(0001) [222], after several failed attempts to synthesize hexagonal flat Bi on Si(111) substrate [223, 224]. A successful synthesis of Bi on $NbSe_2$ led to a discovery of its novel allotrope in a form of compressively strained 2D triangular lattice [225]. Remarkably, stable free-standing bismuthene structures were realized as well [226]. With the experimentally measured bulk gap of 800 meV, bismuthene is amongst the most promising material candidates for a room temperature QSH effect [227, 228]. As yet, there are not many experimental studies on the electronic properties of atomically thin Sb. Only recently, several reports demonstrated a successful fabrication of a monolayer structure of antimony [229–231], with a predicted energy gap of 47.7 meV [229].

To model flat monolayers, we set the buckling d_z to zero and use the lattice constants determined from first-principle calculations [232] for bismuthene ($a = 5.35$ Å) and antimonene ($a = 5.00$ Å). At $d_z = 0$, both systems have the full six-fold rotational symmetry C_6 and, most importantly, the mirror symmetry under $z \to -z$, i. e., the mirror plane parallel to the xy plane, is restored. $\mathcal{M}_z$ symmetry protects a TCI phase, which we firstly confirm by computing the mirror Chern number via the Kubo formula for each mirror sector [174]

$$\mathcal{C}_{\pm} = \frac{1}{2\pi} \int_{BZ} dk_x dk_y \sum_{\epsilon_n < E_F < \epsilon_m} 2\,\mathrm{Im}\, \frac{\langle u^{\pm}_{\mathbf{k}n} | \frac{\partial H}{\partial k_x} | u^{\pm}_{\mathbf{k}m} \rangle \langle u^{\pm}_{\mathbf{k}m} | \frac{\partial H}{\partial k_y} | u^{\pm}_{\mathbf{k}n} \rangle}{(\epsilon_n - \epsilon_m)^2}, \tag{113}$$

where E_F is the Fermi level, while $\epsilon_{n/m}$ are the eigenvalues associated with the eigenstates $|u_{\mathbf{k}n/m}\rangle$ of the Hamiltonian. The $\mathbb{Z}_2$ invariant vanishes for these planar systems, but we obtain non-zero $|\mathcal{C}_{\mathcal{M}}| = 2$ (using Eq. (91)), which is consistent with an even number of edge modes crossing the Fermi level in a ribbon geometry, see Fig. 38 (a, e). Therefore, we conclude that the boundary modes are solely protected by $\mathcal{M}_z$.

The different topological properties of buckled and planar monolayers are also reflected in the orbital composition of the bands around E_F. In Fig. 35, we show the orbital-resolved band structures along the same K-Γ-M-K path for bismuthene and antimonene. In both cases, the

valence bands are mostly composed of p_z orbitals around the K point, where an indirect gap is observed (with $E_{gap} \sim 0.6$ eV for bismuthene and $E_{gap} \sim 0.5$ eV for antimonene).

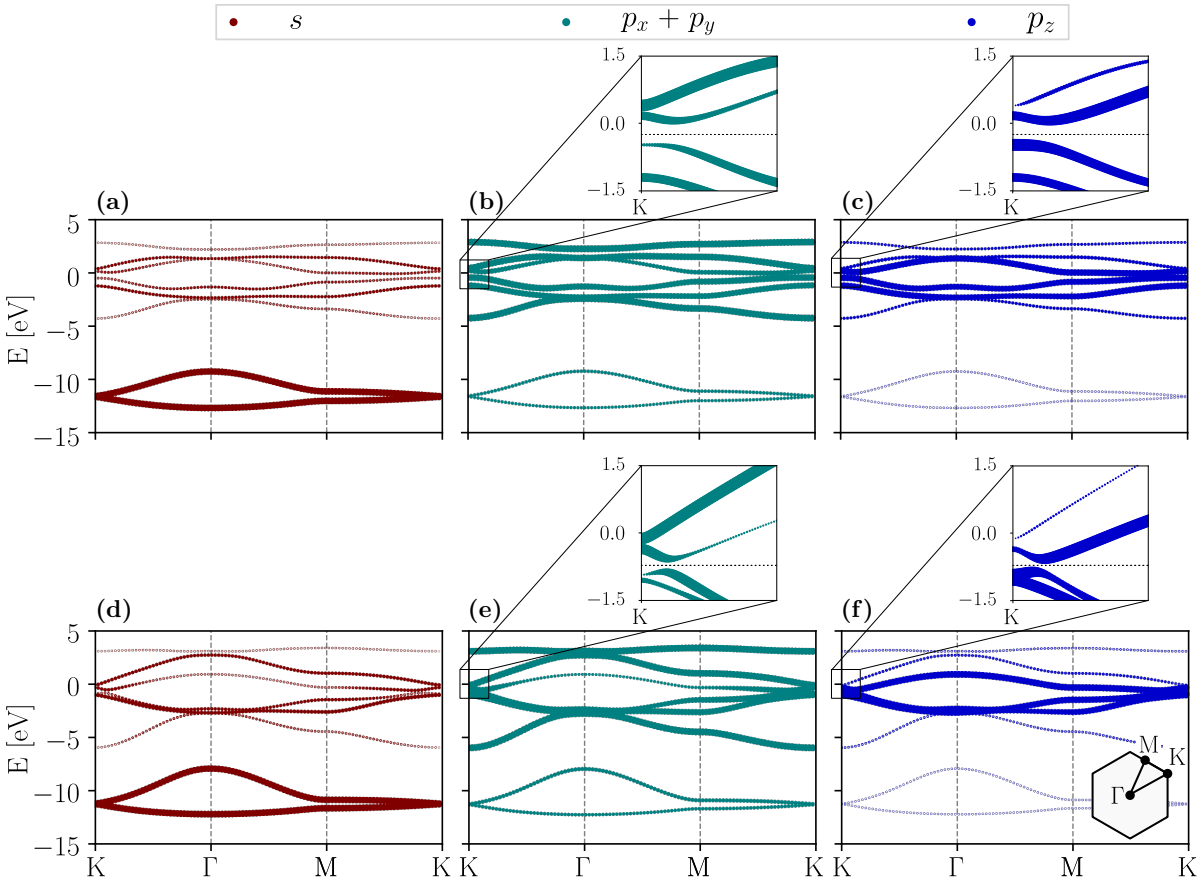

Figure 35: Orbital-projected band structures of **(a, b, c)** bismuthene and **(d, e, f)** antimonene. Valence bands maxima (composed mostly of p_z orbitals) and conduction bands minima (with contributions from all p orbitals) are located close to the K point.

3.5 COUPLING TO SIC SUBSTRATE

A substrate provides mechanical support to deposited layers. However, it may also interact with the layers and greatly influence their properties. Here, we investigate the effect of SiC substrate on bismuth and antimony layers, which is effectively described by shifting the energy of out-of-plane p_z orbitals away from the low-energy sector [222]. We calculate the energy gap while changing the value of energy of E_{p_z} orbitals (but keeping E_{p_x} and E_{p_y} energies fixed) as illustrated in Fig. 36. We note that within this TB model, it is not possible to define the Fermi level at intermediate values of E_{p_z} when the bands are continuously shifting in energy with respect to E_{p_z}. Therefore, we exclude the parameter region around $E_{p_z} \sim -2$ eV (denoted by a yellow color) from the phase diagrams. The determined band gaps for bismuthene and antimonene are, respectively, $E_{gap} \sim 0.9$ eV and $E_{gap} \sim 0.34$ eV, comparable with DFT results from Ref. [232] with structures on the top of SiC under different tensile strains. The energy gap in bismuthene is almost three times larger than the gap in antimonene as well the gap of a bismuth monolayer, $E_{gap} = 0.25$ eV, which was noticed in Ref. [222]. In addition, we show that a weak coupling to the substrate is sufficient to observe a transition from the TCI to a TI phase,

which occurs around $E_{p_z} \sim -2.5$ eV in both structures. After a topological phase transition, the energy gap is stable and only slightly affected by the coupling strength with the substrate.

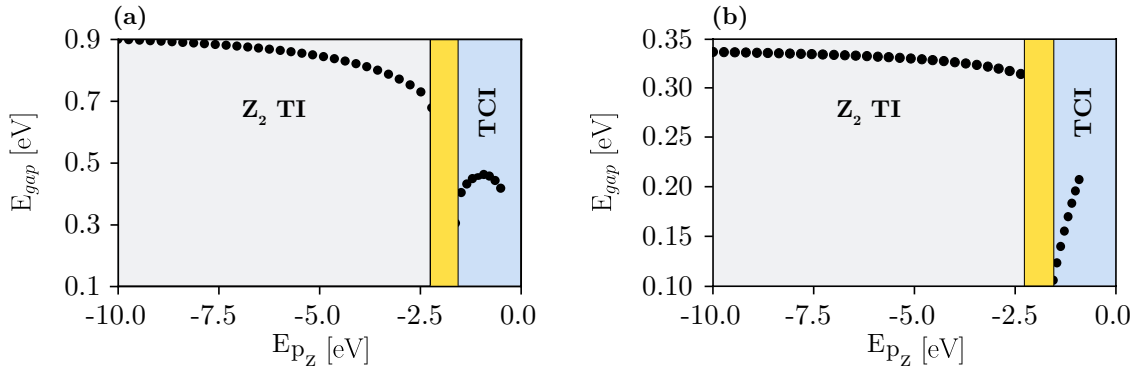

Figure 36: Energy gap E_{gap} as function of interaction with a substrate modelled by changing of energy E_{p_z} of p_z-orbitals for **(a)** bismuthene and **(b)** antimonene. Free-standing monolayer of bismuthene (antimonene) has $E_{p_z} = -0.486$ eV ($E_{p_z} = -0.926$ eV), see Table 2. $E_{p_z} = -10$ eV corresponds to the structures deposited on the SiC substrate. The yellow areas refer to E_{p_z} values with a not-well defined Fermi energy coinciding with transition regions from TCI to TI phases.

We consider also a transition between a buckled bismuth (antimony) monolayer and bismuthene (antimonene) by applying additional strain for structures deposited on the substrate. The coupling to the SiC substrate of buckled structure is modeled by shifting the energy E_{p_z} of p_z orbitals for an upper atom from a unit cell, while a lower atom has the energy of p_z orbital $E_{p_z} = -10$ eV as it is fully coupled to the substrate for all strain values. In Fig. 38, we show that layers deposited on a substrate are topologically trivial. It is observed that a small strain (around 1% for Bi and 4% for Sb) induces a transition to a TI phase. With a larger strain, the band gap monotonically increases up to the largest value at 20% strain corresponding to flat structures.

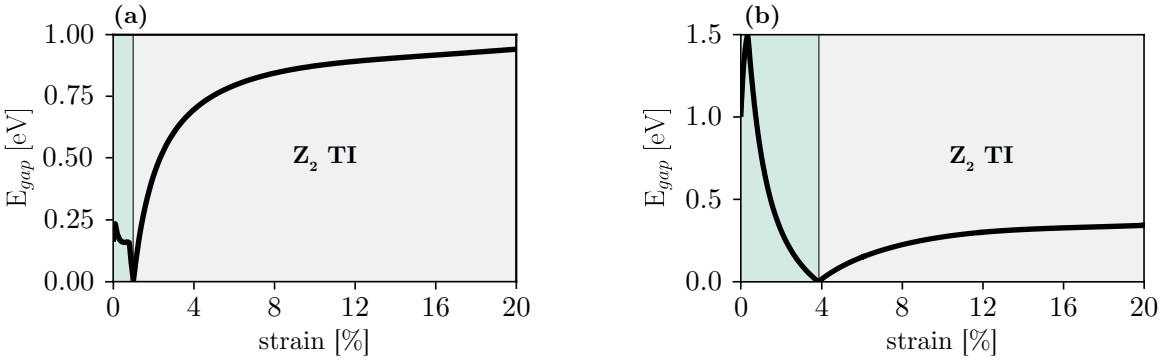

Figure 37: Energy gap E_{gap} as a function of strain for **(a)** bismuth and **(b)** antimony monolayers deposited on the SiC substrate. Unstrained structures are within topologically trivial phase, however a small strain ($\sim$ 1% for Bi and $\sim$ 4% for Sb) leads to a transition to TI phase regime (denoted by a gray background) which is observed over all investigated strain range. At 20% strain, the systems are completely flat.

Finally, in Fig. 38 we compare the entanglement spectra for the systems in distinct topological phases.

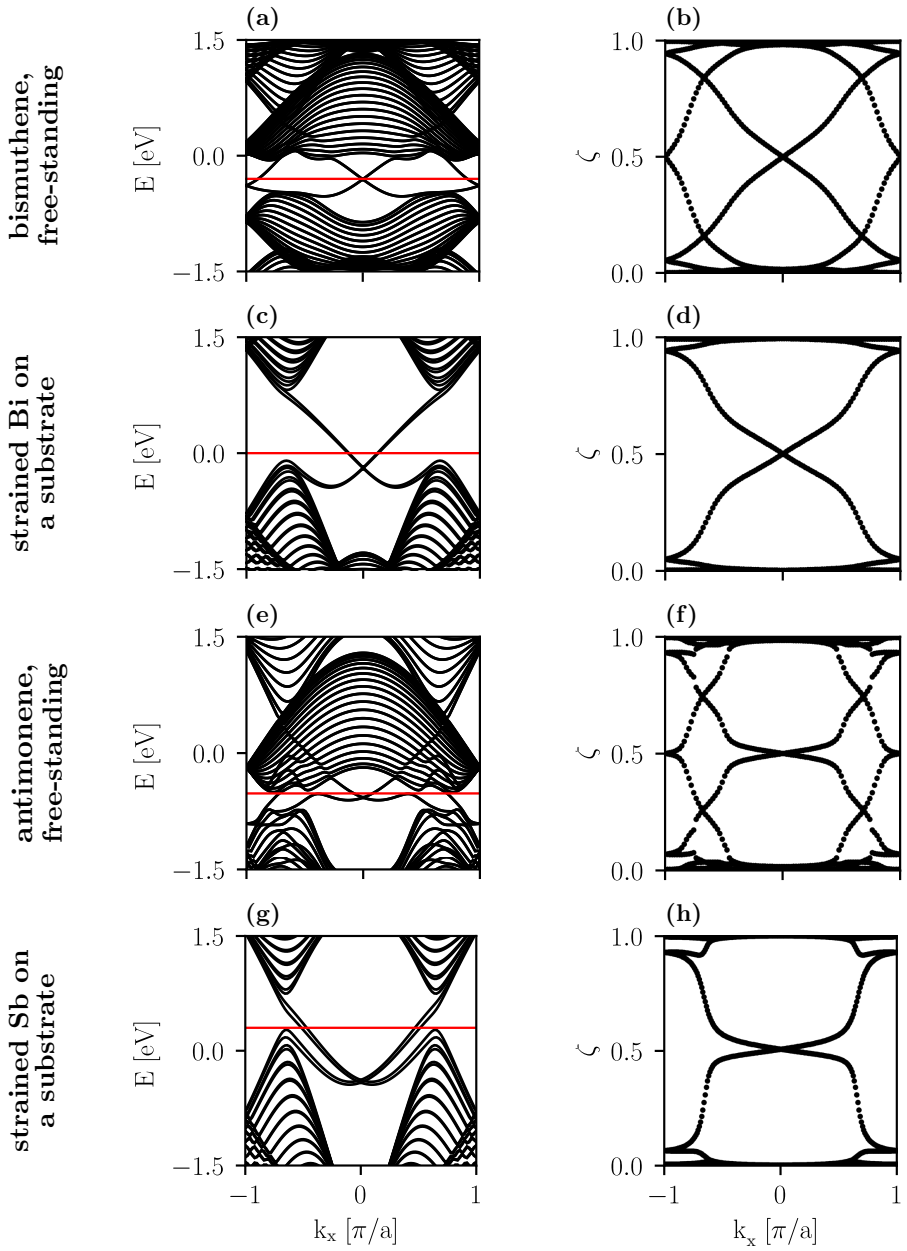

Figure 38: Energy spectra around the Fermi level (denoted by a red line) and corresponding entanglement spectra of free-standing **(a, b)** bismuthene and **(e, f)** antimonene, together with monolayers of **(c, d)** bismuth and **(g, h)** antimony within a TI phase at 12.5% strain on the SiC substrate in a ribbon geometry. The interaction with the substrate splits the double degeneracy of each branch of edge states. The degeneracy of these edge states is removed due to inversion-symmetry breaking as two atoms from a unit cell couple differently to the substrate. Distinct topological phases can be distinguished by the number of branches spectrally connecting 0's and 1's eigenvalues in the entanglement spectrum: there are two pairs of modes in the TCI phase with crossings at $k_x = 0$, π (see **(b)** and **(f)**) and one pair of modes in the TI phase, which crosses at $k_x = 0$ (in **(d)** and **(h)**).

For free-standing bismuthene and antimonene, the ES has two pairs of modes exhibiting spectral flow, which is in an agreement with computed mirror Chern number. In contrast, a single crossing of two modes in the ES is a feature of strained monolayers of Bi and Sb on the substrate exhibiting the TI phase.

4

OBSTRUCTED ATOMIC LIMITS IN TWO DIMENSIONS

In the Chapter 3, we have shown that crystal symmetries may give rise to a wide range of novel topological states of quantum matter dubbed topological crystalline insulators. However, an even more striking consequence of the spatial symmetries is that several adiabatically disconnected atomic limits – electronic phases in which all orbitals are fully localized – can exist. While multiple atomic limits can be discerned, a topological distinction between these bulk phases is only relative and a choice which one has to be labeled as a trivial is arbitrary [233]. These systems can be understood using an intuitive picture of atomic-like Wannier functions [234, 235]. The Wannier functions (WFs), which we present in more details in Appendix A, are constructed from the isolated group of occupied Bloch bands of an insulator. In atomic limits, WFs are exponentially localized and verify the symmetries of the system. Most often, the center of electronic WFs coincide with atomic positions in a lattice, which we call a *trivial atomic limit*. However, a hybridization between atomic orbitals may result in WFs localized far from the atomic sites. The latter situation is referred to as an *obstructed atomic limit* (OAL) [147], where the localized orbitals reside at the (maximal) Wyckoff positions[1].

Conversely, topological phases characterized by a non-vanishing strong topological index such as Chern number cannot be expressed in terms of localized WFs as they exhibit extended edge modes in an open geometry associated with a bulk topology. In other words, a non-zero Chern number imposes a topological obstruction for deforming the ground state into a product state and, as a consequence, to the construction of exponentially localized WFs [236, 237]. The opposite statement – a vanishing topological index implies that a system can be described in terms of WFs – was proven as well [238]. In the case of $\mathbb{Z}_2$ topological insulators, a topological obstruction still applies if a gauge is chosen such that the time-reversal symmetry is preserved and the Wannier states come in time-reversal symmetric pairs [239]. It is important to note that obstructions to the Wannier representation does not always guarantee a stable topology, giving rise to the notion of *fragile* topology [240–247]. Three types of (spatial) symmetry-protected phases: (i) stable topological, (ii) fragile topological, and (iii) obstructed limits are compared in Table 3.

OALs can support point-like boundary states in an open geometry, since the physical boundary of the system may result in 'cutting through' the Wannier centers. At fixed bulk filling, these *dangling* Wannier charge centers become fractionally filled, which allows to define fractional charges [250–255]. Hence, OALs can be perceived as examples of the so-called higher-order topology, which generalizes the bulk-boundary correspondence: a d-dimensional system with a non-trivial bulk topology exhibits boundary modes in a $(d-D)$ dimensions, with a co-dimension $D > 1$ [256, 257, 60, 258–262]. The relation between 2D Wannier centers and corner charge was developed in Refs. [259, 251, 253]. In particular, Ref. [253] uses the algebraic structure of the classifications of C_n-symmetric insulators in class AI to build topological

1 A Wyckoff position w is a generic location in a unit cell such that it has its own site-symmetry (or point-symmetry) group $\mathcal{G}_w$, which is a subgroup of the crystal space group $\mathcal{G}$: $\mathcal{G}_w = \{g = \{p_g|\mathbf{r}_g\} \in \mathcal{G}|p_g\mathbf{r}_w + \mathbf{r}_g = \mathbf{r}_w\}$, where $\mathbf{r}_w$ is the position of the Wyckoff position (we use here the Wigner-Seitz notation). In particular, a maximal Wyckoff position is defined as a point where the site-symmetry group is a maximal subgroup of $\mathcal{G}$.

System	Trivial atomic limit	Obstructed atomic limit	Fragile topological	Stable topological
Wannier representable	yes	yes	no	no
Trivialization by extra degrees of freedom	-	adding unoccupied bands	adding occupied bands	-
Example	atomic insulator	see Sec. 4.7	twisted bilayer graphene [243, 248, 249]	Chern insulators, Z_2 TIs

Table 3: Classification of the band structures corresponding to the (spatial) symmetry-protected phases. All the band structures fall into two categories: *topological* bands, which do not admit representation in terms of Wannier functions, and *atomic* bands, for which the Wannier functions are exponentially localized. Within these two groups, a further distinction is possible. Fragile topological systems can be trivialized into a product state by adding occupied states, i. e., electrons, resulting in the change of the total filling. Adding empty bands to a system realizing an obstructed atomic limit, in which the WFs are located far from the positions of atoms, leads to its trivialization.

indices for corner charge. It has also been recently found that fragile topological phases can also host corner charges [253, 244] and that 2D second-order topological insulators also exhibit fractional charges at the core of defects with curvature singularities in both spinless and spinful insulators [253, 263, 264].

In the absence of internal symmetries, though, 0D states can be pushed out of the bulk gap and hybridized with bulk states by symmetry-preserving potential terms, which destroys their exponential localization. It is in contrast to the first-order phases in which 1D protected edge states demonstrate a spectral flow connecting conduction and valence bands. To define topology in a meaningful way, we employ a notion of a *filling anomaly* [253]: a topological property of the occupied bands of TCIs that counts the mismatch between the number of electrons needed to simultaneously satisfy charge neutrality and preserve the crystal symmetry. If the system with periodic boundary conditions is at the filling corresponding to an insulating band gap, then it has to be metallic with open boundary conditions when all relevant symmetries are respected. Importantly, this notion does not require a spectral symmetry, which is often used to pin boundary modes in the middle of a band gap.

In general, a set of occupied bands (without strong or fragile topology) can be decomposed into subsets of bands stemming from localized orbitals at different Wyckoff positions. Such a set of bands is called a *band representation* [147]. The minimal subblocks that cannot be further decomposed are *elementary band representations* (EBRs), which are a connected set of subbands induced from placing a certain orbital at a given Wyckoff position [265, 266, 147, 267, 268, 241, 269, 270]. For the band representations, the irreducible representations (irreps) of the little group[2] at high symmetry points (HSPs) in the BZ are completely determined by the irreps of the site-symmetry group under which the Wannier functions transform. Ref. [147] introduced EBRs as a means to discern bands that stem entirely from atomic limits from those with strong or fragile topology. Following the approach in Ref. [253], we use the additive structure of

2 A set of symmetry operations $g \in \mathcal{G}$ that leaves a momentum $\mathbf{k}$ invariant up to a reciprocal lattice vector G is called little group $G_{\mathbf{k}}$ of $\mathbf{k}$: $G_{\mathbf{k}} = \{g = \{p_g|\mathbf{r}_g\} \in \mathcal{G}|p_g\mathbf{k} \approx \mathbf{k}\}$.

atomic limits that they provide to establish the correspondence between bulk invariants and corner charges sourced by OAL Wannier charge centers.

In this Chapter, we provide a classification of OALs and formulas for corner charges for all layer groups[3]. As an introduction, we discuss the illustrative example of a charge fractionalization due to inversion symmetry in 1D SSH chain in Section 4.1. We then move to defining the precise meaning of corner charge in 2D in Section 4.2. In particular, we focus on the role of the sample termination in the quantization and robustness of corner charges. In Section 4.3, we present the construction of topological indices based on the occupied subspace of a bulk model represented by a Bloch Hamiltonian: *symmetry indicators* computed from the irreducible representations of the Bloch states or integrals of a connection obtained from the Bloch states over (subsets of) the Brillouin zone, which will be referred to as Berry phase or *Wilson loop type* invariants. We list topological invariants for the systems protected by C_n rotations, with or without an additional 3D inversion symmetry $\mathcal{I}$, in Section 4.4. With the invariants presented here, we can identify OALs in a computationally more efficient way than by explicitly computing maximally localized Wannier functions. Next, we go on to calculate these indices for the elementary band representations of each symmetry class in Section 4.5. Finally, in Section 4.6 we provide the formulas that allow for a determination of the corner charge in all symmetry classes. To support our theoretical findings, in Section 4.7 we present the calculations for material candidates – arsenic and antimony monolayers – which can exhibit two distinct OALs depending on the degree of structural buckling.

4.1 CHARGE FRACTIONALIZATION IN 1D

In the SSH chain [80] (presented in Chapter 1), the chiral symmetry $\mathcal{C}$ is responsible for the topological protection of edge states pinned at zero energy. The model also possess a spatial symmetry – the inversion symmetry $\mathcal{I}$ – realized by σ_x Pauli matrix, $\mathcal{I} = \sigma_x$, which consequences on the macroscopical *polarization* $\mathbf{P}$ and charge fractionalization we explore now.

In finite systems, e. g. molecules, the polarization is straightforwardly defined as a difference between the centers of negative and positive charges in a system. However, this statement breaks down as one starts to consider periodic systems such as band insulators: the choice of a unit cell becomes not unique and the centers of charges of electrons are delocalized. While the polarization $\mathbf{P}$ is not well-defined, its change $\Delta\mathbf{P}$ is finite. This observation underlies the modern theory of polarization [271, 272, 63]. In this formulation, the electric polarization $\mathbf{P}_e$[4] can be computed from the Wannier charge centers (WCCs) [235]. Given the Wannier function $|W_n(\mathbf{R})\rangle$, the WCC is defined as the expectation value of the position operator $\mathbf{r}$, $\langle W_n(\mathbf{R})|\mathbf{r}|W_n(\mathbf{R})\rangle \equiv \bar{\mathbf{r}}_n$, where n labels the occupied bands. In 1D, we can then write

$$P_e = -\frac{e}{V}\sum_{n\in\text{occ}}\langle W_n(0)|x|W_n(0)\rangle \tag{114}$$

with V denoting the volume of the unit cell. Note that we use the WFs only for a single unit cell ($R = 0$).

3 Layer groups are extensions of two-dimensional possible plane symmetry groups called the wallpaper groups with an additional reflection in 3D. Overall, there are 17 wallpaper groups and 80 layer groups.

4 The total polarization $\mathbf{P}$ includes the contribution from the nuclei and from the electrons, $\mathbf{P} = \mathbf{P}_{ion} + \mathbf{P}_e$. The ionic part is not relevant for defining topological properties and therefore can be neglected.

It is possible to express Eq. (114) in terms of the cell-periodic Bloch states $|u_{nk}\rangle$

$$P = -\frac{ie}{N}\sum_n\sum_k \langle u_{nk}|\frac{\partial}{\partial k}|u_{nk}\rangle = -\frac{ea}{2\pi}\sum_n\int_0^{2\pi}\mathcal{A}_n(k)\,dk, \tag{115}$$

where N stands for the total number of unit cells and a is the lattice constant. In fact, we can recognize that the integral in Eq. 115 is just the Berry phase γ_n divided by 2π [272]. The Berry phase of 1D system is often called the Zak phase [273]. As the coordinate of a center of charge is defined only up to modulo lattice translation, the Zak phase is coordinate-dependent. Moreover, it can be shown that the polarization arising from the n-th band is gauge-dependent (due to the U(1) gauge freedom of the Bloch state)

$$P_n \to P_n' = P_n + ema; \quad m \in \mathbb{Z}. \tag{116}$$

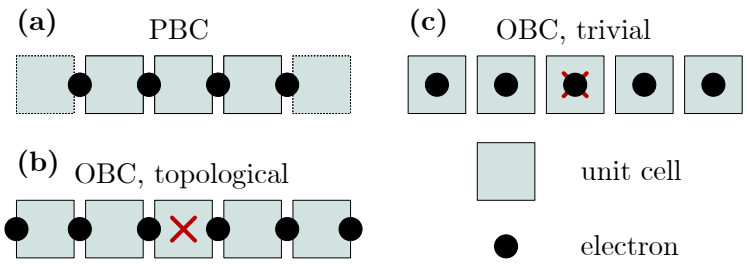

Figure 39: Charge fractionalization in the inversion-symmetric SSH chain. A red cross marks the center of inversion. **(a)** For a periodic chain, there is an ambiguity in the choice of the unit cell. On the other hand, with open boundary conditions, the Wannier centers can reside at inequivalent high-symmetry positions in the unit cell. **(b)** In the topological case, the Wannier centers are located at the unit cell boundary, leading to half charges at the end of an open chain [274, 250, 275]. **(c)** In contrast, a trivial limit (with no charges) corresponds to the configuration in which the Wannier centers are localized within the unit cell. Note that imposing spectral symmetries is required for realizing a strong topological phase, but this simple picture based on the polarization of a single unit cell cannot distinguish between all the different possible phases.

In general, the Zak phase can take any value. However, the presence of the spatial inversion $\mathcal{I}$ imposes the constraints on γ_n (and therefore on P_n). The Berry connection is odd under the action of $\mathcal{I}$, $\mathcal{A}_n(-k) = -\mathcal{A}_n(k)$, which implies $P_n = -P_n \mod |e|a$ and hence

$$P_n = 0 \text{ or } P_n = \frac{|e|a}{2} \mod |e|a. \tag{117}$$

This is exactly the case of the SSH chain, where the WCCs can be located only at 0 (that is, at a lattice site) or $a/2$ (between two lattice sites), which we illustrate in Fig. 39. The latter case corresponds to the topological regime with stronger intercell hoppings, when cutting the system after a full unit cell results in the zero-mode end states. These edge modes carry a fractional charge $|e|/2$. Exactly the same arguments lead to the fractionalization of electrons into Majorana fermions in topological superconductors such as the Kitaev's chain [51].

4.2 BOUNDARY PHENOMENON: CORNER CHARGES

We now move to 2D spinful insulating systems with time-reversal symmetry $\mathcal{T}$ (class AII in the AZ classification, $\mathcal{T}^2 = -1$) and the spatial symmetries corresponding to a symmetry group $\mathcal{G}$. We exclude first-order topological insulators hosting the edge states in co-dimension 1, so that the models we are studying are generically gapped even in a geometry with open boundary conditions. Additionally, we exclude insulators with bulk (TRS) polarization because those have edge-induced filling anomalies that scale with edge length and therefore result in metallic edges that preclude the existence of stable localized corner charges [253].

4.2.1 *Quantization of the corner charge*

We assume a tight-binding description of the system of interest and denote by $\mathbf{a}_1$ and $\mathbf{a}_2$ the translation vectors corresponding to the decomposition of the $\mathcal{G}$-symmetric lattice Λ into l-site unit cells $\mathrm{S} = \{\mathbf{r}_1, \ldots, \mathbf{r}_l\}$, where $\mathbf{r}_i$ denotes the position of site i in the unit cell as measured from the unit cell origin $\mathbf{r}_1 \equiv \mathbf{0}$. (Note that here and in the following, we only treat unit cells that are mapped to themselves under all available point-group symmetries, and do not cut through atomic sites. By these properties, a finite-size termination which does not cut through unit cells becomes possible.) We have

$$\Lambda = \bigcup_{x,y\in\mathbb{Z}} \bigcup_{\mathbf{r}\in\mathrm{S}} (x\mathbf{a}_1 + y\mathbf{a}_2 + \mathbf{r})\,. \tag{118}$$

We are considering tight-binding Hamiltonians of the form

$$H = \sum_{\mathbf{v},\mathbf{w}\in\Lambda} \sum_{\mu,\nu} h_{\mathbf{v}\mu,\mathbf{w}\nu}\, c^\dagger_{\mathbf{v}\mu} c_{\mathbf{w}\nu}, \tag{119}$$

where μ, ν run over orbital degrees of freedom defined at each lattice site and $c^\dagger_{\mathbf{v}\mu}$ creates an electron in the orbital μ at the lattice site $\mathbf{v}$. Hermiticity of H as well as the symmetry requirements posed by T and the symmetry group $\mathcal{G}$ imply some relations among the Hamiltonian elements $h_{\mathbf{v}\mu,\mathbf{w}\nu}$ which we implicitly assume to be fulfilled here and in the following for simplicity.

Given a unit cell decomposition of Λ in terms of S, we define a *trivial atomic limit* by a Hamiltonian that is adiabatically deformable into one for which the implication

$$\mathbf{v} \in \bigcup_{\mathbf{r}\in\mathrm{S}} (x\mathbf{a}_1 + y\mathbf{a}_2 + \mathbf{r}) \not\ni \mathbf{w} \quad \Rightarrow \quad h_{\mathbf{v}\mu,\mathbf{w}\nu} = 0 \tag{120}$$

holds for all choices of x and y, that is, there are no couplings between different unit cells.

To calculate corner charges we consider a finite system of $|\mathrm{F}|$ unit cells, via restricting H to a subset $\Lambda_\mathrm{F} \in \Lambda$ (thereby obtaining H_F), which is given by

$$\Lambda_\mathrm{F} = \bigcup_{x,y\in\mathrm{F}} \bigcup_{\mathbf{r}\in\mathrm{S}} (x\mathbf{a}_1 + y\mathbf{a}_2 + \mathbf{r})\,. \tag{121}$$

We choose Λ_F so as to retain all point group symmetries contained in $\mathcal{G}$, a subgroup we denote by $\mathcal{G}_\mathrm{F}$ (it does not contain translations or non-symmorphic symmetries). Then we consider a subset $\mathrm{C} \subset \Lambda_\mathrm{F}$ comprised of a minimal (but larger than 1) number of disjoint boundary regions

that form an orbit under $\mathcal{G}_F$ and contain an integer number of unit cells each. We choose C to cover all boundaries of Λ_F. A particular boundary region $c \subset C$ has charge

$$Q_c = \sum_{\mathbf{v}\in c} \sum_{\mu} \sum_{l\in \mathrm{occ}} |\langle \mathbf{v}\mu | l\rangle|^2 , \tag{122}$$

where $|l\rangle$ denotes an eigenstate of H_F that is taken out of the occupied subspace occ bounded by E_{Fermi} and we have $|\mathbf{v}\mu\rangle = c^\dagger_{\mathbf{v}\mu}|0\rangle$ where $|0\rangle$ denotes the electronic vacuum. Since we only consider regions c that are related to each other by elements of $\mathcal{G}_F$, they have necessarily the same charge. Now, note that the charge of the full system is an even integer (given by the number of occupied bands |occ| due to the time reversal symmetry). As long as we choose the regions in C large enough to ensure that the eigenstates localized in the complement are pure bulk-like in character and unaffected by the presence of a boundary, the charge of the complement of C is also an even integer. This is always possible when the linear extent by which C penetrates the bulk is much larger than the correlation length set by the bulk gap. We may then view the states contributing to the charge of the complement of C as states of a complete system of reduced size that has periodic boundary conditions and even integer charge. We thus deduce that Q_c is quantized in even integer multiples of $1/q$, where $q = |C|$ denotes the number of elements in C, that is, disjoint boundary regions. See Figs. 40 (a) and (b) for an example with threefold rotational symmetry.

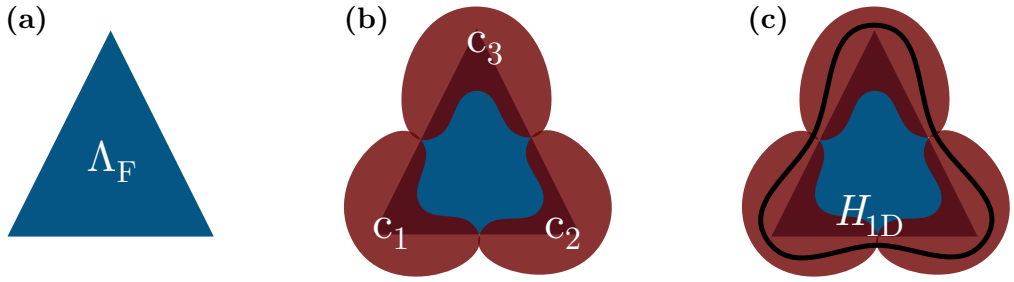

Figure 40: Corner charge fractionalization due to C_3 rotational symmetry. **(a)** The finite system Λ_F on which H_F is defined. **(b)** The boundary regions $c_1, c_2, c_3 \in C$. Due to the C_3 symmetry in $\mathcal{G}_F$, we have that $Q_{c_1} = Q_{c_2} = Q_{c_3}$. Together with $Q_{c_1} + Q_{c_2} + Q_{c_3} \in 2\mathbb{Z}$, this implies a corner charge fractionalization in even multiples of 1/3. **(c)** A 1D edge addition, modeled by the Hamiltonian H_{1D}. We prove in Section 4.2.2 that the corner charges Q_{c_i} are only changed by even integers.

We call Q_c the corner charge since, in a pristine OAL, its fractional part derives from exponentially localized Wannier orbitals that are 'cut through' by corners in the boundary of the system [251–253]: The Wannier orbitals in OALs are localized at maximal Wyckoff positions in the unit cell, and have shapes that respect the little group of their Wyckoff position. When a Wyckoff position lies on the boundary of the unit cell, the boundary cuts through the respective Wannier orbital. The corner charge Q_c can then be calculated conveniently and is equal to the volume that all occupied Wannier functions integrate to in c (where a single Wannier function is normalized to unit volume).

Any trivial atomic limit has $Q_c \in 2\mathbb{Z}$ for any such choice of boundary region: when different unit cells are not coupled to each other, the charge in each unit cell has to be equal to the total charge of the occupied subspace of $H_{F=\{(0,0)\}}$, which is necessarily an even integer. We may then define *corner charge fractionalization* as occurring in systems for which $Q_c \mod 2$ is equal

to non-zero even integer multiples of $1/q$ (odd integer multiples are forbidden by TRS). Note that we assume all systems with non-trivial corner charge to be given by OALs, which have a representation in terms of exponentially localized Wannier functions [235, 147]. However, the corner charge formulas we supply in Section 4.6 apply equally well to fragile phases [240, 241, 243–247]. These can always be adiabatically continued into OALs when other OALs are added. For a calculation of the corner charge in spinful materials, such a 'trivialization' of a fragile phase becomes necessary only in the symmetry class that has C_4 rotational symmetry as its sole crystalline component, since this symmetry does not by itself allow for explicit corner charge formulas in terms of the elementary topological invariants we consider. The classification of corner charge fractionalization in class AII and symmetry group $\mathcal{G}$ is given by the set of inequivalent $Q_c \mod 2$ that cannot be changed without breaking $\mathcal{G}_F$ or closing the bulk gap. Since any finite-size geometry breaks the remaining non-symmorphic symmetries a system might have, we do not need to consider their effect on charge fractionalization.

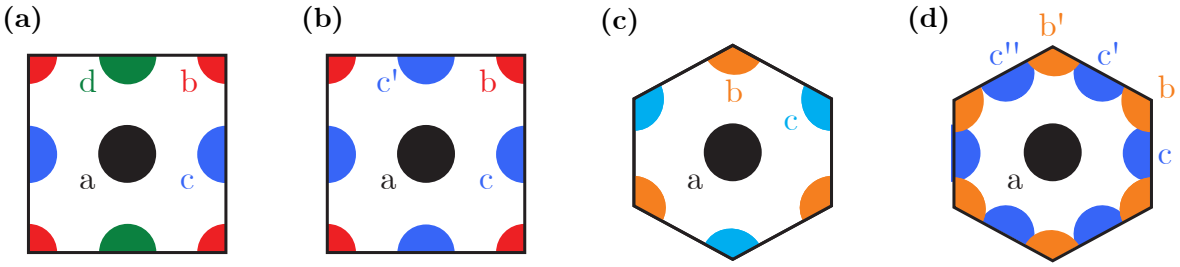

Figure 41: Maximal Wyckoff positions for unit cells with rotational symmetry. **(a)** C_2 symmetry. **(b)** C_4 symmetry. **(c)** C_3 symmetry. **(d)** C_6 symmetry or $C_3 + \mathcal{I}$ symmetry. Boundary charges arise when the Wyckoff positions which Wannier centers are located at are cut through by the crystal termination.

4.2.2 *Stability of the corner charge*

We now discuss to what extent symmetry-preserving edge manipulations can change the corner charge Q_c defined in Eq. (122). We treat an edge manipulation as the introduction of an additional 1D system along the circumference of the finite 2D sample, and ask how the corner charges of the combined system, defined on the appropriately augmented Hilbert space, can differ from those of the original 2D model. Since charges are additive it is enough to determine the possible charges of the 1D system. In the following, we take Q to be the total charge of the 1D addition. It is even due to the requirement that we may only add complete and non-anomalous gapped 1D systems with TRS. We then use the remaining crystalline symmetries to derive further constraints on the charges Q_c that the 1D system contributes to a boundary region c.

We note that the point group symmetries in 2D that $\mathcal{G}_F$ can contain are mirror and n-fold rotational symmetries, where $n \in \{2, 3, 4, 6\}$. We first discuss the latter case of C_n rotational symmetries. For spinful systems with TRS, we have $(C_n)^n = -1$. Let H_{1D} denote a general 1D TRS gapped Hamiltonian defined on a Hilbert space of L lattice sites (with L/n an integer), possibly augmented by orbital degrees of freedom (see also Fig. 40 (c)). A C_n rotational symmetry

$$C_n H_{1D} C_n^\dagger = H_{1D}, \tag{123}$$

implies that we can choose the order of regions $\mathrm{c}_i \in \mathrm{C}$ (which in combination cover all of the L sites of the 1D system) such that in real space the symmetry effects $\mathrm{c}_i \to \mathrm{c}_{i+1 \mod n}$, that is, a translation by L/n sites. Now, due to $(C_n)^n = -1$, rotations are equivalent to translations around a 1D circle that encloses a π-flux. Let t be the operator for translations by a single site, i. e., it shifts site $r \in \{1, \ldots, L\}$ of the 1D lattice to site $r + 1 \mod L$. It is not a symmetry of $H_{1\mathrm{D}}$, however, we can obtain a t-symmetric Hamiltonian (on a ring enclosing a π-flux) by adding up L/n copies of $H_{1\mathrm{D}}$ that are subsequently shifted by one lattice site, to arrive at

$$H_{1\mathrm{D}}^{\mathrm{TRN}} = H_{1\mathrm{D}} \oplus t H_{1\mathrm{D}} t^\dagger \oplus \cdots \oplus t^{L/n-1} H_{1\mathrm{D}} (t^\dagger)^{L/n-1}, \tag{124}$$

which acts on an L/n-fold enlarged Hilbert space. The occupied subspace of $H_{1\mathrm{D}}^{\mathrm{TRN}}$ has a total charge of QL/n and enjoys a translational symmetry that corresponds to L repeated unit cells, with twisted boundary conditions so as to accommodate the π-flux. It is gapped and has TRS just as $H_{1\mathrm{D}}$, and its charge thus necessarily corresponds to an even integer number of filled Bloch bands, which each hold L states. We conclude that its charge per unit cell Q/n is an even integer. Returning our attention to $H_{1\mathrm{D}}$, since all boundaries c carry the same charge, this is exactly the corner charge $Q_{\mathrm{c}} = Q/n$. Thus in the case of C_n-symmetries there is no 1D addition that can trivialize the fractional corner charges of a 2D OAL.

Next, we turn to mirror symmetries, which for spinful systems satisfy $\mathcal{M}^2 = -1$. In the case of two reflections, say $\mathcal{M}_x$ and $\mathcal{M}_y$, we also have a two-fold rotation symmetry $C_2 = \mathcal{M}_x \mathcal{M}_y$, which by the argument above allows us to conclude that all corner charges Q_{c} contributed by any gapped and TRS 1D addition are necessarily even (note that the minimal non-trivial boundary decomposition has $q = 2$). When there is only a single mirror symmetry, we cannot argue along these lines, since it does not act on the 1D real space as a translation. In fact, it 'translates' different sites along the 1D chain by different amounts. Hence, here the symmetry constraint on Q_{c} is the same as that for the 2D bulk, namely that $Q_{\mathrm{c}_i} \in \mathbb{Z}$, $i = 1, 2$, (compare this to the $Q_{\mathrm{c}_i} \in 2\mathbb{Z}$ we obtain for C_2 symmetry) and a fractional charge of $1 \mod 2$ can be trivialized. With a single mirror symmetry, the charges are not robust.

Finally, we note that in the case where we have C_3 symmetry as well as 3D inversion symmetry $\mathcal{I}$ (which is the same as $C_2 M_z$ symmetry), we can define an effective $1/6$ translation by $t_{1/6} = \mathcal{I} C_3^2$ which allows to argue that patches c of size $1/6$ of the linear extent of the full 1D system have even integer charge. This is important for the robustness of the $Q_{\mathrm{c}} = 1/6$ corner charges of this symmetry class. Since any finite-size geometry breaks the remaining non-symmorphic symmetries a system might have, we do not need to consider their effect on charge fractionalization. We conclude that quantized corner charges can be changed by 1D edge manipulations only in the case of a single mirror symmetry.

4.3 BULK INDICES

To identify different EBRs, we employ a combination of symmetry indicator [197, 143, 150, 276, 146, 147, 277, 278, 253] and Wilson loop [279, 61, 280, 273, 150, 281, 266, 241] topological invariants. These can be evaluated from the crystal's Bloch Hamiltonian $\mathcal{H}(\mathbf{k})$ and so do not require a real-space calculation to be performed. The main ingredient for both kinds of invariants is the bundle of occupied Bloch states $|u_m(\mathbf{k})\rangle$. Here, $\mathbf{k}$ is an element of the first Brillouin zone of the crystal.

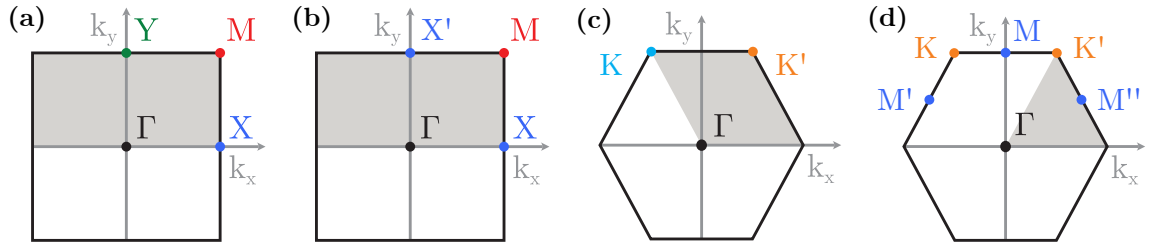

Figure 42: Brillouin zones of crystals with C_2, C_4, C_3, and C_6 symmetries and their rotation invariant points. In C_2-symmetric systems there are three 2-fold HSPs: **X**, **Y**, and **M**. In C_4-symmetric systems there are two 2-fold HSPs: **X** and **X**′, and one 4-fold HSP: **M**. In C_3-symmetric systems there are only two 3-fold HSPs: **K** and **K**′. Finally, in C_6-symmetric systems there are three 2-fold HSPs: **M**, **M**′, and **M**″, as well as two 3-fold HSPs: **K** and **K**′.

4.3.1 *Symmetry indicators*

The Fu-Kane parity criterion for the inversion-symmetric TIs [144] that we introduced in the Chapter 1 is in fact the first instance of a more general framework for symmetry indicators. The symmetry-based methods allow for an efficient diagnosis and characterization of the band structures as they require only symmetry representations of the Bloch states at HSPs [147, 146]. Consider a unitary crystal symmetry $\mathcal{S}$ that is realized on the Bloch Hamiltonian as $\mathcal{S}\mathcal{H}(\mathbf{k})\mathcal{S}^\dagger = \mathcal{H}(\mathcal{S}\mathbf{k})$ and acts on the momenta as $\mathbf{k} \to \mathcal{S}\mathbf{k}$. We can then calculate its corresponding symmetry indicator topological invariants from the eigenvalues of the matrices

$$S_{mn} = \langle u_m(\bar{\mathbf{k}}) | \, \mathcal{S} \, | u_n(\bar{\mathbf{k}}) \rangle \,, \tag{125}$$

where m, n run over the occupied subspace only and $\bar{\mathbf{k}} = \mathcal{S}\bar{\mathbf{k}}$ are high-symmetry points (HSPs) of the Brillouin zone that are left invariant by the symmetry $\mathcal{S}$ (see also Fig. 42). An n-fold symmetry acting on spinful fermions satisfies $\mathcal{S}^n = \pm 1$ (positive sign for 3D inversion, negative sign for 2D mirror and rotational symmetries), this, together with TRS, imposes constraints on the possible eigenvalues of S_{mn} and allows for the definition of topological invariants that capture the different symmetry representations of the occupied bands across the BZ. A trivial atomic limit, being deformable to a momentum-independent Hamiltonian, will have the same representation across HSPs that are invariant under the same symmetry and hence will have trivial symmetry indicator invariants. Non-trivial symmetry indicator invariants, on the other hand, indicate that the bands adopt different representations of the symmetry across the BZ and correspond to OALs.

4.3.2 *Wilson loops*

The Wilson loop (along a closed, non-contractible path γ in the BZ that starts and ends at the momentum $\mathbf{k}^*$) is an operator on the filled band subspace of $\mathcal{H}(\mathbf{k})$ defined as

$$W_\gamma = \prod_{\mathbf{k}}^{\gamma} P(\mathbf{k}), \tag{126}$$

where $P(\mathbf{k}) = \sum_{m\in\text{occ}} |u_m(\mathbf{k})\rangle \langle u_m(\mathbf{k})|$ is the projector onto the subspace of filled bands at momentum $\mathbf{k}$. Note that we choose a gauge where $\mathcal{H}(\mathbf{k}) = \mathcal{H}(\mathbf{k}+\mathbf{G})$ for a reciprocal lattice vector $\mathbf{G}$ and the product is path-ordered along γ. For numerical purposes, the Wilson loop in Eq. (126) can be discretized as

$$\begin{aligned} [W_\gamma]_{mn} &= \langle u_{m,(k_1,\mathbf{k}^*)}| \prod_{k_2}^{\mathbf{k}^*\leftarrow\mathbf{k}^*} P(k_1,k_2)|u_{n,(k_1,\mathbf{k}^*)}\rangle\,; \\ \text{with}\quad \prod_{k_2}^{\mathbf{k}^*\leftarrow\mathbf{k}^*} P(k_1,k_2) &= \lim_{\Delta\to 0} P(k_1,\mathbf{k}^*)P(k_1,\mathbf{k}^*-\Delta)\dots P(k_1,\Delta)P(k_1,\mathbf{k}^*), \end{aligned} \tag{127}$$

where k_1, k_2 are momenta along the path γ. The Wilson loop operator satisfies $W_\gamma W_\gamma^\dagger = P(\mathbf{k}^*)$. Since any projector fulfils $[P(\mathbf{k})]^2 = P(\mathbf{k})$, i. e. is idempotent, its eigenvalues are either zero or of the form $e^{i\theta_\alpha^\gamma}$, $\alpha = 1\dots N$. In the following, we refer to the set of $\{\theta_\alpha^\gamma\}_{\alpha=1\dots N}$ as the Wilson loop spectrum (which is gauge-invariant), suppressing the zero eigenvalues. Note that the θ's phases are only defined modulo 2π. The eigenvalues of the Wilson loop are related to the spectrum of the band-projected position operator $P(\mathbf{k})xP(\mathbf{k})$ or, equivalently, to the centers of hybrid Wannier functions, which are exponentially localized in the one direction and completely delocalized in the remaining directions [281].

The antiunitary TRS $\mathcal{T}$ acts on the Bloch Hamiltonian as $\mathcal{T}\mathcal{H}(\mathbf{k})\mathcal{T}^{-1} = \mathcal{H}(-\mathbf{k})$. For the projectors this implies $\mathcal{T}P(\mathbf{k})\mathcal{T}^{-1} = P(-\mathbf{k})$. When γ is mapped onto itself by TRS, and its starting point satisfies $\mathbf{k}^* = -\mathbf{k}^*$ up to a reciprocal lattice vector, we then have

$$\mathcal{T}W_\gamma\mathcal{T}^\dagger = \prod_{\mathbf{k}}^{\gamma} P(-\mathbf{k}) = W_\gamma^\dagger. \tag{128}$$

Due to $\mathcal{T}$ being antiunitary and $\mathcal{T}^2 = -1$, this implies a Kramers degeneracy of the Wilson loop spectrum, i. e., every θ_α^γ is (at least) two-fold degenerate when γ is mapped onto itself by time reversal.

Now, if there is a crystal symmetry $\mathcal{S}$ that reverses the direction of γ and leaves the starting point invariant so that $\mathbf{k}^* = \mathrm{S}\mathbf{k}^*$ up to a reciprocal lattice vector, we have

$$\mathcal{S}W_\gamma\mathcal{S}^\dagger = \prod_{\mathbf{k}}^{\gamma} \left[\mathcal{S}P(\mathbf{k})\mathcal{S}^\dagger\right] = W_\gamma^\dagger. \tag{129}$$

Since $\mathcal{S}$ is unitary, the Wilson loop is unitarily equivalent to its complex conjugate and so its eigenvalues come in complex conjugated pairs. This implies a symmetry of the Wilson loop spectrum around $\theta = 0$, for every θ_α^γ there is a corresponding $-\theta_\alpha^\gamma \mod 2\pi$.

4.3.2.1 *Nested Wilson loops*

We may furthermore employ nested Wilson loops [256, 258]. Let $W_i(k_j)$, $i \neq j$, denote the Wilson loop along the non-contractible loop $\gamma : (k_i = 0, k_j) \to (k_i = 2\pi, k_j)$, where (k_i, k_j) labels a point in the two-dimensional BZ in some basis (chosen such that $k_{i,j} = 0$ and $k_{i,j} = 2\pi$ are related by reciprocal lattice vectors). Consider the Wilson loop Hamiltonian $H_{W_i}(k_j)$, defined by

$$\left[e^{iH_{W_i}(k_j)}\right]_{mn} = \langle u_m(k_i = 0, k_j)|\, W_i(k_j)\, |u_n(k_i = 0, k_j)\rangle\,. \tag{130}$$

Equations (128) and (129) then imply

$$\begin{aligned} \mathcal{T}_{k_j} H_{W_i}(k_j) \mathcal{T}_{k_j}^\dagger &= H_{W_i}(-k_j), \\ \mathcal{S}_{k_j} H_{W_i}(k_j) \mathcal{S}_{k_j}^\dagger &= -H_{W_i}(\mathsf{S}k_j), \end{aligned} \tag{131}$$

where we defined

$$\begin{aligned} \left(\mathcal{T}_{k_j}\right)_{mn} &= \langle u_m(-k_j)| \mathcal{T} |u_n(k_j)\rangle , \\ \left(\mathcal{S}_{k_j}\right)_{mn} &= \langle u_m(\mathsf{S}k_j)| \mathcal{S} |u_n(k_j)\rangle . \end{aligned} \tag{132}$$

We see that $\mathcal{T}$ implies a TRS of the Wilson loop Hamiltonian, whereas $\mathcal{S}$ implies a particle-hole symmetry. These properties are needed for the definition of quantized topological invariants of the *nested Wilson loop*: We define W_i^{b} as the Wilson loop calculated from a gapped set of eigenstates b of $H_{W_i}(k_j)$ along a closed, non-contractible path $k_j : 0 \to 2\pi$ in the reduced BZ.

We differentiate between three kinds of nested Wilson loops that differ by the choice of the set of eigenstates b: (1) The nested loop W_i^0, which is calculated from the two bands in the spectrum of $H_{W_i}(k_j)$ that at $k_j = 0, \pi$ have a degeneracy pinned to the Wilson eigenvalue 0 (note that any such degeneracy at $k_j = 0$ implies one at $k_j = \pi$ and vice versa due to the absence of Wannier center flow in (obstructed) atomic limits). (2) The nested Wilson loop W_i^λ, calculated for the upper *or* lower half of the bands in the spectrum of $H_{W_i}(k_j)$ that are *not* pinned at $k_j = 0, \pi$ to a Wilson eigenvalue $0, \pi$ (that is, half of the freely dangling Wilson bands, which by the particle hole symmetry come in pairs). (3) The nested loop W_i^π, which is calculated from the two bands in the spectrum of $H_{W_i}(k_j)$ that at $k_j = 0, \pi$ have a degeneracy pinned to the Wilson eigenvalue π.

The nested Wilson loops of type (1) and (3) cannot be trivialized by transformations that preserve $\mathcal{S}$ and $\mathcal{T}$ and are adiabatic with respect to the bulk gap. The reason is that the invariants calculated from these loops are equal to the partial polarizations of Wilson bands pinned to eigenvalues 0 or π by $\mathcal{S}$ at the transverse momenta $k_j = 0, \pi$. Wilson gap closings that preserve the energy gap can only occur in pairs (due to $\mathcal{S}$) at intermediate transverse momenta $k_j, -k_j$. It is rigorously shown in Appendix A of Ref. [282] that these gap closings together always contribute integer multiples of 2π to the nested partial polarization, and therefore cannot trivialize Wilson loops of type (1) and (3). Here, we do not consider invariants derived from Wilson loops of type (2).

4.4 CLASSIFICATION WITH RESPECT TO C_n AND INVERSION SYMMETRIES

We now list the topological invariants that can be defined for a given point group. We find that often the inclusion of the $\mathcal{I}$ symmetry allows for the replacement of Wilson-loop invariants by symmetry indicator invariants. For the discussion of symmetry indicators, we make use of the definitions and derivations presented in Sections B.1 and C of the Appendix. Note that in the following, and as motivated at the beginning of Section 4.2, we explicitly exclude invariants that characterize topological insulators because they are necessarily gapless along the edges in a 2D geometry with open boundary conditions, and so do not allow for stable quantized corner charges. In addition to removing some invariants from our analysis altogether, this imposes constraints on the Wilson loops.

As shown in Section 4.2.2, mirror symmetries can protect fractional corner charges only when they are combined to yield a twofold rotational symmetry. The protecting symmetries we consider are therefore C_n rotations, with or without an additional 3D inversion symmetry $\mathcal{I}$. The inclusion of the $\mathcal{I}$ symmetry allows us to extend our discussion to the experimentally relevant case of 2D honeycomb monolayers with non-zero buckling. We note that inversion effectively replaces C_2 in its role of enforcing a $Q_c = 0, 1 \mod 2$ quantization of the corner charge, but due to $\mathcal{I}^2 = +1$ (whereas $(C_2)^2 = -1$) allows for symmetry indicator invariants. Furthermore, in the case of C_4 symmetry, we find that we require an additional inversion symmetry in order to be able to read off the corner charge from the available topological invariants. Inversion symmetry is however, unlike C_4, not necessary for the topological robustness of the corner charge.

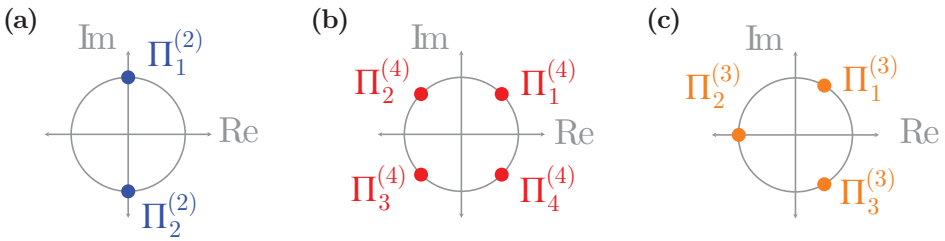

Figure 43: Sets of allowed eigenvalues for spinful rotational symmetries. **(a)** C_2 symmetry. **(b)** C_4 symmetry. **(c)** C_3 symmetry. The possible eigenvalues of C_6 symmetry are not shown, since they do not allow for the definition of symmetry indicators (there is at most one C_6-symmetric point in any two-dimensional Brillouin zone).

We emphasize that our list of invariants may not be exhaustive. As noted in Ref. [241], it is in general difficult to identify all possibly non-trivial Wilson loop invariants. We only treat 'straight' (nested) Wilson loops, which for a given a starting point go around one of the two inequivalent non-contractible loops of the Brillouin zone torus.

4.4.1 C_2 *symmetry*

Symmetry indicator invariants

The BZ has four HSPs, see Fig. 42 (a). All the points are invariant under C_2. Thus, they all have C_2 eigenvalues $+\mathrm{i}, -\mathrm{i}$ (consult Fig. 43 (a)). However, since all the HSPs are also time-reversal invariant momenta, the eigenvalues have to come in complex-conjugate pairs, leading to a single available 2D irreducible representation. Therefore, the C_2 eigenvalues do not distinct different topological phases and there are no symmetry indicator invariants.

Wilson-loop invariants

For every closed high-symmetry line γ (which connects two HSPs) of the 2D BZ that is left invariant by C_2, we can define a Wilson loop that is TRS and C_2 symmetric. Due to Eqs. (128) and (129), the parities of the numbers of $\theta_\alpha^\gamma = 0$ and $\theta_\alpha^\gamma = \pi$ eigenvalues in its spectrum cannot be changed under adiabatic deformations of $\mathcal{H}(\mathbf{k})$: adiabatic perturbations of the Hamiltonian at most move eigenvalues in or out of 0 (resp. π) in pairs due to the Kramers symetry induced

by particle-hole symmetry. A topological invariant of W_γ with spectrum $\{\theta_\alpha^\gamma\}_{\alpha=1\ldots N}$ is therefore given by

$$\nu_\gamma = -\frac{\mathrm{i}}{\pi}\log\left(\prod_{\alpha=1,3,\ldots,N-1} e^{\mathrm{i}\theta_\alpha^\gamma}\right) \mod 2, \tag{133}$$

where the product is taken over only one eigenvalue of each Wilson loop Kramers pair. We call $\nu_\gamma = 0$ trivial and $\nu_\gamma = 1$ non-trivial. This invariant is equivalent to the TRS polarization [283] and counts the parity number of Wilson loop pairs of eigenvalues equal to π. We also define

$$\mu_\gamma = -\frac{\mathrm{i}}{\pi}\log\left(\prod_{\alpha=1,3,\ldots,N-1} e^{\mathrm{i}(\pi-\theta_\alpha^\gamma)}\right) \mod 2, \tag{134}$$

which counts the number of Wilson loop pairs of eigenvalues equal to 0. The invariants ν_γ and μ_γ are not independent when the total number of bands N is fixed. They obey

$$\mu_\gamma = \nu_\gamma + \frac{N}{2} \mod 2. \tag{135}$$

Therefore, we drop μ_γ as it provides redundant topological information. In the following, we consider Wilson loops that go through high-symmetry points in the 2D BZ. We denote by $\nu_{\mathbf{AB}}$ the loop that goes from point **A** to point **B** and then back to **A** via the shortest non-contractible loop around the BZ torus.

There are in total four TRIMs and three topologically inequivalent straight and C_2-symmetric Wilson loops. This can be seen by noting that, holding one of the four C_2-symmetric momenta fixed as a starting point, there are two incontractible loops around the Brillouin zone torus (which necessarily go through one other C_2-symmetric momentum). Keeping in mind that path-reversed Wilson loops are not independent (as per Eq. (129)), this naively yields the set of Wilson loop invariants $\{\nu_{\mathbf{\Gamma X}}, \nu_{\mathbf{\Gamma Y}}, \nu_{\mathbf{XM}}, \nu_{\mathbf{YM}}\}$. We note however that the path denoted by $\mathbf{\Gamma Y} - \mathbf{\Gamma X} - \mathbf{XM}$ is topologically equivalent to the path denoted by **YM** and so we have

$$\nu_{\mathbf{YM}} = \nu_{\mathbf{\Gamma Y}}\nu_{\mathbf{\Gamma X}}\nu_{\mathbf{XM}}. \tag{136}$$

The remaining invariants are further constrained due to the requirement that the $\mathbb{Z}_2$ TI invariant Δ_{TI} vanishes: we have that

$$\begin{aligned} \Delta_{\mathrm{TI}} &= \nu_{\mathbf{\Gamma X}} + \nu_{\mathbf{YM}} \mod 2 \\ &= \nu_{\mathbf{\Gamma Y}} + \nu_{\mathbf{XM}} \mod 2. \end{aligned} \tag{137}$$

We are left with two Wilson loop invariants.

Similarly, we may define the quantized invariants $\nu_{x,y}^{0,\pi}$ and $\mu_{x,y}^{0,\pi}$ from the nested Wilson loops $W_{x,y}^{0,\pi}$, since these are calculated for particle-hole symmetric sets of bands [262, 244] (in contrast to $W_{x,y}^{\lambda}$, which does not satisfy Eq. (131)): the anti-commutativity with the Wilson loop Hamiltonian that distinguishes particle-hole symmetry from a reflection symmetry is irrelevant from the point of view of the nested Wilson loop, as long as the latter is defined via a projector onto a particle-hole symmetric set of bands. We may therefore define $\nu_{x,y}^{0,\pi}$ and $\mu_{x,y}^{0,\pi}$ just as in Eqs. (133) and (134), where θ_α^γ this time refers to the spectrum of the nested Wilson loop. As

before, we drop the μ invariants since they are not independent when the number of occupied Wilson bands is held fixed. Taking into account the constraints [282]

$$\begin{aligned} \nu_x^0 + \nu_x^\pi \mod 2 &= \nu_{\Gamma Y}, \\ \nu_y^0 + \nu_y^\pi \mod 2 &= \nu_{\Gamma X}, \\ \nu_x^\pi &= \nu_y^\pi, \end{aligned} \tag{138}$$

reduces the number of independent invariants to three. The third equation can be seen in the following way: ν_x^π is non-zero if and only if the occupied subspace hosts an odd number of Wannier-Kramers pairs whose centers are shifted by $1/2$ in both x and y direction (taking the lattice constant to be 1) with respect to the center of the unit cell, i. e., if there is an odd number of Kramers pairs at Wyckoff position $1b$ of the crystal (see also Table 5). This Wyckoff position stays unchanged when exchanging x and y, we therefore obtain that ν_x^π is non-zero if and only if ν_y^π is non-zero. Note that the corresponding statement does not hold for ν_x^0 and ν_y^0, since these indicate Wannier-Kramers pairs at the $1c$ and $1d$ Wyckoff positions, respectively. We therefore choose the classification to be given by

$$\chi^{(2)} = \{\nu_{\Gamma X}, \nu_{\Gamma Y}, \nu_x^\pi\}. \tag{139}$$

With inversion symmetry

$C_2 + \mathcal{I}$ symmetry is equivalent to $\mathcal{I}$ symmetry for all our purposes. Inversion symmetry allows us to replace the $\mathbb{Z}_2$ valued Wilson-loop invariants by $2\mathbb{Z}$-valued symmetry indicators. The BZ has the $\mathcal{I}$-invariant points $\mathbf{\Gamma}$, $\mathbf{X}$, $\mathbf{Y}$ and $\mathbf{M}$, which support the six inversion eigenvalue invariants

$$\begin{aligned} [X_i^\mathcal{I}] &= \#X_i^\mathcal{I} - \#\Gamma_i^\mathcal{I}, \\ [Y_i^\mathcal{I}] &= \#Y_i^\mathcal{I} - \#\Gamma_i^\mathcal{I}, \\ [M_i^\mathcal{I}] &= \#M_i^\mathcal{I} - \#\Gamma_i^\mathcal{I}, \end{aligned} \tag{140}$$

where $\#X_i^\mathcal{I}$ ($\#\Gamma_i^\mathcal{I}$, $\#Y_i^\mathcal{I}$, and $\#M_i^\mathcal{I}$) is the number of occupied states with inversion eigenvalue $X_i^\mathcal{I}$ ($\Gamma_i^\mathcal{I}$, $Y_i^\mathcal{I}$, and $M_i^\mathcal{I}$, respectively). The inversion eigenvalues labeled by $i = 1, 2$ are $\{1, -1\}$. Due to the fixed number of occupied bands, we have the constraints

$$\begin{aligned} [X_1^\mathcal{I}] + [X_2^\mathcal{I}] &= 0, \\ [Y_1^\mathcal{I}] + [Y_2^\mathcal{I}] &= 0, \\ [M_1^\mathcal{I}] + [M_2^\mathcal{I}] &= 0. \end{aligned} \tag{141}$$

The three remaining invariants completely fix [281] the Wilson loops in Eq. (139). They are necessarily even integers due to TRS. We retain the classification

$$\chi_\mathcal{I}^{(2)} = \{[X_2^\mathcal{I}], [Y_2^\mathcal{I}], [M_2^\mathcal{I}]\}. \tag{142}$$

4.4.2 C_3 *symmetry*

Symmetry indicator invariants

The BZ only has the C_3-invariant points $\mathbf{K}$ and $\mathbf{K}'$, see also Fig. 42 (c). Now, we discuss the invariants that compare the representations at the $\mathbf{K}$ ($\mathbf{K}'$) and $\mathbf{\Gamma}$ points of the BZ,

$$[K_i^{(3)}] = \#K_i^{(3)} - \#\Gamma_i^{(3)}, \tag{143}$$

where $K_{i=1,2,3}^{(3)}$, $\Gamma_{i=1,2,3}^{(3)} = \{e^{\mathrm{i}\pi/3}, -1, e^{-\mathrm{i}\pi/3}\}$, and similarly for $\mathbf{K}'$ (see Fig. 43 (c)). Unlike $\mathbf{M}$, the HSP $\mathbf{K}$ is *not* a TRIM. Instead, TRS relates $\mathbf{K}$ and $\mathbf{K}'$. TRS imposes the constraints,

$$\begin{aligned} [K_1^{(3)}] &= [K_3'^{(3)}], \\ [K_2^{(3)}] &= [K_2'^{(3)}], \\ [K_3^{(3)}] &= [K_1'^{(3)}]. \end{aligned} \tag{144}$$

The six invariants are subject to the constraints (144) along with

$$\begin{aligned} [K_1^{(3)}] + [K_2^{(3)}] + [K_3^{(3)}] &= 0, \\ [K_1'^{(3)}] + [K_2'^{(3)}] + [K_3'^{(3)}] &= 0. \end{aligned} \tag{145}$$

due to the constant number of occupied states across the BZ. The symmetry-indicated part of the classification is given by the two invariants

$$\chi^{(3)} = \{[K_1^{(3)}], [K_2^{(3)}]\}. \tag{146}$$

Wilson-loop invariants

There are no Wilson loop invariants in this class due to the lack of a twofold symmetry.

With inversion symmetry

Inversion symmetry implies $[K_i^{(3)}] = [K_i'^{(3)}]$, $i = 1, 2, 3$. We therefore drop $[K_1^{(3)}]$ from the list of independent invariants. The BZ has the $\mathcal{I}$-invariant points $\mathbf{M}$, $\mathbf{M}'$ and $\mathbf{M}''$, which support the invariants

$$[M_i^{\mathcal{I}}] = \#M_i^{\mathcal{I}} - \#\Gamma_i^{\mathcal{I}}, \tag{147}$$

where $M_{i=1,2}^{\mathcal{I}}$, $\Gamma_{i=1,2}^{\mathcal{I}} = \{1, -1\}$, and similarly for $\mathbf{M}'$ and $\mathbf{M}''$. TRS implies that the states belonging to a Kramers pair have equal inversion eigenvalue. C_3 imposes the constraints

$$\begin{aligned} [M_1^{\mathcal{I}}] &= [M_1'^{\mathcal{I}}] = [M_1''^{\mathcal{I}}], \\ [M_2^{\mathcal{I}}] &= [M_2'^{\mathcal{I}}] = [M_2''^{\mathcal{I}}]. \end{aligned} \tag{148}$$

In addition we have

$$[M_1^{\mathcal{I}}] + [M_2^{\mathcal{I}}] = 0. \tag{149}$$

We retain $[M_2^{\mathcal{I}}]$ as the invariant that determines the classification, in addition to the C_3 invariant $[K_2^{(3)}]$:

$$\chi_{\mathcal{I}}^{(3)} = \{[M_2^{\mathcal{I}}], [K_2^{(3)}]\}. \tag{150}$$

4.4.3 C_4 *symmetry*

Symmetry indicator invariants

The BZ has four HSPs (Fig. 42 (b)). Two of them are invariant under C_2 and give rise to trivial indicators due to time reversal symmetry. We can then only build indices that compare the C_4 symmetry representations at $\mathbf{M}$ with those at $\mathbf{\Gamma}$ as follows:

$$[M_i^{(4)}] = \#M_i^{(4)} - \#\Gamma_i^{(4)}, \quad i \in \{1,2,3,4\}, \tag{151}$$

where the eigenvalues are taken from $M_{i=1,2,3,4}^{(4)}, \Gamma_{i=1,2,3,4}^{(4)} = \{e^{i\pi/4}, e^{i3\pi/4}, e^{-i3\pi/4}, e^{-i\pi/4}\}$, respectively (see Fig. 43 (b)). Since all the HSPs are also TRIMs, the rotation eigenvalues have to come in complex-conjugate pairs. Therefore, we have the constraints on the invariants

$$\begin{aligned} [M_1^{(4)}] &= [M_4^{(4)}], \\ [M_2^{(4)}] &= [M_3^{(4)}]. \end{aligned} \tag{152}$$

Since the number of occupied states is constant across the BZ, we have that $\sum_i \#M_i^{(4)} = \sum_i \#\Gamma_i^{(4)}$, or

$$[M_1^{(4)}] + [M_2^{(4)}] + [M_3^{(4)}] + [M_4^{(4)}] = 0. \tag{153}$$

With the constraints in (152) and (153), we eliminate the redundant invariants $[M_2^{(4)}]$, $[M_3^{(4)}]$, and $[M_4^{(4)}]$. Thus, the classification due to C_4 symmetry has only one symmetry-indicator invariant, $[M_1^{(4)}]$.

Wilson-loop invariants

C_4 symmetry implies having C_2 symmetry as well and so we can immediately take over the Wilson loops given in Eq. (139) as possible invariants, where due to C_4 we have $\nu_{\mathbf{\Gamma X}} = \nu_{\mathbf{\Gamma Y}}$. Therefore, the classification is given by

$$\chi^{(4)} = \left\{\nu_{\mathbf{\Gamma X}}, \nu_x^{\pi}, [M_1^{(4)}]\right\}. \tag{154}$$

With inversion symmetry

The invariants given in Eq. (142) (together with the C_4 constraint $[X_2^{\mathcal{I}}] = [Y_2^{\mathcal{I}}]$) allow us to replace $\nu_{\mathbf{\Gamma X}}, \nu_{\mathbf{YM}}$. We conclude that the classification with inversion symmetry is given by

$$\chi_{\mathcal{I}}^{(4)} = \left\{[X_2^{\mathcal{I}}], [M_2^{\mathcal{I}}], [M_1^{(4)}]\right\}. \tag{155}$$

4.4.4 C_6 *symmetry*

Symmetry indicator invariants

In a C_6-symmetric BZ, there are two inequivalent HSPs, **M**, which is invariant under C_2, and **K**, which is invariant under C_3 (Fig. 42 (d)). All other points are related by rotations, and thus provide redundant representations for the purpose of classification. Furthermore, **M** is both a HSP and a TRIM. Thus, from the analysis of the previous classifications, no invariants can be derived from its representations. Now, we discuss the invariants that compare the representations at the **K** and **Γ** points of the BZ,

$$[K_i^{(3)}] = \#K_i^{(3)} - \#\Gamma_i^{(3)}, \tag{156}$$

where $K^{(3)}_{i=1,2,3}$, $\Gamma^{(3)}_{i=1,2,3} = \{e^{i\pi/3}, -1, e^{-i\pi/3}\}$. Unlike **M**, the HSP **K** is *not* a TRIM. Instead, TRS relates **K** and **K**′. TRS imposes the constraints,

$$\begin{aligned} [K_1^{(3)}] &= [K_3'^{(3)}], \\ [K_2^{(3)}] &= [K_2'^{(3)}], \\ [K_3^{(3)}] &= [K_1'^{(3)}]. \end{aligned} \tag{157}$$

But the representations at **K** and **K**′ are the same due to C_6 symmetry,

$$\begin{aligned} [K_1^{(3)}] &= [K_1'^{(3)}], \\ [K_2^{(3)}] &= [K_2'^{(3)}], \\ [K_3^{(3)}] &= [K_3'^{(3)}]. \end{aligned} \tag{158}$$

The last two sets of constraints leave us with only two non-redundant invariants, $[K_1^{(3)}]$ and $[K_2^{(3)}]$. However, due to the constant number of occupied states, we have $\sum_i \#K_i^{(3)} = \sum_i \#\Gamma_i^{(3)}$ or $2[K_1^{(3)}] + [K_2^{(3)}] = 0$, which makes one of these invariants redundant too. We choose the symmetry-indicated part of the classification to be given by $[K_2^{(3)}]$.

Wilson-loop invariants

C_6 symmetry implies having C_2 symmetry as well and so we can define $\mu_{\Gamma\mathbf{M}}$ as an invariant due to Eq. (134). We choose $\mu_{\Gamma\mathbf{M}}$ here instead of $\nu_{\Gamma\mathbf{M}}$ since it directly indicates Wannier centers at the 3*c* Wyckoff position (see Fig. 41 (d) and Table 8) of the hexagonal unit cell. We do not consider nested Wilson loops in this symmetry class because the corner charge can be completely determined without them. In conclusion, we have

$$\chi^{(6)} = \{\mu_{\Gamma\mathbf{M}}, [K_2^{(3)}]\}. \tag{159}$$

With inversion symmetry

The BZ has the $\mathcal{I}$-invariant points **M**, **M**′ and **M**″, which support the invariants

$$[M_i^{\mathcal{I}}] = \#M_i^{\mathcal{I}} - \#\Gamma_i^{\mathcal{I}}, \tag{160}$$

where $M^{\mathcal{I}}_{i=1,2}$, $\Gamma^{\mathcal{I}}_{i=1,2} = \{1, -1\}$, and similarly for $\mathbf{M}'$ and $\mathbf{M}''$. TRS implies that the states belonging to a Kramers pair have equal inversion eigenvalue. C_6 imposes the constraints

$$\begin{aligned}[M_1^{\mathcal{I}}] = [M_1'^{\mathcal{I}}] = [M_1''^{\mathcal{I}}],\\ [M_2^{\mathcal{I}}] = [M_2'^{\mathcal{I}}] = [M_2''^{\mathcal{I}}].\end{aligned} \tag{161}$$

In addition we have

$$[M_1^{\mathcal{I}}] + [M_2^{\mathcal{I}}] = 0. \tag{162}$$

We retain $[M_2^{\mathcal{I}}]$ as the invariant that determines the classification. Due to C_6 symmetry [253] and TRS, $[M_2^{\mathcal{I}}] \in 4\mathbb{Z}$. We conclude that

$$\chi_{\mathcal{I}}^{(6)} = \{[M_2^{\mathcal{I}}], [K_2^{(3)}]\}. \tag{163}$$

4.4.5 *Summary*

In Table 4, we present all the invariants obtained by combining Wilson loops and symmetry indicators.

$\mathcal{S}$	without $\mathcal{I}$	with $\mathcal{I}$
$\mathcal{I}$	none	$[X_2^{\mathcal{I}}], [Y_2^{\mathcal{I}}], [M_2^{\mathcal{I}}]$
C_2	$\nu_{\Gamma X}, \nu_{\Gamma Y}, \nu_x^{\pi}$	$[X_2^{\mathcal{I}}], [Y_2^{\mathcal{I}}], [M_2^{\mathcal{I}}]$
C_3	$[K_1^{(3)}], [K_2^{(3)}]$	$[M_2^{\mathcal{I}}], [K_2^{(3)}]$
C_4	$\nu_{\Gamma X}, \nu_x^{\pi}, [M_1^{(4)}]$	$[X_2^{\mathcal{I}}], [M_2^{\mathcal{I}}], [M_1^{(4)}]$
C_6	$\mu_{\Gamma M}, [K_2^{(3)}]$	$[M_2^{\mathcal{I}}], [K_2^{(3)}]$

Table 4: Summary of Wilson loop and symmetry indicator invariants.

4.5 DECOMPOSITION INTO EBRS

Tables 5–8 list the EBRs [265, 266, 147, 267, 268, 241, 280, 273] supported by systems with C_n rotational symmetry, together with their invariants and corner charges. The minimal block sizes correspond to the multiplicities of the respective Wyckoff positions (multiplied by two to account for spin). If multiple choices for the site-symmetry group [147] representation at a Wyckoff position W are available, we denote the representation with eigenvalues $e^{i\alpha}$ as $W|_{\alpha}$.

C_2	$\nu_{\Gamma X}$	$\nu_{\Gamma Y}$	ν_x^{π}	Q_c
$1a$	0	0	0	0
$1b$	1	1	1	1
$1c$	1	0	0	0
$1d$	0	1	0	0

Table 5: EBRs with C_2 symmetry induced from the maximal Wyckoff positions listed in the first column (see Fig. 41 (a)), and their invariants. All atomic limits can be decomposed into EBRs formed by single Kramers pairs.

C_4	$\nu_{\Gamma X}$	ν_x^π	$[M_1^{(4)}]$	Q_c
$1a$	0	0	0	0
$1b\|_{\pm\frac{\pi}{4}}$	1	1	-1	1/2
$1b\|_{\pm\frac{3\pi}{4}}$	1	1	1	1/2
$2c$	1	0	0	0
$1b\|_{\pm\frac{\pi}{4}} \oplus 1b\|_{\pm\frac{3\pi}{4}}$	0	0	0	1

Table 6: EBRs with C_4 symmetry induced from the maximal Wyckoff positions listed in the first column (see Fig. 41 (b)), and their invariants. All atomic limits can be decomposed into EBRs formed by at most two Kramers pairs. Importantly, the (non-elementary) band representation $1b|_{\pm\frac{\pi}{4}} \oplus 1b|_{\pm\frac{3\pi}{4}}$ has trivial C_4 invariants but non-zero corner charge. In systems with C_4 as the sole crystalline symmetry, this obstructs a determination of the corner charge in terms of topological invariants.

C_3	$[K_1^{(3)}]$	$[K_2^{(3)}]$	Q_c
$1a$	0	0	0
$1b\|_{\pi}$	0	-2	2/3
$1b\|_{\pm\frac{\pi}{3}}$	0	1	2/3
$1c\|_{\pi}$	2	-2	0
$1c\|_{\pm\frac{\pi}{3}}$	-1	1	0

Table 7: EBRs with C_3 symmetry induced from the maximal Wyckoff positions listed in the first column (see Fig. 41 (c)), and their invariants. All atomic limits can be decomposed into EBRs formed by single Kramers pairs.

C_6	$\mu_{\Gamma M}$	$[K_2^{(3)}]$	Q_c
$1a$	0	0	0
$2b\|_{\pi}$	0	-4	4/3
$2b\|_{\pm\frac{\pi}{3}}$	0	2	4/3
$3c$	1	0	1

Table 8: EBRs with C_6 symmetry induced from the maximal Wyckoff positions listed in the first column (see Fig. 41 (d)), and their invariants. All atomic limits can be decomposed into EBRs formed by at most three Kramers pairs.

We show in Section C of the Appendix how the symmetry indicator invariants for different EBRs can be derived. The (nested) Wilson loop invariants can be obtained by the mapping of Wilson loop spectra to the Wannier centers [235].

4.6 FORMULAS FOR CORNER CHARGES

In this Section, we provide explicit formulas for the corner charge in terms of the topological invariants as evaluated on the entire occupied subspace of a given model. For systems with $\mathcal{I}$, C_3, and $C_3 + \mathcal{I}$ symmetry, we can uniquely identify the spinless limit of a given spinful model.

In this case we can employ the results of Ref. [253]. In the remaining cases we deduce the formulas from the EBR tables given in Section 4.5. Importantly, all corner charges appearing in these formulas as well as in the EBR tables apply only to crystal terminations where Λ_F in Eq. (121) has corners at the intersection of 1D edges that are obtained from translating unit cells with crystal lattice vectors [253], but not necessarily primitive ones.

As noted before, in the case where we only have C_4 symmetry at our disposal, no corner charge formula can be constructed from our invariants. We leave the investigation of this symmetry class and instead consider the case of $C_4 + \mathcal{I}$ symmetry here.

4.6.1 *Inversion symmetry*

Inversion symmetry becomes equal to C_2 symmetry in the spinless case. This means that, using inversion eigenvalues, we can uniquely read off the C_2 eigenvalues of the spinless version of any model at hand, and may then use the formula presented in Ref. [253] for spinless C_2 symmetry to infer the corner charge of our model. Note that the doubling of the corner charge, which comes with going from spinless to spinful and imposing TRS, is automatically taken into account by the fact that the inversion eigenvalues are equal for Kramers partners. We therefore obtain

$$Q_c = \frac{1}{4}\left([X_2^{\mathcal{I}}] + [Y_2^{\mathcal{I}}] - [M_2^{\mathcal{I}}]\right) \mod 2. \tag{164}$$

A non-zero value implies two equal fractional corner charges at $\mathcal{I}$-related sectors with $Q_c = 1$.

4.6.2 *C_2 symmetry*

Comparing with Table 5, we have

$$Q_c = \nu_x^{\pi}, \tag{165}$$

where, if $H_{W_x}(k_y = 0, \pi)$ does not have pinned bands at eigenvalue π, we declare $\nu_x^{\pi} = 0$. We note that ν_x^{π} is $\mathbb{Z}_2$ valued, in accordance with the fact that two Wannier-Kramers pairs at $1b$ are trivial in that they can be removed from $1b$ and moved around the unit cell in a C_2 symmetric fashion. A non-zero value of $Q_c = 1$ implies two equal fractional corner charges at C_2-related sectors.

4.6.3 *C_3 symmetry*

There is a one-to-one mapping between the C_3 eigenvalues of the spinless and spinful cases (consult Appendix B.4). It implies that

$$Q_c = \frac{2}{3}\left([K_1^{(3)}] + [K_2^{(3)}]\right) \mod 2. \tag{166}$$

A non-zero value implies three equal fractional corner charges at C_3-related corners, with possibilities $Q_c = \frac{2}{3}$ or $Q_c = \frac{4}{3}$.

4.6.4 C_3 + *inversion symmetry*

The one-to-one mapping of C_3 eigenvalues from Appendix B.4, as well the observation that inversion symmetry becomes the same as C_2 symmetry in the spinless case, yields

$$Q_c = -\frac{1}{4}[M_2^{\mathcal{I}}] - \frac{1}{3}[K_2^{(3)}] \mod 2. \tag{167}$$

A non-zero value implies six equal fractional corner charges at $C_3, \mathcal{I}$-related corners, with possibilities $Q_c = \frac{1}{3}$, $Q_c = \frac{2}{3}$, $Q_c = 1$, $Q_c = \frac{4}{3}$, or $Q_c = \frac{5}{3}$.

4.6.5 C_4 + *inversion symmetry*

While $\mathcal{I}$ symmetry only allows for the decomposition of the sample into two halves, and therefore for a corner charge quantized in units of $1 \mod 2$, C_4 symmetry affords a further halving, so that the corner charge is quantized in units of $1/2 \mod 2$. Any $\mathcal{I}$ protected corner charge can in this way be split up into two $C_4 + \mathcal{I}$ protected corner charges of half the size. Using Eq. (164), we therefore obtain

$$Q_c = \frac{[X_2^{\mathcal{I}}]}{4} - \frac{[M_2^{\mathcal{I}}]}{8} \mod 2, \tag{168}$$

which we simplified by the C_4 constraint $[X_2^{\mathcal{I}}] = [Y_2^{\mathcal{I}}]$. A non-zero value of Q_c implies four equal fractional corner charges at C_4-related corners (this configuration is automatically $\mathcal{I}$ symmetric), with possibilities $Q_c = \frac{1}{2}$, $Q_c = 1$, $Q_c = \frac{3}{2}$.

4.6.6 C_6 *symmetry*

Comparing with Table 8, we have

$$Q_c = \mu_{\Gamma\mathbf{M}} - \frac{1}{3}[K_2^{(3)}] \mod 2, \tag{169}$$

where $\mu_{\Gamma\mathbf{M}}$ denotes the parity of the number of $W_{\Gamma\mathbf{M}}$ zero eigenvalue pairs. A non-zero value implies six equal fractional corner charges at C_6-related corners, with possibilities $Q_c = \frac{1}{3}$, $Q_c = \frac{2}{3}$, $Q_c = 1$, $Q_c = \frac{4}{3}$, or $Q_c = \frac{5}{3}$.

4.6.7 *Summary and classification of the layer groups*

To sum up, we collect the obtained formulas for corner charges and present them in Table 9. We can then apply our results and classify the 80 layer groups labeled in Ref. [284]. First, we drop all layer groups that involve non-symmorphic symmetries, since these are broken by any finite geometry with corners. Then we acknowledge that in some groups, only a subgroup is responsible for quantizing corner charges to fractional values, while the remaining symmetry operations at most pose constraints on the sample geometry and corner charge localization. The corner charge classification of these groups is therefore already determined by a minimal

set S of layer groups that covers all possible ways of enforcing quantization. This set and its classification are given by Table 13 at the end of this Chapter.

$\mathcal{S}$	Q_c
$\mathcal{I}$	$\frac{1}{4}\left([X_2^{\mathcal{I}}]+[Y_2^{\mathcal{I}}]-[M_2^{\mathcal{I}}]\right)$
C_2	ν_x^{π}
C_3	$\frac{2}{3}([K_1^{(3)}]+[K_2^{(3)}])$
$C_3+\mathcal{I}$	$-\frac{1}{4}[M_2^{\mathcal{I}}]-\frac{1}{3}[K_2^{(3)}]$
$C_4+\mathcal{I}$	$\frac{[X_2^{\mathcal{I}}]}{4}-\frac{[M_2^{\mathcal{I}}]}{8}$
C_6	$\mu_{\Gamma\mathrm{M}}-\frac{1}{3}[K_2^{(3)}]$

Table 9: Summary of corner charge formulas.

4.7 MATERIAL CANDIDATES

We propose the group-V buckled honeycomb monolayers of elemental antimony (Sb) and arsenic (As) as material realizations of protected fractional corner charges[5]. Free-standing monolayers with non-zero buckling d_z have a three-fold rotational symmetry C_3 as well as inversion $\mathcal{I}$ symmetry (consult Fig. 44 (d)). In practice, we consider weak substrate coupling so that the inversion symmetry is approximately retained. Applying strain leads to a decreasing d_z parameter up to a fully flat structure with six-fold symmetry. In Figs. 44 (a), (b) and (c), we present the band gap evolution of Bi, Sb and As as a function of tensile strain, which is modeled by a modification to the in-plane lattice parameter (larger strain corresponds to a longer in-plane distance between atoms). First, we note the qualitative similarity of the phase diagrams for all three investigated materials. At $d_z = 0$ (which corresponds to a large strain around $\sim 25\%$), there is an additional mirror symmetry M_z, and all structures are in an topological crystalline insulating phase, protected by a mirror Chern number, which we verified in addition by Wilson loop calculations (not shown here). This phase does not have exponentially localized Wannier functions that respect all symmetries of the model.

A small buckling breaks the mirror symmetry and then materials realize an OAL with localized Wannier orbitals centered at the center of the hexagons in the honeycomb lattice (Wyckoff position $1a$ of the crystal). Upon further decreasing strain, a transition to a $\mathbb{Z}_2$ topological insulator (TI) is observed via a band gap closing around $d_z = 0.6$ Å. To confirm this topological phase transition, we compute the $\mathbb{Z}_2$ topological index Δ_{TI} given by the Fu-Kane formula [144] and obtain $\Delta_{\mathrm{TI}} = 1$. As strain decreases further, another band gap closing occurs. Here, the Bi monolayer reenters a TI phase (with different symmetry indicator invariants as shown in Table 10), as confirmed by the $\mathbb{Z}_2$ index remaining non-trivial. In contrast, the almost fully buckled Sb and As monolayers enter once again in an OAL phase, this time with bands induced from the Wyckoff positions $3c$ (which is located on the bonds of the hexagon, see Fig. 41 (d)). Hence, our results reveal more details on the previously investigated strain-induced topological phase transitions in these materials [215, 285, 286].

Let us consider the systems with open boundary conditions. To establish the presence of corner charges, we perform open flake calculations for distinct OALs. We firstly investigated

5 Recently, an atomically thin carbon allotrope called graphdiyne was also predicted to host quantized corner charges [255, 254].

finite structures by employing the same tight-binding model as defined in Chapter 3 (consult Eq. (110) therein). Then, we performed refined calculations using the localized basis DFT method SIESTA [287]. We point out that the results are qualitatively the same and first-principle calculations allow for a better quantitative agreement with experimental reports. In Fig. 44 (e, f), we show results for a fully buckled antimony flake as a representative of the 3*c* OAL. The most direct indicator of fractional corner charges are corner-localized midgap states. If present, they are expected to appear close to the Fermi level. However, they are not necessarily well-separated from the bulk or edge modes. Therefore, we passivate the structure with tellurium atoms (marked with stars in Fig. 44 (f)) in order to remove spurious dangling edge states from the bulk gap. The energy spectrum (see Fig. 44 (e)) then exhibits 12 exactly degenerate corner states at the Fermi level, with only half of them filled. We thus obtain a fractional corner charge of $Q_c = 1 \mod 2$ per corner, realizing a filling anomaly [253].

We confirm this corner charge using the topological indices developed in Section 4.3. In Table 10, we evaluate the symmetry indicators for all discussed phases. We may then compute the corner charge of the 3*c* OAL on a hexagonal flake using Eq. (167). The relevant unit cell is the hexagonal cell, shown in Fig. 41 (d), which contains three primitive unit cells of the honeycomb lattice [space group 164 ($P\bar{3}m1$)]. The symmetry indicators in Table 10 are given for the primitive unit cell. To obtain the corresponding indicators for the hexagonal cell, we note that an enlargement of the unit cell results in a BZ folding, where the K and K' points are mapped onto Γ, while the M, M' and M'' points are left unchanged. Referring to Table 10, this implies $\chi_{\mathcal{I}}^{(3)} = (4, 0)$ for the hexagonal cell, from which we obtain $Q_c = 1 \mod 2$ by Eq. (167). This is in agreement with the numerical results presented in Figs. 44 (e) and (f).

Correspondingly, in the case of the 1*a* OAL, we obtain $\chi_{\mathcal{I}}^{(3)} = (0, 0)$ for the hexagonal cell (the primitive cell cannot be used to build a C_3-symmetric finite geometry). We conclude that there are no fractional charges. This is a case in point: although the 1*a* atomic limit is obstructed, in the sense that the electrons are localized away from the atomic sites, which are located at the 2*b* Wyckoff position of the crystal, there are no protected corner charges[6].

phase	$\#\Gamma_2^{\mathcal{I}}$	$\#M_2^{\mathcal{I}}$	$[M_2^{\mathcal{I}}]$	$\#\Gamma_2^{(3)}$	$\#K_2^{(3)}$	$[K_2^{(3)}]$	$\chi_{\mathcal{I}}^{(3)} = ([M_2^{\mathcal{I}}], [K_2^{(3)}])$	Δ_{TI}
TI 1	4	6	2	0	4	4	(2, 4)	1
TI 2	4	6	2	2	4	2	(2, 2)	1
3*c* OAL	2	6	4	2	4	2	(4, 2)	0
1*a* OAL	4	4	0	2	4	2	(0, 2)	0

Table 10: Topological invariants and symmetry indicators $\chi_{\mathcal{I}}^{(3)}$ corresponding to different regions in the phase diagrams: The symmetry indicators were calculated using the primitive 2-site unit cell of the honeycomb lattice (see Table 11 for a decomposition in terms of elementary band representations). The indices $\chi_{\mathcal{I}}^{(3)}$ allow for a more refined classification even of the strong TIs. We find that the 3*c* and 1*a* OALs differ in their inversion indicator $[M_2^{\mathcal{I}}]$ and thus, as explained in the main text, inversion-symmetric flakes built from their hexagonal unit cells differ by a protected corner charge equal to $1 \mod 2$.

6 There may however be such charges in C_3-symmetric geometries that are terminated by cutting through unit cells. We do not consider these geometries here, mainly because there is no bulk-boundary correspondence in this case, and the actual corner charge is dependent on how the boundary unit cells are cut.

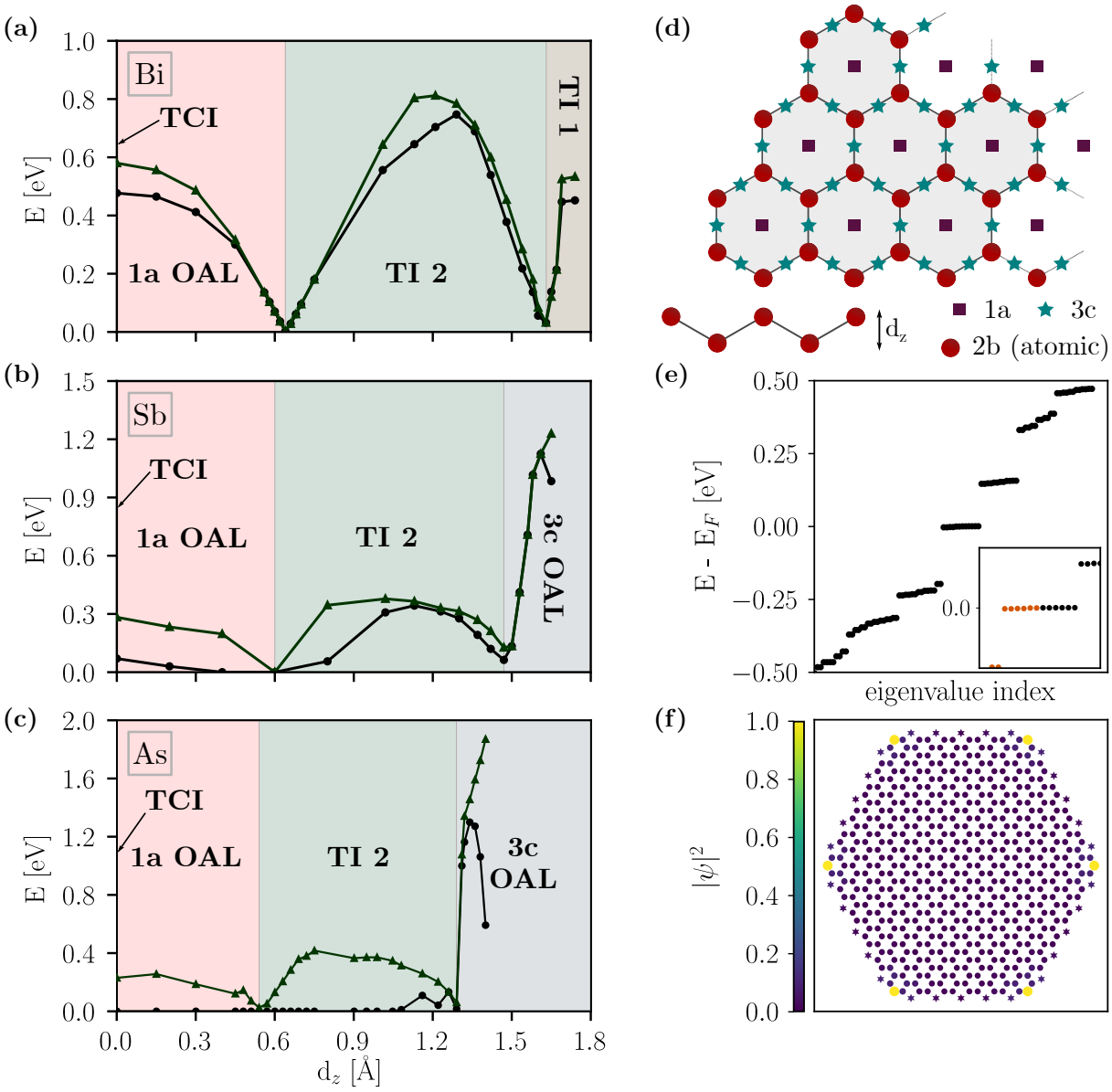

Figure 44: Energy gap as a function of the buckling parameter d_z for **(a)** bismuth, **(b)** antimony and **(c)** arsenic monolayers. The black line (circles) indicates the indirect gap, while the green line (triangles) indicates the direct gap. Top and side views of the lattice structure are illustrated in **(d)**, together with the Wyckoff positions of the space group 164. **(e)** Low-energy spectrum of a finite armchair-terminated flake of the 3*c* OAL. The inset presents the energies around the Fermi level, with filled states in orange. **(f)** The electronic densities of the corner states with color scale proportional to the normalized square modulus $|\psi_i|^2$ of the eigenstates (normalized with respect to the largest $|\psi_i|^2$). The tellurium atoms used for edge passivation are shown as stars.

We present the band representations of the space groups 164 ($P\bar{3}m1$) and 191 ($P6/mmm$) relevant for discussed materials. To deduce Wyckoff positions from which EBRs can be induced, we use data collected from the Bilbao Crystallographic Server [284, 288, 147, 289]. Note that we discard Wyckoff positions with non-zero z-component as they are irrelevant for a 2D geometry. The irreducible representations of bands at high-symmetry points were obtained using the `irrep` code [290, 291], which relies on the double space group character tables [292] published on the Bilbao Crystallographic server [293].

SG	phase	band representation	EBRs
164	TI 1	$(3\bar{\Gamma}_8 \oplus 2\bar{\Gamma}_9, 2\bar{M}_3\bar{M}_4 \oplus 3\bar{M}_5\bar{M}_6, 2\bar{K}_4\bar{K}_5 \oplus 3\bar{K}_6)$	–
164	TI 2	$(2\bar{\Gamma}_8 \oplus 2\bar{\Gamma}_9 \oplus \bar{\Gamma}_4\bar{\Gamma}_5, 2\bar{M}_3\bar{M}_4 \oplus 3\bar{M}_5\bar{M}_6, 2\bar{K}_4\bar{K}_5 \oplus 3\bar{K}_6)$	–
164	$3c$ OAL	$(3\bar{\Gamma}_8 \oplus \bar{\Gamma}_9 \oplus \bar{\Gamma}_4\bar{\Gamma}_5, 2\bar{M}_3\bar{M}_4 \oplus 3\bar{M}_5\bar{M}_6, 2\bar{K}_4\bar{K}_5 \oplus 3\bar{K}_6)$	$\bar{E}_1(2d) \oplus {}^1\bar{E}_g^2\bar{E}_g(3c)$
164	$1a$ OAL	$(2\bar{\Gamma}_8 \oplus 2\bar{\Gamma}_9 \oplus \bar{\Gamma}_4\bar{\Gamma}_5, 3\bar{M}_3\bar{M}_4 \oplus 2\bar{M}_5\bar{M}_6, 2\bar{K}_4\bar{K}_5 \oplus 3\bar{K}_6)$	$\bar{E}_{1g}(1a) \oplus \bar{E}_{1u}(1a) \oplus \bar{E}_1(2d) \oplus {}^1\bar{E}_g^2\bar{E}_g(1a)$
191	TCI	$(\bar{\Gamma}_7 \oplus \bar{\Gamma}_8 \oplus \bar{\Gamma}_9 \oplus \bar{\Gamma}_{11} \oplus \bar{\Gamma}_{12}, 3\bar{M}_5 \oplus 2\bar{M}_6, 2\bar{K}_7 \oplus \bar{K}_8 \oplus 2\bar{K}_9)$	–

Table 11: Band representations corresponding to distinct phases as shown in Fig. 44. '–' indicates that a given band representation cannot be written as a combination of EBRs.

4.7.1 *Details on ab-initio calculations*

Fully relativistic DFT calculations were performed via the Vienna *ab initio* simulation package (VASP) [294, 295] by employing the Perdew-Burke-Ernzerhof (PBE) [296, 297] exchange-correlation functional and projected augmented-wave pseudopotentials [298, 299]. For the self-consistent calculations, we used a $19 \times 19 \times 1$ $\mathbf{k}$ point grid generated for the Monkhorst-Pack method in case of Bi and Sb, and a $17 \times 17 \times 1$ mesh for As. The plane wave basis cutoff was set to 400 eV (Bi and Sb) or 350 eV (As). A finer grid of $30 \times 30 \times 1$ $\mathbf{k}$ points was used later on in order to obtain the energy gaps and band representations. The lattice parameters in the equilibrium configuration, which are in good agreement with previous reports [300–302], are summarized in Table 12.

	Bi	Sb	As
a [Å]	4.39	4.04	3.61
d_z [Å]	1.74	1.65	1.40

Table 12: Lattice constant and buckling parameter for the unstrained (free-standing) buckled structures.

For open flake calculations, we employed the Siesta code [287]. We used pseudo-atomic orbitals (PAO) with a basis of double zeta plus polarization orbitals (DZP) and norm-conserving fully relativistic pseudopotentials from the PseudoDojo library [303]. The bulk crystal structure was terminated to obtain a hexagonal structure of 546 Sb atoms, and 30 Te atoms were added

to the edges in order to passivate the edge states (as shown in Fig. 44 (f)). The distance between Te and edge Sb atoms was set to a value 3.02 Å, which was determined from the structure relaxation of an armchair Sb ribbon with Te adatoms at the edge. The DFT data post-processing was performed with the `sisl` Python package [304].

group	generators	classification	Q_c mod 2	same classification
1	-	$\mathbb{Z}_1$	$\{0\}$	4, 5, 8, 9, 10, 11, 12, 13, 27, 28, 29, 30, 31, 32, 33, 34, 35, 36
2	I	$\mathbb{Z}_2$	$\{0,1\}$	7, 14, 15, 16, 17, 18, 39, 43, 44, 45, 46, 52, 62, 64
3	C_2^z	$\mathbb{Z}_2$	$\{0,1\}$	19, 20, 21, 24, 25
6	I, C_2^z	$\mathbb{Z}_2$	$\{0,1\}$	40
22	C_2^x, C_2^y	$\mathbb{Z}_2$	$\{0,1\}$	
23	$\mathcal{M}_x, \mathcal{M}_y$	$\mathbb{Z}_2$	$\{0,1\}$	26
37	$\mathcal{M}_x, \mathcal{M}_y, M_z$	$\mathbb{Z}_2$	$\{0,1\}$	47
38	$\mathcal{M}_x, I$	$\mathbb{Z}_2$	$\{0,1\}$	41, 42, 48
49	C_4^z	$\mathbb{Z}_4$	$\{0,1/2,1,3/2\}$	52, 54, 56
50	$C_4^z I$	$\mathbb{Z}_4$	$\{0,1/2,1,3/2\}$	58, 60
51	C_4^z, I	$\mathbb{Z}_4$	$\{0,1/2,1,3/2\}$	63
53	C_4^z, C_2^x, C_2^y	$\mathbb{Z}_4$	$\{0,1/2,1,3/2\}$	62
55	$C_4^z, \mathcal{M}_x, \mathcal{M}_y$	$\mathbb{Z}_4$	$\{0,1/2,1,3/2\}$	64
57	$C_4^z I, C_2^x, C_2^y$	$\mathbb{Z}_4$	$\{0,1/2,1,3/2\}$	
59	$C_4^z I, \mathcal{M}_x, \mathcal{M}_y$	$\mathbb{Z}_4$	$\{0,1/2,1,3/2\}$	
61	C_4^z, I, C_2^x, C_2^y	$\mathbb{Z}_4$	$\{0,1/2,1,3/2\}$	
65	C_3^z	$\mathbb{Z}_3$	$\{0,2/3,4/3\}$	
67	C_3^z, C_2^x	$\mathbb{Z}_3$	$\{0,2/3,4/3\}$	68
69	$C_3^z, \mathcal{M}_x$	$\mathbb{Z}_3$	$\{0,2/3,4/3\}$	70
71	$C_3^z, \mathcal{M}_x, I$	$\mathbb{Z}_6$	$\{0,1/3,2/3,1,4/3,5/3\}$	72
73	C_6^z	$\mathbb{Z}_6$	$\{0,1/3,2/3,1,4/3,5/3\}$	
74	$C_6^z I$	$\mathbb{Z}_6$	$\{0,1/3,2/3,1,4/3,5/3\}$	
75	C_6^z, I	$\mathbb{Z}_6$	$\{0,1/3,2/3,1,4/3,5/3\}$	
76	C_6^z, C_2^x	$\mathbb{Z}_6$	$\{0,1/3,2/3,1,4/3,5/3\}$	
77	$C_6^z, \mathcal{M}_x$	$\mathbb{Z}_6$	$\{0,1/3,2/3,1,4/3,5/3\}$	
78	$C_6^z I, \mathcal{M}_x$	$\mathbb{Z}_6$	$\{0,1/3,2/3,1,4/3,5/3\}$	79
80	$C_6^z, I, \mathcal{M}_x$	$\mathbb{Z}_6$	$\{0,1/3,2/3,1,4/3,5/3\}$	

Table 13: Corner charge classification and topological indices of S. The boundary classification of any layer group l is given by that of the group $s \in S$, where s is the largest possible subgroup of l contained in S. In the case where l contains non-symmorphic operations, its classification is the same as that of the layer group l' that consists of the symmorphic part of l.

Part III:

THE INTERPLAY BETWEEN TOPOLOGY AND NON-HERMITICITY

5

TOPOLOGY IN NON-HERMITIAN SYSTEMS

Almost all axioms of quantum mechanics are rooted in fundamental physical requirements. For instance, the time evolution of a quantum system has to be governed by a unitary operator $e^{-\mathrm{i}Ht}$, because it conserves probability. Conjointly, the energy spectra have to be bounded from below, which means that a stable lowest-energy state exists, and has to be real-valued as they correspond to the possible outcomes of a measurement. These prerequisites are instantaneously fulfilled by assuming that the Hamiltonian H describing the dynamics of a system is Hermitian, i. e. equal to its adjoint, $H = H^\dagger$. However, Bender and Boettcher [305] pointed out that Hermiticity is a sufficient, but not a *necessary* condition that guarantees the eigenvalues to be real. It can actually be relaxed to a weaker condition, where the combined action of the parity $\mathcal{P}$ and the time-reversal $\mathcal{T}$ operators, $[H, \mathcal{PT}] = 0$[1], constrains the realness of the energies.

$\mathcal{PT}$-symmetric systems can be regarded as systems that interact diffusively with the environment as their potential energy is often complex. A potential with a positive imaginary part characterizes a system which gains energy from its environment. Conversely, a potential with a negative imaginary part corresponds to a system losing energy. In the presence of the $\mathcal{PT}$-symmetry, gain and loss are balanced and the system can reach an equilibrium state [306]. This initial proposal of $\mathcal{PT}$-symmetric systems was firstly extended to the field of optics [307–309], where one can straightforwardly realize the $\mathcal{PT}$-symmetry condition by coupling two identical waveguides, one with gain and the other with the equal amount of loss. Then, the $\mathcal{P}$-symmetry interchanges the subsystems, while the $\mathcal{T}$-symmetry swaps between gain and loss. In parallel, $\mathcal{PT}$-symmetry has been exploited in other experimental setups, including electronics [310] or metamaterials [311, 312].

$\mathcal{PT}$-symmetric Hamiltonians can be thought as a special class of the general non-Hermitian (nH) formalism in which the physics of open systems, i. e. systems that do not conserve energy or particle number, is captured at an *effective* level. The concept of non-Hermitian effective Hamiltonians dates back to the studies on alpha decay [313]. It was shown that a particle may escape the nucleus at a tunnelling rate given by its complex-valued eigenenergies with the real (imaginary) part of these energies being associated with the levels (widths) of the nuclear resonances. Later on, complex, non-Hermitian potentials were introduced to describe the scattering between nuclei and neutrons [314]. These approaches, though, are rather phenomenological than fully mathematically justified. A more careful treatment of dissipative systems coupled to the environment can be for instance based on Lindblad master equations [315], originally introduced in the context of quantum optics and spin systems. Assuming an open system to be described by a density matrix ρ, the non-unitary (but Markovian) time evolution of ρ is then given by the equation $\dot{\rho} = -\mathrm{i}[H, \rho] + \sum_\mu (2L_\mu \rho L_\mu^\dagger -$

1 Suppose the Hamiltonian H is expressed in terms of the position $\mathbf{x}$ and momentum $\mathbf{p} = -\mathrm{i}\nabla$ operators, $H = \mathbf{p}^2 + V(\mathbf{x})$, where $V(\mathbf{x})$ is a potential energy. The space reflection operator $\mathcal{P}$ flips the sign of the $\mathbf{x}$ and $\mathbf{p}$ operators, $\mathcal{P} : \mathbf{x} \to -\mathbf{x}$, $\mathbf{p} \to -\mathbf{p}$, while the time-reversal operator $\mathcal{T} : \mathbf{x} \to \mathbf{x}$, $\mathbf{p} \to -\mathbf{p}$, $\mathrm{i} \to -\mathrm{i}$. If the Hamiltonian has to be $\mathcal{PT}$-symmetric, then the potential $V(\mathbf{x})$ satisfies $\mathcal{PT}V(\mathbf{x})\mathcal{TP} = V^*(-\mathbf{x}) = V(\mathbf{x})$. This condition implies that $V(\mathbf{x})$ is in general a complex function where the real part is an even function and the imaginary is an odd function of $\mathbf{x}$.

$\{L_\mu^\dagger L_\mu, \rho\}) = \mathcal{L}[\rho]$ with $\mathcal{L}[\rho]$ as a superoperator called Lindbladian[2] [316]. H is a Hermitian Hamiltonian generating unitary dynamics, L_μ denotes the Lindblad operators (loss channels such as spin flips due to the coupling to the environment) and each $L_\mu \rho L_\mu^\dagger$ term induces a quantum jump. The short-time evolution (before the occurrence of a quantum jump) can be then written as $\dot{\rho} = -\mathrm{i}\,(H_{\mathrm{eff}}\rho - \rho H_{\mathrm{eff}}^\dagger)$ with the effective non-Hermitian Hamiltonian $H_{\mathrm{eff}} = H - \mathrm{i}\sum_\mu L_\mu^\dagger L_\mu$. Other powerful methods, such as the idea of Feynman and Vernon [317] explaining the effects of an environment on the system in terms of an influence functional or with Keldysh diagrammatic technique [318], are also widely employed. However, the high complexity of aforementioned tools usually reduces their applicability and non-Hermitian effective Hamiltonians can then serve as a simple, macroscopic description.

It is only recently that the interplay between non-Hermiticity and topology has received immense interest. Topological phases supported by non-Hermitian Hamiltonians yields qualitatively novel phenomena [319, 320], such as the occurrence of stable defective degeneracy points called exceptional points [321, 322]. In two-dimensional systems [43], these exceptional points can be connected by bulk Fermi arcs [323], which are usually only observed in 3D Weyl semimetals. Another exotic feature resolved through the band theory description of open systems is the non-Hermitian skin effect [324], where *all* of the eigenstates of a one-dimensional system can localize at one of its boundaries. The skin effect is a manifestation of the breakdown of bulk-boundary correspondence, a core principle of topological band theory in closed systems [325–328]. The non-Hermitian skin effect has been discussed in one-dimensional systems, and was initially assumed to require a non-reciprocal Bloch Hamiltonian usually realized through asymmetric, direction-dependent hoppings. Reciprocal versions of the one-dimensional skin effect can be constructed by introducing additional degrees of freedom. Their protection against hybridization is realized by demanding additional symmetries such as mirror symmetry [329, 330]. In this work, we present a generalized skin effect in reciprocal systems, that is enabled by non-Hermiticity in dimensions higher than one. For simplicity, we constrain ourselves to two spatial dimensions. The basic idea is that, while a reciprocal model cannot localize all of its OBC eigenstates at just one boundary, it may still do so for states of a particular boundary momentum. Reciprocity then implies that eigenstates at opposite momenta are localized at opposite boundaries.

The reciprocal skin effect dramatically expands the scenarios in which anomalous extensive skin mode localization [327] can be found in nature. As a paradigmatic experimental realization within a framework of high accessibility and tunability, we implement the reciprocal skin effect within a topolectrical circuit setup. Similar to many other classical platforms of synthetic topological matter, this roots in the insight that phenomena related to the Berry phase [61, 273] can be also observed in classical physics [331], since they do not concern phase space, but parameter space. The realization of topological phases in photonic [332], mechanical [333, 334] and electrical systems [335–341, 338, 342–344] demonstrates this connection between topological aspects of quantum and classical systems. The non-Hermitian band theory of open quantum systems can similarly be mirrored by classical systems that involve gain and loss. Electric circuits whose circuit Laplacian [338] is modeled in analogy to a quantum Bloch Hamiltonian are particularly suited for this: loss and gain can be directly implemented by resistors and active circuit elements [340], respectively, while Hermitian hybridization elements

2 A superoperator is a map acting on operators. Here, the superoperator $\mathcal{L}$ connects the initial density matrix to the time-evolved one, $\rho(t) = \rho(0) + \int_0^t \mathcal{L}(\rho(t'))dt'$. $\mathcal{L}$ has to be positive, linear, and preserve trace and Hermiticity.

are realized by inductive and capacitive links between circuit nodes. We design, describe, and measure [345] a non-Hermitian topolectrical circuit that displays, among exceptional points, the reciprocal skin effect, and is built entirely from capacitors, inductors, and resistors, *without* the need for non-reciprocal active elements such as operational amplifiers. Being a passive circuit network, its convenient translation into alternative platforms of synthetic topological matter promises ubiquitous realizations and applications in optics, mechanics, and acoustics. The structure of this Chapter is following: in Section 5.1, we introduce the basic notions underlying the non-Hermitian band theory and present in more detail the unique non-Hermitian phenomena, without any Hermitian counterparts. We then move to discussing the quantum lattice π-flux model in Section 5.2 and show how the novel features arise due to the additional non-Hermitian terms. Finally, Section 5.3 presents a connection between the model within tight-binding approximation and a circuit Laplacian used for designing the topolectical circuit, together with the experimental results.

5.1 NON-HERMITIAN TOPOLOGICAL BAND THEORY

Non-Hermiticity has a profound effect on topological band theory. Some nH topological systems can be regarded as generalizations of well-studied topological phases, both gapped and gapless, described by Hermitian Hamiltonians. Examples include nH extensions of Chern insulators [43, 346], Weyl semimetals [347], Floquet systems [348, 349] or higher-order TIs [350–352]. But more importantly, nH topological systems exhibit novel phenomena which are not observed in the Hermitian limit. The goal of this Section is to bring up the essential notions required to define band topology in nH Hamiltonians, which are often differently formulated than in Hermitian systems. In particular, non-Hermiticity enriches the standard ten-fold classification as new types of symmetries arise. On that line, we continue with discussing the exceptional structures - spectral degeneracies associated with a Hamiltonian defectiveness that solely origin from the non-Hermiticity. The lack of a complete basis set affects the eigenstate localization properties and, in general, allows to pile up all states at the same edge of a system. Finally, the sensitivity of the eigenstates of nH Hamiltonians to the boundary conditions leads to the revision of the bulk-boundary correspondence principle. For more information, we refer the reader to the excellent Refs. [353, 354].

5.1.1 *Complex energy gap and winding number*

As the eigenvalues of nH Hamiltonians are in general complex, the definition of the energy gap is no longer unique. Various extensions of this concept are possible, such as identifying the bands to be separable or inseparable [43][3] and the prohibition of touching a base energy E_B, which is typically set to zero [319]. The energies can be represented on the complex plane, where the real (imaginary) part of the energy corresponds to the x (y) axis (cf. Fig. 45). In the Hermitian case, the gapped spectrum lies in two segments on the real axis, separated by the

3 Consider a nH Hamiltonian with PBC, whose eigenstates are Bloch states with energies $E_n(\mathbf{k})$ depending on the crystal momentum $\mathbf{k}$ in the BZ. The n-th band is said to be *separable* if its energy $E_n(\mathbf{k}) \neq E_m(\mathbf{k})$ for all $m \neq n$ and $\mathbf{k}$. Then, the n-th band is *isolated* if $E_n(\mathbf{k}) \neq E_m(\mathbf{k}')$ for all $m \neq n$ and $\mathbf{k}$, $\mathbf{k}'$. If at some momentum $\mathbf{k}$ two or more complex energies are degenerate (so that they have the same real and imaginary parts), then a band is called *inseparable*. Definitions of separable, isolated and inseparable bands are corresponding, respectively, to gapped, fully gapped and gapless bands in Hermitian systems.

imaginary axis and never touching the base energy. Non-Hermitian systems, however, exhibit two type of gaps:

1. a *point* gap [319]. The eigenvalues may form loops in the complex energy plane and if the base energy E_B lies inside one of the loops, the loop cannot be deformed onto a point without touching the base. This is a genuinely nH case, without any Hermitian equivalent.

2. a *line* gap [42, 328] is defined by a line in the complex energy plane, which separates the energy bands. Hermitian systems follow naturally this definition, and nH line-gapped systems share some similarities with Hermitian systems. Models with a line gap always have a point gap.

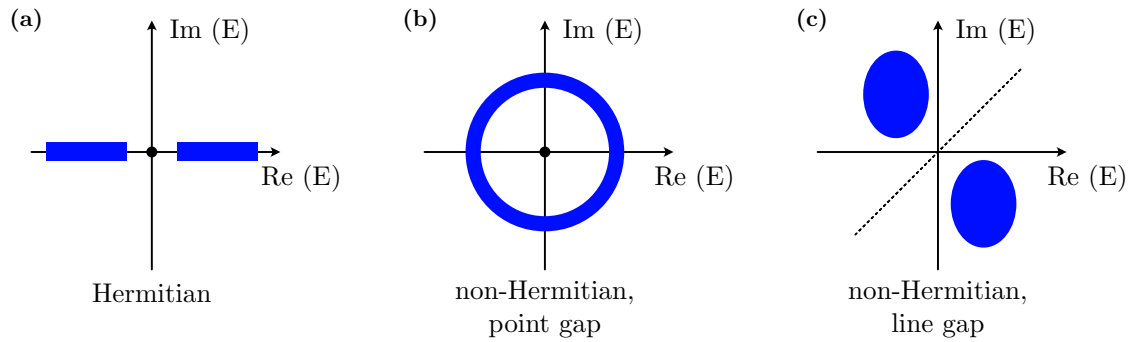

Figure 45: Schematic representation of an energy gap in Hermitian and non-Hermitian Hamiltonians. **(a)** For Hermitian systems, all energies are represented on the real axis and separated by a gap with the Fermi energy denoted by a black dot. In the non-Hermitian case, the energies can be either separated by **(b)** a point gap or **(c)** a line gap.

In Hermitian systems, a minimal model that can exhibit non-trivial topology has to have at least two bands as the total Berry curvature summed over all bands must be zero. Moreover, topological states are absent in $1D$ systems without enforcing symmetries [79, 28]. A hallmark of nH systems is that they can posses some topological features even within a single band. For the one-dimensional nH Bloch Hamiltonian $\mathcal{H}(k)$ with a point gap spectrum, it is possible to define the winding number [330] (also called vorticity [43])

$$W = \frac{1}{2\pi \mathrm{i}} \int_0^{2\pi} dk\, \partial_k \log\left[\det(\mathcal{H}(k) - E_B\, \mathbb{1})\right], \tag{170}$$

which measures the number of times the complex eigenenergies encircle E_B. Remarkably, this winding number refers only to *eigenvalues*, not eigenvectors, and takes integer values. To illustrate the non-zero winding in a minimal setup, let us consider the Hatano-Nelson model [355] with asymmetric hoppings J_R, $J_L \in \mathbb{R}$

$$H = \sum_i (J_R\, c_{i+1}^\dagger c_i + J_L\, c_i^\dagger c_{i+1}), \tag{171}$$

which is non-Hermitian if $J_R \neq J_L^*$. In reciprocal space, the Bloch Hamiltonian has the energy spectrum $E(k) = (J_L + J_R)\cos(k) + \mathrm{i}(J_L - J_R)\sin(k)$. As it is a one-band model, we can replace $\det \mathcal{H}(k)$ term in Eq. (170) by $E(k)$. To compute the winding number W, we track how $E(k)$

winds around the base energy E_B (which we take here to be zero) with respect to k. When $|J_L|/|J_R| < 1$ (> 1), $E(k)$ winds (counter)-clockwise and results in a winding number -1 ($+1$). These two phases characterized by $W = \pm 1$ are separated by a topological phase transition at $|J_R| = |J_L|$, where the spectrum touches the base energy.

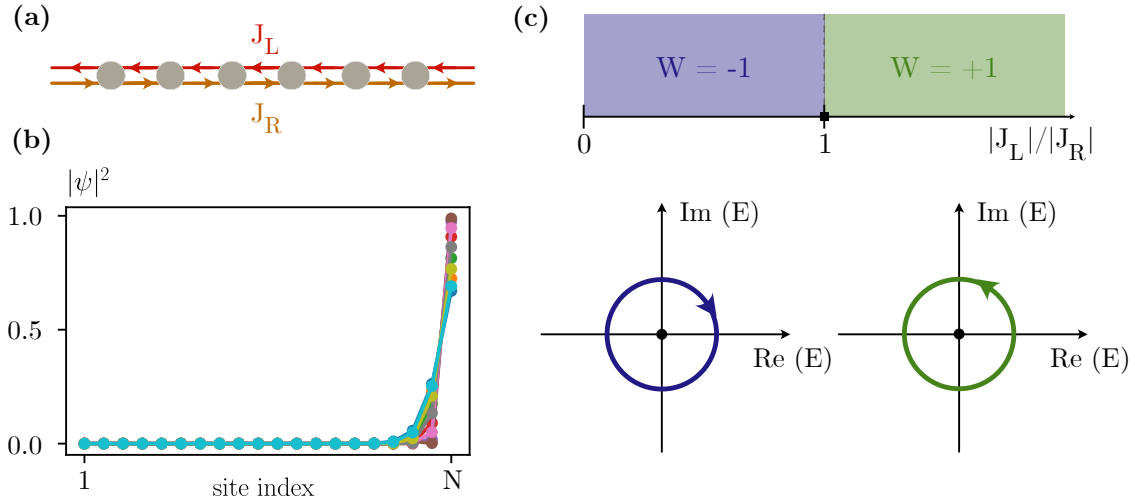

Figure 46: The Hatano-Nelson model. **(a)** Schematic depiction of a one-dimensional chain with asymmetric hoppings J_R (J_L) in the right (left) direction. **(b)** The Direction-dependent hopping terms induce an anomalous localization of all eigenstates at the edge in a system with open boundary conditions. Here, we set $|J_L|/|J_R| = 0.1$, which leads to the manifestation of the skin effect at the right boundary. **(c)** The phase diagram as a function of the ratio $|J_L|/|J_R|$. In the range $|J_L|/|J_R| \in [0, 1)$, the winding $W = -1$, while for $|J_L|/|J_R| > 1$, $W = 1$. At $|J_L|/|J_R| = 1$, the system undergoes a topological phase transition and all complex energies collapse along a single line crossing the origin. Below, we depict the spectral winding around the base energy. An arrow indicates the direction in which the energies wind as k increases, determining the sign of W.

In general, the spectral winding number W defined in Eq. (170) allows for a $\mathbb{Z}$ classification and does not require any symmetry. It is in a stark contrast to the winding number in the Hermitian case (discussed in the Chapter 1), which requires chiral symmetry.

5.1.2 *Biorthogonal quantum mechanics*

Topological invariants such as polarization or Wilson loop can be generalized to the non-Hermitian case by introducing the notion of biorthogonality, which is weaker than the orthogonality observed in the Hermitian limit. Biorthogonality establishes the relationship between the eigenstates of the operator and its self-adjoint. The eigenstates of an operator are not necessarily orthogonal to each other but they are orthogonal to the eigenstates of the self-adjoint of the operator. This is the core of biorthogonal quantum mechanics, which is valid as long as we have no exceptional points and reduces to the standard quantum mechanics in the Hermitian limit. For this part, we closely follow Ref. [356]. A generic nH-Hamiltonian H, decomposed into two Hermitian parts $H = H_1 - iH_2$ with $H_1 = H_1^\dagger$ and $H_2 = H_2^\dagger$, has distinct left $|\psi_L\rangle$ and right $|\psi_R\rangle$ eigenvectors satisfying

$$H|\psi_{R,i}\rangle = E_i|\psi_{R,i}\rangle\,, \quad \langle\psi_{L,i}|H = E_i\langle\psi_{L,i}| \Leftrightarrow H^\dagger|\psi_{L,i}\rangle = E_i^*|\psi_{L,i}\rangle\,. \tag{172}$$

In the Hermitian case, the left and right eigenvectors would be equal, $|\psi_{L,i}\rangle = |\psi_{R,i}\rangle$, and a set $\{|\psi_{R,i}\rangle\}$ would form an orthogonal basis. However, if the matrix is nH, the eigenstates are not necessarily orthogonal, i. e. the inner product $\langle\psi_{R,i}|\psi_{R,j}\rangle$ (and analogously for $|\psi_{L,i}\rangle$) is not zero for all eigenstates

$$\langle\psi_{R,i}|\psi_{R,j}\rangle = 2\,\frac{\langle\psi_{R,i}|H_1|\psi_{R,j}\rangle}{E_i^* - E_j} = 2\,\mathrm{i}\frac{\langle\psi_{R,i}|H_2|\psi_{R,j}\rangle}{E_i^* - E_j}, \quad i \neq j, \tag{173}$$

where $2\mathrm{i}H_2 = H^\dagger - H$ and $2H_1 = H^\dagger - H$. On the other hand, the basis sets $\{|\psi_L, i\rangle\}$ and $\{|\psi_R, i\rangle\}$ form a biorthogonal basis such that

$$\langle\psi_{L,i}|\psi_{R,j}\rangle = \delta_{ij}. \tag{174}$$

All the expectation values can be then expressed in terms of a biorthogonal basis, $\langle\psi_{L,i}|O|\psi_{R,i}\rangle$, for any operator O. Conventional Hermitian expressions for topological invariants can then be adapted by replacing the bra states by the left eigenstates and the ket states by the right eigenstates.

5.1.3 *Symmetry classification*

NH Hamiltonians are not longer equivalent to their self-adjoint representation, which allows for distinct combinations of symmetries generalizing the AZ classification. For instance, the particle-hole symmetry states that $\mathcal{P}H^*\mathcal{P}^{-1} = -H$. In the Hermitian case, complex conjugation coincides with transposition, $H^* = H^\mathrm{T}$, and therefore PHS can be also defined as $\mathcal{P}H^\mathrm{T}\mathcal{P}^{-1} = -H$. In nH systems, however, these two operations are no longer equivalent and the action of the particle-hole symmetry splits into two different symmetry conditions. A similar situation occurs for the chiral symmetry $\mathcal{C} = \mathcal{P}\mathcal{T}$, equivalent to the sublattice symmetry in Hermitian systems. In the absence of Hermiticity, $\mathcal{C}^{-1}H^\dagger\mathcal{C} \neq \mathcal{C}H\mathcal{C}^{-1}$. Therefore, non-Hermiticity enables the so-called pseudo-Hermiticity to be a new internal symmetry, defined as $\eta H^\dagger\eta^{-1} = H$ with $\eta^2 = 1$. In fact, η generalizes the notion of Hermiticity and play a role akin to the parity-time symmetry [357]. Exhausting all internal symmetries that may appear in nH systems extends the standard 10-fold symmetry classification to 38-fold classification[4] [42, 319, 43, 41, 359]. The topological classification incorporating both non-Hermiticity and the crystal symmetries is an active research direction, with recent developments including studies on symmetry-protected nodal phases [360] or nH systems with reflection symmetry [361].

4 A first attempt to classify non-Hermitian random matrices was firstly proposed by Bernard and LeClair [358], in which they recognized four fundamental classes of symmetries
- C symmetry: $cH^\mathrm{T}c^{-1} = \varepsilon_c H, \quad cc^* = \pm 1,$
- P symmetry: $pHp^{-1} = -H, \quad p^2 = 1,$
- Q symmetry: $qH^\dagger q^{-1} = H, \quad q^2 = 1,$
- K symmetry: $kH^*k^{-1} = H, \quad kk^* = \pm 1.$

Here, $\varepsilon_c = \pm 1$ and c, p, q and k are unitary operators. Overall, their considerations led to a 43-fold classification that was subsequently refined to 38 symmetry classes.

5.1.4 *Exceptional points*

Exceptional points (EPs) are singularities in parameter space at which the matrix becomes defective. As the eigenbasis becomes incomplete at these points, the matrix cannot be therefore diagonalized. Instead, it admits a Jordan normal form[5]. Suppose a Hamiltonian H takes the form $H = H_0 + \lambda H_1$, where H_0 and H_1 are generic Hermitian Hamiltonians, while λ serves as a parameter. If λ is real, then a change in λ leads to level repulsion and avoided crossings. However, allowing λ to be complex-valued may cause two or more eigenvalues and their corresponding eigenvectors to coalesce, i. e. the eigenstates become linearly dependent. This is different from the degeneracies occurring in Hermitian systems, where only eigenvalues are the same. The eigenvalue surface of a nH matrix then forms a self-intersecting Riemann sheet in which the EP is located at the point of intersection. Close to EPs, the shape of the energy surface is not analytical and therefore breaks the adiabatic theorem, which yields qualitatively different behavior of the system close to them. This includes numerous interesting phenomena such as topological energy transfer [362] or loss-induced transparency [363]. Higher-order EPs – the exceptional points where more than two eigenstates coalesce[6] – can be used for enhanced sensing [364].

To illustrate the exceptional points, consider a simple 2D nH Hamiltonian given by

$$H = k_1\sigma_1 + k_2\sigma_2 + \mathrm{i}r\sigma_2; \quad r \neq 0. \tag{175}$$

In analogy to Weyl points – generic degeneracies in 3D Hermitian systems – EPs cannot be removed by any small perturbations and may annihilate only when they are brought together. In Fig. 47 (b), we present the real and imaginary parts of the spectrum of the Hamiltonian in Eq. (175), where the parameter space is the momentum space (k_x, k_y). Encircling the EPs in parameter space gives rise to a geometric phase [365, 366], which can be captured by the winding number of the eigenvectors. In a two-band model, the eigenvectors of a Hamiltonian are $4\pi-$periodic as k evolves. After a single loop around an exceptional point, the two eigenvectors swap; in order to come back to the initial situation, an EP has to be encircled twice. Hence, the winding number takes a fractional value of $1/2$ [321].

5.1.5 *Breakdown of the bulk-boundary correspondence and the skin effect*

Bulk-boundary correspondence [58] allows for the prediction of universal boundary phenomena from the bulk properties and relies on the fact that changing boundary conditions does not affect the bulk states at large. However, in nH systems, opening the boundaries often leads to non-perturbative change in the energy spectrum, which obscures the bulk topology. It is accompanied by an anomalous localization of all eigenstates at a single boundary called the skin effect. With the Hatano-Nelson model given in Eq. (171) as example, we illustrate this effect in Fig. 46 (b). For $|J_R| > |J_L|$ ($|J_R| < |J_L|$), all states are (left-)right-localized.

5 A matrix in its Jordan form is block diagonal, with each block taken to be $\alpha\mathbb{1} + J$, with J the matrix with ones on the first superdiagonal and zero elsewhere. The α's are the eigenvalues of the matrix, and each block corresponds to a different eigenspace. A diagonalizable matrix is in fact a special case of a Jordan matrix, which has only one-dimensional blocks on the diagonal.

6 The $N-$th order exceptional point EP is formed by N coalescing eigenstates.

The topological origin of the skin effect has been recognized only recently [330, 367] and was associated with point gap topology. Several authors proposed restoration schemes to recover the relation between bulk and boundary degrees of freedom. Using the biorthogonal formalism, it is possible to introduce real-space invariants such as the biorthogonal polarization [326] or the Chern number [368], which correctly predict the presence of edge states. An alternative is to entirely shift the description of band topology in terms of a singular value decomposition[7] [369]. In this formulation, the issue with the sensitivity to boundary conditions and numerical instabilities is overcome by investigating the singular spectra. In addition, redefining the Bloch wave vector $\mathbf{k}$ to be complex-valued allows to construct the generalized Brillouin zone, which carries more information [324, 346, 370]. However, this formalism can break down at the criticality, where eigenenergies and eigenstates may exhibit a discontinuity across a critical point [371]. Experimental evidences of generalized bulk-boundary correspondence were observed, for instance, in discrete-time non-unitary quantum-walk dynamics of single photons [372] and active topolectrical circuits [373].

5.2 NON-HERMITIAN π-FLUX MODEL

We move to the π-flux model defined on a square lattice with a non-Hermitian extension, which exhibits the aforementioned intriguing features. To do so, let us firstly introduce a Hermitian version of the model, which is characterized by a nearest-neighbor hopping t, where exactly one of the four sides of each plaquette has a negative hopping amplitude compared to the three others. These hoppings require an enlarged unit cell of two plaquettes of the square lattice (see Fig. 47 (a)). Therefore, the Bloch Hamiltonian yielding the momenta k_x and k_y, can be written as

$$\begin{aligned}\mathcal{H}_\pi(k_x,k_y) &= [1+\cos(k_x)]\,\sigma_x + \sin(k_x)\,\sigma_y + 2\cos(k_y)\,\sigma_z \\ &= t\begin{pmatrix} 2\cos\,k_y & 1+e^{-\mathrm{i}k_x} \\ 1+e^{\mathrm{i}k_x} & -2\cos\,k_y \end{pmatrix}.\end{aligned} \tag{176}$$

The model has two Dirac-like band touchings at momenta $(k_x,k_y)=(\pi,\pi/2)$ and $(k_x,k_y)=(\pi,3\pi/2)$, which can be seen in the band structure in Fig. 47 (a). Applying open boundary conditions to the π-flux model in the y-direction in a cylindrical geometry results in a pair of counter-propagating modes in the boundary Brillouin zone, as the two Dirac cones are projected onto the same point, but there are no topological boundary modes in this configuration. On the other hand, open boundaries in x-direction preserve the separation of the Dirac crossings at $k_y=\pi/2,3\pi/2$.

If we treat k_y as a parameter instead of as a variable in Eq. (176), we end up with an effectively one-dimensional hopping model, that is equivalent to a hopping model on a 1D chain with an additional chiral symmetry breaking mass of $m=2\cos(k_y)$ parametrized by k_y. As the amplitudes of the intracell and intercell hoppings of the chain are identical, there will be no topological edge states for open boundary conditions and in particular no flat band joining the two projected Dirac cones in the k_y boundary Brillouin zone.

7 The Weyl's inequalities provide an upper bound to the change in the eigenspectrum of a Hermitian matrix due to small perturbation. NH matrices, however, are sensitive to small perturbations, which may lead to macroscopic changes. In contrast, the SVD *always* satisfies the Weyl's inequalities.

5.2.1 *Non-Hermitian extension*

Now, we add a non-Hermitian (gain/loss) term in the form of a diagonal hopping through one of the plaquettes in the unit cell (consult Fig. 47 (a)). It assigns a complex amplitude ir (with r a real number) to the the process of a particle hopping along the diagonal toward the upper right, and the exact same amplitude ir to the reversed process. Hermiticity would require that the latter process has the complex conjugated amplitude, that is $-\mathrm{i}r$. As such, the addition

$$\begin{aligned}\mathcal{H}(k_x, k_y) &= H_\pi - \mathrm{i}r\,\cos(k_y)\,\sigma_x + \mathrm{i}r\,\sin(k_y)\,\sigma_y \\ &= \mathcal{H}_\pi(k_x, k_y) - \mathrm{i}r \begin{pmatrix} 0 & e^{ik_y} \\ e^{-ik_y} & 0 \end{pmatrix}\end{aligned} \tag{177}$$

violates Hermiticity for this diagonal hopping term. Despite its non-Hermiticitiy, the model still is reciprocal as it satisfies

$$\mathcal{H}(k_x, k_y) = \mathcal{H}^{\mathrm{T}}(-k_x, -k_y) \tag{178}$$

under transposition. The Hamiltonian given in Eq. (177) has two complex-valued energy bands which touch in two pairs of exceptional points. Upon introducing a finite r, the Dirac points of the original π-flux model each split into a pair of these exceptional points, which are located at $k_x = \pi$ and $k_y = 1/2\,\arccos(r^2/2 - 1)$. For $r = 1$, which we use through this work, the four PBC exceptional points are pinned to $k_y = \pm\pi/3, \pm 2\pi/3 \mod 2\pi$. We illustrate the band structure close to an exceptional point in Fig. 47 (b). In Fig. 48, we plot the energy spectra and singular values for OBC and PBC along the k_y. The band structures are manifestly different demonstrating the non-trivial spectral flow, but the singular value decomposition is almost identical for both choices of boundary conditions. The singular spectrum in Fig. 48 (f) has additional $\sigma_i = 0$ values around $k_y = \pi/2$ and $k_y = 3\pi/2$, however these topologically stable SVD zero modes do not imply the existence of boundary eigenmodes [369].

The effectively one-dimensional model obtained by treating k_y as a parameter is extended by two non-Hermitian terms resulting in

$$\mathcal{H}_{k_y}(k_x) = \left[1 + \cos(k_x) - \mathrm{i}r_x\right]\,\sigma_x + \left[\sin(k_x) + \mathrm{i}r_y\right]\,\sigma_y + m\,\sigma_z \tag{179}$$

with $r_x = r\cos(k_y)$, $r_y = r\sin(k_y)$ and $m = 2\cos(k_y)$. If we fix k_y to one particular value, which means taking r_x, r_y and m as constants, $H_{k_y}(k_x)$ breaks reciprocity due to the term $\mathrm{i}r_y\sigma_y$. In one dimension, the combined breaking of reciprocity and Hermiticity in this model gives rise to the skin effect for $r_y \neq 0$ [324, 325, 327]. The effective 1D model for a given k_y exhibits the non-Hermitian skin effect as discussed in Refs. [324, 374]: The eigenstates of a Hermitian system form an orthonormal basis whose squared amplitudes, when summed over all states, are equal on all lattice sites. In a non-Hermitian system this need not be the case, since right (left) eigenstates of a non-Hermitian matrix do not individually form an orthonormal basis. As a result, they can all be localized at only one edge of the system, which defines the skin effect. In our model, the skin effect is realized due to the term proportional to r in Eq. (177), which renders the hopping probability for going right different from the probability for going left. This leads to an accumulation of all eigenstates towards only one edge.

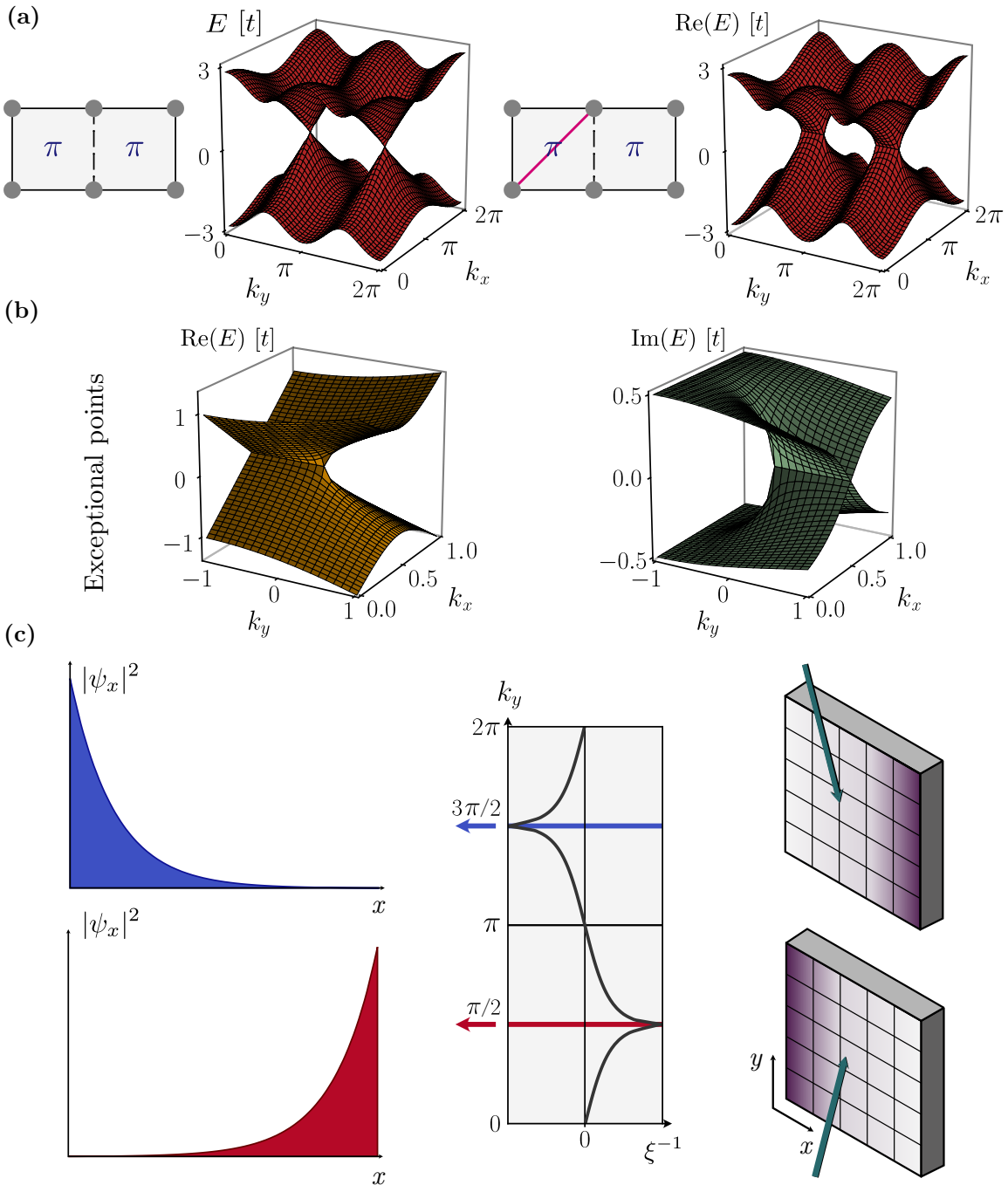

Figure 47: (a) Left: unit cell and spectrum of the π-flux model defined in Eq. (176) with periodic boundary conditions. Solid and dashed lines correspond to hopping amplitudes t and $-t$, respectively. Bands touch in two Dirac points. Right: π-flux model with a non-Hermitian diagonal hopping (pink) included, as defined in Eq. (177). Each Dirac point splits into a pair of exceptional points. **(b)** Real and imaginary part of eigenvalues in the vicinity of an exceptional point, at which two complex eigenvalues are degenerate. **(c)** Schematic of the reciprocal skin effect for OBC in x and PBC in y direction: near two opposite momenta, $k_y = \pi/2$ and $k_y = 3\pi/2$, all eigenstates are exponentially localized with localization length ξ to the left and right of the system, respectively. At $k_y = 0$, π the modes are completely delocalized. Right: The reciprocal skin effect could serve as a direction detector for incident electromagnetic waves: dependent on the propagation direction and polarization, a voltage will build up on the left or right edge of the system, as shown schematically.

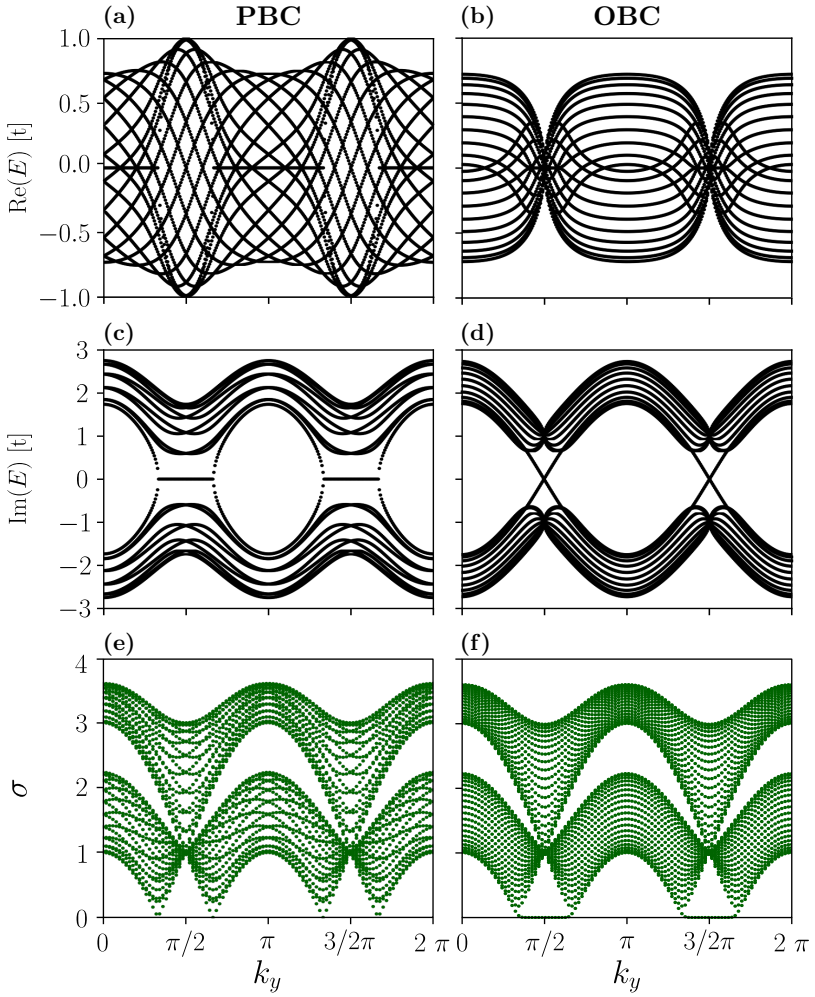

Figure 48: Numerical calculation of the complex eigenspectrum and singular value decomposition of the non-Hermitian π-flux model with $r = 1$. Real part of the **(a)** PBC and **(b)** OBC spectrum, imaginary part of the **(c)** PBC and **(d)** OBC spectrum, together with the singular values for **(e)** PBC and **(f)** OBC. Non-perturbative change in the energy spectra manifests the breakdown of bulk-boundary correspondence associated with the extensive localization of eigenmodes. However, the singular spectra closely resemble each other, with the only difference in additional zero singular values around $k_y = \pi/2$ and $k_y = 3\pi/2$ observed for OBC. This indicates a change in the band gap topology.

Due to the inclusion of non-Hermitian terms, topological states can emerge in the full Hamiltonian, which are not present in the initial Hermitian π-flux model. Our discussion closely follows Ref. [324]. To study the topological aspects in a system with N unit cells, we perform a *non-unitary* transformation $\mathcal{H}'_{k_y} = S^{-1}\mathcal{H}_{k_y}S$ with $S = \mathrm{diag}(1, a, a, a^2, a^2, \ldots, a^{N-1}, a^N)$ and $a = \sqrt{(1 - ir_x - r_y)/(1 - ir_x + r_y)}$, where open boundary conditions are implied. The transformed Hamiltonian under application of PBC can be rewritten as a reciprocal SSH chain with complex coefficients,

$$\mathcal{H}'_{k_y} = \big[t_0 + \cos(k_x)\big]\,\sigma_x + \big[\sin(k_x)\big]\,\sigma_y + m\,\sigma_z, \tag{180}$$

where $t_0 = \sqrt{(1 - ir_x)^2 - r_y^2} \in \mathbb{C}$. We point out that the transformation has to be firstly performed on the Hamiltonian with OBC and after that the PBC are applied. This is not

equivalent to the case, when the transformation is done for the already periodic system. SSH-type edge modes exist on both edges of the system, if $|t_0| < 1$, which translates to a topological regime for

$$\cos(k_y) < \sqrt{\frac{1}{2} - \left(\frac{r}{2}\right)^2}, \tag{181}$$

parametrized by the momentum k_y. The bulk spectrum of $\mathcal{H}'_{k_y}$ is gapped, if either $t_0 \neq 1$ or $m \neq 0$. The gap closes at $r = \sqrt{2}$ for $k_y = \pi/2$, which marks the topological phase transition in r. If $r \geq \sqrt{2}$, there are no topological states. As the spectra of $\mathcal{H}'_{k_y}$ and $\mathcal{H}_{k_y}$ are identical, the total Hamiltonian with OBC in the x-direction exhibits a bulk gap for all k_y in the boundary Brillouin zone for $r \neq \sqrt{2}$. The topological phase transition does in general not occur at the PBC band closings, but is instead parametrically displaced due to the non-Hermiticity. Only for the special choice of $r = 1$, the two conditions coincide, resulting in topological transitions at the PBC exceptional points for $k_y = \pm\pi/3, \pm 2\pi/3$. The topological boundary modes disperse with $\pm m = \pm 2\cos(k_y)$ and assume a linear dispersion at the original location of the Dirac crossings in the non-Hermitian model at $k_y = \pi/2, 3\pi/2$ in the boundary Brillouin zone. Note that the bulk is gapped at those points, while the edge states cross at zero energy. The analysis shows that SSH-type modes can coexist with skin modes in the non-Hermitian model with open boundaries along x.

5.2.2 *Reciprocal skin effect*

We proceed to consider the Hamiltonian (177) with OBC in the x-direction, which leaves $k_y \in [0, 2\pi]$ as a well-defined momentum, and denote $\tilde{\mathcal{H}}(k_y)$ as the Hamiltonian for a ribbon geometry. While $\tilde{\mathcal{H}}^{\mathrm{T}}(k_y) = \tilde{\mathcal{H}}(-k_y)$ guarantees reciprocity of the full system, each instance of $\tilde{\mathcal{H}}(k_y)$ *locally* breaks reciprocity for a fixed k_y when seen as a purely one-dimensional model, except for $k_y = -k_y$. The reciprocal skin effect is characterized by a k_y-dependence of this localization property. The bulk modes of the Hamiltonian with OBC in the x direction are localized on one boundary of the system with $\psi_x \sim e^{-x/\xi}$, where

$$\xi^{-1} = \frac{1}{4}\ln\left(\frac{1 + r^2 + 2r\sin(k_y)}{1 + r^2 - 2r\sin(k_y)}\right). \tag{182}$$

We illustrate the localization length ξ in Fig. 47 (c). ξ is positive, if $k_y \in (0, \pi)$ and negative if $k_y \in (\pi, 2\pi)$ in the boundary Brillouin zone with open boundaries along x. This leads to left edge localized modes, if $k_y \in (0, \pi)$ and to right edge localization, if $k_y \in (\pi, 2\pi)$. The strongest localization is found at the original positions of the Dirac crossings in the boundary Brillouin zone, $k_y = \pi/2, 3\pi/2$. At those points, ξ vanishes for $r \to 1$ leading to infinite localization, which is accompanied by exceptional points at finite energy in the OBC spectrum of the model. The localization length inherits the reciprocal symmetry from the full model as $\xi(-k_y) = -\xi(k_y)$. A state at k_y has a reciprocal partner mode at $-k_y \mod 2\pi$, which possesses the same absolute localization length, but is localized on the opposite edge. Combining those partners preserves reciprocity in the full model. For $k_y = 0$ or the self-symmetric momenta, the localization length diverges. The corresponding bulk eigenstates are delocalized and bulk-boundary correspondence is restored. This can be observed in Fig. 48, where at $k_y = 0$ and

$k_y = \pi$, the PBC and OBC spectra match and they do not form any loops in the complex plane [330, 367].

It is important to highlight that the reciprocal skin effect in two dimensions is fundamentally different to a doubled and reciprocity-enhanced 1D skin effect, as realized for instance by two reciprocity-reversed Hatano-Nelson chains [355]. To conceptualize this, consider an analogy to the 2D Chern insulator and the 3D Weyl semimetal [375]. Coupling two time-reversed copies of a Chern insulator with chiral edge states constitutes the $\mathbb{Z}_2$ topological insulator with helical edge states and restores time-reversal symmetry [15]. In a similar fashion, one can create an overall reciprocal system out of two Hatano-Nelson chains, whose exponentially localized modes are not protected by symmetry. Only by the demand of additional symmetries which square to -1, the precise notion of a $\mathbb{Z}_2$ skin effect is defined [330]. In distinction to this symmetry enhancement, we consider dimensional enhancement. The Weyl semimetal in 3D can be composed of 'slices' of momentum space, which are characterized by a 2D Chern insulator. By analogy, we extend the 1D (non-reciprocal) skin effect to two dimensions, arriving at the reciprocal skin effect, with momentum space slices that host the 1D skin effect. Slices at opposite momenta are connected by the reciprocity transformation. In contrast to one-dimensional systems, hybridization of those reciprocal partners is intrinsically prevented by the translational symmetry of the two-dimensional system.

5.2.2.1 *Theoretical derivation of the skin effect via non-unitary transformation*

Here, we show the explicit derivation of the reciprocal skin effect. We expand the Hamiltonian in Eq. (177) to linear order in the momentum deviations δk_y around the exceptional points and in r (i. e., we drop a term $\mathcal{O}(r\,\delta k_y)$). Let us denote by $H^{(\pm)}_{x\alpha,x'\alpha'}(\delta k_y)$ the matrix elements for the such expanded strip Hamiltonian, where $x, x' = 1, \cdots, L$ labels the unit cell across the strip and $\alpha, \alpha' \in \{1, 2\}$ refers to the two sublattices. We show now that, under OBC (but not PBC), this non-Hermitian Hamiltonian is related to a pair of well-known Hermitian Hamiltonians by *non-unitary* transformations. Our discussion closely follows Ref. [324]. The transformation (setting $t = 1$)

$$O^{(\pm)}_{x,x'} = \delta_{x,x'} \left(\sqrt{\frac{1 \mp r}{1 \pm r}} \right)^{x} M^{(\pm)}(r), \tag{183}$$

with $M^{(\pm)}(r)$ an appropriate 2×2 non-singular matrix acting on the sublattice space, maps $\tilde{H}^{(\pm)}(\delta k_y) = \left(O^{(\pm)}\right)^{-1} H^{(\pm)}(\delta k_y) O^{(\pm)}$, with

$$\tilde{H}^{(\pm)}_{x,x'}(\delta k_y) = \delta_{x,x'} \begin{pmatrix} 2\delta k_y & -\sqrt{1-r^2} \\ -\sqrt{1-r^2} & -2\delta k_y \end{pmatrix} - \begin{pmatrix} 0 & \delta_{x',x+1} \\ \delta_{x',x-1} & 0 \end{pmatrix}. \tag{184}$$

For $\delta k_y = 0$, Eq. (184) is the tight-binding Hamiltonian for a dimerized chain, known as the Su-Schrieffer-Heeger model (see Fig. 49). For $-1 < r < 1$, $r \neq 0$, the chain is bulk insulating but has one SSH-type midgap state localized at each end of the chain. Its bulk states are of delocalized Bloch character, while the end states are exponentially localized with a ratio $\tilde{\psi}_{x,\alpha} / \tilde{\psi}_{x\pm1,\alpha} = \sqrt{1-r^2}$ of wave function amplitudes on neighboring lattice sites. We denote by $\psi_{x,\alpha}(\delta k_y)$ and $\tilde{\psi}_{x,\alpha}(\delta k_y)$ the eigenstates of $H^{(\pm)}(\delta k_y)$ and $\tilde{H}^{(\pm)}(\delta k_y)$, respectively. Finite but small δk_y mainly has the effect of lifting the degeneracy of the SSH-type end states from eigenvalue 0 to $\pm 2\delta k_y$.

Being related by $O^{(\pm)}$, $\tilde{H}^{(\pm)}(\delta k_y)$ and the non-Hermitian Hamiltonian $H^{(\pm)}(\delta k_y)$ are isospectral, but their eigenstates differ in important ways. The x-dependent factor in $O^{(\pm)}$ turns *all* the Bloch-type bulk states into exponentially localized states, with $\psi_{x,\alpha}/\psi_{x\pm1,\alpha} \approx \sqrt{2/(1\pm r)-1}$ – which is a stronger exponential decay than that of the SSH-type end states. This implies that the two topological edge states become localized at the same end of the chain after the non-unitary transformation. Whether the localization is on the left or right edge of the system depends on the sign of r and is opposite for $H^{(+)}(\delta k_y)$ and $H^{(-)}(\delta k_y)$. We conclude that on a strip geometry all eigenmodes of the model in Eq. (177) are localized on one side of the sample for $k_y \sim \pi/2$ and on the opposite side for $k_y \sim 3\pi/2$. This constitutes the reciprocal skin effect, enabled by the non-Hermiticity of the Hamiltonian.

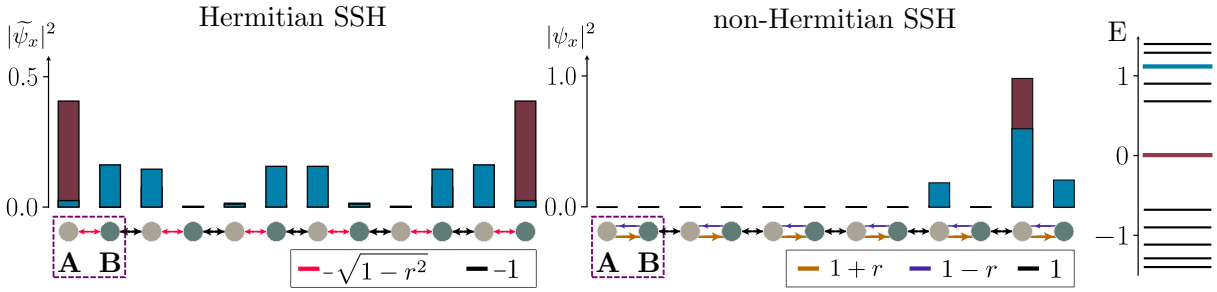

Figure 49: Relation between the Hermitian ($r = 0$) and non-Hermitian ($r = 0.9$) dimerized chain, the SSH model. The spectrum of both models is equal with open boundary conditions, including SSH-type end states. However, all states in the non-Hermitian model are localized on one side of the system. The amplitude at each lattice site for the two eigenstates marked in the spectrum on the right are plotted with the respective color.

5.3 EXPERIMENTAL TOPOLECTRICAL CIRCUIT REALIZATION

In principle, various non-Hermitian, i. e. lossy, classical systems could be deliberately tailored to study the physical effects outlined above. Topolectrical circuits in particular, however, offer an important advantage due to the only mild limitation imposed by local connectivity constraints otherwise typical to many other metamaterial settings. Most importantly, a connection between the leftmost and rightmost site of a circuit can simply be toggled on/off to change between PBC and OBC. This way, the breakdown of bulk-boundary correspondence can be studied most directly. We experimentally implemented a circuit which realizes the non-Hermitian but reciprocal model given in Eq. (177) through its response function within linear circuit theory. The circuit Laplacian matrix $J(\omega)$ takes the role of the reciprocal Hamiltonian introduced above. More concretely, it connects the input currents $I_a(\omega)$ at node a of the system to the voltages $V_b(\omega)$ measured at b via Kirchhoff's law, represented in the frequency domain by $I_a(\omega) = J_{ab}(\omega)V_b(\omega)$.

5.3.1 *Laplacian formalism*

In a passive circuit network of capacitors (C), inductors (L), and resistors (R), currents and voltages are linearly related through a discretized version of the Laplacian operator as a second order spatial derivative. However, in such a circuit system, energy is not necessarily conserved

as it can dissipate in an irreversible heating process occurring in resistors. In contrast to purely capacitive or inductive couplings, which oppose the *change* of electric currents or voltages, a resistor opposes the *flow* of an electric current and is, as such, intrinsically non-Hermitian. To be able to analyze the present circuit setup, which involves all of the passive components R, L, C, we rely on non-Hermitian linear circuit theory.

Define V_a and I_a to be the voltage and external input current on node a of a circuit network. Using Kirchhoff's and Ohm's laws, we obtain a coupled system of differential equations for the circuit,

$$\dot{I}_a = \Gamma_{ab}\,\ddot{V}_b + \Sigma_{ab}\,\dot{V}_b + \Lambda_{ab}\,V_b, \tag{185}$$

where Γ_{ab}, Σ_{ab} and Λ_{ab} are the reduced Laplacian matrices of capacitances, conductances and inverse inductances, and the summation over repeated indices is implied. The diagonal components $a = b$ of the Laplacians are defined by

$$X_{aa} = -X_{a0} - \sum_{b=1,2,\cdots} X_{ab}, \qquad X \in \{\Gamma, \Sigma, \Lambda\}, \tag{186}$$

including the circuit elements X_{a0} between node a and the ground.

A Fourier transformation of Eq. (185) from the time to frequency domain results in

$$I_a = \left(\mathrm{i}\omega\,\Gamma_{ab} + \Sigma_{ab} - \frac{\mathrm{i}}{\omega}\,\Lambda_{ab}\right) V_b = J_{ab}(\omega)\,V_b, \tag{187}$$

where we defined $J_{ab}(\omega)$ as the (grounded) circuit Laplacian [338]. Note that ω is treated as a parameter of the system which is fixed by the external AC driving frequency.

A natural observable in a circuit is the impedance response Z_{a0}, which is the ratio of the voltage at node a measured with respect to ground due to an input current $I_j = I_0\,\delta_{j,a}$ that enters through a and exits through ground. Mathematically, Z_{a0} involves the inversion of Eq. (187)

$$Z_{a0}(\omega) = \frac{V_a}{I_0} = \sum_j \frac{G_{aj}\,I_i}{I_0} = G_{aa} = \sum_n \frac{\psi_{n,a}\,\phi^*_{n,a}}{j_n}, \tag{188}$$

where $J_{ab}(\omega) = \sum_n j_n(\omega)\psi_{n,a}\phi^*_{n,b}$ defines the spectral representation of the Laplacian with its right and left eigenvectors, ψ_n and ϕ_n. The frequency dependence of the Laplacian eigenvectors remains implicit. As the inverse of the Laplacian, the Green's function $G_{ab}(\omega) = \sum_n j_n^{-1}(\omega)\psi_{n,a}\,\phi^*_{n,b}$ contains the voltage response to an external current excitation and fundamentally determines both the excitation pattern of individual eigenmodes and the circuit's impedance profile with frequency. The grounding impedances are given by the diagonal elements of G.

The off-diagonal components of the Green's function are accessible using an arrangement of measurements similar to that of the impedance response $Z_{a0}(\omega)$. We feed a current I_a at node a and measure the voltage response $V_b^{(a)}$ at all the other nodes. By repeating this for all input nodes, the Green's function can be reconstructed as

$$G_{ab} = \frac{V_b^{(a)}}{I_a}. \tag{189}$$

In the circuit formalism, the Green's function as a direct observable contains full information on admittance eigenvalues and eigenmodes of the Laplacian, which can be extracted through

numerical diagonalization. The procedure to measure the Green's function can be simplified in periodic models using spatial Fourier transform [345].

5.3.1.1 *Derivation of the circuit Laplacian*

We realize the reciprocal skin effect in an electrical circuit whose unit cell is shown in Fig. 50 (a), with the conceptually important elements of each plaquette shown in Fig. 50 (b). The two-point Laplacian of a capacitor is given by

$$\begin{pmatrix} I_{\text{in},1} \\ I_{\text{in},2} \end{pmatrix} = \mathrm{i}\omega \left[C \begin{pmatrix} 1 & -1 \\ -1 & 1 \end{pmatrix} \right] \begin{pmatrix} V_1 \\ V_2 \end{pmatrix}. \tag{190}$$

Omitting the prefactor $\mathrm{i}\omega$ results in the symmetric and Hermitian Laplacian matrix. The Laplacian for an inductor takes a similar form

$$\begin{pmatrix} I_{\text{in},1} \\ I_{\text{in},2} \end{pmatrix} = \mathrm{i}\omega \left[-\frac{1}{\omega^2 L} \begin{pmatrix} 1 & -1 \\ -1 & 1 \end{pmatrix} \right] \begin{pmatrix} V_1 \\ V_2 \end{pmatrix}, \tag{191}$$

that differs in the frequency-dependent admittance prefactor and, importantly, in the overall sign. At the resonance frequency $\omega_0 = 1/\sqrt{LC}$ of an LC resonator, the inductor effectively acts a negative capacitor, where $-1/(\omega_0^2 L) = -C$ in front of the Laplacian matrix. Therefore, one circuit plaquette of the π-flux model consists of three capacitors (representing t) and an inductor (representing $-t$ at resonance), all of which are Hermitian and reciprocal. At nodes of sublattice A, the diagonal contributions in the Laplacian add to 4C, whereas for $\omega = \omega_0$ the capacitive and inductive contributions cancel each other in the diagonal term at sublattice B. To avoid the sublattice asymmetry contributing to a σ_z term, we ground nodes of type A with an inductor $L_g \approx L/4$ such that the diagonal contribution to the Laplacian vanishes for both sublattices at resonance frequency. In total, the circuit Laplacian in momentum space is given by

$$\begin{aligned} J_\pi(k_x, k_y) = \mathrm{i}\omega \Bigg[&- \begin{pmatrix} 2C\cos(k_y) & C(1+e^{-\mathrm{i}k_x}) \\ C(1+e^{\mathrm{i}k_x}) & 2/(\omega^2 L)\cos(k_y) \end{pmatrix} \\ &+ \begin{pmatrix} 4C - 1/(\omega^2 L_g) & 0 \\ 0 & 2C - 2/(\omega^2 L) \end{pmatrix} \Bigg] \end{aligned} \tag{192}$$

resembling the π-flux tight-binding model for $\omega \to \omega_0$, where the second term vanishes. Additional to $J_\pi(k_x, k_y)$, we introduce a resistor connecting nodes A and B of adjacent unit cells in the y-direction (see Figs. 50 (a) and (b)). Its admittance representation reads

$$\begin{pmatrix} I_{\text{in},1} \\ I_{\text{in},2} \end{pmatrix} = \mathrm{i}\omega \left[-\frac{i}{\omega R} \begin{pmatrix} 1 & -e^{\mathrm{i}k_y} \\ -e^{-\mathrm{i}k_y} & 1 \end{pmatrix} \right] \begin{pmatrix} V_1 \\ V_2 \end{pmatrix} \equiv J_r \begin{pmatrix} V_1 \\ V_2 \end{pmatrix}. \tag{193}$$

The total Laplacian is given by $J = J_\pi + J_r$. With $\mathrm{i}\omega$ factored out, the added Laplacian J_r is non-Hermitian and breaks time-reversal symmetry. For an arbitrary circuit network described by $J(k_y, k_y)$, reciprocity is defined as $J^{\mathrm{T}}(k_x, k_y) = J(-k_x, -k_y)$. Thus, a resistor is a reciprocal circuit element. However, if one considers a fixed k_y slice of the model, reciprocity is broken as $e^{\mathrm{i}k_y} \neq e^{-\mathrm{i}k_y}$ for arbitrary $k_y \neq 0, \pi$.

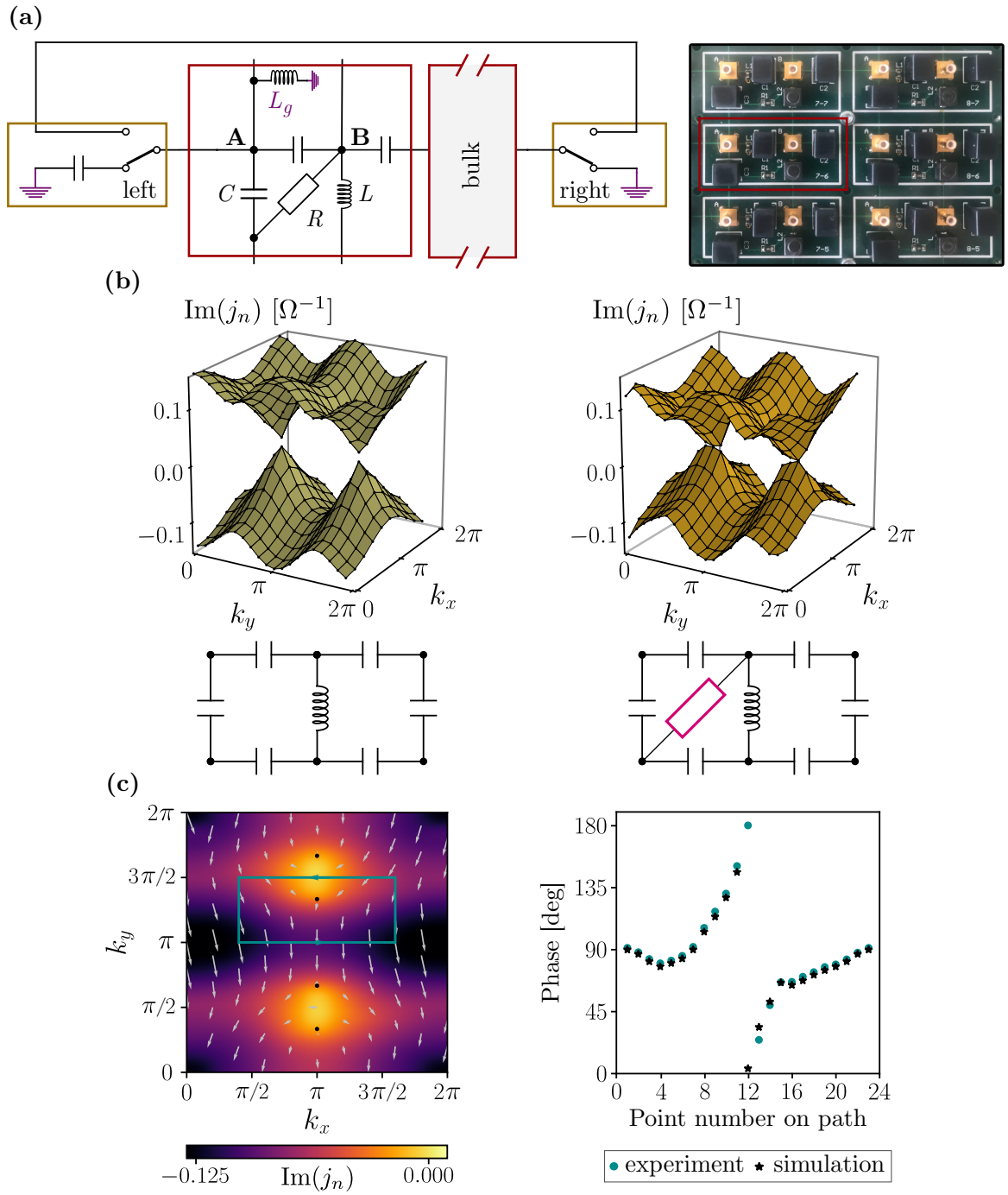

Figure 50: Experimental topolectrical circuit realization of the reciprocal skin effect and exceptional points. **(a)** Bulk unit cell and boundary terminations of the circuit, together with a photography of six unit cells of the assembled circuit board. Section 5.3.1.1 details the connection of this circuit cell to the lattice model in Eq. (177) using the Laplacian formalism. **(b)** Measured spectra with PBC of the circuit Laplacian and schematic unit cell of the circuit that corresponds to the π-flux model (left) and the non-Hermitian model (right) from Eq. (177) (cf. Fig. 47 (a)). Only the imaginary part of the eigenvalues is plotted. The formation of a branch cut from the Dirac point is visible, the ends of which are host to exceptional points. **(c)** Left: Imaginary part and phase of the band with smaller imaginary part. The phase of the eigenvalue along the path indicated is plotted in the right panel. It shows a clear jump by π, indicative of an enclosed exceptional point. Stars denote a LTspice simulation of the circuit, while dots correspond to the measured spectrum.

5.3.2 *Non-Hermitian topolectric circuit*

In a Hermitian circuit, all eigenvalues of $J(\omega)$ are purely imaginary ($\mathrm{i}J(\omega)$ is a Hermitian matrix), while the inclusion of resistors generates complex eigenvalues. Interpreting $J(\omega)$ at a fixed frequency ω_0 as a hopping matrix, one observes that the sign change of t necessary to implement the π-flux model is achieved by connecting one of the three bonds surrounding a plaquette in a square lattice with an inductor and three with a capacitor (consult Fig. 50 (a) and (b)). We fabricated a circuit with 10×20 unit cells using this model.

Assuming translation invariance (realized to the accuracy of the circuit element specifications), we can represent the voltages and input currents in terms of Fourier modes in reciprocal space. This leads to the k-space representation of the Laplacian as well as its voltage eigenmodes and allows for the definition of a complex-valued admittance band structure. The latter can be understood as a complex mapping from wave vector k to admittance eigenvalues of the Laplacian. In a measurement, we can decompose the voltage response to an external current excitation and find the eigensystem of the Laplacian for both periodic and open boundary conditions. Fig. 50 (b, left) shows the measured bands including the two Dirac-cone band touchings expected for the π-flux model. The Dirac points are broadened into branch cuts, each of which spans between a pair of exceptional points. To demonstrate this, we plot the phase of the eigenvalue for the band $j_n(\omega_0, k_x, k_y)$ with smaller imaginary part along a closed path in Fig. 50 (c). The observed winding and phase jump by π is direct evidence that the path encircles an exceptional point in momentum space, which is topologically stable exactly through this half-integer winding number of the band eigenvalue around it.

Having confirmed that the circuit realizes the desired physics of an exceptional point band structure with PBC, we now present measurements with OBC in x-direction to demonstrate the reciprocal skin effect. Edge terminations are chosen such that the circuit grounding does not introduce undesired off-sets due to a change in the total node conductance at the edge sites, see Fig. 50 (a). The measured k_y-resolved spectra are shown in Fig. 51, in comparison to an equivalent representation of the data for PBC. The eigenvalues with small imaginary part around $k_y \sim \pi/2, 3\pi/2$ indeed show the expected reorganization from a spectrum with two exceptional points in the bulk towards much fewer states with OBC – a breakdown of the Hermitian bulk-boundary correspondence. The reciprocal skin effect is encoded in the coloring of the data points: red and blue dots correspond to right and left localized eigenstates. (Note that through the measurement of the full matrix $J(\omega_0)$ not only do we have access to its spectrum, but also to all of its eigenstates.). The degree of localization of eigenstates is quantified by the inverse participation ratio (IPR) [376]. Remarkably, *all* states near $k_y \sim \pi/2$ are right-localized, while *all* states near $k_y \sim 3\pi/2$ are left-localized.

5.3.3 *Representation of the Laplacian spectra in the complex plane*

In addition, we present an alternative representation of the complex spectra of the circuit Laplacian, both theoretical and experimental. For this, we consider k_y as a parameter and plot for each fixed k_y the set of eigenvalues in the complex plane $\mathrm{Re}(j_n)$-$\mathrm{Im}(j_n)$. This generates a two-dimensional closed surface, as shown in Fig. 52 (a) for PBC. As a function of k_y, the eigenvalues trace out either a single circle or two circles in the $\mathrm{Re}(j_n)$-$\mathrm{Im}(j_n)$ plane. The transitions between these two topologically distinct situations are exceptional points. The planes $k_y = 0$ and $k_y = \pi$

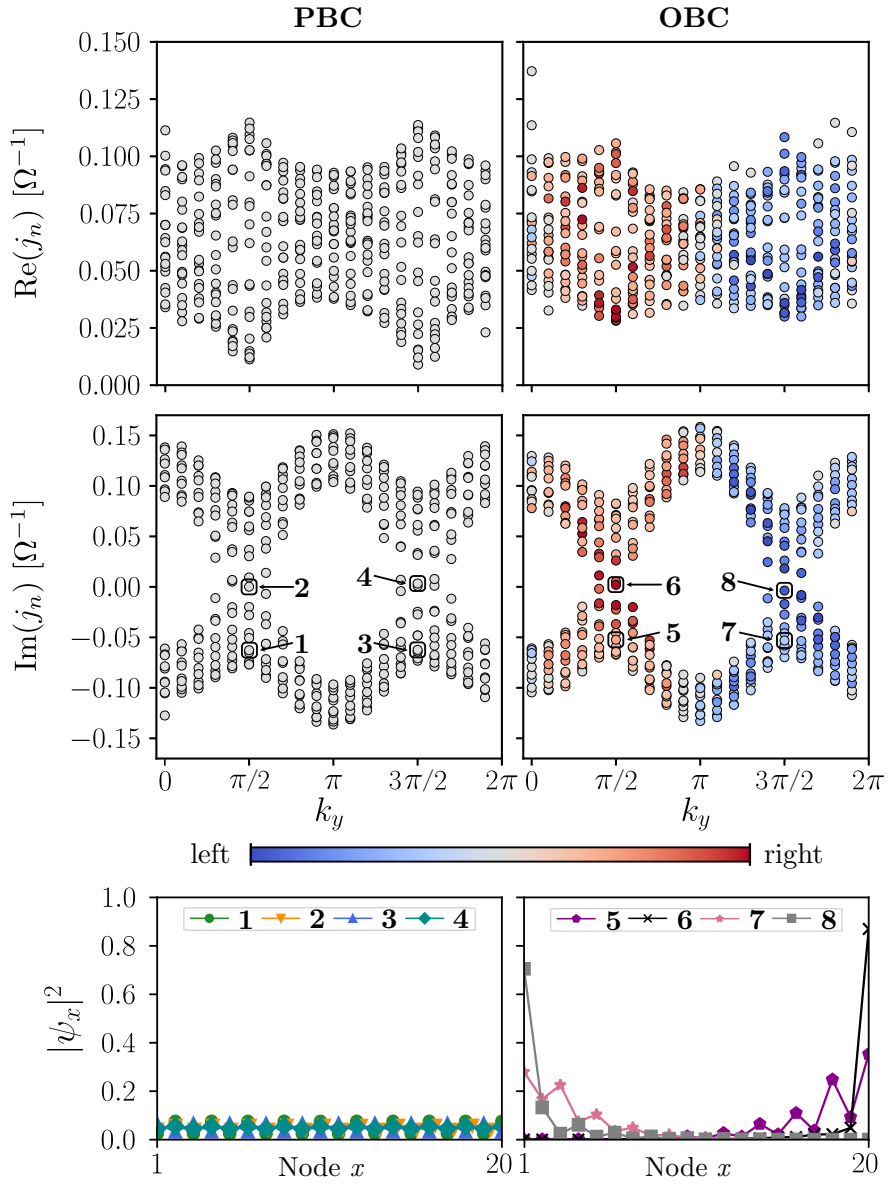

Figure 51: Measured spectra of the circuit Laplacian as a function of k_y for OBC and PBC along the x direction. Localization properties of each eigenstate are indicated by color and determined from the inverse participation ratio. The bottom panel shows the localization properties of representative individual eigenstates at $k_y = \pi/2$ and $k_y = 3\pi/2$, both for PBC and OBC. The fact that *all* OBC and PBC eigenstates differ non-perturbatively constitutes the reciprocal skin effect, with those around $k_y \sim \pi/2$ right-localized and those around $k_y \sim 3\pi/2$ left-localized.

are special, because the path traced out in the complex plane as a function of k_x is reciprocal on them. Therefore, it collapses into lines on which each non-end point is visited two times as k_x is varied [327].

Since we have two pairs of exceptional points, the two-dimensional eigenvalue surface in k_y-Re(j_n)-Im(j_n) space has genus three [377]. We can plot the experimental spectra of $J(\omega_0)$ in a similar fashion, shown in Fig. 52 (c). We observe, for PBC, a clear change between slices at constant k_y with a single circle and two circles in the complex plane of eigenvalues. This strongly indicates the presence of exceptional points between these two slices. Moreover, we note that the two cases – at $k_y = \pi/2$ and $k_y = 3\pi/4$ – presented in Fig. 52 (b) exhibit the skin effect as there exist base energies such that the complex eigenspectrum has a non-trivial winding number [330, 367].

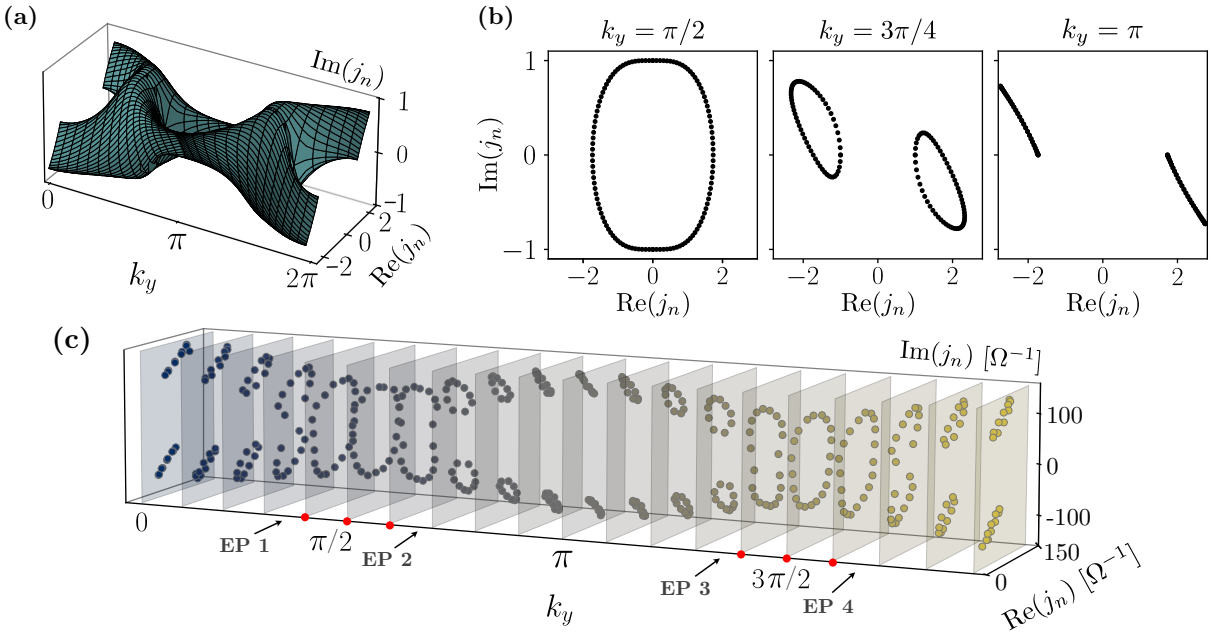

Figure 52: Representation of the circuit Laplacian spectra for PBC in the complex plane as a function of k_y. **(a)** Theoretically computed spectrum showing a genus three surface with four exceptional points. **(b)** Slice plots obtained from **(a)** for three different k_y. **(c)** Measured spectra, where each of the four transitions from a single circle in the complex plane to two circles marks an exceptional point (EP1–EP4) as a function of k_y.

5.3.4 *Response of the reciprocal skin-effect circuit to bulk perturbations*

A distinct feature of the reciprocal skin effect, which may lead to applications for polarization detection of electromagnetic waves, is the response to the circuit to perturbations in the bulk. From Eq. (187) we deduce that the voltage response at site a to a driving current at frequency ω is given by

$$V_a = G_{ab}(\omega) I_b. \tag{194}$$

Since our circuit has finite resistivity, $J_{ab}(\omega)$ has no zero eigenvalues at real frequencies, and can therefore be readily inverted. To model the experimental situation, we consider PBC in y-direction and OBC in x-direction. We then apply a minimal driving current to two bulk sites aligned along the y-direction, where we assign the current at one site a $+\pi/2$ ($-\pi/2$) phase

shift with respect to the current at the other site. We therefore expect the current to excite the circuit Laplacian eigenstates at $k_y = \pi/2$ ($k_y = 3\pi/2$), which are right (left) localized in x-direction due to the reciprocal skin effect. Fig. 53 shows the theoretically calculated response of the circuit that is obtained by inverting the real-space version of the Hamiltonian given by Eq. (177). We find that the two driving current patterns indeed lead to non-local voltage responses at the far right (left) of the circuit. The reciprocal skin effect could therefore be the basis of a polarization detection device for electromagnetic radiation.

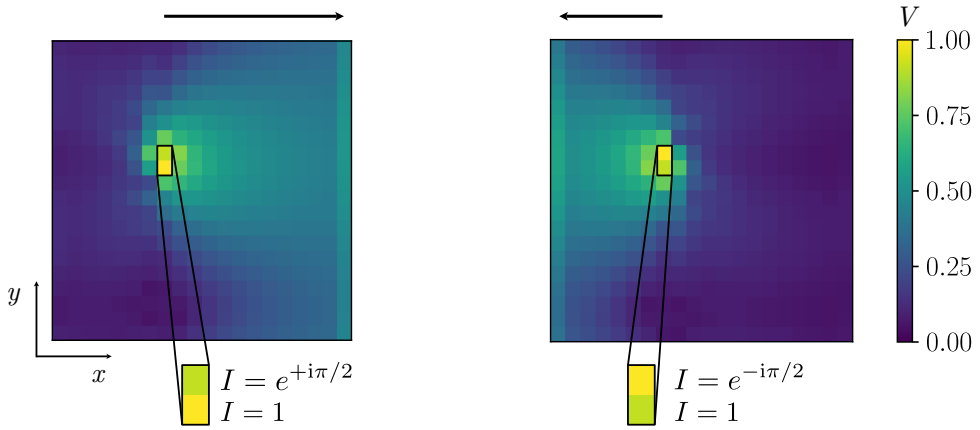

Figure 53: Reciprocal skin effect voltage response due to a localized bulk driving current with phase shift. The sites where the current is applied are framed in black, the zoom-ins show how the relative phase is implemented. Importantly, for a phase shift of $+\pi/2$ ($-\pi/2$) we find a non-local voltage response at the far right (left) side of the circuit with OBC, which is absent for phase shifts 0 and π. The arrows show the direction of voltage accumulation.

6

CONCLUSIONS AND OUTLOOK

The immense interest in the field of topological matter over the last years, both from theoretical and experimental perspectives, has significantly extended the number of known topological phases. In this thesis, we have explored selected low-dimensional non-interacting fermionic phases which fall outside the classification of topological insulators and superconductors based on internal symmetries – the ten-fold way. Below, we summarize the original results from Chapters 2– 5 and suggest potential research directions.

CHAPTER 2

In Chapter 2, we have discussed possible realization of topological phases in fractal geometries with a non-integer Hausdorff dimension. By means of a case study, we investigated the Hofstadter model defined on the Sierpiński carpet and gasket. We showed that both systems exhibit a hierarchy of the edge-localized states at different levels of fractals depth in a finite magnetic field. Using the Bott index and the real-space formulation of the Chern number, we distinguished topologically non-trivial regions in the spectrum and probed them by performing the level statistics analysis in the presence of disorder. Therefore, a key finding is that characteristic features of quantum Hall systems in two dimensions are also observed in *almost* two-dimensional lattice models.

It is imperative to ask what dimensional and connectivity properties a graph must have in order to support topological states. Our results call for an extension of the ten-fold way to more general graphs and question the bulk-boundary correspondence in systems without a sharp distinction between the bulk and the edge. Also, the realization of topologically ordered phases in fractal geometries still remains essentially uncharted (only recently, Ref. [378] provided a method to construct FQH states on fractal lattices hosting anyons). An interesting research direction would be to provide a systematic classification for scale-invariant systems and define topological invariants in analogy to the ones based on occupied Bloch states. While the Chern number definitely brought valuable insight into topological states on fractals, it is an open question whether it is truly the appropriate invariant in systems with fractional Hausdorff dimension. Consequently, more careful studies should be carried out for fractals with an integer Hausdorff dimension, but embedded in a higher-dimensional space such as Sierpiński tetrahedron – a three-dimensional object, but characterized by a d_H equal to 2.

CHAPTER 3

Going further, in Chapter 3 we discussed the role of crystal symmetries in symmetry-protected topological phases. We focused on topological crystalline insulating states protected by the mirror symmetry, with the concrete examples of bismuth and antimony monolayers due to their highly-tunable electronic properties. Using a tight-binding model, we showed how to drive a system to a topological phase, but also how to induce a topological phase transition between

topologically distinct TI and TCI phases. In addition, we demonstrated that single-particle entanglement measures can provide supplemental information on the topological properties of systems compared to standard band structure analysis, even for small system sizes.

Composition- and strain-induced phase transitions reveal a finite discontinuity in the entanglement entropy. On the other hand, the electric field-driven topological phase transition seems to have a qualitatively different character as the entanglement entropy remains a continuous function with respect to the electric field strength, while its first derivative is discontinuous. We relate this difference to the breaking of inversion symmetry in the latter case, however additional checks should be carried out. A long-standing belief was that a TPT between trivial and non-trivial phases is always of the second order as the band gap continuously changes with respect to model parameters. Including electron-electron interactions may result in a first-order transition [379–381], but even more interesting is that such a transition may happen at the level of non-interacting systems [382], signatures of which were most likely observed in Sn-doped PbSe [383] in the TCI phase. We speculate that careful studies of the scaling of EE across the critical point would allow to characterize the order of TPTs.

In this Chapter, we considered only one type of spatial bipartition and kept the length between the subsystems ℓ constant, but systematic studies of the scaling of entanglement entropy depending on the size and shape of the spatial cut may be insightful. For instance, observing the area law around a critical point by changing ℓ would allow to extract the central charge and, ultimately, find the universality class of the second-order phase transition. General arguments may be formulated by investigating the sign of the correlation function constructed from Wannier functions and the corresponding correlation length close to criticality [384].

CHAPTER 4

As established in Refs. [274, 250, 275] for insulators with bulk polarization and more recently in Refs. [251, 253] for second-order topological insulators, the non-trivial bulk topology of OALs can be revealed via the charge fractionalization at their boundaries. This represents the simplest mechanism for a topological bulk-boundary correspondence that is protected by crystalline symmetries. In Chapter 4, we presented theory and material candidates for charge fractionalization at corners in 2D systems with significant spin-orbit coupling, thus providing a broader picture than the one presented in some previous treatments of this phenomenon [251–253]. Corner charges in topological insulators are well-defined when there is no edge spectral flow but also only in the absence of an edge-induced filling anomaly due to (time-reversal) bulk polarization. Since there is no crystalline symmetry-protected edge spectral flow in 2D (assuming the symmetry acts at least in part non-locally), corner charges are well-defined for all 2D systems that are not strong or weak first-order topological insulators, or M_z mirror Chern insulators [145, 39].

Diagnosing spinful OALs with time-reversal symmetry in 2D was particularly challenging because the irreducible representations of the occupied bands at HSPs are usually two-dimensional, yielding trivial symmetry indicator invariants at C_2-invariant HSPs. Symmetry indicators were therefore insufficient to identify the Wannier centers in C_6, C_4, and C_2 symmetric insulators. To overcome this difficulty, we considered Wilson loop and nested Wilson loop invariants, which could better 'resolve' the positions of the Wannier centers. Wilson loops, however, are essentially one dimensional objects that extract projections of the 2D positions of

the Wannier centers along particular directions. Nested Wilson loops are a best-effort attempt to localize the Wannier centers in 2D, but cannot always be interpreted literally due to the possible non-commutation of Wilson loops along different directions. In the presence of crystalline symmetries, however, Wilson and nested Wilson loops have eigenvalues with quantized phases, which clearly distinguish different OALs in C_6 and C_2 symmetric insulators, but are insufficient for insulators which only have C_4 symmetry. Therefore, finding a formula for the corner charge in such C_4-symmetric systems would be a possible future research direction.

We studied the protection due to spatial symmetries only because corner charge fractionalization is a robust observable that does not require additional spectral symmetries such as chiral or particle-hole symmetry. However, when particle-hole symmetry is present, we can additionally predict topologically protected zero-energy corner states. These are characterized by the charge $Q_c = 1 \mod 2$: Consider a system with an n-fold symmetry in a phase with $2n$ degenerate midgap states (the 2 is due to TRS). At half-filling, n midgap states are occupied and there is no gap. To arrive at a gapped system (as required for the corner charge to be well defined), we need to either fill n more states or remove n electrons from the charge-neutral system. When maintaining the crystal symmetry, this implies an excess (or missing) charge of $Q_c = 1 \mod 2$ for each of the n corners [253].

Interestingly, we find that there are obstructed atomic limits, where the electrons are localized away from the atomic sites, which still do not have non-trivial corner charges. These may instead be diagnosed by their response to crystal defects [253, 264]. Topological defects such as dislocations have been proven to be useful in probing the bulk properties of conventional TCIs [385], HOTIs [386, 387] and boundary-obstructed phases [388]. We leave the exploration of the defect response of obstructed atomic limits with significant spin-orbit coupling to future work.

The developed formulas for the corner charges, in particular based on symmetry indicators, may be applicable in high-throughput calculations for materials discovery. So far, large-scale computations have been performed for strong topological [389, 390, 149, 391] and fragile [247] phases. Hence, it would be of a great interest to systematically study OALs in a similar way.

CHAPTER 5

Finally, in Chapter 5, we introduced and experimentally demonstrated the concept of the reciprocal skin effect, where the breakdown of bulk-boundary correspondence occurs in the absence of any non-reciprocal coupling. Instead of having extensive mode accumulation all along one boundary, an equal number of eigenmodes localizes along opposite boundaries, with the direction of localization tied to the momentum component parallel to the boundary. Key to their realization is the gain/loss associated with couplings across different sites, which effectively behave like non-reciprocal couplings at a fixed transverse momentum. The reciprocal skin effect can in principle exist in two or higher dimensions when the non-Hermitian reciprocal couplings connect different internal degrees of freedom and the momentum space structure protects the skin modes from hybridization.

We observed the reciprocal skin effect in an electric circuit with solely passive linear circuit elements. The breakdown of bulk-boundary correspondence becomes evident by comparing the PBC system with exceptional points with the markedly different OBC case, featuring oppositely localized skin modes. Our circuit, and more generally the reciprocal skin effect, facilitates

novel functionalities when coupled to electromagnetic waves. For instance, it lends itself to potential applications for polarization and direction detectors for electromagnetic waves, where differently directed or polarized input signals are substantially accumulated towards opposite directions.

A slightly different question to the problem investigated here is whether it is possible to *suppress* the skin effect intrinsically present in a system. In Ref. [392], the authors proposed to consider a many-body wave function, which includes the fermionic statistics and therefore prevents the states to pile up at the edges due to the Pauli exclusion principle. A natural way to preclude the anomalous localization at the boundary would be to introduce disorder into the system, which is a subject of recent studies [393, 394]. We also speculate that incorporating crystal symmetries in the discussed non-Hermitian π-flux model may prevent it from forming the skin effect. Only recently, the concept of higher-order skin effect has been introduced [395–397]. In analogy to higher-order TIs, the skin states can localize in the corners of 2D systems and on the hinges in 3D in the presence of spatial symmetries.

Another not fully explored direction is the interplay between non-Hermiticity and interactions. Several non-Hermitian extensions to the interacting problems were proposed, for example Kondo lattice models [398, 399] or FQH states [400]. Conceivably, there may be a way to construct novel non-Hermitian topologically ordered states without Hermitian equivalent. In general, non-Hermitian systems are challenging to study from the numerical perspective as ill-conditioned matrices often give rise to numerical instabilities. Therefore, it would be highly relevant to adapt well-developed numerical techniques for the many-body problems such as tensor networks to efficiently describe non-Hermitian states.

A

WANNIER FUNCTIONS

The Wannier functions (WFs) [234], a complete set of orthogonal functions localized in real space, allow for an intuitive description of topological invariants. In this Section, we briefly recap the essential properties of Wannier states. For more details, we refer the reader to Ref. [235].

Suppose the ground state of a periodic system is described by extended Bloch functions $|\psi_{n\mathbf{k}}\rangle$, where n labels the bands and $\mathbf{k}$ stands for the crystal momentum. An alternative representation can be given in terms of localized Wannier functions, which are related to the Bloch functions by a Fourier transform

$$|W_n(\mathbf{R})\rangle = \frac{V}{(2\pi)^3}\int_{\mathrm{BZ}} d\mathbf{k}\, e^{i\mathbf{k}\cdot(\mathbf{r}-\mathbf{R})}\,|u_{n\mathbf{k}}\rangle\,. \tag{195}$$

V is the real-space primitive cell volume, $|u_{n\mathbf{k}}\rangle = e^{-i\mathbf{k}\cdot\mathbf{r}}|\psi_{n\mathbf{k}}\rangle$ is a cell-periodic function, and $\mathbf{R}$ corresponds to a real-space lattice vector. $|W_n(\mathbf{R})\rangle$ form an orthonormal set. As the transformation is unitary, the Bloch states can be exactly reproduced from a linear combination of the WFs. The definition in Eq. (195) indicates that WFs are not unique; each occupied Bloch band can be multiplied by a $\mathrm{U}(1)$ phase factor, which acts locally in reciprocal space and leaves the physical observables invariant, but it changes the shape of WFs in real space. This gives rise to a $\mathrm{U}(N)$ gauge freedom

$$|u_{n\mathbf{k}}\rangle \longrightarrow \sum_m U_{mn}(\mathbf{k})\,|u_{m\mathbf{k}}\rangle\,. \tag{196}$$

As the WFs are expected to be localized in real space, the gauge choice ambiguity can be removed by enforcing a gauge that minimizes the spread of WFs[1]. The procedure of finding the maximally-localized Wannier functions basically boils down to minimizing the localization criterion

$$\Omega = \sum_n \left[\langle W_n(\mathbf{0})|r^2|W_n(\mathbf{0})\rangle - \langle W_n(\mathbf{0})|\mathbf{r}|W_n(\mathbf{0})\rangle^2\right] = \sum_n \left[\langle r^2\rangle_n - \bar{\mathbf{r}}_n^2\right]. \tag{197}$$

$\bar{\mathbf{r}}_n$ is the expectation value of the position operator $\mathbf{r} = i\nabla_{\mathbf{k}}$ called the Wannier charge center. The localization functional Ω can be further decompose into gauge-invariant Ω_I and gauge-dependent $\tilde{\Omega}$ part, $\Omega = \Omega_I + \tilde{\Omega}$, where

$$\begin{aligned}\Omega_I &= \sum_n \left[\langle r^2\rangle_n - \sum_{\mathbf{R}m} |\,\langle W_m(\mathbf{R})|\mathbf{r}|W_n(\mathbf{0})\rangle\,|^2\right],\\ \tilde{\Omega} &= \sum_n \sum_{\mathbf{R}m\neq\mathbf{0}n} |\,\langle W_m(\mathbf{R})|\mathbf{r}|W_n(\mathbf{0})\rangle\,|^2.\end{aligned} \tag{198}$$

It fact, the minimization procedure of Ω corresponds to minimization of $\tilde{\Omega}$ part only. In $1D$, it is possible to find a unique gauge in which the maximally localized WFs are eigenstates

1 A reasonable set of Wannier functions can be also constructed by imposing different constrains, such as symmetries [401, 402].

of the band-projected position operator PxP with $P = \sum_{nk} |\psi_{nk}\rangle \langle \psi_{nk}|$. If PBC are used, the standard position operator x is ill-defined and the unitary operator $X = e^{i2\pi x/L}$ should be used instead [403]. In $2D$ and $3D$, though, WFs cannot be simultaneously localized in all directions due to non-commutativity of the operators PxP, PyP and PzP. There are also further obstructions to the construction of exponentially localized WFs in 2D systems with a non-zero Chern number [236–238] and non-trivial $\mathbb{Z}_2$ index [239].

We see that $1D$ systems are special, i. e. there are no topological obstructions to obtain maximally localized WFs. Therefore, it is possible to construct the WFs for higher dimensions in a way that they are exponentially localized in one direction, but Bloch-like in the other dimensions. Assuming z to be the direction in which the states will have Wannier-like character, we define the hybrid Wannier functions as

$$|W_{nl}(k_x, k_y)\rangle = \frac{1}{2\pi} \int dk_z e^{i\mathbf{k}\cdot(\mathbf{r}-lz)} |u_{n\mathbf{k}}\rangle , \tag{199}$$

where l is a layer index in z direction and the lattice constant between the layers is set to 1. Regardless of topological properties of a system, the hybrid WFs in Eq. (199) can be constructed at each (k_x, k_y) and their centers $\bar{z}_n(k_x, k_y) = \langle W_n(0)|z|W_n(0)\rangle$ are the eigenvalues of PzP. Momenta k_x and k_y remain good quantum numbers, hence $\bar{z}_n(k_x, k_y)$ can be plotted over the same $2D$ BZ, similar to the energy bands. The evolution of the Wannier centers along the line on (k_x, k_y)-plane is called the Wannier bands.

In continuum, the Wannier center $\bar{\mathbf{r}}_n$ can be computed as

$$\bar{\mathbf{r}}_n = \frac{V}{(2\pi)^3} \int_{\mathrm{BZ}} \langle u_{n\mathbf{k}}|i\nabla_{\mathbf{k}} u_{n\mathbf{k}}\rangle \, d\mathbf{k}, \tag{200}$$

which in $1D$ becomes

$$\bar{x}_n = \frac{a}{2\pi} \int_0^{2\pi} \langle u_{nk}|i\partial_k u_{nk}\rangle \, dk = a\frac{\gamma_n}{2\pi}. \tag{201}$$

Eq. (201) states that a Berry phase γ_n evolving from 0 to 2π corresponds to a Wannier center evolving from $x = 0$ to $x = a$.

B

ROTATION SYMMETRIES IN OBSTRUCTED ATOMIC LIMITS

B.1 CONSEQUENCES OF ROTATION SYMMETRY

To obtain the constraints on the symmetry eigenvalues used in the Chapter 4, we here derive the consequences of rotational symmetry for the Bloch eigenstates of a crystal. Rotation symmetry is expressed as

$$\hat{r}h(\mathbf{k})\hat{r}^\dagger = h(R\mathbf{k}). \tag{202}$$

Here, $\hat{r}$ is the n-fold rotation operator (we could also write this operator as $\hat{r}_n$, but we will omit the subscript for simplicity) and R is the matrix that rotates the crystal momentum by an angle of $\frac{2\pi}{n}$. For systems in class AII, the rotation operator obeys $\hat{r}^n = -1$. From (202), it follows that

$$h(R\mathbf{k})\hat{r}\left|u^n_{\mathbf{k}}\right\rangle = \hat{r}h(\mathbf{k})\left|u^n_{\mathbf{k}}\right\rangle = \epsilon_n(\mathbf{k})\hat{r}\left|u^n_{\mathbf{k}}\right\rangle. \tag{203}$$

Thus, $\hat{r}\left|u^n_{\mathbf{k}}\right\rangle$ is an eigenstate of $h(R\mathbf{k})$ with energy $\epsilon_n(\mathbf{k})$. This means that we can write the expansion

$$\hat{r}\left|u^n_{\mathbf{k}}\right\rangle = \sum_m \left|u^m_{R\mathbf{k}}\right\rangle \left\langle u^m_{R\mathbf{k}}\right| \hat{r}\left|u^n_{\mathbf{k}}\right\rangle = \sum_m \left|u_{R\mathbf{k}}\right\rangle B^{mn}_{\mathbf{k}}, \tag{204}$$

where $B^{mn}_{\mathbf{k}} = \left\langle u^m_{R\mathbf{k}}\right| \hat{r}\left|u^n_{\mathbf{k}}\right\rangle$ is the sewing matrix, which is unitary:

$$B^{ml}_{\mathbf{k}}(B^\dagger_{\mathbf{k}})^{ln} = \sum_l \left\langle u^m_{R\mathbf{k}}\right| \hat{r}\left|u^l_{\mathbf{k}}\right\rangle \left\langle u^l_{\mathbf{k}}\right| \hat{r}^\dagger \left|u^n_{R\mathbf{k}}\right\rangle = \left\langle u^m_{R\mathbf{k}}\right| \hat{r}\hat{r}^\dagger \left|u^n_{R\mathbf{k}}\right\rangle = \delta_{mn}. \tag{205}$$

As before, let us use (202) to do the following calculation:

$$\begin{aligned} h(R\mathbf{k})\hat{r}\left|u^n_{\mathbf{k}}\right\rangle &= \epsilon_n(\mathbf{k})\hat{r}\left|u^n_{\mathbf{k}}\right\rangle = \epsilon_n(\mathbf{k})\sum_m \left|u^m_{R\mathbf{k}}\right\rangle B^{mn}_{\mathbf{k}} \\ &= h(R\mathbf{k})\sum_m \left|u^m_{R\mathbf{k}}\right\rangle B^{mn}_{\mathbf{k}} = \sum_m \epsilon_m(R\mathbf{k})\left|u^m_{R\mathbf{k}}\right\rangle B^{mn}_{\mathbf{k}}, \end{aligned} \tag{206}$$

from which it follows that

$$\sum_m \left|u^m_{R\mathbf{k}}\right\rangle B^{mn}_{\mathbf{k}}(\epsilon_n(\mathbf{k}) - \epsilon_m(R\mathbf{k})) = 0. \tag{207}$$

for every n. Since the eigenstates form an orthonormal basis, the expression above implies that

$$B^{mn}_{\mathbf{k}}(\epsilon_n(\mathbf{k}) - \epsilon_m(R\mathbf{k})) = 0. \tag{208}$$

for every m and n. Equation (208) implies that the sewing matrix $B^{mn}_{\mathbf{k}}$ only connects states at $\mathbf{k}$ and $R\mathbf{k}$ having the same energy.

B.2 INVARIANT POINTS UNDER ROTATION

Now we focus on the high symmetry points of the BZ (HSPs). These are points that obey

$$R\mathbf{\Pi} = \mathbf{\Pi} \tag{209}$$

up to a reciprocal lattice vector. These points are shown in Fig. 42 for all the $C_{n=2,3,4,6}$ symmetries. At HSPs, Eq. (202) reduces to $\hat{r}h(\mathbf{\Pi})\hat{r}^\dagger = h(\mathbf{\Pi})$, where $\hat{r}$ here corresponds to the rotation operator of the little group at the HSP $\mathbf{\Pi}$. This expression is compactly written as

$$[\hat{r}, h(\mathbf{\Pi})] = 0. \tag{210}$$

Thus, it is possible to choose a gauge in which the energy eigenstates are also eigenstates of the rotation operator,

$$\hat{r}\left|u^n_{\mathbf{\Pi}}\right\rangle = r^n_{\mathbf{\Pi}}\left|u^n_{\mathbf{\Pi}}\right\rangle. \tag{211}$$

This is automatic if there are no degeneracies, but if energy degeneracies exist, one can always choose a gauge such that the above expression is possible. At these invariant points, the sewing matrix is diagonal:

$$B^{mn}_{\mathbf{\Pi}} = \left\langle u^m_{\mathbf{\Pi}}\right|\hat{r}\left|u^n_{\mathbf{\Pi}}\right\rangle = r^n_{\mathbf{\Pi}}\left\langle u^m_{\mathbf{\Pi}}\right\rangle u^n_{\mathbf{\Pi}} = r^n_{\mathbf{\Pi}}\delta_{mn}. \tag{212}$$

We show that the rotation eigenvalues of HSPs that are related by symmetry are equal. Consider the rotation by an angle ϕ in a crystal with $C_{2\pi/\phi}$ symmetry. This rotation symmetry relates HSPs that are invariant under rotations by a larger angle $\theta = n\phi$, for n integer. Call these HSPs $\mathbf{\Pi}_\theta$. Here, we are interested in knowing how the rotation eigenvalues of $\mathbf{\Pi}_\theta$ and $R_\phi\mathbf{\Pi}_\theta$ are related. In particular, this applies to two cases:

- In C_6-symmetric crystals, $\phi = 2\pi/6$. For $\theta_1 = 2\pi/3 = 2\phi$ we have $\mathbf{K} = R_\phi\mathbf{K}'$, while for $\theta_2 = \pi = 3\phi$ we have $\mathbf{M}' = R_\phi\mathbf{M} = R^2_\phi\mathbf{M}''$
- in C_4-symmetric crystals, $\phi = \pi/2$, for $\theta = \pi = 2\phi$ we have $\mathbf{X}' = R_\phi\mathbf{X}$.

Let us start by asking what we get from applying $\hat{r}_\theta\left|u^n_{R_\phi\mathbf{\Pi}_\theta}\right\rangle$. Since $R_\phi\mathbf{\Pi}_\theta$ is invariant under $\hat{r}_\theta$, we have

$$\hat{r}_\theta\left|u^n_{R_\phi\mathbf{\Pi}_\theta}\right\rangle = r^n_{R_\theta\mathbf{\Pi}_\theta}\left|u^n_{R_\phi\mathbf{\Pi}_\theta}\right\rangle. \tag{213}$$

Since $R_\phi\mathbf{\Pi}_\theta$ and $\mathbf{\Pi}_\theta$ are related by $C_{2\pi/\phi}$ symmetry, we can expand

$$\hat{r}_\phi\left|u^n_{\mathbf{\Pi}_\theta}\right\rangle = \sum_m \left|u^m_{R_\phi\mathbf{\Pi}_\theta}\right\rangle\left\langle u^m_{R_\phi\mathbf{\Pi}_\theta}\right|\hat{r}_\phi\left|u^n_{\mathbf{\Pi}_\theta}\right\rangle = \sum_m \left|u^m_{R_\phi\mathbf{\Pi}_\theta}\right\rangle B^{mn}_{\mathbf{\Pi}_\theta}, \tag{214}$$

where $B^{mn}_{\mathbf{\Pi}_\theta} = \left\langle u^m_{R_\phi\mathbf{\Pi}_\theta}\right|\hat{r}_\phi\left|u^n_{\mathbf{\Pi}_\theta}\right\rangle$ is the sewing matrix, with the properties shown before. Conversely, we also have that

$$\left|u^n_{R_\phi\mathbf{\Pi}_\theta}\right\rangle = \sum_m \hat{r}_\phi\left|u^m_{\mathbf{\Pi}_\theta}\right\rangle\left[B^\dagger_{\mathbf{\Pi}_\theta}\right]^{mn}. \tag{215}$$

So, replacing this expansion in (213), we have

$$\hat{r}_\theta\left|u^n_{R_\phi\mathbf{\Pi}_\theta}\right\rangle = \hat{r}_\phi\sum_m r^n_{R_\theta\mathbf{\Pi}_\theta}\left|u^m_{\mathbf{\Pi}_\theta}\right\rangle\left[B^\dagger_{\mathbf{\Pi}_\theta}\right]^{mn}. \tag{216}$$

Taking a different approach, we calculate directly the rotation eigenvalues in the expansion (215) to get

$$\begin{aligned}\hat{r}_\theta \left|u^n_{R_\phi \mathbf{\Pi}_\theta}\right\rangle &= \hat{r}_\theta \sum_m \hat{r}_\phi \left|u^m_{\mathbf{\Pi}_\theta}\right\rangle \left[B^\dagger_{\mathbf{\Pi}_\theta}\right]^{mn} \\ &= \hat{r}_\phi \sum_m \hat{r}_\theta \left|u^m_{\mathbf{\Pi}_\theta}\right\rangle \left[B^\dagger_{\mathbf{\Pi}_\theta}\right]^{mn} \\ &= \hat{r}_\phi \sum_m r^m_{\mathbf{\Pi}_\theta} \left|u^m_{\mathbf{\Pi}_\theta}\right\rangle \left[B^\dagger_{\mathbf{\Pi}_\theta}\right]^{mn}.\end{aligned} \tag{217}$$

So, comparing the last two results we conclude that

$$\sum_m (r^n_{R_\phi \mathbf{\Pi}_\theta} - r^m_{\mathbf{\Pi}_\theta}) \left|u^m_{\mathbf{\Pi}_\theta}\right\rangle \left[B^\dagger_{\mathbf{\Pi}_\theta}\right]^{mn} = 0. \tag{218}$$

for all n. Furthermore, since the eigenstates form an orthonormal basis, we have

$$(r^n_{R_\phi \mathbf{\Pi}_\theta} - r^m_{\mathbf{\Pi}_\theta}) \left[B^\dagger_{\mathbf{\Pi}_\theta}\right]^{mn} = 0, \tag{219}$$

for all m and n. Now, the sewing matrix will have non-zero elements for equal energies at the two different HSPs $R_\phi \mathbf{\Pi}_\theta$ and $\mathbf{\Pi}_\theta$. Thus, for $\epsilon_m(R_\phi \mathbf{\Pi}_\theta) = \epsilon_n(\mathbf{\Pi}_\theta)$, we need $r^m_{\mathbf{\Pi}_\theta} = r^n_{R_\phi \mathbf{\Pi}_\theta}$, i.e., the rotation spectra at $R_\phi \mathbf{\Pi}_\theta$ and $\mathbf{\Pi}_\theta$ are equal for bands having equal energies. In particular, we have the relations

$$\begin{aligned}\{r^n_{\mathbf{K}}\} &\overset{C_6}{=} \{r^n_{\mathbf{K}'}\}, \\ \{r^n_{\mathbf{M}}\} &\overset{C_6}{=} \{r^n_{\mathbf{M}'}\} \overset{C_6}{=} \{r^n_{\mathbf{M}''}\}, \\ \{r^n_{\mathbf{X}}\} &\overset{C_4}{=} \{r^n_{\mathbf{X}'}\}.\end{aligned} \tag{220}$$

B.3 CONSTRAINTS ON THE ROTATION EIGENVALUES DUE TO TIME-REVERSAL SYMMETRY

Now we look at the interplay between TRS and rotation symmetry. The two operators commute:

$$[\mathcal{T}, \hat{r}] = 0. \tag{221}$$

Thus, on one hand we have

$$\mathcal{T}\left(\hat{r}\left|u^l_{\mathbf{k}}\right\rangle\right) = \mathcal{T}\left(\sum_n \left|u^n_{R\mathbf{k}}\right\rangle B^{nl}_{\mathbf{k}}\right) = \sum_{m,n} \left|u^m_{-R\mathbf{k}}\right\rangle V^{mn}_{R\mathbf{k}} B^{nl*}_{\mathbf{k}}, \tag{222}$$

where V is the sewing matrix for TRS. On the other hand, we have

$$\hat{r}\left(\mathcal{T}\left|u^l_{\mathbf{k}}\right\rangle\right) = \hat{r}\left(\sum_m \left|u^n_{-\mathbf{k}}\right\rangle V^{nl}_{\mathbf{k}}\right) = \sum_{m,n} \left|u^m_{-R\mathbf{k}}\right\rangle B^{mn}_{-\mathbf{k}} V^{nl}_{\mathbf{k}}. \tag{223}$$

In the last expression, we have used the fact that $R(-\mathbf{k}) = -R\mathbf{k}$. From these two expressions we conclude that

$$\sum_{m,n} \left|u^m_{-R\mathbf{k}}\right\rangle \left(V^{mn}_{R\mathbf{k}} B^{nl*}_{\mathbf{k}} - B^{mn}_{-\mathbf{k}} V^{nl}_{\mathbf{k}}\right) = 0 \tag{224}$$

for all l. Since the eigenstates are orthonormal, this relation implies that

$$\sum_n \left(V^{mn}_{R\mathbf{k}} B^{nl*}_{\mathbf{k}} - B^{mn}_{-\mathbf{k}} V^{nl}_{\mathbf{k}} \right) = 0 \tag{225}$$

for all m, l. As noted earlier, of particular interest are the HSPs. At these points, $B^{mn}_{\mathbf{\Pi}} = r^n_{\mathbf{\Pi}} \delta_{mn}$ in the gauge in which $\{|u^n_{\mathbf{\Pi}}\rangle\}$ are rotation eigenstates. Then, at these points, the previous relation results in

$$V^{ml}_{\mathbf{\Pi}} \left(r^{l*}_{\mathbf{\Pi}} - r^m_{-\mathbf{\Pi}} \right) = 0 \tag{226}$$

for all l, m. Thus, if $V^{ml}_{\mathbf{\Pi}} \neq 0$, $r^{l*}_{\mathbf{\Pi}} = r^m_{-\mathbf{\Pi}}$. This is possible only if $\epsilon_m(-\mathbf{\Pi}) = \epsilon_l(\mathbf{\Pi})$. Thus, we have that, under TRS,

$$\{r^n_{\mathbf{\Pi}}\} \overset{\text{TRS}}{=} \{r^{n*}_{-\mathbf{\Pi}}\}. \tag{227}$$

More specifically, for equal energies at $\mathbf{k} = \mathbf{\Pi}$ and $\mathbf{k} = -\mathbf{\Pi}$, their rotation eigenvalues are complex conjugates of each other [if, on the other hand, $\epsilon_m(-\mathbf{\Pi}) \neq \epsilon_l(\mathbf{\Pi})$, we have that $V^{ml}_{\mathbf{\Pi}} = 0$, which means that there is no restriction on the rotation eigenvalues]. In particular, at TRIMs which are also HSPs, $\mathbf{\Pi} = -\mathbf{\Pi}$, we have that $r^{l*}_{\mathbf{\Pi}} = r^m_{\mathbf{\Pi}}$ for equal energies $\epsilon_m(\mathbf{\Pi}) = \epsilon_l(\mathbf{\Pi})$. This imposes the following constraints on the rotation eigenvalues:

- for a non-degenerate state labeled by n, $r^{n*}_{\mathbf{\Pi}} = r^n_{\mathbf{\Pi}}$, i.e., its rotation eigenvalue is real: $r^n_{\mathbf{\Pi}} = \pm 1$
- for two degenerate states $n = 1, 2$ one could have $r^1_{\mathbf{\Pi}} = \lambda$ and $r^2_{\mathbf{\Pi}} = \lambda^*$, so that $r^{1*}_{\mathbf{\Pi}} = \lambda^* = r^2_{\mathbf{\Pi}}$ and $r^{2*}_{\mathbf{\Pi}} = \lambda = r^1_{\mathbf{\Pi}}$, that is, in energy-degenerate states, the rotation eigenvalues can be complex, but have to come in complex conjugate pairs.

As said before, these constraints follow for HSPs that are also TRIM. This is the case for all the HSPs except $\mathbf{K}$ and $\mathbf{K}'$, which map into each other under TRS.

B.4 MAPPING BETWEEN SPINLESS AND SPINFUL C_3 EIGENVALUES

We start with the spinless indicators

$$[\tilde{K}^{(3)}_i] = \#\tilde{K}^{(3)}_i - \#\tilde{\Gamma}^{(3)}_i, \tag{228}$$

where $\tilde{K}^{(3)}_{i=1,2,3}$, $\tilde{\Gamma}^{(3)}_{i=1,2,3} = \{1, e^{i2\pi/3}, e^{-i2\pi/3}\}$. Upon introducing spin degree of freedom, each spinless eigenvalue λ contributes two spinful eigenvalues $\lambda\, e^{\pm i\pi/3}$. From this we obtain the relations

$$\begin{aligned} [K^{(3)}_1] &= [\tilde{K}^{(3)}_1] + [\tilde{K}^{(3)}_2], \\ [K^{(3)}_2] &= [\tilde{K}^{(3)}_2] + [\tilde{K}^{(3)}_3], \\ [K^{(3)}_3] &= [\tilde{K}^{(3)}_3] + [\tilde{K}^{(3)}_1], \end{aligned} \tag{229}$$

where the $[K^{(3)}_i]$, $i = 1, 2, 3$, are defined in Eq. (143). Together with the constraints in Eq. (145) this implies

$$\begin{aligned} [\tilde{K}^{(3)}_1] &= -[K^{(3)}_2], \\ [\tilde{K}^{(3)}_2] &= -[K^{(3)}_3], \\ [\tilde{K}^{(3)}_3] &= -[K^{(3)}_1], \end{aligned} \tag{230}$$

providing a mapping between spinless and spinful C_3 eigenvalues.

C

INDUCTION OF BAND REPRESENTATIONS FROM MAXIMAL WYCKOFF POSITIONS AND RELATION TO SYMMETRY INDICATOR INVARIANTS

Here, we explicitly induce the energy band representations at HSPs of the BZ following the prescription in Ref. [268]. Given a site symmetry representation, the induced band representation will allow us to identify the symmetry indicator invariants associated with a maximal Wyckoff position. In this section, we induce the band representations and corresponding symmetry indicator invariants for all the allowed site symmetry representations of spinful time-reversal symmetric orbitals at each maximal Wyckoff position. In the following, ρ refers to the representation of the site symmetry group, while $\rho_G^{\mathbf{k}}$ refers to the band representation at crystal momentum $\mathbf{k}$. We treat each case separately. For C_4 and C_2 symmetries, we use the following primitive vectors $\mathbf{a}_1 = (1,0)$, $\mathbf{a}_2 = (0,1)$, and for both C_6 and C_3 symmetries, we use the following primitive vectors $\mathbf{a}_1 = (1,0)$, $\mathbf{a}_2 = (\frac{1}{2}, \frac{\sqrt{3}}{2})$ and $\mathbf{a}_3 = (-\frac{1}{2}, \frac{\sqrt{3}}{2})$.

C.1 C_4 SYMMETRY: REPRESENTATIONS INDUCED FROM $2c$

Given a site symmetry representation $\rho(C_2)$ of the orbitals at $2c$, the band representations are

$$\rho_G^{\mathbf{k}}(C_4) = \begin{pmatrix} 0 & e^{i\mathbf{k}\cdot\mathbf{a}_1}\rho(C_2) \\ 1 & 0 \end{pmatrix}, \quad \rho_G^{\mathbf{k}}(C_2) = \begin{pmatrix} e^{i\mathbf{k}\cdot\mathbf{a}_1} & 0 \\ 0 & e^{i\mathbf{k}\cdot\mathbf{a}_2} \end{pmatrix} \rho(C_2). \tag{231}$$

We consider the only possible site-symmetry representation, $\rho(C_2) = e^{i\frac{\pi}{2}\sigma_z}$. For C_4, the band representations at HSPs are

$$\rho_G^{\Gamma}(C_4) = \begin{pmatrix} 0 & e^{i\frac{\pi}{2}\sigma_z} \\ 1 & 0 \end{pmatrix}, \quad \rho_G^{\mathbf{M}}(C_4) \ = \begin{pmatrix} 0 & -e^{i\frac{\pi}{2}\sigma_z} \\ 1 & 0 \end{pmatrix}.$$

Both of these matrices have the four eigenvalues $e^{i\pi/4}$, $e^{-i\pi/4}$, $e^{3i\pi/4}$, $e^{-3i\pi/4}$. Therefore, $[M_1^{(4)}] = 0$. For C_2, the band representations at HSPs are

$$\begin{aligned} \rho_G^{\Gamma}(C_2) &= \sigma_0 e^{i\frac{\pi}{2}\sigma_z}, \quad & \rho_G^{\mathbf{X}}(C_2) &= -\sigma_z e^{i\frac{\pi}{2}\sigma_z}, \\ \rho_G^{\mathbf{Y}}(C_2) &= \sigma_z e^{i\frac{\pi}{2}\sigma_z}, \quad & \rho_G^{\mathbf{M}}(C_2) &= -\sigma_0 e^{i\frac{\pi}{2}\sigma_z}. \end{aligned} \tag{232}$$

All these matrices have eigenvalues $+i$, $+i$, $-i$, $-i$, also leading to vanishing symmetry indicators. As we will see, this is also the case when the band representations are induced from $1b$: in fact, with spinful time-reversal symmetry, the only possible EBR is given by a pair of states with C_2 eigenvalues $(+i, -i)$. Therefore, no symmetry indicators exist associated with the band representations of C_2.

C.2 C_4 SYMMETRY: REPRESENTATIONS INDUCED FROM $1b$

Given a site symmetry representation $\rho(C_4)$ of the orbitals at $1b$, the band representations are

$$\rho_G^{\mathbf{k}}(C_4) = e^{i\mathbf{k}\cdot\mathbf{a}_1}\rho(C_4), \quad \rho_G^{\mathbf{k}}(C_2) = e^{i\mathbf{k}\cdot(\mathbf{a}_1+\mathbf{a}_2)}\rho(C_2). \tag{233}$$

where $\rho(C_2) = \rho^2(C_4)$. Let us consider the site symmetry representation $\rho(C_4) = e^{i\frac{\pi}{4}\sigma_z}$. For C_4, the band representations at HSPs are

$$\rho_G^{\mathbf{\Gamma}}(C_4) = e^{i\frac{\pi}{4}\sigma_z}, \quad \rho_G^{\mathbf{M}}(C_4) = -e^{i\frac{\pi}{4}\sigma_z}.$$

The matrix for the band representation of C_4 at $\mathbf{\Gamma}$ has eigenvalues $e^{i\pi/4}$, $e^{-i\pi/4}$, while the one at $\mathbf{M}$ has eigenvalues $e^{3i\pi/4}$, $e^{-3i\pi/4}$. Thus, $[M_1^{(4)}] = 1$. Now, if the site symmetry representation were $\rho(C_4) = -e^{i\frac{\pi}{4}\sigma_z}$ instead, the band representations at $\mathbf{\Gamma}$ and $\mathbf{M}$ would flip. This leads to the symmetry indicator invariant $[M_1^{(4)}] = -1$. For C_2, the band representations are always of the form $\pm e^{i\frac{\pi}{2}\sigma_z}$, which has eigenvalues $+i$, $-i$, leading to vanishing symmetry indicators.

Let us now consider obstructions arising from the band representation when multiple orbitals localize at $1b$. If the two orbitals have the same representation, e. g., $\rho(C_4) = e^{i\frac{\pi}{4}\sigma_z}$, the overall site symmetry representation, $\sigma_0\, e^{i\frac{\pi}{4}\sigma_z}$, induces a band representation with invariant $[M_1^{(4)}] = 2$. If, on the other hand, the representations at the two orbitals differ, the induced band representations will have an invariant $[M_1^{(4)}] = 0$. Both cases, however, are obstructed, because it is not possible to smoothly move two Kramers pairs from $1b$ to $1a$ in a C_4 symmetric way. We see from this analysis that other invariants must exist beyond symmetry indicators that capture the obstruction of the case of two Kramers pairs with $[M_1^{(4)}] = 0$.

C.3 C_6 SYMMETRY: REPRESENTATIONS INDUCED FROM $2b$

Let $\rho(C_3)$ be a site-symmetry representation of the orbitals at $2b$. Therefore, the band representations are

$$\begin{aligned}\rho_G^{\mathbf{k}}(C_3) &= \begin{pmatrix} e^{i\mathbf{k}\cdot a_1} & 0 \\ 0 & e^{-i\mathbf{k}\cdot a_1}\end{pmatrix}\rho(C_3),\\ \rho_G^{\mathbf{k}}(C_2) &= \begin{pmatrix} 0 & -1 \\ 1 & 0\end{pmatrix}\mathbb{1}_{2N\times 2N},\end{aligned} \tag{234}$$

where N is the number of Kramers pairs in the site $2b$. Consider one Kramers pair at $2b$. For C_3, the band representations at the HSPs are

$$\rho_G^{\mathbf{\Gamma}}(C_3) = \rho(C_3), \quad \rho_G^{\mathbf{K}}(C_3) = e^{i\frac{2\pi}{3}\sigma_z}\rho(C_3).$$

Thus, for the site symmetry representation $\rho(C_3) = e^{in\frac{\pi}{3}\sigma_z}$ (for $n = 1$ or $n = 3$), the eigenvalues are $e^{in\frac{\pi}{3}}$, $e^{-in\frac{\pi}{3}}$ at $\mathbf{\Gamma}$, and $e^{i\frac{\pi}{3}(n+2)}$, $e^{-i\frac{\pi}{3}(n+2)}$ at $\mathbf{K}$. This yields the invariants in Table 14.

Notice, from the invariants in Table 14, that the obstruction is lifted only if three Kramers pairs locate at $2b$, two with representations $e^{i\frac{\pi}{3}\sigma_z}$ and one with $-\sigma_0$. This illustrates the fact that the number of Kramers pairs at a maximal Wyckoff position alone does not determine whether an OAL is trivial. The site symmetry representation is crucial; they determine whether the Kramers pairs are free to move symmetrically or not. Regarding C_2, it follows from the lack of dependence of $\rho_G^{\mathbf{k}}(C_2)$ on the crystal momentum, that all invariants vanish.

Site symmetry	Eigenvalues $\mathbf{\Gamma}$	Eigenvalues $\mathbf{K}$	Invariants
$e^{\mathrm{i}\frac{\pi}{3}\sigma_z}$	$\#\Gamma_1 = 2$	$\#K_1 = 1$	$[K_1^{(3)}] = -1$
	$\#\Gamma_2 = 0$	$\#K_2 = 2$	$[K_2^{(3)}] = 2$
	$\#\Gamma_3 = 2$	$\#K_3 = 1$	$[K_3^{(3)}] = -1$
$-\sigma_0$	$\#\Gamma_1 = 0$	$\#K_1 = 2$	$[K_1^{(3)}] = 2$
	$\#\Gamma_2 = 4$	$\#K_2 = 0$	$[K_2^{(3)}] = -4$
	$\#\Gamma_3 = 0$	$\#K_3 = 2$	$[K_3^{(3)}] = 2$

Table 14: C_6 symmetry: C_3 invariants induced from Wyckoff position $2b$ with different site symmetry representations

C.4 C_6 SYMMETRY: REPRESENTATIONS INDUCED FROM $3c$

With a site-symmetry representation $\rho(C_2)$ of the orbitals at $3c$, the band representations are

$$\begin{aligned}\rho_G^{\mathbf{k}}(C_3) &= \begin{pmatrix} 0 & 0 & -1 \\ 1 & 0 & 0 \\ 0 & 1 & 0 \end{pmatrix} \mathbb{1}_{2N\times 2N}, \\ \rho_G^{\mathbf{k}}(C_2) &= \begin{pmatrix} e^{\mathrm{i}\mathbf{k}\cdot\mathbf{a}_2} & 0 & \\ 0 & e^{-\mathrm{i}\mathbf{k}\cdot\mathbf{a}_1} & 0 \\ 0 & 0 & e^{-\mathrm{i}\mathbf{k}\cdot\mathbf{a}_3} \end{pmatrix} \rho(C_2),\end{aligned} \tag{235}$$

where N denotes the number of Kramers pairs in the site $3c$. For C_3, the band representation is constant across the C_3-invariant HSPs. Therefore, all invariants are trivial. For C_2, the band representations at the HSPs are

$$\rho_G^{\mathbf{\Gamma}}(C_2) = \mathbb{1}_{2\times 2}\,\rho(C_2), \quad \rho_G^{\mathbf{M}}(C_2) = \begin{pmatrix} -1 & 0 & 0 \\ 0 & -1 & 0 \\ 0 & 0 & 1 \end{pmatrix} \rho(C_2). \tag{236}$$

But since the site representation for a Kramers pair, $\rho(C_2) = e^{\mathrm{i}\frac{\pi}{2}\sigma_z}$, has eigenvalues $+i$, $-i$, the band representations at $\mathbf{\Gamma}$ and $\mathbf{M}$ are the same.

C.5 C_3 SYMMETRY: REPRESENTATIONS INDUCED FROM $1b$

For a given site-symmetry representation $\rho(C_3)$ of the orbitals at $1b$, the band representations are

$$\rho_G^{\mathbf{k}}(C_3) = e^{\mathrm{i}\mathbf{k}\cdot\mathbf{a}_2}\rho(C_3). \tag{237}$$

The band representations at the HSPs are then

$$\rho_G^{\mathbf{\Gamma}}(C_3) = \rho(C_3), \quad \rho_G^{\mathbf{K}}(C_3) = e^{\mathrm{i}\frac{2\pi}{3}}\rho(C_3), \quad \rho_G^{\mathbf{K}'}(C_3) = e^{-\mathrm{i}\frac{2\pi}{3}}\rho(C_3).$$

Thus, the invariants depend on the site symmetry representation $\rho(C_3)$. They are shown in Table 15. Since TRS relates $\mathbf{K}$ with $\mathbf{K}'$, we only provide the representations at $\mathbf{\Gamma}$ and $\mathbf{K}$. Note

Site symmetry	Eigenvalues $\mathbf{\Gamma}$	Eigenvalues $\mathbf{K}$	Invariants
$e^{\mathrm{i}\frac{\pi}{3}\sigma_z}$	$\#\Gamma_1 = 1$ $\#\Gamma_2 = 0$ $\#\Gamma_3 = 1$	$\#K_1 = 1$ $\#K_2 = 1$ $\#K_3 = 0$	$[K_1^{(3)}] = 0$ $[K_2^{(3)}] = 1$ $[K_3^{(3)}] = -1$
$-\sigma_0$	$\#\Gamma_1 = 0$ $\#\Gamma_2 = 2$ $\#\Gamma_3 = 0$	$\#K_1 = 0$ $\#K_2 = 0$ $\#K_3 = 2$	$[K_1^{(3)}] = 0$ $[K_2^{(3)}] = -2$ $[K_3^{(3)}] = 2$

Table 15: C_3 symmetry: C_3 invariants induced from Wyckoff position $1b$ with different site symmetry representations.

that, in order to have a trivial insulator with three movable Kramers pairs at $1b$, two of them need to have the representation $e^{\mathrm{i}\frac{\pi}{3}\sigma_z}$ and the third one the representation $-\sigma_0$.

C.6 C_3 SYMMETRY: REPRESENTATIONS INDUCED FROM $1c$

Given a site-symmetry representation $\rho(C_3)$ of the orbitals at $1c$, the band representations read

$$\rho_G^{\mathbf{k}}(C_3) = e^{\mathrm{i}\mathbf{k}\cdot\mathbf{a}_1}\rho(C_3). \tag{238}$$

Then, the band representations at the HSPs are

$$\rho_G^{\mathbf{\Gamma}}(C_3) = \rho(C_3), \quad \rho_G^{\mathbf{K}}(C_3) = e^{-\mathrm{i}\frac{2\pi}{3}}\rho(C_3), \quad \rho_G^{\mathbf{K}'}(C_3) = e^{\mathrm{i}\frac{2\pi}{3}}\rho(C_3).$$

As in the case of $1b$, the invariants depend on the site symmetry representation $\rho(C_3)$. We are show them in Table 16. In order to have a trivial insulator with three movable Kramers pairs at

Site symmetry	Eigenvalues $\mathbf{\Gamma}$	Eigenvalues $\mathbf{K}$	Invariants
$e^{\mathrm{i}\frac{\pi}{3}\sigma_z}$	$\#\Gamma_1 = 1$ $\#\Gamma_2 = 0$ $\#\Gamma_3 = 1$	$\#K_1 = 0$ $\#K_2 = 1$ $\#K_3 = 1$	$[K_1^{(3)}] = -1$ $[K_2^{(3)}] = 1$ $[K_3^{(3)}] = 0$
$-\sigma_0$	$\#\Gamma_1 = 0$ $\#\Gamma_2 = 2$ $\#\Gamma_3 = 0$	$\#K_1 = 2$ $\#K_2 = 0$ $\#K_3 = 0$	$[K_1^{(3)}] = 2$ $[K_2^{(3)}] = -2$ $[K_3^{(3)}] = 0$

Table 16: C_3 symmetry: C_3 invariants induced from Wyckoff position $1c$ with different site symmetry representations.

$1c$, two of them need to have the representation $e^{\mathrm{i}\frac{\pi}{3}\sigma_z}$ and the third one the representation $-\sigma_0$.

C.7 C_2 SYMMETRY: REPRESENTATIONS INDUCED FROM ANY C_2 INVARIANT HSP

All the invariants due to C_2 are trivial, since all C_2-invariants points are also TRIM points and the C_2 eigenvalues of the site symmetry group of Kramers pairs is always $+\mathrm{i}$, $-\mathrm{i}$, which exhausts the representations.

BIBLIOGRAPHY

1. V. L. Ginzburg, L. D. Landau, "On the Theory of superconductivity", *Zh. Eksp. Teor. Fiz.* **20**, 1064–1082 (1950).
2. V. Berezinsky, "Destruction of long range order in one-dimensional and two-dimensional systems having a continuous symmetry group. I. Classical systems", *Sov. Phys. JETP* **32**, 493–500 (1971).
3. V. L. Berezinsky, "Destruction of Long-range Order in One-dimensional and Two-dimensional Systems Possessing a Continuous Symmetry Group. II. Quantum Systems.", *Sov. Phys. JETP* **34**, 610 (1972).
4. J. M. Kosterlitz, D. J. Thouless, "Long range order and metastability in two dimensional solids and superfluids", *Journal of Physics C: Solid State Physics* **5**, L124–L126 (1972).
5. J. M. Kosterlitz, D. J. Thouless, "Ordering, metastability and phase transitions in two-dimensional systems", *Journal of Physics C: Solid State Physics* **6**, 1181–1203 (1973).
6. K. v. Klitzing, G. Dorda, M. Pepper, "New Method for High-Accuracy Determination of the Fine-Structure Constant Based on Quantized Hall Resistance", *Phys. Rev. Lett.* **45**, 494–497 (6 1980).
7. D. C. Tsui, H. L. Stormer, A. C. Gossard, "Two-Dimensional Magnetotransport in the Extreme Quantum Limit", *Phys. Rev. Lett.* **48**, 1559–1562 (22 1982).
8. P. J. Mohr, D. B. Newell, B. N. Taylor, "CODATA Recommended Values of the Fundamental Physical Constants: 2014", *Journal of Physical and Chemical Reference Data* **45**, 043102 (2016).
9. D. J. Thouless, M. Kohmoto, M. P. Nightingale, M. den Nijs, "Quantized Hall Conductance in a Two-Dimensional Periodic Potential", *Phys. Rev. Lett.* **49**, 405–408 (6 1982).
10. Y. Hatsugai, "Chern number and edge states in the integer quantum Hall effect", *Phys. Rev. Lett.* **71**, 3697–3700 (22 1993).
11. X.-G. Wen, "Colloquium: Zoo of quantum-topological phases of matter", *Rev. Mod. Phys.* **89**, 041004 (4 2017).
12. C. Nayak, S. H. Simon, A. Stern, M. Freedman, S. Das Sarma, "Non-Abelian anyons and topological quantum computation", *Rev. Mod. Phys.* **80**, 1083–1159 (3 2008).
13. F. D. M. Haldane, "Model for a Quantum Hall Effect without Landau Levels: Condensed-Matter Realization of the "Parity Anomaly"", *Phys. Rev. Lett.* **61**, 2015–2018 (18 1988).
14. C. L. Kane, E. J. Mele, "Quantum Spin Hall Effect in Graphene", *Phys. Rev. Lett.* **95**, 226801 (22 2005).
15. C. L. Kane, E. J. Mele, "Z_2 Topological Order and the Quantum Spin Hall Effect", *Phys. Rev. Lett.* **95**, 146802 (14 2005).
16. B. A. Bernevig, T. L. Hughes, S.-C. Zhang, "Quantum Spin Hall Effect and Topological Phase Transition in HgTe Quantum Wells", *Science* **314**, 1757–1761 (2006).

17. M. König, S. Wiedmann, C. Brüne, A. Roth, H. Buhmann, L. W. Molenkamp, X.-L. Qi, S.-C. Zhang, "Quantum Spin Hall Insulator State in HgTe Quantum Wells", *Science* **318**, 766–770 (2007).

18. L. Fu, C. L. Kane, E. J. Mele, "Topological Insulators in Three Dimensions", *Phys. Rev. Lett.* **98**, 106803 (10 2007).

19. J. E. Moore, L. Balents, "Topological invariants of time-reversal-invariant band structures", *Phys. Rev. B* **75**, 121306 (12 2007).

20. R. Roy, "Topological phases and the quantum spin Hall effect in three dimensions", *Phys. Rev. B* **79**, 195322 (19 2009).

21. D. Hsieh, D. Qian, L. Wray, Y. Xia, Y. S. Hor, R. J. Cava, M. Z. Hasan, "A topological Dirac insulator in a quantum spin Hall phase", *Nature* **452**, 970–974 (2008).

22. H. Zhang, C.-X. Liu, X.-L. Qi, X. Dai, Z. Fang, S.-C. Zhang, "Topological insulators in Bi2Se3, Bi2Te3 and Sb2Te3 with a single Dirac cone on the surface", *Nature Physics* **5**, 438–442 (2009).

23. Y. Xia, D. Qian, D. Hsieh, L. Wray, A. Pal, H. Lin, A. Bansil, D. Grauer, Y. S. Hor, R. J. Cava, M. Z. Hasan, "Observation of a large-gap topological-insulator class with a single Dirac cone on the surface", *Nature Physics* **5**, 398–402 (2009).

24. A. P. Schnyder, S. Ryu, A. Furusaki, A. W. W. Ludwig, "Classification of topological insulators and superconductors in three spatial dimensions", *Phys. Rev. B* **78**, 195125 (19 2008).

25. S. Ryu, A. P. Schnyder, A. Furusaki, A. W. W. Ludwig, "Topological insulators and superconductors: tenfold way and dimensional hierarchy", *New Journal of Physics* **12**, 065010 (2010).

26. A. Kitaev, "Periodic table for topological insulators and superconductors", *AIP Conference Proceedings* **1134**, 22–30 (2009).

27. A. Altland, M. R. Zirnbauer, "Nonstandard symmetry classes in mesoscopic normal-superconducting hybrid structures", *Phys. Rev. B* **55**, 1142–1161 (2 1997).

28. X.-L. Qi, S.-C. Zhang, "Topological insulators and superconductors", *Rev. Mod. Phys.* **83**, 1057–1110 (4 2011).

29. Z. Zhou, L.-L. Wan, Z.-F. Xu, "Classification of Topological Excitations in Quadratic Bosonic Systems", *arXiv:1905.07989* (2019).

30. R. Süsstrunk, S. D. Huber, "Classification of topological phonons in linear mechanical metamaterials", *Proceedings of the National Academy of Sciences* **113**, E4767–E4775 (2016).

31. J. Hu, S.-Y. Xu, N. Ni, Z. Mao, "Transport of Topological Semimetals", *Annual Review of Materials Research* **49**, 207–252 (2019).

32. A. P. Schnyder, P. M. R. Brydon, "Topological surface states in nodal superconductors", *Journal of Physics: Condensed Matter* **27**, 243201 (2015).

33. T. Morimoto, A. Furusaki, "Topological classification with additional symmetries from Clifford algebras", *Phys. Rev. B* **88**, 125129 (12 2013).

34. C.-K. Chiu, A. P. Schnyder, "Classification of reflection-symmetry-protected topological semimetals and nodal superconductors", *Phys. Rev. B* **90**, 205136 (20 2014).

35. C.-K. Chiu, J. C. Y. Teo, A. P. Schnyder, S. Ryu, "Classification of topological quantum matter with symmetries", *Rev. Mod. Phys.* **88**, 035005 (3 2016).

36. R. Roy, F. Harper, "Periodic table for Floquet topological insulators", *Phys. Rev. B* **96**, 155118 (15 2017).

37. K. Shiozaki, M. Sato, "Topology of crystalline insulators and superconductors", *Phys. Rev. B* **90**, 165114 (16 2014).

38. E. Cornfeld, A. Chapman, "Classification of crystalline topological insulators and superconductors with point group symmetries", *Phys. Rev. B* **99**, 075105 (7 2019).

39. Y. Ando, L. Fu, "Topological Crystalline Insulators and Topological Superconductors: From Concepts to Materials", *Annual Review of Condensed Matter Physics* **6**, 361–381 (2015).

40. F. Schindler, Z. Wang, M. G. Vergniory, A. M. Cook, A. Murani, S. Sengupta, A. Y. Kasumov, R. Deblock, S. Jeon, I. Drozdov, H. Bouchiat, S. Guéron, A. Yazdani, B. A. Bernevig, T. Neupert, "Higher-order topology in bismuth", *Nature Physics* **14**, 918–924 (2018).

41. C. C. Wojcik, X.-Q. Sun, T. Bzdušek, S. Fan, "Homotopy characterization of non-Hermitian Hamiltonians", *Phys. Rev. B* **101**, 205417 (20 2020).

42. K. Kawabata, K. Shiozaki, M. Ueda, M. Sato, "Symmetry and Topology in Non-Hermitian Physics", *Phys. Rev. X* **9**, 041015 (4 2019).

43. H. Shen, B. Zhen, L. Fu, "Topological Band Theory for Non-Hermitian Hamiltonians", *Phys. Rev. Lett.* **120**, 146402 (14 2018).

44. M. Nakahara, *Geometry, Topology and Physics, Second Edition* (Taylor & Francis, 2003).

45. E. Wigner, H. Massey, *Group Theory: And Its Application to the Quantum Mechanics of Atomic Spectra* (Elsevier Science, 2013).

46. F. J. Dyson, "The Threefold Way. Algebraic Structure of Symmetry Groups and Ensembles in Quantum Mechanics", *Journal of Mathematical Physics* **3**, 1199–1215 (1962).

47. P. W. Anderson, "Absence of Diffusion in Certain Random Lattices", *Phys. Rev.* **109**, 1492–1505 (5 1958).

48. L. Fidkowski, A. Kitaev, "Effects of interactions on the topological classification of free fermion systems", *Phys. Rev. B* **81**, 134509 (13 2010).

49. N. Read, D. Green, "Paired states of fermions in two dimensions with breaking of parity and time-reversal symmetries and the fractional quantum Hall effect", *Phys. Rev. B* **61**, 10267–10297 (15 2000).

50. T. Mizushima, Y. Tsutsumi, M. Sato, K. Machida, "Symmetry protected topological superfluid ^{3}He-B", *Journal of Physics: Condensed Matter* **27**, 113203 (2015).

51. A. Y. Kitaev, "Unpaired Majorana fermions in quantum wires", *Physics-Uspekhi* **44**, 131–136 (2001).

52. T. Ozawa, H. M. Price, "Topological quantum matter in synthetic dimensions", *Nature Reviews Physics* **1**, 349–357 (2019).

53. H. Nielsen, M. Ninomiya, "The Adler-Bell-Jackiw anomaly and Weyl fermions in a crystal", *Physics Letters B* **130**, 389–396 (1983).

54. J. Kellendonk, T. Richter, H. Schulz-Baldes, "Edge current channels and Chern numbers in the integer quantum Hall effect", *Reviews in Mathematical Physics* **14**, 87–119 (2002).

55. T. Fukui, K. Shiozaki, T. Fujiwara, S. Fujimoto, "Bulk-Edge Correspondence for Chern Topological Phases: A Viewpoint from a Generalized Index Theorem", *Journal of the Physical Society of Japan* **81**, 114602 (2012).

56. T. A. Loring, "K-theory and pseudospectra for topological insulators", *Annals of Physics* **356**, 383–416 (2015).

57. G. M. Graf, M. Porta, "Bulk-Edge Correspondence for Two-Dimensional Topological Insulators", *Communications in Mathematical Physics* **324**, 851–895 (2013).

58. E. Prodan, H. Schulz-Baldes, *Bulk and boundary invariants for complex topological insulators* (Springer).

59. J. C. Y. Teo, C. L. Kane, "Topological defects and gapless modes in insulators and superconductors", *Phys. Rev. B* **82**, 115120 (11 2010).

60. F. Schindler, A. M. Cook, M. G. Vergniory, Z. Wang, S. S. P. Parkin, B. A. Bernevig, T. Neupert, "Higher-order topological insulators", *Science Advances* **4** (2018).

61. M. V. Berry, "Quantal phase factors accompanying adiabatic changes", *Proceedings of the Royal Society of London. A. Mathematical and Physical Sciences* **392**, 45–57 (1984).

62. D. Xiao, M.-C. Chang, Q. Niu, "Berry phase effects on electronic properties", *Rev. Mod. Phys.* **82**, 1959–2007 (3 2010).

63. R. Resta, D. Vanderbilt, in *Physics of Ferroelectrics* (Springer, 2007), 31.

64. C. Kittel, *Introduction to Solid State Physics* (Wiley, 1968).

65. R. B. Laughlin, "Quantized Hall conductivity in two dimensions", *Phys. Rev. B* **23**, 5632–5633 (10 1981).

66. D. J. Thouless, M. Kohmoto, M. P. Nightingale, M. den Nijs, "Quantized Hall Conductance in a Two-Dimensional Periodic Potential", *Phys. Rev. Lett.* **49**, 405–408 (6 1982).

67. J. E. Avron, R. Seiler, B. Simon, "Homotopy and Quantization in Condensed Matter Physics", *Phys. Rev. Lett.* **51**, 51–53 (1 1983).

68. C.-Z. Chang, J. Zhang, X. Feng, J. Shen, Z. Zhang, M. Guo, K. Li, Y. Ou, P. Wei, L.-L. Wang, Z.-Q. Ji, Y. Feng, S. Ji, X. Chen, J. Jia, X. Dai, Z. Fang, S.-C. Zhang, K. He, Y. Wang, L. Lu, X.-C. Ma, Q.-K. Xue, "Experimental Observation of the Quantum Anomalous Hall Effect in a Magnetic Topological Insulator", *Science* **340**, 167–170 (2013).

69. G. Jotzu, M. Messer, R. Desbuquois, M. Lebrat, T. Uehlinger, D. Greif, T. Esslinger, "Experimental realization of the topological Haldane model with ultracold fermions", *Nature* **515**, 237–240 (2014).

70. Y. Ding, Y. Peng, Y. Zhu, X. Fan, J. Yang, B. Liang, X. Zhu, X. Wan, J. Cheng, "Experimental Demonstration of Acoustic Chern Insulators", *Phys. Rev. Lett.* **122**, 014302 (1 2019).

71. H. Min, J. E. Hill, N. A. Sinitsyn, B. R. Sahu, L. Kleinman, A. H. MacDonald, "Intrinsic and Rashba spin-orbit interactions in graphene sheets", *Phys. Rev. B* **74**, 165310 (16 2006).

72. Y. Yao, F. Ye, X.-L. Qi, S.-C. Zhang, Z. Fang, "Spin-orbit gap of graphene: First-principles calculations", *Phys. Rev. B* **75**, 041401 (4 2007).

73. B. A. Bernevig, S.-C. Zhang, "Quantum Spin Hall Effect", *Phys. Rev. Lett.* **96**, 106802 (10 2006).

74. J. Maciejko, T. L. Hughes, S.-C. Zhang, "The Quantum Spin Hall Effect", *Annual Review of Condensed Matter Physics* **2**, 31–53 (2011).

75. F. Matusalem, M. Marques, L. K. Teles, L. Matthes, J. Furthmüller, F. Bechstedt, "Quantization of spin Hall conductivity in two-dimensional topological insulators versus symmetry and spin-orbit interaction", *Phys. Rev. B* **100**, 245430 (24 2019).

76. C. Xu, J. E. Moore, "Stability of the quantum spin Hall effect: Effects of interactions, disorder, and $\mathbb{Z}_2$ topology", *Phys. Rev. B* **73**, 045322 (4 2006).

77. D. N. Sheng, Z. Y. Weng, L. Sheng, F. D. M. Haldane, "Quantum Spin-Hall Effect and Topologically Invariant Chern Numbers", *Phys. Rev. Lett.* **97**, 036808 (3 2006).

78. L. Fu, C. L. Kane, "Time reversal polarization and a Z_2 adiabatic spin pump", *Phys. Rev. B* **74**, 195312 (19 2006).

79. M. Z. Hasan, C. L. Kane, "Colloquium: Topological insulators", *Rev. Mod. Phys.* **82**, 3045–3067 (4 2010).

80. W. P. Su, J. R. Schrieffer, A. J. Heeger, "Solitons in Polyacetylene", *Phys. Rev. Lett.* **42**, 1698–1701 (25 1979).

81. D. Shechtman, I. Blech, D. Gratias, J. W. Cahn, "Metallic Phase with Long-Range Orientational Order and No Translational Symmetry", *Phys. Rev. Lett.* **53**, 1951–1953 (20 1984).

82. Y. E. Kraus, Y. Lahini, Z. Ringel, M. Verbin, O. Zilberberg, "Topological States and Adiabatic Pumping in Quasicrystals", *Phys. Rev. Lett.* **109**, 106402 (10 2012).

83. R. Chen, C.-Z. Chen, J.-H. Gao, B. Zhou, D.-H. Xu, "Higher-Order Topological Insulators in Quasicrystals", *Phys. Rev. Lett.* **124**, 036803 (3 2020).

84. D. Varjas, A. Lau, K. Pöyhönen, A. R. Akhmerov, D. I. Pikulin, I. C. Fulga, "Topological Phases without Crystalline Counterparts", *Phys. Rev. Lett.* **123**, 196401 (19 2019).

85. A. Agarwala, V. B. Shenoy, "Topological Insulators in Amorphous Systems", *Phys. Rev. Lett.* **118**, 236402 (23 2017).

86. I. C. Fulga, B. van Heck, J. M. Edge, A. R. Akhmerov, "Statistical topological insulators", *Phys. Rev. B* **89**, 155424 (15 2014).

87. B. Mandelbrot, W. Freeman, Company, *The Fractal Geometry of Nature* (Henry Holt and Company, 1983).

88. Y. Gefen, B. B. Mandelbrot, A. Aharony, "Critical Phenomena on Fractal Lattices", *Phys. Rev. Lett.* **45**, 855–858 (11 1980).

89. J. M. Carmona, U. M. B. Marconi, J. J. Ruiz-Lorenzo, A. Tarancón, "Critical properties of the Ising model on Sierpinski fractals: A finite-size scaling-analysis approach", *Phys. Rev. B* **58**, 14387–14396 (21 1998).

90. T. Nakayama, K. Yakubo, *Fractal concepts in condensed matter physics* (Springer Science & Business Media, 2013), vol. 140.

91. E. van Veen, S. Yuan, M. I. Katsnelson, M. Polini, A. Tomadin, "Quantum transport in Sierpinski carpets", *Phys. Rev. B* **93**, 115428 (11 2016).

92. E. van Veen, A. Tomadin, M. Polini, M. I. Katsnelson, S. Yuan, "Optical conductivity of a quantum electron gas in a Sierpinski carpet", *Phys. Rev. B* **96**, 235438 (23 2017).

93. T. Westerhout, E. van Veen, M. I. Katsnelson, S. Yuan, "Plasmon confinement in fractal quantum systems", *Phys. Rev. B* **97**, 205434 (20 2018).

94. B. Pal, A. Chakrabarti, "Staggered and extreme localization of electron states in fractal space", *Phys. Rev. B* **85**, 214203 (21 2012).

95. B. Pal, P. Patra, J. P. Saha, A. Chakrabarti, "Engineering wave localization in a fractal waveguide network", *Phys. Rev. A* **87**, 023814 (2 2013).

96. A. Kosior, K. Sacha, "Localization in random fractal lattices", *Phys. Rev. B* **95**, 104206 (10 2017).

97. Pal, B., Chakrabarti, A., "Nature of electron states and magneto-transport in a graphene geometry with a fractal distribution of holes", *Eur. Phys. J. B* **85**, 307 (2012).

98. T. L. Chen, D. J. Dikken, J. C. Prangsma, F. Segerink, J. L. Herek, "Characterization of Sierpinski carpet optical antenna at visible and near-infrared wavelengths", *New Journal of Physics* **16**, 093024 (2014).

99. S. N. Kempkes, M. R. Slot, S. E. Freeney, S. J. M. Zevenhuizen, D. Vanmaekelbergh, I. Swart, C. M. Smith, "Design and characterization of electrons in a fractal geometry", *Nature Physics* **15**, 127–131 (2019).

100. J. Shang, Y. Wang, M. Chen, J. Dai, X. Zhou, J. Kuttner, G. Hilt, X. Shao, J. M. Gottfried, K. Wu, "Assembling molecular Sierpinski triangle fractals", *Nature Chemistry* **7**, 389–393 (2015).

101. K. Falconer, *Fractal Geometry: Mathematical Foundations and Applications* (Wiley, 2004).

102. Y. Gefen, A. Aharony, B. B. Mandelbrot, "Phase transitions on fractals. I. Quasi-linear lattices", *Journal of Physics A: Mathematical and General* **16**, 1267–1278 (1983).

103. D. Ben-avraham, S. Havlin, D. Movshovitz, "Infinitely ramified fractal lattices and percolation", *Philosophical Magazine B* **50**, 297–306 (1984).

104. O. Penrose, "Phase transitions on fractal lattices with long-range interactions", *Journal of Statistical Physics* **45**, 69–88 (1986).

105. Y. Gefen, A. Aharony, B. B. Mandelbrot, "Phase transitions on fractals. III. Infinitely ramified lattices", *Journal of Physics A: Mathematical and General* **17**, 1277–1289 (1984).

106. Y. Gefen, A. Aharony, Y. Shapir, B. B. Mandelbrot, "Phase transitions on fractals. II. Sierpinski gaskets", *Journal of Physics A: Mathematical and General* **17**, 435–444 (1984).

107. S. Sachdev, *Quantum Phase Transitions* (Cambridge University Press, ed. 2, 2011).

108. J. Ghez, Y. Y. Wang, R. Rammal, B. Pannetier, J. Bellissard, "Band spectrum for an electron on a Sierpinski gasket in a magnetic field", *Solid State Communications* **64**, 1291–1294 (1987).

109. S. Alexander, "Some properties of the spectrum of the Sierpinski gasket in a magnetic field", *Phys. Rev. B* **29**, 5504–5508 (10 1984).

110. R. Rammal, G. Toulouse, "Spectrum of the Schrödinger Equation on a Self-Similar Structure", *Phys. Rev. Lett.* **49**, 1194–1197 (16 1982).

111. B. Lindquist, R. Riklund, "Effects of deterministic aperiodic and self-similar on-site potentials on the structure of the Hofstadter butterfly", *Phys. Rev. B* **60**, 10054–10061 (14 1999).

112. A. Agarwala, S. Pai, V. B. Shenoy, "Fractalized Metals", arXiv:1803.01404 (2018).

113. S. Pai, A. Prem, "Topological states on fractal lattices", *Phys. Rev. B* **100**, 155135 (15 2019).

114. M. Fremling, M. van Hooft, C. M. Smith, L. Fritz, "Existence of robust edge currents in Sierpiński fractals", *Phys. Rev. Research* **2**, 013044 (1 2020).

115. A. A. Iliasov, M. I. Katsnelson, S. Yuan, "Hall conductivity of a Sierpiński carpet", *Phys. Rev. B* **101**, 045413 (4 2020).

116. L. Kong, X.-G. Wen, "Braided fusion categories, gravitational anomalies, and the mathematical framework for topological orders in any dimensions", arXiv:1405.5858 (2014).

117. D. S. Freed, "Short-range entanglement and invertible field theories", arXiv:1406.7278 (2014).

118. F. D. M. Haldane, "Berry Curvature on the Fermi Surface: Anomalous Hall Effect as a Topological Fermi-Liquid Property", *Phys. Rev. Lett.* **93**, 206602 (20 2004).

119. R. Peierls, "Zur Theorie des Diamagnetismus von Leitungselektronen", *Zeitschrift für Physik* **80**, 763–791 (1933).

120. B. Bernevig, T. Hughes, *Topological Insulators and Topological Superconductors* (Princeton University Press, 2013).

121. D. R. Hofstadter, "Energy levels and wave functions of Bloch electrons in rational and irrational magnetic fields", *Phys. Rev. B* **14**, 2239–2249 (6 1976).

122. P. Streda, "Quantised Hall effect in a two-dimensional periodic potential", *Journal of Physics C: Solid State Physics* **15**, L1299–L1303 (1982).

123. E. Domany, S. Alexander, D. Bensimon, L. P. Kadanoff, "Solutions to the Schrödinger equation on some fractal lattices", *Phys. Rev. B* **28**, 3110–3123 (6 1983).

124. J. R. Banavar, L. Kadanoff, A. M. M. Pruisken, "Energy spectrum for a fractal lattice in a magnetic field", *Phys. Rev. B* **31**, 1388–1395 (3 1985).

125. X. R. Wang, "Magnetic-field effects on localization in a fractal lattice", *Phys. Rev. B* **53**, 12035–12039 (18 1996).

126. E. Prodan, "Disordered topological insulators: a non-commutative geometry perspective", *Journal of Physics A: Mathematical and Theoretical* **44**, 113001 (2011).

127. T. A. Loring, M. B. Hastings, "Disordered topological insulators via C*-algebras", *Europhysics Letters* **92**, 67004 (2010).

128. M. B. Hastings, T. A. Loring, "Topological insulators and C*-algebras: Theory and numerical practice", *Annals of Physics* **326**, 1699–1759 (2011).

129. D. Monaco, G. Panati, A. Pisante, S. Teufel, "The Localization Dichotomy for gapped periodic quantum systems", arXiv:1612.09557 (2016).

130. T. A. Loring, "A Guide to the Bott Index and Localizer Index", arXiv:1907.11791 (2019).

131. D. Toniolo, "On the equivalence of the Bott index and the Chern number on a torus, and the quantization of the Hall conductivity with a real space Kubo formula", arXiv:1708.05912 (2017).

132. Y. Ge, M. Rigol, "Topological phase transitions in finite-size periodically driven translationally invariant systems", *Phys. Rev. A* **96**, 023610 (2 2017).

133. H. Huang, F. Liu, "Quantum Spin Hall Effect and Spin Bott Index in a Quasicrystal Lattice", *Phys. Rev. Lett.* **121**, 126401 (12 2018).

134. D. Toniolo, "Time-dependent topological systems: A study of the Bott index", *Phys. Rev. B* **98**, 235425 (23 2018).

135. H. Huang, F. Liu, "Theory of spin Bott index for quantum spin Hall states in nonperiodic systems", *Phys. Rev. B* **98**, 125130 (12 2018).

136. A. Kitaev, "Anyons in an exactly solved model and beyond", *Annals of Physics* **321**, January Special Issue, 2–111 (2006).

137. D. N. Sheng, Z. Y. Weng, "Disappearance of Integer Quantum Hall Effect", *Phys. Rev. Lett.* **78**, 318–321 (2 1997).

138. R. B. Laughlin, "Levitation of Extended-State Bands in a Strong Magnetic Field", *Phys. Rev. Lett.* **52**, 2304–2304 (25 1984).

139. M. Onoda, Y. Avishai, N. Nagaosa, "Localization in a Quantum Spin Hall System", *Phys. Rev. Lett.* **98**, 076802 (7 2007).

140. J. Li, R.-L. Chu, J. K. Jain, S.-Q. Shen, "Topological Anderson Insulator", *Phys. Rev. Lett.* **102**, 136806 (13 2009).

141. C. W. Groth, M. Wimmer, A. R. Akhmerov, J. Tworzydło, C. W. J. Beenakker, "Theory of the Topological Anderson Insulator", *Phys. Rev. Lett.* **103**, 196805 (19 2009).

142. E. Prodan, T. L. Hughes, B. A. Bernevig, "Entanglement Spectrum of a Disordered Topological Chern Insulator", *Phys. Rev. Lett.* **105**, 115501 (11 2010).

143. C. Fang, M. J. Gilbert, B. A. Bernevig, "Bulk topological invariants in noninteracting point group symmetric insulators", *Phys. Rev. B* **86**, 115112 (11 2012).

144. L. Fu, C. L. Kane, "Topological insulators with inversion symmetry", *Phys. Rev. B* **76**, 045302 (4 2007).

145. L. Fu, "Topological Crystalline Insulators", *Phys. Rev. Lett.* **106**, 106802 (10 2011).

146. H. C. Po, A. Vishwanath, H. Watanabe, "Symmetry-based indicators of band topology in the 230 space groups", *Nature Communications* **8**, 50 (2017).

147. B. Bradlyn, L. Elcoro, J. Cano, M. G. Vergniory, Z. Wang, C. Felser, M. I. Aroyo, B. A. Bernevig, "Topological quantum chemistry", *Nature* **547**, 298–305 (2017).

148. H. Watanabe, H. C. Po, A. Vishwanath, "Structure and topology of band structures in the 1651 magnetic space groups", *Science advances* **4**, eaat8685 (2018).

149. F. Tang, H. C. Po, A. Vishwanath, X. Wan, "Efficient topological materials discovery using symmetry indicators", *Nature Physics* **15**, 470–476 (2019).

150. R.-J. Slager, A. Mesaros, V. Juricic, J. Zaanen, "The space group classification of topological band-insulators", *Nature Physics* **9**, 98–102 (2013).

151. K. Shiozaki, M. Sato, K. Gomi, "Topological crystalline materials: General formulation, module structure, and wallpaper groups", *Phys. Rev. B* **95**, 235425 (23 2017).

152. X.-Y. Dong, C.-X. Liu, "Classification of topological crystalline insulators based on representation theory", *Phys. Rev. B* **93**, 045429 (4 2016).

153. M. Diez, D. I. Pikulin, I. C. Fulga, J. Tworzydło, "Extended topological group structure due to average reflection symmetry", *New Journal of Physics* **17**, 043014 (2015).

154. L. Fu, C. L. Kane, "Topology, Delocalization via Average Symmetry and the Symplectic Anderson Transition", *Phys. Rev. Lett.* **109**, 246605 (24 2012).

155. R. S. K. Mong, J. H. Bardarson, J. E. Moore, "Quantum Transport and Two-Parameter Scaling at the Surface of a Weak Topological Insulator", *Phys. Rev. Lett.* **108**, 076804 (7 2012).

156. K. Kobayashi, T. Ohtsuki, K.-I. Imura, "Disordered Weak and Strong Topological Insulators", *Phys. Rev. Lett.* **110**, 236803 (23 2013).

157. H. Obuse, S. Ryu, A. Furusaki, C. Mudry, "Spin-directed network model for the surface states of weak three-dimensional $\mathbb{Z}_2$ topological insulators", *Phys. Rev. B* **89**, 155315 (15 2014).

158. T. H. Hsieh, H. Lin, J. Liu, W. Duan, A. Bansil, L. Fu, "Topological crystalline insulators in the SnTe material class", *Nature Communications* **3**, 982 (2012).

159. Y. Tanaka, Z. Ren, T. Sato, K. Nakayama, S. Souma, T. Takahashi, K. Segawa, Y. Ando, "Experimental realization of a topological crystalline insulator in SnTe", *Nature Physics* **8**, 800–803 (2012).

160. P. Dziawa, B. J. Kowalski, K. Dybko, R. Buczko, A. Szczerbakow, M. Szot, E. Łusakowska, T. Balasubramanian, B. M. Wojek, M. H. Berntsen, O. Tjernberg, T. Story, "Topological crystalline insulator states in $Pb_{1x}Sn_xSe$", *Nature Materials* **11**, 1023–1027 (2012).

161. S.-Y. Xu, C. Liu, N. Alidoust, M. Neupane, D. Qian, I. Belopolski, J. D. Denlinger, Y. J. Wang, H. Lin, L. A. Wray, G. Landolt, B. Slomski, J. H. Dil, A. Marcinkova, E. Morosan, Q. Gibson, R. Sankar, F. C. Chou, R. J. Cava, A. Bansil, M. Z. Hasan, "Observation of a topological crystalline insulator phase and topological phase transition in $Pb_{1x}Sn_xTe$", *Nature Communications* **3**, 1192 (2012).

162. Y. Tanaka, T. Sato, K. Nakayama, S. Souma, T. Takahashi, Z. Ren, M. Novak, K. Segawa, Y. Ando, "Tunability of the *k*-space location of the Dirac cones in the topological crystalline insulator $Pb_{1-x}Sn_xTe$", *Phys. Rev. B* **87**, 155105 (15 2013).

163. B. M. Wojek, R. Buczko, S. Safaei, P. Dziawa, B. J. Kowalski, M. H. Berntsen, T. Balasubramanian, M. Leandersson, A. Szczerbakow, P. Kacman, T. Story, O. Tjernberg, "Spin-polarized (001) surface states of the topological crystalline insulator $Pb_{0.73}Sn_{0.27}Se$", *Phys. Rev. B* **87**, 115106 (11 2013).

164. J. Ma, C. Yi, B. Lv, Z. Wang, S. Nie, L. Wang, L. Kong, Y. Huang, P. Richard, P. Zhang, K. Yaji, K. Kuroda, S. Shin, H. Weng, B. A. Bernevig, Y. Shi, T. Qian, H. Ding, "Experimental evidence of hourglass fermion in the candidate nonsymmorphic topological insulator KHgSb", *Science Advances* **3** (2017).

165. Z. Wang, A. Alexandradinata, R. J. Cava, B. A. Bernevig, "Hourglass fermions", *Nature* **532**, 189–194 (2016).

166. J. Shen, Y. Jung, A. S. Disa, F. J. Walker, C. H. Ahn, J. J. Cha, "Synthesis of SnTe Nanoplates with {100} and {111} Surfaces", *Nano Letters* **14**, 4183–4188 (2014).

167. J. Liu, T. H. Hsieh, P. Wei, W. Duan, J. Moodera, L. Fu, "Spin-filtered edge states with an electrically tunable gap in a two-dimensional topological crystalline insulator", *Nature Materials* **13**, 178–183 (2014).

168. H. Ozawa, A. Yamakage, M. Sato, Y. Tanaka, "Topological phase transition in a topological crystalline insulator induced by finite-size effects", *Phys. Rev. B* **90**, 045309 (4 2014).

169. Y.-z. Jia, W.-x. Ji, C.-w. Zhang, P. Li, S.-f. Zhang, P.-j. Wang, S.-s. Li, S.-s. Yan, "Prediction of topological crystalline insulators and topological phase transitions in two-dimensional PbTe films", *Phys. Chem. Chem. Phys.* **19**, 29647–29652 (43 2017).

170. C. Niu, P. M. Buhl, G. Bihlmayer, D. Wortmann, S. Blügel, Y. Mokrousov, "Two-Dimensional Topological Crystalline Insulator and Topological Phase Transition in TlSe and TlS Monolayers", *Nano Letters* **15**, 6071–6075 (2015).

171. Y.-p. Wang, W.-x. Ji, C.-w. Zhang, P. Li, P.-j. Wang, "A new topological crystalline insulator in two-dimensional PbPo with tunable large bulk gaps", *J. Mater. Chem. C* **4**, 8745–8749 (37 2016).

172. M. Kindermann, "Topological Crystalline Insulator Phase in Graphene Multilayers", *Phys. Rev. Lett.* **114**, 226802 (22 2015).

173. C. Niu, P. M. Buhl, G. Bihlmayer, D. Wortmann, S. Blügel, Y. Mokrousov, "Two-dimensional topological crystalline insulator phase in quantum wells of trivial insulators", *2D Materials* **3**, 025037 (2016).

174. C.-H. Hsu, Z.-Q. Huang, C. P. Crisostomo, L.-Z. Yao, F.-C. Chuang, Y.-T. Liu, B. Wang, C.-H. Hsu, C.-C. Lee, H. Lin, A. Bansil, "Two-dimensional Topological Crystalline Insulator Phase in Sb/Bi Planar Honeycomb with Tunable Dirac Gap", *Scientific Reports* **6**, 18993 (2016).

175. X. Wang, G. Bian, C. Xu, P. Wang, H. Hu, W. Zhou, S. A. Brown, T.-C. Chiang, "Topological phases in double layers of bismuthene and antimonene", *Nanotechnology* **28**, 395706 (2017).

176. Y. Liu, R. E. Allen, "Electronic structure of the semimetals Bi and Sb", *Phys. Rev. B* **52**, 1566–1577 (3 1995).

177. I. Peschel, "Calculation of reduced density matrices from correlation functions", *Journal of Physics A: Mathematical and General* **36**, L205 (2003).

178. L. Amico, R. Fazio, A. Osterloh, V. Vedral, "Entanglement in many-body systems", *Rev. Mod. Phys.* **80**, 517–576 (2 2008).

179. J. Eisert, M. Cramer, M. B. Plenio, "Colloquium: Area laws for the entanglement entropy", *Rev. Mod. Phys.* **82**, 277–306 (1 2010).

180. J. D. Bekenstein, "Black Holes and Entropy", *Phys. Rev. D* **7**, 2333–2346 (8 1973).

181. M. B. Hastings, "An area law for one-dimensional quantum systems", *Journal of Statistical Mechanics: Theory and Experiment* **2007**, P08024–P08024 (2007).

182. M. B. Plenio, J. Eisert, J. Dreißig, M. Cramer, "Entropy, Entanglement, and Area: Analytical Results for Harmonic Lattice Systems", *Phys. Rev. Lett.* **94**, 060503 (6 2005).

183. M. M. Wolf, "Violation of the Entropic Area Law for Fermions", *Phys. Rev. Lett.* **96**, 010404 (1 2006).

184. D. Gioev, I. Klich, "Entanglement Entropy of Fermions in Any Dimension and the Widom Conjecture", *Phys. Rev. Lett.* **96**, 100503 (10 2006).

185. B. Swingle, "Entanglement Entropy and the Fermi Surface", *Phys. Rev. Lett.* **105**, 050502 (5 2010).

186. A. Kitaev, J. Preskill, "Topological Entanglement Entropy", *Phys. Rev. Lett.* **96**, 110404 (11 2006).

187. M. Levin, X.-G. Wen, "Detecting Topological Order in a Ground State Wave Function", *Phys. Rev. Lett.* **96**, 110405 (11 2006).

188. E. Fradkin, *Field Theories of Condensed Matter Physics* (Cambridge University Press, 2013).

189. A. M. Läuchli, E. J. Bergholtz, M. Haque, "Entanglement scaling of fractional quantum Hall states through geometric deformations", *New Journal of Physics* **12**, 075004 (2010).

190. S. Furukawa, G. Misguich, "Topological entanglement entropy in the quantum dimer model on the triangular lattice", *Phys. Rev. B* **75**, 214407 (21 2007).

191. M. Haque, O. Zozulya, K. Schoutens, "Entanglement Entropy in Fermionic Laughlin States", *Phys. Rev. Lett.* **98**, 060401 (6 2007).

192. H. Li, F. D. M. Haldane, "Entanglement Spectrum as a Generalization of Entanglement Entropy: Identification of Topological Order in Non-Abelian Fractional Quantum Hall Effect States", *Phys. Rev. Lett.* **101**, 010504 (1 2008).

193. L. Fidkowski, "Entanglement Spectrum of Topological Insulators and Superconductors", *Phys. Rev. Lett.* **104**, 130502 (13 2010).

194. G. De Chiara, L. Lepori, M. Lewenstein, A. Sanpera, "Entanglement Spectrum, Critical Exponents, and Order Parameters in Quantum Spin Chains", *Phys. Rev. Lett.* **109**, 237208 (23 2012).

195. A. Chandran, M. Hermanns, N. Regnault, B. A. Bernevig, "Bulk-edge correspondence in entanglement spectra", *Phys. Rev. B* **84**, 205136 (20 2011).

196. A. Chandran, V. Khemani, S. L. Sondhi, "How Universal Is the Entanglement Spectrum?", *Phys. Rev. Lett.* **113**, 060501 (6 2014).

197. T. L. Hughes, E. Prodan, B. A. Bernevig, "Inversion-symmetric topological insulators", *Phys. Rev. B* **83**, 245132 (24 2011).

198. A. M. Turner, Y. Zhang, A. Vishwanath, "Entanglement and inversion symmetry in topological insulators", *Phys. Rev. B* **82**, 241102 (24 2010).

199. A. Alexandradinata, T. L. Hughes, B. A. Bernevig, "Trace index and spectral flow in the entanglement spectrum of topological insulators", *Phys. Rev. B* **84**, 195103 (19 2011).

200. S. Ryu, Y. Hatsugai, "Entanglement entropy and the Berry phase in the solid state", *Phys. Rev. B* **73**, 245115 (24 2006).

201. D. Hsieh, Y. Xia, L. Wray, D. Qian, A. Pal, J. H. Dil, J. Osterwalder, F. Meier, G. Bihlmayer, C. L. Kane, Y. S. Hor, R. J. Cava, M. Z. Hasan, "Observation of Unconventional Quantum Spin Textures in Topological Insulators", *Science* **323**, 919–922 (2009).

202. P. Roushan, J. Seo, C. V. Parker, Y. S. Hor, D. Hsieh, D. Qian, A. Richardella, M. Z. Hasan, R. J. Cava, A. Yazdani, "Topological surface states protected from backscattering by chiral spin texture", *Nature* **460**, 1106–1109 (2009).

203. J. C. Y. Teo, L. Fu, C. L. Kane, "Surface states and topological invariants in three-dimensional topological insulators: Application to $Bi_{1-x}Sb_x$", *Phys. Rev. B* **78**, 045426 (4 2008).

204. H.-J. Zhang, C.-X. Liu, X.-L. Qi, X.-Y. Deng, X. Dai, S.-C. Zhang, Z. Fang, "Electronic structures and surface states of the topological insulator $Bi_{1-x}Sb_x$", *Phys. Rev. B* **80**, 085307 (8 2009).

205. Z. Liu, C.-X. Liu, Y.-S. Wu, W.-H. Duan, F. Liu, J. Wu, "Stable Nontrivial Z_2 Topology in Ultrathin Bi (111) Films: A First-Principles Study", *Phys. Rev. Lett.* **107**, 136805 (13 2011).

206. S. Murakami, "Quantum Spin Hall Effect and Enhanced Magnetic Response by Spin-Orbit Coupling", *Phys. Rev. Lett.* **97**, 236805 (23 2006).

207. I. K. Drozdov, A. Alexandradinata, S. Jeon, S. Nadj-Perge, H. Ji, R. Cava, B. A. Bernevig, A. Yazdani, "One-dimensional topological edge states of bismuth bilayers", *Nature Physics* **10**, 664–669 (2014).

208. N. Kawakami, C.-L. Lin, M. Kawai, R. Arafune, N. Takagi, "One-dimensional edge state of Bi thin film grown on Si (111)", *Applied Physics Letters* **107**, 031602 (2015).

209. F. Yang, L. Miao, Z. F. Wang, M.-Y. Yao, F. Zhu, Y. R. Song, M.-X. Wang, J.-P. Xu, A. V. Fedorov, Z. Sun, G. B. Zhang, C. Liu, F. Liu, D. Qian, C. L. Gao, J.-F. Jia, "Spatial and Energy Distribution of Topological Edge States in Single Bi(111) Bilayer", *Phys. Rev. Lett.* **109**, 016801 (1 2012).

210. A. A. Taskin, S. Sasaki, K. Segawa, Y. Ando, "Manifestation of Topological Protection in Transport Properties of Epitaxial Bi_2Se_3 Thin Films", *Phys. Rev. Lett.* **109**, 066803 (6 2012).

211. C.-X. Liu, H. Zhang, B. Yan, X.-L. Qi, T. Frauenheim, X. Dai, Z. Fang, S.-C. Zhang, "Oscillatory crossover from two-dimensional to three-dimensional topological insulators", *Phys. Rev. B* **81**, 041307 (4 2010).

212. T. Hirahara, G. Bihlmayer, Y. Sakamoto, M. Yamada, H. Miyazaki, S.-i. Kimura, S. Blügel, S. Hasegawa, "Interfacing 2D and 3D Topological Insulators: Bi(111) Bilayer on Bi_2Te_3", *Phys. Rev. Lett.* **107**, 166801 (16 2011).

213. P. Zhang, Z. Liu, W. Duan, F. Liu, J. Wu, "Topological and electronic transitions in a Sb(111) nanofilm: The interplay between quantum confinement and surface effect", *Phys. Rev. B* **85**, 201410 (20 2012).

214. K.-H. Jin, S.-H. Jhi, "Quantum anomalous Hall and quantum spin-Hall phases in flattened Bi and Sb bilayers", *Scientific reports* **5** (2015).

215. F.-C. Chuang, C.-H. Hsu, C.-Y. Chen, Z.-Q. Huang, V. Ozolins, H. Lin, A. Bansil, "Tunable topological electronic structures in Sb(111) bilayers: A first-principles study", *Applied Physics Letters* **102**, 022424 (2013).

216. D. Wang, L. Chen, H. Liu, X. Wang, "Topological phase transitions in Sb (111) films driven by external strain and electric field", *Europhysics Letters* **104**, 57011 (2014).

217. J. C. Slater, G. F. Koster, "Simplified LCAO Method for the Periodic Potential Problem", *Phys. Rev.* **94**, 1498–1524 (6 1954).

218. D. J. Chadi, "Spin-orbit splitting in crystalline and compositionally disordered semiconductors", *Phys. Rev. B* **16**, 790–796 (2 1977).

219. M. Dzero, J. Xia, V. Galitski, P. Coleman, "Topological Kondo Insulators", *Annual Review of Condensed Matter Physics* **7**, 249–280 (2016).

220. J. Liu, D. Vanderbilt, "Spin-orbit spillage as a measure of band inversion in insulators", *Phys. Rev. B* **90**, 125133 (12 2014).

221. W. Harrison, *Electronic Structure and the Properties of Solids: The Physics of the Chemical Bond* (Dover Publications, 1989).

222. F. Reis, G. Li, L. Dudy, M. Bauernfeind, S. Glass, W. Hanke, R. Thomale, J. Schäfer, R. Claessen, "Bismuthene on a SiC substrate: A candidate for a high-temperature quantum spin Hall material", *Science* **357**, 287–290 (2017).

223. T. Kuzumaki, T. Shirasawa, S. Mizuno, N. Ueno, H. Tochihara, K. Sakamoto, "Re-investigation of the Bi-induced Si(111)-(3×3) surfaces by low-energy electron diffraction", *Surface Science* **604**, 1044–1048 (2010).

224. R. H. Miwa, T. M. Schmidt, G. P. Srivastava, "Bi covered Si(111) surface revisited", *Journal of Physics: Condensed Matter* **15**, 2441–2447 (2003).

225. A. Fang, C. Adamo, S. Jia, R. J. Cava, S.-C. Wu, C. Felser, A. Kapitulnik, "Bursting at the seams: Rippled monolayer bismuth on NbSe2", *Science Advances* **4** (2018).

226. F. Yang, A. O. Elnabawy, R. Schimmenti, P. Song, J. Wang, Z. Peng, S. Yao, R. Deng, S. Song, Y. Lin, M. Mavrikakis, W. Xu, "Bismuthene for highly efficient carbon dioxide electroreduction reaction", *Nature Communications* **11**, 1088 (2020).

227. G. Li, W. Hanke, E. M. Hankiewicz, F. Reis, J. Schäfer, R. Claessen, C. Wu, R. Thomale, "Theoretical paradigm for the quantum spin Hall effect at high temperatures", *Phys. Rev. B* **98**, 165146 (16 2018).

228. F. Dominguez, B. Scharf, G. Li, J. Schäfer, R. Claessen, W. Hanke, R. Thomale, E. M. Hankiewicz, "Testing topological protection of edge states in hexagonal quantum spin Hall candidate materials", *Phys. Rev. B* **98**, 161407 (16 2018).

229. Y. Shao, Z.-L. Liu, C. Cheng, X. Wu, H. Liu, C. Liu, J.-O. Wang, S.-Y. Zhu, Y.-Q. Wang, D.-X. Shi, K. Ibrahim, J.-T. Sun, Y.-L. Wang, H.-J. Gao, "Epitaxial Growth of Flat Antimonene Monolayer: A New Honeycomb Analogue of Graphene", *Nano Letters* **18**, PMID: 29457727, 2133–2139 (2018).

230. J. Ji, X. Song, J. Liu, Z. Yan, C. Huo, S. Zhang, M. Su, L. Liao, W. Wang, Z. Ni, *et al.*, "Two-dimensional antimonene single crystals grown by van der Waals epitaxy", *Nature communications* **7**, 13352 (2016).

231. M. Fortin-Deschênes, O. Waller, T. O. Menteş, A. Locatelli, S. Mukherjee, F. Genuzio, P. L. Levesque, A. Hébert, R. Martel, O. Moutanabbir, "Synthesis of Antimonene on Germanium", *Nano Letters* **17**, 4970–4975 (2017).

232. C.-H. Hsu, Z.-Q. Huang, F.-C. Chuang, C.-C. Kuo, Y.-T. Liu, H. Lin, A. Bansil, "The nontrivial electronic structure of Bi/Sb honeycombs on SiC(0001)", *New Journal of Physics* **17**, 025005 (2015).

233. Y. Fuji, F. Pollmann, M. Oshikawa, "Distinct Trivial Phases Protected by a Point-Group Symmetry in Quantum Spin Chains", *Phys. Rev. Lett.* **114**, 177204 (17 2015).

234. G. H. Wannier, "The Structure of Electronic Excitation Levels in Insulating Crystals", *Phys. Rev.* **52**, 191–197 (3 1937).

235. N. Marzari, A. A. Mostofi, J. R. Yates, I. Souza, D. Vanderbilt, "Maximally localized Wannier functions: Theory and applications", *Rev. Mod. Phys.* **84**, 1419–1475 (4 2012).

236. D. J. Thouless, "Wannier functions for magnetic sub-bands", *Journal of Physics C: Solid State Physics* **17**, L325–L327 (1984).

237. T. Thonhauser, D. Vanderbilt, "Insulator/Chern-insulator transition in the Haldane model", *Phys. Rev. B* **74**, 235111 (23 2006).

238. C. Brouder, G. Panati, M. Calandra, C. Mourougane, N. Marzari, "Exponential Localization of Wannier Functions in Insulators", *Phys. Rev. Lett.* **98**, 046402 (4 2007).

239. A. A. Soluyanov, D. Vanderbilt, "Wannier representation of $\mathbb{Z}_2$ topological insulators", *Phys. Rev. B* **83**, 035108 (3 2011).

240. H. C. Po, H. Watanabe, A. Vishwanath, "Fragile Topology and Wannier Obstructions", *Phys. Rev. Lett.* **121**, 126402 (12 2018).

241. B. Bradlyn, Z. Wang, J. Cano, B. A. Bernevig, "Disconnected elementary band representations, fragile topology, and Wilson loops as topological indices: An example on the triangular lattice", *Phys. Rev. B* **99**, 045140 (4 2019).

242. A. Bouhon, A. M. Black-Schaffer, R.-J. Slager, "Wilson loop approach to fragile topology of split elementary band representations and topological crystalline insulators with time-reversal symmetry", *Phys. Rev. B* **100**, 195135 (19 2019).

243. J. Ahn, S. Park, B.-J. Yang, "Failure of Nielsen-Ninomiya Theorem and Fragile Topology in Two-Dimensional Systems with Space-Time Inversion Symmetry: Application to Twisted Bilayer Graphene at Magic Angle", *Phys. Rev. X* **9**, 021013 (2 2019).

244. B. J. Wieder, B. A. Bernevig, "The Axion Insulator as a Pump of Fragile Topology", *arXiv:1810.02373* (2018).

245. M. B. de Paz, M. G. Vergniory, D. Bercioux, A. Garcıa-Etxarri, B. Bradlyn, "Engineering fragile topology in photonic crystals: Topological quantum chemistry of light", *Phys. Rev. Research* **1**, 032005 (3 2019).

246. J. L. Mañes, "Fragile phonon topology on the honeycomb lattice with time-reversal symmetry", *Phys. Rev. B* **102**, 024307 (2 2020).

247. Z.-D. Song, L. Elcoro, Y.-F. Xu, N. Regnault, B. A. Bernevig, "Fragile Phases as Affine Monoids: Classification and Material Examples", *Phys. Rev. X* **10**, 031001 (3 2020).

248. Z. Song, Z. Wang, W. Shi, G. Li, C. Fang, B. A. Bernevig, "All Magic Angles in Twisted Bilayer Graphene are Topological", *Phys. Rev. Lett.* **123**, 036401 (3 2019).

249. H. C. Po, L. Zou, T. Senthil, A. Vishwanath, "Faithful tight-binding models and fragile topology of magic-angle bilayer graphene", *Phys. Rev. B* **99**, 195455 (19 2019).

250. G. van Miert, C. Ortix, "Excess charges as a probe of one-dimensional topological crystalline insulating phases", *Phys. Rev. B* **96**, 235130 (23 2017).

251. G. van Miert, C. Ortix, "Higher-order topological insulators protected by inversion and rotoinversion symmetries", *Phys. Rev. B* **98**, 081110 (8 2018).

252. M. Ezawa, "Minimal models for Wannier-type higher-order topological insulators and phosphorene", *Phys. Rev. B* **98**, 045125 (4 2018).

253. W. A. Benalcazar, T. Li, T. L. Hughes, "Quantization of fractional corner charge in C_n-symmetric higher-order topological crystalline insulators", *Phys. Rev. B* **99**, 245151 (24 2019).

254. E. Lee, R. Kim, J. Ahn, B.-J. Yang, "Two-dimensional higher-order topology in monolayer graphdiyne", *npj Quantum Materials* **5**, 1 (2020).

255. X.-L. Sheng, C. Chen, H. Liu, Z. Chen, Z.-M. Yu, Y. X. Zhao, S. A. Yang, "Two-Dimensional Second-Order Topological Insulator in Graphdiyne", *Phys. Rev. Lett.* **123**, 256402 (25 2019).

256. W. A. Benalcazar, B. A. Bernevig, T. L. Hughes, "Quantized electric multipole insulators", *Science* **357**, 61–66 (2017).

257. J. Langbehn, Y. Peng, L. Trifunovic, F. von Oppen, P. W. Brouwer, "Reflection-Symmetric Second-Order Topological Insulators and Superconductors", *Phys. Rev. Lett.* **119**, 246401 (24 2017).

258. W. A. Benalcazar, B. A. Bernevig, T. L. Hughes, "Electric multipole moments, topological multipole moment pumping, and chiral hinge states in crystalline insulators", *Phys. Rev. B* **96**, 245115 (24 2017).

259. Z. Song, Z. Fang, C. Fang, "$(d-2)$-Dimensional Edge States of Rotation Symmetry Protected Topological States", *Phys. Rev. Lett.* **119**, 246402 (24 2017).

260. E. Khalaf, "Higher-order topological insulators and superconductors protected by inversion symmetry", *Phys. Rev. B* **97**, 205136 (20 2018).

261. M. Geier, L. Trifunovic, M. Hoskam, P. W. Brouwer, "Second-order topological insulators and superconductors with an order-two crystalline symmetry", *Phys. Rev. B* **97**, 205135 (20 2018).

262. Z. Wang, B. J. Wieder, J. Li, B. Yan, B. A. Bernevig, "Higher-Order Topology, Monopole Nodal Lines, and the Origin of Large Fermi Arcs in Transition Metal Dichalcogenides XTe_2 $(X = Mo, W)$", *Phys. Rev. Lett.* **123**, 186401 (18 2019).

263. S. Liu, A. Vishwanath, E. Khalaf, "Shift Insulators: Rotation-Protected Two-Dimensional Topological Crystalline Insulators", *Phys. Rev. X* **9**, 031003 (3 2019).

264. T. Li, P. Zhu, W. A. Benalcazar, T. L. Hughes, "Fractional disclination charge in two-dimensional C_n-symmetric topological crystalline insulators", *Phys. Rev. B* **101**, 115115 (11 2020).

265. R.-J. Slager, A. Mesaros, V. Juričić, J. Zaanen, "The space group classification of topological band-insulators", *Nature Physics* **9**, 98 EP - (2012).

266. J. Kruthoff, J. de Boer, J. van Wezel, C. L. Kane, R.-J. Slager, "Topological Classification of Crystalline Insulators through Band Structure Combinatorics", *Phys. Rev. X* **7**, 041069 (4 2017).

267. J. Cano, B. Bradlyn, Z. Wang, L. Elcoro, M. G. Vergniory, C. Felser, M. I. Aroyo, B. A. Bernevig, "Topology of Disconnected Elementary Band Representations", *Phys. Rev. Lett.* **120**, 266401 (26 2018).

268. J. Cano, B. Bradlyn, Z. Wang, L. Elcoro, M. G. Vergniory, C. Felser, M. I. Aroyo, B. A. Bernevig, "Building blocks of topological quantum chemistry: Elementary band representations", *Phys. Rev. B* **97**, 035139 (3 2018).

269. J. Zak, "Symmetry Specification of Bands in Solids", *Phys. Rev. Lett.* **45**, 1025–1028 (12 1980).

270. J. Zak, "Band representations and symmetry types of bands in solids", *Phys. Rev. B* **23**, 2824–2835 (6 1981).

271. R. Resta, "Theory of the electric polarization in crystals", *Ferroelectrics* **136**, 51–55 (1992).

272. D. Vanderbilt, R. D. King-Smith, "Electric polarization as a bulk quantity and its relation to surface charge", *Phys. Rev. B* **48**, 4442–4455 (7 1993).

273. J. Zak, "Berry's phase for energy bands in solids", *Phys. Rev. Lett.* **62**, 2747–2750 (23 1989).

274. G. van Miert, C. Ortix, C. M. Smith, "Topological origin of edge states in two-dimensional inversion-symmetric insulators and semimetals", *2D Materials* **4**, 015023 (2016).

275. J.-W. Rhim, J. Behrends, J. H. Bardarson, "Bulk-boundary correspondence from the intercellular Zak phase", *Phys. Rev. B* **95**, 035421 (3 2017).

276. W. A. Benalcazar, J. C. Y. Teo, T. L. Hughes, "Classification of two-dimensional topological crystalline superconductors and Majorana bound states at disclinations", *Phys. Rev. B* **89**, 224503 (22 2014).

277. Z. Song, T. Zhang, Z. Fang, C. Fang, "Quantitative mappings between symmetry and topology in solids", *Nature Communications* **9**, 3530 (2018).

278. E. Khalaf, H. C. Po, A. Vishwanath, H. Watanabe, "Symmetry Indicators and Anomalous Surface States of Topological Crystalline Insulators", *Phys. Rev. X* **8**, 031070 (3 2018).

279. F. Wilczek, A. Zee, "Appearance of Gauge Structure in Simple Dynamical Systems", *Phys. Rev. Lett.* **52**, 2111–2114 (24 1984).

280. J. Zak, "Band Center—A Conserved Quantity in Solids", *Phys. Rev. Lett.* **48**, 359–362 (5 1982).

281. A. Alexandradinata, X. Dai, B. A. Bernevig, "Wilson-loop characterization of inversion-symmetric topological insulators", *Phys. Rev. B* **89**, 155114 (15 2014).

282. S. H. Kooi, G. van Miert, C. Ortix, "Classification of crystalline insulators without symmetry indicators: Atomic and fragile topological phases in twofold rotation symmetric systems", *Phys. Rev. B* **100**, 115160 (11 2019).

283. A. Lau, J. van den Brink, C. Ortix, "Topological mirror insulators in one dimension", *Phys. Rev. B* **94**, 165164 (16 2016).

284. M. Aroyo, J. Perez-Mato, D. Orobengoa, E. Tasci, G. De La Flor, A. Kirov, "Crystallography online: Bilbao crystallographic server", *Bulgarian Chemical Communications* **43**, 183–197 (2011).

285. Y.-p. Wang, C.-w. Zhang, W.-x. Ji, R.-w. Zhang, P. Li, P.-j. Wang, M.-j. Ren, X.-l. Chen, M. Yuan, "Tunable quantum spin Hall effect via strain in two-dimensional arsenene monolayer", *Journal of Physics D: Applied Physics* **49**, 055305 (2016).

286. Z.-Q. Huang, C.-H. Hsu, F.-C. Chuang, Y.-T. Liu, H. Lin, W.-S. Su, V. Ozolins, A. Bansil, "Strain driven topological phase transitions in atomically thin films of group IV and V elements in the honeycomb structures", *New Journal of Physics* **16**, 105018 (2014).

287. J. M. Soler, E. Artacho, J. D. Gale, A. Garcıa, J. Junquera, P. Ordejón, D. Sánchez-Portal, "The SIESTA method for ab initio order-N materials simulation", *Journal of Physics: Condensed Matter* **14**, 2745–2779 (2002).

288. M. I. Aroyo, A. Kirov, C. Capillas, J. M. Perez-Mato, H. Wondratschek, "Bilbao Crystallographic Server. II. Representations of crystallographic point groups and space groups", *Acta Crystallographica Section A* **62**, 115–128 (2006).

289. M. G. Vergniory, L. Elcoro, Z. Wang, J. Cano, C. Felser, M. I. Aroyo, B. A. Bernevig, B. Bradlyn, "Graph theory data for topological quantum chemistry", *Phys. Rev. E* **96**, 023310 (2 2017).

290. "`irrep` code" `https://github.com/stepan-tsirkin/irrep`.

291. M. Iraola, J. L. Mañes, B. Bradlyn, T. Neupert, M. G. Vergniory, S. S. Tsirkin, "IrRep: symmetry eigenvalues and irreducible representations of ab initio band structures", arXiv:2009.01764 (2020).

292. L. Elcoro, B. Bradlyn, Z. Wang, M. G. Vergniory, J. Cano, C. Felser, B. A. Bernevig, D. Orobengoa, G. de la Flor, M. I. Aroyo, "Double crystallographic groups and their representations on the Bilbao Crystallographic Server", *Journal of Applied Crystallography* **50**, 1457–1477 (2017).

293. "Bilbao Crystallographic Server" `http://www.cryst.ehu.eus`.

294. G. Kresse, J. Furthmüller, "Efficiency of ab-initio total energy calculations for metals and semiconductors using a plane-wave basis set", *Computational Materials Science* **6**, 15–50 (1996).

295. G. Kresse, J. Furthmüller, "Efficient iterative schemes for ab initio total-energy calculations using a plane-wave basis set", *Phys. Rev. B* **54**, 11169–11186 (16 1996).

296. J. P. Perdew, K. Burke, M. Ernzerhof, "Generalized Gradient Approximation Made Simple", *Phys. Rev. Lett.* **77**, 3865–3868 (18 1996).

297. J. P. Perdew, K. Burke, M. Ernzerhof, "Generalized Gradient Approximation Made Simple [Phys. Rev. Lett. 77, 3865 (1996)]", *Phys. Rev. Lett.* **78**, 1396–1396 (7 1997).

298. P. E. Blöchl, "Projector augmented-wave method", *Phys. Rev. B* **50**, 17953–17979 (24 1994).

299. G. Kresse, D. Joubert, "From ultrasoft pseudopotentials to the projector augmented-wave method", *Phys. Rev. B* **59**, 1758–1775 (3 1999).

300. E. Aktürk, O. Ü. Aktürk, S. Ciraci, "Single and bilayer bismuthene: Stability at high temperature and mechanical and electronic properties", *Phys. Rev. B* **94**, 014115 (1 2016).

301. O. Ü. Aktürk, V. O. Özçelik, S. Ciraci, "Single-layer crystalline phases of antimony: Antimonenes", *Phys. Rev. B* **91**, 235446 (23 2015).

302. C. Kamal, M. Ezawa, "Arsenene: Two-dimensional buckled and puckered honeycomb arsenic systems", *Phys. Rev. B* **91**, 085423 (8 2015).

303. M. van Setten, M. Giantomassi, E. Bousquet, M. Verstraete, D. Hamann, X. Gonze, G.-M. Rignanese, "The PseudoDojo: Training and grading a 85 element optimized norm-conserving pseudopotential table", *Computer Physics Communications* **226**, 39–54 (2018).

304. N. Papior, "zerothi/sisl: v0.9.5" (2018).

305. C. M. Bender, S. Boettcher, "Real Spectra in Non-Hermitian Hamiltonians Having PT Symmetry", *Phys. Rev. Lett.* **80**, 5243–5246 (24 1998).

306. C. M. Bender, "PT-symmetric quantum theory", *Journal of Physics: Conference Series* **631**, 012002 (2015).

307. A. A. Zyablovsky, A. P. Vinogradov, A. A. Pukhov, A. V. Dorofeenko, A. A. Lisyansky, "PT-symmetry in optics", *Physics-Uspekhi* **57**, 1063–1082 (2014).

308. R. El-Ganainy, K. G. Makris, M. Khajavikhan, Z. H. Musslimani, S. Rotter, D. N. Christodoulides, "Non-Hermitian physics and PT symmetry", *Nature Physics* **14**, 11–19 (2018).

309. Ş. K. Özdemir, S. Rotter, F. Nori, L. Yang, "Parity–time symmetry and exceptional points in photonics", *Nature Materials* **18**, 783–798 (2019).

310. J. Schindler, A. Li, M. C. Zheng, F. M. Ellis, T. Kottos, "Experimental study of active LRC circuits with $\mathcal{PT}$ symmetries", *Phys. Rev. A* **84**, 040101 (4 2011).

311. M. Kang, F. Liu, J. Li, "Effective spontaneous $\mathcal{PT}$-symmetry breaking in hybridized metamaterials", *Phys. Rev. A* **87**, 053824 (5 2013).

312. R. Fleury, D. L. Sounas, A. Alù, "Negative Refraction and Planar Focusing Based on Parity-Time Symmetric Metasurfaces", *Phys. Rev. Lett.* **113**, 023903 (2 2014).

313. G. Gamow, "Zur Quantentheorie des Atomkernes", *Zeitschrift für Physik* **51**, 204–212 (1928).

314. H. Feshbach, C. E. Porter, V. F. Weisskopf, "Model for Nuclear Reactions with Neutrons", *Phys. Rev.* **96**, 448–464 (2 1954).

315. G. Lindblad, "On the generators of quantum dynamical semigroups", *Communications in Mathematical Physics* **48**, 119–130 (1976).

316. H. Breuer, P. Breuer, F. Petruccione, S. Petruccione, *The Theory of Open Quantum Systems* (Oxford University Press, 2002).

317. R. Feynman, F. Vernon, "The Theory of a General Quantum System Interacting with a Linear Dissipative System", *Annals of Physics* **281**, 547–607 (2000).

318. L. V. Keldysh *et al.*, "Diagram technique for nonequilibrium processes", *Sov. Phys. JETP* **20**, 1018–1026 (1965).

319. Z. Gong, Y. Ashida, K. Kawabata, K. Takasan, S. Higashikawa, M. Ueda, "Topological Phases of Non-Hermitian Systems", *Phys. Rev. X* **8**, 031079 (3 2018).

320. L. E. F. Foa Torres, "Perspective on topological states of non-Hermitian lattices", *Journal of Physics: Materials* (2019).

321. T. E. Lee, "Anomalous Edge State in a Non-Hermitian Lattice", *Phys. Rev. Lett.* **116**, 133903 (13 2016).

322. V. M. Martinez Alvarez, J. E. Barrios Vargas, L. E. F. Foa Torres, "Non-Hermitian robust edge states in one dimension: Anomalous localization and eigenspace condensation at exceptional points", *Phys. Rev. B* **97**, 121401 (12 2018).

323. H. Zhou, C. Peng, Y. Yoon, C. W. Hsu, K. A. Nelson, L. Fu, J. D. Joannopoulos, M. Soljačić, B. Zhen, "Observation of bulk Fermi arc and polarization half charge from paired exceptional points", *Science* **359**, 1009–1012 (2018).

324. S. Yao, Z. Wang, "Edge States and Topological Invariants of Non-Hermitian Systems", *Phys. Rev. Lett.* **121**, 086803 (8 2018).

325. Y. Xiong, "Why does bulk boundary correspondence fail in some non-hermitian topological models", *Journal of Physics Communications* **2**, 035043 (2018).

326. F. K. Kunst, E. Edvardsson, J. C. Budich, E. J. Bergholtz, "Biorthogonal Bulk-Boundary Correspondence in Non-Hermitian Systems", *Phys. Rev. Lett.* **121**, 026808 (2 2018).

327. C. H. Lee, R. Thomale, "Anatomy of skin modes and topology in non-Hermitian systems", *Phys. Rev. B* **99**, 201103 (20 2019).

328. D. S. Borgnia, A. J. Kruchkov, R.-J. Slager, "Non-Hermitian Boundary Modes and Topology", *Phys. Rev. Lett.* **124**, 056802 (5 2020).

329. W. B. Rui, M. M. Hirschmann, A. P. Schnyder, "PT-symmetric non-Hermitian Dirac semimetals", *Phys. Rev. B* **100**, 245116 (24 2019).

330. N. Okuma, K. Kawabata, K. Shiozaki, M. Sato, "Topological Origin of Non-Hermitian Skin Effects", *Phys. Rev. Lett.* **124**, 086801 (8 2020).

331. F. D. M. Haldane, "Path dependence of the geometric rotation of polarization in optical fibers", *Opt. Lett.* **11**, 730–732 (1986).

332. F. D. M. Haldane, S. Raghu, "Possible Realization of Directional Optical Waveguides in Photonic Crystals with Broken Time-Reversal Symmetry", *Phys. Rev. Lett.* **100**, 013904 (1 2008).

333. C. L. Kane, T. C. Lubensky, "Topological boundary modes in isostatic lattices", *Nat Phys* **10**, 39–45 (2014).

334. Z. Yang, F. Gao, X. Shi, X. Lin, Z. Gao, Y. Chong, B. Zhang, "Topological Acoustics", *Phys. Rev. Lett.* **114**, 114301 (11 2015).

335. J. Ningyuan, C. Owens, A. Sommer, D. Schuster, J. Simon, "Time- and Site-Resolved Dynamics in a Topological Circuit", *Phys. Rev. X* **5**, 021031 (2 2015).

336. V. V. Albert, L. I. Glazman, L. Jiang, "Topological Properties of Linear Circuit Lattices", *Phys. Rev. Lett.* **114**, 173902 (17 2015).

337. W. Hu, J. C. Pillay, K. Wu, M. Pasek, P. P. Shum, Y. D. Chong, "Measurement of a Topological Edge Invariant in a Microwave Network", *Phys. Rev. X* **5**, 011012 (1 2015).

338. C. H. Lee, S. Imhof, C. Berger, F. Bayer, J. Brehm, L. W. Molenkamp, T. Kiessling, R. Thomale, "Topolectrical Circuits", *Communications Physics* **1**, 39 (2018).

339. S. Imhof, C. Berger, F. Bayer, J. Brehm, L. W. Molenkamp, T. Kiessling, F. Schindler, C. H. Lee, M. Greiter, T. Neupert, R. Thomale, "Topolectrical-circuit realization of topological corner modes", *Nature Physics* **14**, 925–929 (2018).

340. T. Hofmann, T. Helbig, C. H. Lee, M. Greiter, R. Thomale, "Chiral Voltage Propagation and Calibration in a Topolectrical Chern Circuit", *Phys. Rev. Lett.* **122**, 247702 (24 2019).

341. C. H. Lee, T. Hofmann, T. Helbig, Y. Liu, X. Zhang, M. Greiter, R. Thomale, "Imaging nodal knots in momentum space through topolectrical circuits", *arXiv:1904.10183* (2019).

342. M. Ezawa, "Non-Hermitian boundary and interface states in nonreciprocal higher-order topological metals and electrical circuits", *Phys. Rev. B* **99**, 121411 (12 2019).

343. M. Ezawa, "Electric circuits for non-Hermitian Chern insulators", *Phys. Rev. B* **100**, 081401 (8 2019).

344. Y. Wang, L.-J. Lang, C. H. Lee, B. Zhang, Y. Chong, "Topologically enhanced harmonic generation in a nonlinear transmission line metamaterial", *Nature communications* **10**, 1102 (2019).

345. T. Helbig, T. Hofmann, C. H. Lee, R. Thomale, S. Imhof, L. W. Molenkamp, T. Kiessling, "Band structure engineering and reconstruction in electric circuit networks", *Phys. Rev. B* **99**, 161114 (16 2019).

346. S. Yao, F. Song, Z. Wang, "Non-Hermitian Chern Bands", *Phys. Rev. Lett.* **121**, 136802 (13 2018).

347. E. J. Bergholtz, J. C. Budich, "Non-Hermitian Weyl physics in topological insulator ferromagnet junctions", *Phys. Rev. Research* **1**, 012003 (1 2019).

348. X. Zhang, J. Gong, "Non-Hermitian Floquet topological phases: Exceptional points, coalescent edge modes, and the skin effect", *Phys. Rev. B* **101**, 045415 (4 2020).

349. B. Höckendorf, A. Alvermann, H. Fehske, "Topological origin of quantized transport in non-Hermitian Floquet chains", *Phys. Rev. Research* **2**, 023235 (2 2020).

350. T. Liu, Y.-R. Zhang, Q. Ai, Z. Gong, K. Kawabata, M. Ueda, F. Nori, "Second-Order Topological Phases in Non-Hermitian Systems", *Phys. Rev. Lett.* **122**, 076801 (7 2019).

351. M. Ezawa, "Non-Hermitian higher-order topological states in nonreciprocal and reciprocal systems with their electric-circuit realization", *Phys. Rev. B* **99**, 201411 (20 2019).

352. E. Edvardsson, F. K. Kunst, E. J. Bergholtz, "Non-Hermitian extensions of higher-order topological phases and their biorthogonal bulk-boundary correspondence", *Phys. Rev. B* **99**, 081302 (8 2019).

353. E. J. Bergholtz, J. C. Budich, F. K. Kunst, "Exceptional Topology of Non-Hermitian Systems", *arXiv:1912.10048* (2019).

354. Y. Ashida, Z. Gong, M. Ueda, "Non-Hermitian Physics", *arXiv:2006.01837* (2020).

355. N. Hatano, D. R. Nelson, "Localization Transitions in Non-Hermitian Quantum Mechanics", *Phys. Rev. Lett.* **77**, 570–573 (3 1996).

356. D. C. Brody, "Biorthogonal quantum mechanics", *Journal of Physics A: Mathematical and Theoretical* **47**, 035305 (2013).

357. A. Mostafazadeh, "Pseudo-Hermiticity versus PT symmetry: The necessary condition for the reality of the spectrum of a non-Hermitian Hamiltonian", *Journal of Mathematical Physics* **43**, 205–214 (2002).

358. D. Bernard, A. LeClair, "A Classification of Non-Hermitian Random Matrices", *Statistical Field Theories*, 207–214 (2002).

359. H. Zhou, J. Y. Lee, "Periodic table for topological bands with non-Hermitian symmetries", *Phys. Rev. B* **99**, 235112 (23 2019).

360. J. C. Budich, J. Carlström, F. K. Kunst, E. J. Bergholtz, "Symmetry-protected nodal phases in non-Hermitian systems", *Phys. Rev. B* **99**, 041406 (4 2019).

361. C.-H. Liu, H. Jiang, S. Chen, "Topological classification of non-Hermitian systems with reflection symmetry", *Phys. Rev. B* **99**, 125103 (12 2019).

362. H. Xu, D. Mason, L. Jiang, J. G. E. Harris, "Topological energy transfer in an optomechanical system with exceptional points", *Nature* **537**, 80–83 (2016).

363. A. Guo, G. J. Salamo, D. Duchesne, R. Morandotti, M. Volatier-Ravat, V. Aimez, G. A. Siviloglou, D. N. Christodoulides, "Observation of $\mathcal{PT}$-Symmetry Breaking in Complex Optical Potentials", *Phys. Rev. Lett.* **103**, 093902 (9 2009).

364. H. Hodaei, A. U. Hassan, S. Wittek, H. Garcia-Gracia, R. El-Ganainy, D. N. Christodoulides, M. Khajavikhan, "Enhanced sensitivity at higher-order exceptional points", *Nature* **548**, 187–191 (2017).

365. A. A. Mailybaev, O. N. Kirillov, A. P. Seyranian, "Geometric phase around exceptional points", *Phys. Rev. A* **72**, 014104 (1 2005).

366. C. Dembowski, B. Dietz, H.-D. Gräf, H. L. Harney, A. Heine, W. D. Heiss, A. Richter, "Encircling an exceptional point", *Phys. Rev. E* **69**, 056216 (5 2004).

367. K. Zhang, Z. Yang, C. Fang, "Correspondence between winding numbers and skin modes in non-hermitian systems", *arXiv:1910.01131* (2019).

368. F. Song, S. Yao, Z. Wang, "Non-Hermitian Topological Invariants in Real Space", *Phys. Rev. Lett.* **123**, 246801 (24 2019).

369. L. Herviou, J. H. Bardarson, N. Regnault, "Defining a bulk-edge correspondence for non-Hermitian Hamiltonians via singular-value decomposition", *Phys. Rev. A* **99**, 052118 (5 2019).

370. K. Yokomizo, S. Murakami, "Non-Bloch Band Theory of Non-Hermitian Systems", *Phys. Rev. Lett.* **123**, 066404 (6 2019).

371. L. Li, C. H. Lee, S. Mu, J. Gong, "Critical non-Hermitian Skin Effect", *arXiv:2003.03039* (2020).

372. L. Xiao, T. Deng, K. Wang, G. Zhu, Z. Wang, W. Yi, P. Xue, "Non-Hermitian bulk–boundary correspondence in quantum dynamics", *Nature Physics* (2020).

373. T. Helbig, T. Hofmann, S. Imhof, M. Abdelghany, T. Kiessling, L. W. Molenkamp, C. H. Lee, A. Szameit, M. Greiter, R. Thomale, "Generalized bulk–boundary correspondence in non-Hermitian topolectrical circuits", *Nature Physics* **16**, 747–750 (2020).

374. F. Song, S. Yao, Z. Wang, "Non-Hermitian Skin Effect and Chiral Damping in Open Quantum Systems", *Phys. Rev. Lett.* **123**, 170401 (17 2019).

375. S. Murakami, "Phase transition between the quantum spin Hall and insulator phases in 3D: emergence of a topological gapless phase", *New Journal of Physics* **9**, 356–356 (2007).

376. F. Evers, A. D. Mirlin, "Anderson transitions", *Rev. Mod. Phys.* **80**, 1355–1417 (4 2008).

377. C. H. Lee, G. Li, Y. Liu, T. Tai, R. Thomale, X. Zhang, "Tidal surface states as fingerprints of non-Hermitian nodal knot metals", *arXiv:1812.02011* (2018).

378. S. Manna, B. Pal, W. Wang, A. E. B. Nielsen, "Anyons and fractional quantum Hall effect in fractal dimensions", *Phys. Rev. Research* **2**, 023401 (2 2020).

379. A. Amaricci, J. C. Budich, M. Capone, B. Trauzettel, G. Sangiovanni, "First-Order Character and Observable Signatures of Topological Quantum Phase Transitions", *Phys. Rev. Lett.* **114**, 185701 (18 2015).

380. B. Roy, P. Goswami, J. D. Sau, "Continuous and discontinuous topological quantum phase transitions", *Phys. Rev. B* **94**, 041101 (4 2016).

381. J. Imriška, L. Wang, M. Troyer, "First-order topological phase transition of the Haldane-Hubbard model", *Phys. Rev. B* **94**, 035109 (3 2016).

382. V. Juričić, D. S. L. Abergel, A. V. Balatsky, "First-order quantum phase transition in three-dimensional topological band insulators", *Phys. Rev. B* **95**, 161403 (16 2017).

383. B. M. Wojek, P. Dziawa, B. J. Kowalski, A. Szczerbakow, A. M. Black-Schaffer, M. H. Berntsen, T. Balasubramanian, T. Story, O. Tjernberg, "Band inversion and the topological phase transition in (Pb,Sn)Se", *Phys. Rev. B* **90**, 161202 (16 2014).

384. W. Chen, M. Legner, A. Rüegg, M. Sigrist, "Correlation length, universality classes, and scaling laws associated with topological phase transitions", *Phys. Rev. B* **95**, 075116 (7 2017).

385. M. Geier, I. C. Fulga, A. Lau, "Bulk-boundary-defect correspondence at disclinations in crystalline topological insulators and superconductors", *arXiv:2007.13781* (2020).

386. R. Queiroz, I. C. Fulga, N. Avraham, H. Beidenkopf, J. Cano, "Partial Lattice Defects in Higher-Order Topological Insulators", *Phys. Rev. Lett.* **123**, 266802 (26 2019).

387. B. Roy, V. Juričić, "Dislocation as a bulk probe of higher-order topological insulators", *arXiv:2006.04817* (2020).

388. A. Tiwari, A. Jahin, Y. Wang, "Chiral Dirac Superconductors: Second-order and Boundary-obstructed Topology", arXiv:2005.12291 (2020).

389. M. G. Vergniory, L. Elcoro, C. Felser, N. Regnault, B. A. Bernevig, Z. Wang, "A complete catalogue of high-quality topological materials", *Nature* **566**, 480–485 (2019).

390. F. Tang, H. C. Po, A. Vishwanath, X. Wan, "Topological materials discovery by large-order symmetry indicators", *Science Advances* **5** (2019).

391. T. Olsen, E. Andersen, T. Okugawa, D. Torelli, T. Deilmann, K. S. Thygesen, "Discovering two-dimensional topological insulators from high-throughput computations", *Phys. Rev. Materials* **3**, 024005 (2 2019).

392. E. Lee, H. Lee, B.-J. Yang, "Many-body approach to non-Hermitian physics in fermionic systems", *Phys. Rev. B* **101**, 121109 (12 2020).

393. H. Jiang, L.-J. Lang, C. Yang, S.-L. Zhu, S. Chen, "Interplay of non-Hermitian skin effects and Anderson localization in nonreciprocal quasiperiodic lattices", *Phys. Rev. B* **100**, 054301 (5 2019).

394. J. Claes, T. L. Hughes, "Skin effect and winding number in disordered non-Hermitian systems", *arXiv:2007.03738* (2020).

395. K. Kawabata, M. Sato, K. Shiozaki, "Higher-order non-Hermitian skin effect", arXiv:2008.07237 (2020).

396. Y. Fu, S. Wan, "Non-Hermitian Second-Order Skin and Topological Modes", arXiv:2008.09033 (2020).

397. R. Okugawa, R. Takahashi, K. Yokomizo, "Second-order topological non-Hermitian skin effects", arXiv:2008.03721 (2020).

398. T. Yoshida, R. Peters, N. Kawakami, "Non-Hermitian perspective of the band structure in heavy-fermion systems", *Phys. Rev. B* **98**, 035141 (3 2018).

399. M. Nakagawa, N. Kawakami, M. Ueda, "Non-Hermitian Kondo Effect in Ultracold Alkaline-Earth Atoms", *Phys. Rev. Lett.* **121**, 203001 (20 2018).

400. T. Yoshida, K. Kudo, Y. Hatsugai, "Non-Hermitian fractional quantum Hall states", *Scientific Reports* **9**, 16895 (2019).

401. B. Sporkmann, H. Bross, "Calculation of Wannier functions for fcc transition metals by Fourier transformation of Bloch functions", *Phys. Rev. B* **49**, 10869–10876 (16 1994).

402. B. Sporkmann, H. Bross, "Calculation of Wannier functions for zinc-blende-type semiconductors", *Journal of Physics: Condensed Matter* **9**, 5593–5608 (1997).

403. R. Resta, "Quantum-Mechanical Position Operator in Extended Systems", *Phys. Rev. Lett.* **80**, 1800–1803 (9 1998).

CURRICULUM VITAE

PERSONAL DATA

Name	Marta Agnieszka Brzezińska
Date of Birth	August 22, 1991
Place of Birth	Legnica, Poland

EDUCATION

since 2015	Ph. D. in Physics, Faculty of Fundamental Problems of Technology, Wrocław University of Science and Technology, Poland Supervisors: Prof. Arkadiusz Wójs, Prof. Titus Neupert
2013 – 2015	M. Sc. in Physics (specialization: Physical Foundations of Computer Science), Faculty of Fundamental Problems of Technology, Wrocław University of Science and Technology, Poland Thesis: Entanglement entropy in d-dimensional interacting many-body systems Supervisor: Prof. Arkadiusz Wójs *Grade:* 5.5 (excellent)
2010 – 2013	B. Sc. in Physics, Faculty of Fundamental Problems of Technology, Wrocław University of Science and Technology, Poland *Grade:* 5.0 (very good)

SCHOLARSHIPS & AWARDS

Apr 2020	University scholarship from the Own Scholarship Fund of Wrocław University of Science and Technology
Nov 2019	Rector's Award for Best PhD Students in the academic year 2018/2019, Wrocław University of Science and Technology
Sep 2019 – Aug 2020	The Iwanowska Programme for Doctoral Students from Polish National Agency for Academic Exchange (NAWA)
Oct 2018 – Sep 2019	Statutory Grant of the Wrocław University of Science and Technology for Young Researches
Sep 2018 – Aug 2019	Swiss Government Excellence Scholarship from Federal Commission for Scholarships for Foreign Students
Jun 2015	Dean's Award for Best Students, Wrocław University of Science and Technology